Oceanic cycling of rare earth elements and the application of Nd isotopes to assess changes in Mesozoic ocean circulation

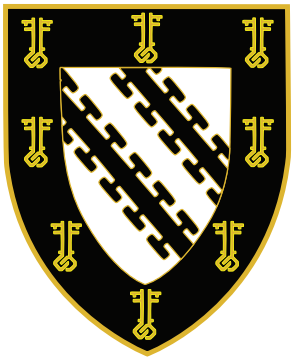

by

Xin-Yuan Zheng

(郑新源)

Thesis submitted to University of Oxford for the degree of Doctor of Philosophy

Department of Earth Sciences

Exeter College

Michaelmas Term 2013

Supervisors: Dr. Gideon M. Henderson & Dr. Hugh C. Jenkyns

Oceanic cycling of rare earth elements and the application of Nd isotopes to assess changes in Mesozoic ocean circulation

Xinyuan Zheng
Department of Earth Sciences & Exeter College, University of Oxford
Michaelmas Term 2013
Thesis submitted to University of Oxford for the degree of Doctor of Philosophy

ABSTRACT

Rare earth elements (REEs) and their isotopes (such as Nd isotopes) can be potentially used to trace a wide range of oceanic processes in both modern and ancient oceans, but their successful application as tracers requires a comprehensive understanding of REE cycling in the modern ocean.

Previous studies of REEs in seawater were largely constrained by analytical difficulties in generating accurate and precise REE data from seawater, which typically contain REE concentrations at a sub-ppt to ppt level. A new, and relatively simple, analytical method for precise and accurate determination of all dissolved REE concentrations in reasonably small (~100 ml) seawater samples is presented in this thesis.

With the application of the new method, this thesis reports the first full-depth, zonal ocean section of all dissolved REE concentrations, collected during the CoFeMUG cruise along ~12°S in the South Atlantic. The section approach of this study places the distribution of dissolved REE concentrations in a well-constrained hydrographic context, allowing the first quantitative assessment (by an inverse model) of the relative importance of hydrographic controls resulting from advection/mixing of ocean circulation, together with non-conservative controls resulting from local particle scavenging and remineralization, in controlling the distribution of dissolved REEs in this region. A noteworthy decoupling of Ce and Mn with respect to their cycling in the water column was also observed in this study.

The application of Nd isotopes as a tracer to reconstruct changes in ocean circulation in the NW European chalk shelf sea during rapid climatic events, including the mid-Cenomanian Event and oceanic anoxic event 2 (OAE 2), suggests a tight coupling between ocean circulation and transient climatic cooling during the general warm Late Cretaceous. An advected volcanic signal during OAE 2 was registered in the seawater Nd-isotope record from the English Chalk, probably suggesting a period of enhanced ocean ventilation/mixing at this time.

Oceanic cycling of rare earth elements and the application of Nd isotopes to assess changes in Mesozoic ocean circulation

Xinyuan Zheng

Department of Earth Sciences & Exeter College, University of Oxford

Michaelmas Term 2013

Thesis submitted to University of Oxford for the degree of Doctor of Philosophy

EXTENDED ABSTRACT

This thesis considers rare earth elements (REEs) and Nd isotopes in oceanic environments. REEs and their isotopes (such as Nd isotopes) can be potentially used to trace a wide range of oceanic processes in both modern and ancient oceans, but their successful application as reliable tracers requires a comprehensive understanding of REE cycling in the modern ocean. The thesis contains essentially two parts of research; the first part is focused on the REE cycling in the modern ocean, and the second part is focused on the application of Nd isotopes to reconstruct ocean circulation during the Cretaceous.

Previous studies of REEs in seawater were largely constrained by analytical difficulties in generating accurate and precise REE data from seawater, which typically contain REE concentrations at a sub-ppt to ppt level. The isotope dilution thermal ionization mass spectrometry (ID–TIMS) method offers some of the best REE data in terms of precision and accuracy, using typical ~1L seawater. But the ID–TIMS method is labour-intensive and cannot determine 4 monoisotopic rare earth elements (Pr, Tb, Ho and Tm). In Chapter 2, a new, and relatively simple, analytical method for precise and accurate determination of all dissolved REE concentrations is presented. The new method involves the use of the isotope-dilution method on only 3 rare earth elements (Ce, Nd and Yb), and an inductively coupled mass spectrometer (ICP-MS) with a desolvating sample introduction system, routinely producing

concentration data of all dissolved REEs (*d*REE) at precision of <3% (1σ) on relatively small seawater samples (~100 ml). Compared to the ID–TIMS method, this new method allows simultaneous determination of all 14 naturally occurring REEs at similarly high precision, but uses smaller samples, and has higher sample throughput. Clearly, the new method is more advantageous than the ID–TIMS in generating high-quality seawater REE data.

With the application of the new method, this thesis reports the first full-depth, zonal ocean section of all dissolved REE concentrations, collected during the CoFeMUG cruise along ~12°S in the South Atlantic (Chapter 3). The new dataset largely fills the gap in study of the REE cycling in the South Atlantic. The distribution of *d*REE concentrations in the upper water column (<~1000 m) is affected by coastal REE inputs and the cycling of Fe and Mn associated with their redox transformation in a subsurface oxygen minimum zone (OMZ) near the continental shelf of Africa. In deep water (>1000 m), *d*REE data were analyzed by an inverse model to quantitatively assess the relative importance of hydrographic controls resulting from advection/mixing of ocean circulation, together with non-conservative controls resulting from local particle scavenging and remineralization, in affecting the distribution of dissolved REEs in this region. The modelling results suggest a large hydrographic control (>80%) on the distribution of dissolved REE concentrations in deep waters (>~1000 m) at ~12°S. REE additions in the deep Angola Basin (>1000 m) are apparent at two water depths, namely ~1500 m and >~4000 m, near the continental margin of Africa. The shallower *d*REE addition may result from advected metal-rich waters from reducing sediments on the margin, and the deeper addition is more likely to be caused by remineralization of particles *in-situ* in the water column, or in bottom sediments.

Ce concentrations and Ce anomalies in surface waters are possibly controlled by a dynamic balance between O_2-dependent Ce oxidation and a REE-input effect. At depth of ~1500 m, a prominent decoupling of the marine cycling of Ce and Mn was observed, although the cause of this phenomenon remains unknown.

In the second half of this thesis, Nd isotopes, recovered primarily from fossil fish debris in the English Chalk, are adopted as a tracer to reconstruct changes in ocean circulation in the NW European shelf sea during two rapid climatic events, namely oceanic anoxic event 2 (OAE 2) at the Cenomanian–Turonian boundary (Chapter 4) and the mid-Cenomanian Event during the middle Cenomanian (Chapter 5).

The high-resolution Nd-isotope record from the English Chalk at Eastbourne shows a well-resolved negative ε_{Nd} excursion, immediately followed by a positive ε_{Nd} excursion during OAE 2. The former negative ε_{Nd} excursion is interpreted as due to a stronger influence of northerly-sourced watermasses (probably the Boreal Sea) in the bottom ocean of the NW European shelf sea, in coincidence with the onset of a transient cooling episode during OAE 2. The later positive ε_{Nd} excursion is interpreted as due to an advected volcanic signal, associated with eruptions of the High Arctic large igneous province (LIP) and/or the Caribbean LIP. The registration of this advected volcanic signal in the European shelf sea may suggest a period of enhanced ocean ventilation/mixing during the transient cooling episode within OAE 2.

The high-resolution Nd-isotope record across the mid-Cenomanian Event in the NW European shelf sea is featured by two negative ε_{Nd} excursions. Similar to the interpretation of the negative ε_{Nd} excursion observed at Eastbourne during OAE 2, the two negative ε_{Nd} excursions during the mid-Cenomanian Event are explained as due to increased influence of boreal seawater in the NW European shelf sea. Strikingly,

the two negative ε_{Nd} excursions coincide with two discrete beds containing unique boreal index faunas. Similar intrusion of boreal faunas occurred during OAE 2 (i.e. "the Plenus Cold Event"), and was considered as an indication of a climate cooling. The southward migration of the same or similar faunas during the mid-Cenomanian Event, therefore, may also suggest a cooling. The coincidence of the two negative ε_{Nd} excursions and the two beds containing the boreal faunas indicates a tight coupling of changes in ocean circulation in the NW European shelf sea and climate (i.e. cooling). This phenomenon is the same as observed from the Nd-isotope record during OAE 2, suggesting recurrent changes in ocean circulation in the NW European shelf sea in response to climatic cooling. In contrast, no positive ε_{Nd} excursion was observed during the mid-Cenomanian event, when LIP volcanism was probably weak. This observation reinforces our interpretation of the positive ε_{Nd} excursion during OAE 2 as due to an advected volcanic signal, rather than a sole change in ocean circulation as proposed in previous studies.

ACKNOWLEDGEMENTS

I would like to firstly thank my supervisors Dr. Gideon Henderson and Dr. Hugh Jenkyns, who have been invaluable sources of scientific inspiration and guidance. Their wisdom about science has not only helped me with the research conducted in this thesis, but also shaped my general views towards how to discover and approach important scientific questions. It is my great privilege and honor to learn from them during my D.Phil at Oxford.

I also would like to thank my collaborators – Andy Gale, David Ward, Mak Saito and Abigail Noble – who made samples available to me, and also contributed thoughts during interpretations of results. My gratitude also goes to Yves Plancherel who firstly directed my attention to the OMP method, and drowned me in his sea of knowledge on statistics and various oceanographic and climatic models, and kindly offered his help on commenting a bulk portion of this thesis. Steve Wyatt, Phil Holdship, Nick Belshaw and Andrew Mason are gratefully thanked for their help offered at the time I worked in clean lab or ran mass spectrometers. Thanks to Samar Khatiwala for teaching me his magic Transport Matrix Model, and introducing great food in the NYC during my visit at LDEO. Special thanks go to all current and past members of the Climotope Group, who have been always friendly to me, and helpful during discussions on my research. My research of course would not be possible without financial supports from various individuals and funding agencies, including the Clarendon Scholarship from Oxford University, Mr. Alan Lammin who generously established the Mandarin Scholarship at Exeter College, the Burdett Coutts Funds at the Department of Earth Sciences, Chinese Student Awards from the Great Britain-China Educational Trust, W Wing Yip & Brothers Bursaries and a charitable trust that would like to remain anonymous to the public.

I am grateful to all my friends in and outside the department, who made my time at Oxford enjoyable and amazing experiences. Particularly, the small Chinese community in the department, including Alan, Chao, Crystal, Feifei, Jie, Linhao, Qingfeng, Qiong, Weimu and Yu, is extremely supportive.

Finally, I would like to express my deepest appreciation to my wife, Beibei Zhu, and my parents whose love and supports are the strongest impetus inspiring me to accomplish this degree.

CONTENT

FIGURE LIST

TABLE LIST

Chapter 1

Introduction

This thesis mainly considers rare earth elements (REEs) and an isotopic system of one element in the REE-group, namely neodymium (Nd) isotopes, in oceanic environments. The study comprises two parts; one is to understand the modern cycling of dissolved REEs, with a case study in the water column of the South Atlantic, and the other is to probe changes in ocean circulation during the Cretaceous by using Nd isotopes as a tracer. Although the two projects are somewhat distinct in terms of timescales and primary foci, they are intrinsically linked by the fact that a comprehensive understanding of cycling of these trace-metals in modern seawater can shed light on both the potential, and also the limitations, of applying REEs and their isotopes as tracers to reconstruct the past.

The thesis can be divided broadly into four main parts, organized as follows: (1) the first part is Chapter 1, which gives a brief overview of background relevant to research reported in this thesis, and motivations for each study; (2) The second part is composed of Chapters 2–3, which report the analytical approach and the results for the measurement of dissolved REEs in modern seawater. Chapter 2 describes development of a new analytical protocol that permits highly precise and accurate determinations of all naturally occurring REEs in seawater, using reasonably small samples (~100 ml). Chapter 3 presents a new dataset of dissolved REE concentrations, obtained with the new analytical protocol, in the subequatorial South Atlantic along ~12°S. The new dataset offers the first full-depth, E–W zonal section of all 14 dissolved REEs in the South Atlantic, enabling a relatively comprehensive

investigation of oceanic distributions of dissolved REEs in this region, and various processes that control the observed REE-distributions; (3) Part three includes Chapters 4–5 (and Appendix A), which are focused on reconstructions of Cretaceous ocean circulation, using Nd isotopes primarily preserved in fossil fish debris. Respectively, Chapter 4 and 5 report two high-resolution Nd-isotope records from the English chalk, spanning the oceanic anoxic event 2 (OAE 2) at the Cenomanian–Turonian stage boundary, and the Mid-Cenomanian Event (MCE) during the middle Cenomanian. These records offer new insights into the coupling between ocean circulation in the Late Cretaceous NW European chalk shelf sea and rapid perturbations in the global carbon cycle. Details on the methodology of measuring Nd isotopes in fossil fish debris are given in the Appendix A; (4) the final part is Chapter 6, which provides a brief summary of the above studies, and proposes directions for future research.

1.1 Studying cycling of rare earth elements in the modern ocean

1.1.1 Rare earth elements in the ocean

Rare earth elements (REEs), also known as the lanthanides, are a collection of 15 elements with atomic numbers from 57 (lanthanum, La) to 71 (lutetium, Lu) (Figure 1.1). Because promethium (Pm) – an element in the REE-group – is radioactive, and rarely occurs naturally, only 14 elements in the group are of interest in most geosciences research. Frequently, the REE-group is referred to as two sub-groups of light rare earth elements (LREEs; lanthanum–gadolinium) and heavy rare earth elements (HREEs; terbium–lutetium), or three sub-groups with an additional one of middle rare earth elements (MREEs: europium–dysprosium) between LREEs and HREEs. The division of these sub-groups is somewhat subjective, and varies

slightly from author to author. It is important to note that the division of these sub-groups is mostly for the convenience of discussion, rather than being an indication of abrupt changes in behaviour between sub-groups, as chemical properties of REEs show a gradual change across the series.

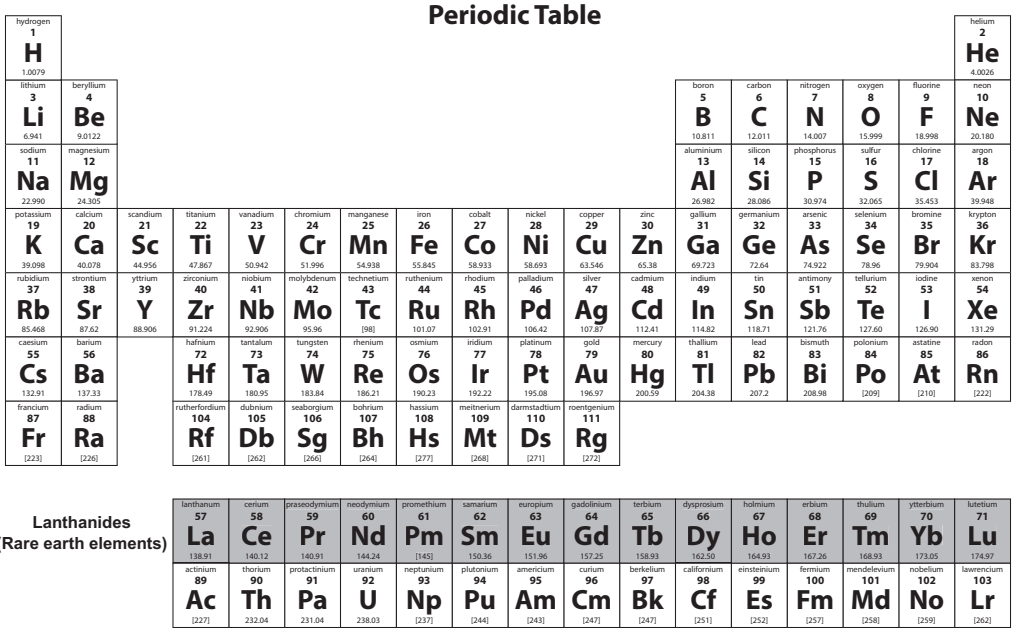

Figure 1.1 Positions of the rare earth elements in the periodic table

Chemical properties of REEs exhibit subtle, but systematic, variations across the group, due to a progressive decrease in their ionic radii from La to Lu – a phenomenon known as lanthanide contraction, due to the poor shielding effect of the 4f electrons (Figure 1.2). This chemical coherence, varying in a predictable way across the group, makes REEs a unique set of tracers for a wide range of geological processes under both high- and low-temperature conditions (e.g. Elderfield et al., 1988; Hanson, 1980). This is because processes that lead to relative fractionations among the REE-group can be conveniently detected by comparing elements with one another. This is the primary reason why REEs have attracted considerable attention in research of geosciences over the past several decades.

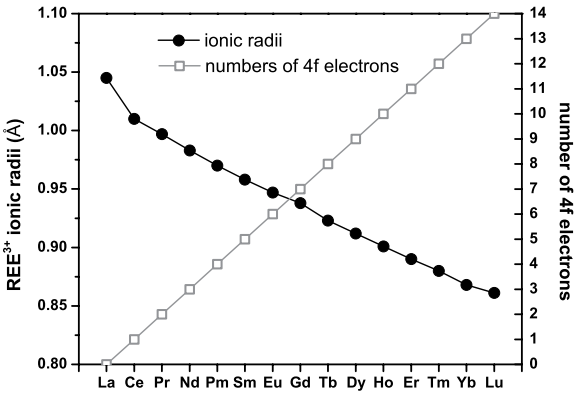

Figure 1.2 The progressive decrease in ionic radii from La to Lu (i.e. lanthanide contraction) is accompanied by gradually filling in 4f electrons (data from Encyclopædia Britannica online, http://www.britannica.com/EBchecked/topic/491579/rare-earth-element?anchor=ref622029)

The inter-elemental comparison between REEs in samples of interest is usually achieved through examining their "REE-patterns", which are normalized to REE-values of a reference material. Selection of a reference for REE-normalization depends on the purpose of each study. Commonly, chondrites are chosen as a reference for studies of high-temperature processes, and average shales, such as Post-Archean Australian Shale (PAAS) (Table 1.1), are selected for studies of low-temperature processes, including oceanography. The purpose of normalization is twofold: (1) it removes rhythmic variations in natural abundance of elements that result from the odd-even effect (Figure 1.3); and (2) it makes small fractionations between various REEs in the group more easily perceptible.

Table 1.1

REE values of PAAS

PAAS[1]	La	Ce	Pr	Nd	Sm	Eu	Gd	Tb	Dy	Ho	Er	Tm	Yb	Lu
(ppm)	38.200	79.600	8.830	33.900	5.550	1.080	4.660	0.774	4.680	0.991	2.850	0.405	2.820	0.433

[1] data from McLennan (1989).

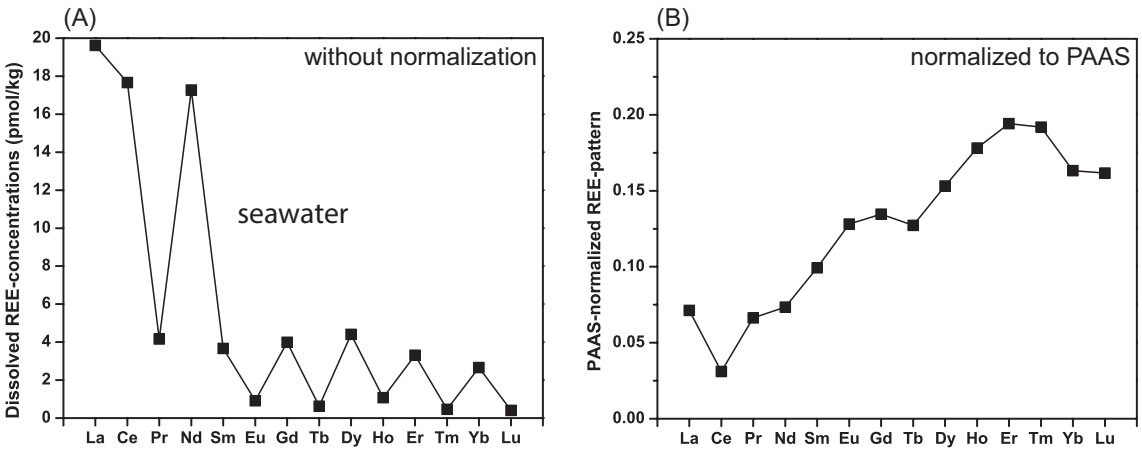

Figure 1.3 (A) An example of the seawater REE-pattern without normalization. (B) The shale- (PAAS) normalized REE-pattern of the same data. Dissolved REE data in the figure are from a surface sample reported in Chapter 3 of this thesis.

There are wide applications of REEs in the geosciences, but this thesis only considers REEs in the ocean. Pioneering work on REEs in the ocean emerged in the 1960s (e.g. Balashov and Khitrov, 1961; Goldberg et al., 1963; Høgdahl et al., 1968), offering a first glimpse of the oceanic behaviour of REEs. However, early studies faced huge challenges in clean sampling of trace metals from seawater and instrumental analysis, due to low REE concentrations (typically at parts per trillion; ppt) in seawater. Early oceanic REE-data were, therefore, limited in numbers, and generally of low precision and accuracy.

Although it remains an analytical challenge, with the development of clean sampling techniques for trace metals at sea and improved in-house analytical instruments, high-quality seawater REE data have gradually become available since the 1980s. Isotope-dilution thermal ionization mass spectrometry (ID-TIMS) and neutron activation analysis were two major analytical approaches that were adopted to produce high-quality seawater REE data in the 1980s (e.g. Elderfield and Greaves, 1982; De Baar et al., 1983), and then inductively coupled plasma mass spectrometer

(ICP-MS) came into play in the 1990s (e.g. Zhang and Nozaki, 1996). Analytical developments enabled studies on REEs in hydrothermal fluids, rivers, dust and marine particulates, aiming at quantifying sources and sinks of REEs in the ocean (e.g. Alibo and Nozaki, 1999; Elderfield et al., 1990; German et al., 1990; Goldstein and Jacobsen, 1988; Greaves et al., 1994; Klinkhammer et al., 1994; Nozaki and Alibo, 2003; Sholkovitz et al., 1994). Meanwhile, laboratory experiments and theoretical calculations were also conducted to understand the physicochemical controls on the behaviour of REEs in seawater (e.g. Byrne and Kim, 1990; Lee and Byrne, 1992; Millero, 1992; Wood, 1990a; Wood, 1990b). A general picture of the oceanic geochemistry of REEs and their cycling in the ocean has become clearer with these joint efforts.

Oceanic geochemistry and cycling of REEs have been overviewed in detail in previous literature (e.g. Byrne and Sholkovitz, 1996; Elderfield et al., 1988; Nozaki, 2001a), and only a brief summary, together with an overview of recent advances, is given here. All REEs predominately exist as REE^{3+} in seawater, although Ce and Eu have an additional oxidation state of 4+ and 2+ respectively. Carbonate (CO_3^{2-}) complexes are commonly thought as the dominant species of dissolved REEs in seawater (e.g. Byrne and Sholkovitz, 1996), while REE-complexes with silicic acid ($Si(OH)_4$) are recently proposed as a neglected, but quantitatively important species in large areas of the ocean, such as the surface ocean and the deep Pacific (Akagi, 2013; Akagi et al., 2011). In hydrothermal fluids, chloride and fluoride complexes dominate the REE-species (e.g. Craddock et al., 2010; Douville et al., 1999; Wood, 1990a). Organic ligands impose important influence on solution complexation of many trace metals, such as iron (Fe) and copper (Cu), in seawater (e.g. Sander and Koschinsky, 2011; Sander et al., 2007), but their influence on complexation of REEs in marine

environments is not well understood. Early studies suggest that organic ligands do not significantly change solution complexation of REEs, but their presence outside marine particulates as organic films greatly affects scavenging of REEs onto particles, enhancing preferential scavenging of LREEs (e.g. Byrne and Kim, 1990; Byrne and Sholkovitz, 1996). A recent laboratory study, however, found that trihydroxamate siderophore desferrioxamine B (DFOB), which is an organic ligand with extremely strong affinity for Fe^{3+}, can be bound with REEs to form complexes that are many orders of magnitude more stable than the carbonate complexes at seawater ionic strength (Christenson and Schijf, 2011). An incubation experiment indicates that the presence of DFOB significantly promotes mobilization of REEs from volcanic ashes into river waters, leading to speculation on the potential importance of siderophore-promoted REE-mobilization from shelf sediments to the ocean (Bau et al., 2013). The results of recent experiments imply that organic ligands may play an important role in REE cycling in the ocean, but it is clear that further studies are required to validate/invalidate this conjecture.

Rivers and atmospheric dust are traditionally considered as major sources of REEs to the ocean, but recent studies on Nd isotopes in seawater suggest that sedimentary sources from continental margins are likely to be more important than rivers and dust, at least for Nd. REE concentrations in rivers are significantly (typically hundreds of times) higher than those in seawater, and REE-patterns of river waters are highly variable, showing a strong pH-dependence (e.g. Elderfield et al., 1990; Goldstein and Jacobsen, 1988). Direct input of dissolved REEs from rivers to seawater has to overcome intense REE-removal that occurs at low-salinity (~0-5) regions of estuaries due to coagulation of colloidal REEs (e.g. Elderfield et al., 1990; Sholkovitz, 1995). It is estimated that ~70-95% of riverine LREEs, and ~40-70% of

riverine HREEs, is removed in estuaries (Sholkovitz, 1995). Riverine particles deposited in sediments in the high-salinity regions of estuaries, however, can release dissolved REEs into coastal seawater, acting as a source of REEs to the ocean (e.g. Sholkovitz, 1995). Partial dissolution of atmospheric dust is another important source (at least locally) of REEs to seawater (e.g. Greaves et al., 1994; Rickli et al., 2010; Tachikawa et al., 1999a), and REE-fluxes from partial dissolution of atmospheric dust are estimated to be ~30-130% of riverine REE-fluxes globally (Greaves et al., 1994). Sediments deposited along continental margins have been increasingly recognized as an important source of Nd to seawater, based on studies of Nd isotopes in seawater (e.g. Jeandel et al., 2007; Lacan and Jeandel, 2005b). Modelling studies suggest that fluxes of Nd from continental margins are estimated to be ~1×10^{10} g/yr, much higher than Nd-fluxes from river discharge (~2.6-3.4$\times10^{8}$ g/yr) and partial dissolution of dust (~1.0-2.6$\times10^{8}$ g/yr) (e.g. Arsouze et al., 2009; Rempfer et al., 2011). Few studies have tried to quantify fluxes of other REEs from continental margins to the ocean, but REE-patterns of seawater in several regions of the ocean do show evidence of lithogenic input from continental margins to the ocean (e.g. Sholkovitz et al., 1999; Zhang et al., 2008). Given the overall similarity of chemical behaviour of the various REEs, sedimentary sources from continental margins may also play a vitally important role in delivering other REEs to the ocean.

Hydrothermal input is usually believed to have a negligible impact on the global budget of dissolved REEs in the ocean. Although hydrothermal fluids typically exhibit REE concentrations as much as three orders of magnitude higher than seawater, hydrothermally derived REEs are quickly removed from the water column by scavenging onto Fe-Mn oxides near venting sites (e.g. Douville et al., 1999; German et al., 1990; Halliday et al., 1992; Mitra et al., 1994). Hydrothermal fluids

normally possess excessive Eu in their chondrite-normalized REE-patterns compared to Sm and Gd values. This is known as a "Eu anomaly" (e.g. Douville et al., 1999; Mitra et al., 1994) (Figure 1.4). Although Eu has two valence states (3+ and 2+), redox of Eu does not occur at low-temperature conditions. The observed large Eu positive anomalies have been attributed either to dissolution of plagioclase enriched in Eu due to substitution of Ca^{2+} by Eu^{2+} during magmatic processes (e.g. Douville et al., 1999), or elemental partitioning between fluids and minerals controlled by fluid chemistry (e.g. Allen and Seyfried Jr, 2005; Craddock et al., 2010).

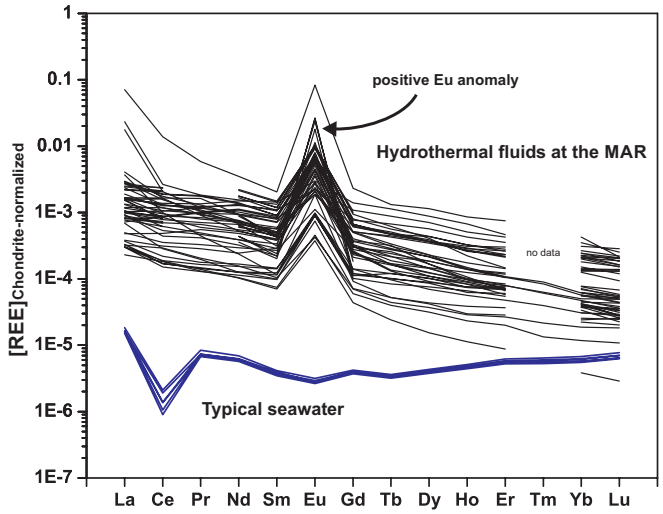

Figure 1.4 Chondrite-normalized REE patterns of hydrothermal fluids collected at the Mid-Atlantic Ridge, and those of typical seawater. REE patterns of hydrothermal fluids show prominent positive Eu anomalies. REE data from hydrothermal fluids are compiled from the literature (see Chapter 3). Seawater REE data are from this study (Chapter 3).

Dissolved REEs in the ocean are mainly removed via particle scavenging. Fe-Mn oxides or organics outside marine particles are thought to be the main carriers of seawater REEs during scavenging (e.g. Byrne and Kim, 1990; Sholkovitz et al., 1994). REE affinity to marine particles gradually decreases from LREEs to HREEs, because of the increased carbonate complexation from La to Lu in solution.

Preferential scavenging of dissolved LREEs over HREEs in seawater, therefore, results in a monotonic increase in REE-patterns from La to Lu, except for Ce (Figure 1.5). Cerium behaves differently in seawater from its neighbouring elements (i.e. La, Pr), because of its redox transformation between Ce^{3+} and Ce^{4+} under typical low-temperature oceanic environments. In addition to Ce removal by particle scavenging, oxidation of Ce^{3+} to insoluble Ce^{4+} removes Ce from the water column. This additional removal of Ce leads to a deficiency in dissolved Ce concentrations compared to the theoretical values that would result from only particle scavenging of Ce in seawater (as demonstrated by interpolation between its neighbouring elements) (Figure 1.5). This deficiency in Ce concentrations is termed as "Ce anomaly", characterizing oxidative removal of Ce. Compared to other trace metals with redox properties in seawater, such as manganese (Mn), the ability to quantify the oxidative removal of Ce (by comparison with other REE concentrations) makes Ce a powerful monitor of redox processes in the ocean.

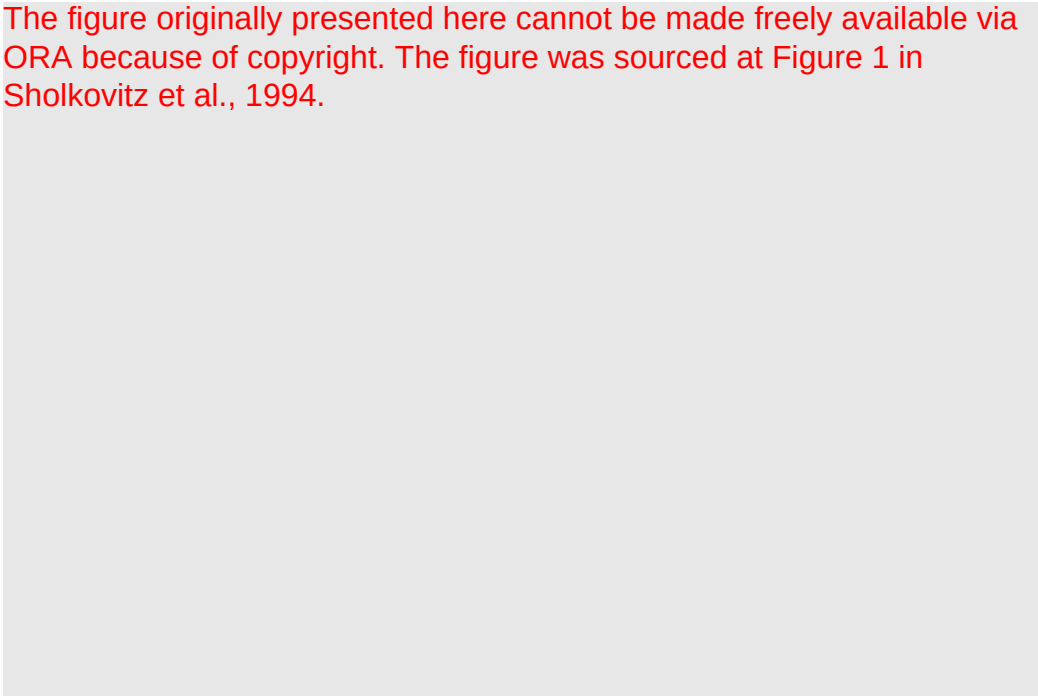

Figure 1.5 A Schematic diagram to describe scavenging of dissolved REEs in seawater by particulates and oxidative removal of Ce. (After Sholkovitz *et al.*, 1994)

1.1.2 Motivations for the thesis chapters on REEs in seawater

Chapter 2: Although reliable data on dissolved REEs in the ocean are available now, it remains an analytical challenge to obtain precise and accurate values, particularly when sample sizes of seawater are limited. The ID-TIMS method has provided some of the best REE data in terms of precision (i.e. <5%, 1σ) and accuracy, using typical sample sizes of 1L seawater (e.g. Greaves et al., 1989). However, the ID-TIMS method is labour-intensive, and has the disadvantage of low sample throughput, because it requires calibration of multiple REE spikes and separation of REEs into at least three fractions (i.e. La and Ce; Nd, Sm, Eu and Gd; Dy, Er and Yb) through column chemistry. In addition, measurement of REEs on TIMS requires preparation of filaments, and long periods of data acquisition on the mass spectrometer. Furthermore, four monoisotopic REEs (i.e. Pr, Tb, Ho and Tm) cannot be measured by this method.

The recent development of online pre-concentration systems, coupled to ICP-MS instruments, makes fast measurements of seawater REEs with sample sizes down to several millilitres possible (e.g. Haley and Klinkhammer, 2003; Hathorne et al., 2012). An example of such technique is a commercially available system called "seaFAST", which is able to analyse REEs in ~7 ml seawater with a high sample throughput (~15 min/sample), and requires essentially no pre-treatment of seawater samples (Hathorne et al., 2012). The "seaFAST" system is advantageous for rapid acquisition of REE data from a large suite of seawater samples. However, precision achieved by the seaFAST is ~10% (1σ) (Hathorne et al., 2012), which is outperformed by the ID-TIMS method.

Given that natural variability of REEs in seawater is sometimes only on the order of ten to several tens of percent, higher analytical precision will provide richer

information on the processes controlling their cycling. To approach this goal, a method is required that offers analytical precision of REE-measurement similar to that of the ID-TIMS, but uses smaller sample sizes and has a faster sample throughput. In Chapter 2, a new analytical procedure that combines isotope dilution and ICP-MS is reported to measure REEs in ~100 ml seawater. This method is relatively straightforward, and has a higher sample throughput, compared to ID-TIMS. Although the new protocol is not as easy as the seaFAST, it routinely gives reproducibility <3% (1σ) for all REEs, better than, or comparable to, that achieved by ID-TIMS measurement. The method has been successfully applied to measure a large suite of seawater samples collected from the South Atlantic, as reported in Chapter 3.

Chapter 3: This chapter investigates the distribution of dissolved REEs in the South Atlantic along ~12°S. The study of REE cycling in seawater is ultimately motivated by the prospects of using REEs as tracers for a range of oceanic processes operating in both the modern and ancient oceans. As summarized above (Section 1.1.1), the geochemistry of REEs in seawater, and the ability to distinguish small inter-elemental variations between the REEs make them potential proxies for many oceanic processes, such as metal inputs from difference sources, particle scavenging and redox cycling.

Large datasets of seawater REE concentrations in the ocean are currently lacking, and there is no published ocean section of REE concentrations. Such data would be very valuable in improving understanding of the oceanic behaviour of REEs and their development as tracers.

Since the bloom of studies on REEs in the ocean in 1990s, studies have been increasingly focused on the marine cycling of only Nd, because of the successful application of Nd isotopes as a watermass tracer (see details in section 1.2.1). This

trend of research is demonstrated by a global compilation of data; there are many more published water-column profiles of Nd alone than profiles of other REEs (Figure 1.6). REE data other than Nd from the South Atlantic are particularly sparse, and only available from one station in the Cape Basin at ~40°S (German et al., 1995). However, studying the whole group of REEs provide more information than studying Nd alone. The overall similarity in chemical properties of REEs essentially offers a group of natural analogues for Nd in seawater, and subtle chemical differences of these elements potentially permit clear identification of controlling processes that might not be seen from measurement of Nd (or Nd isotopes) alone.

Despite decades of study on REEs in the ocean, current knowledge on their oceanic cycling is far from complete. This situation is particularly the case at continental margins where cycling of REEs seems to be complicated, as has been assessed from observations of dissolved Nd concentrations and isotopes in the water column (Carter et al., 2012; Lacan and Jeandel, 2005b; Singh et al., 2012). Such work raises largely unanswered questions about the underlying mechanisms and sizes of the boundary fluxes.

A further complication in the cycling of REEs in the ocean comes from recent discoveries of the role of metal-binding organic ligands in governing metal fluxes from hydrothermal systems to seawater. Larger fluxes than previously believed to be possible are observed for trace metals that were thought to be quantitatively removed from the water column near hydrothermal vents, such as Fe (e.g. Klunder et al., 2012; Saito et al., 2013; Sander and Koschinsky, 2011). These new observations raise questions as to whether similar cases apply to REEs. Another uncertainty regarding REE-cycling in the ocean is the relative importance of advective and vertical processes in determining the observed distributions of dissolved REEs in seawater. It

has been proposed that profiles of Nd (and other REEs) in the ocean are controlled by hydrographic signals resulted from the large-scale advection of ocean circulation, together with REE association/disassociation with marine particles as they settle through the water column (e.g. Oka et al., 2009; Siddall et al., 2008). A quantitative understanding on the relative importance of the two processes remains unclear.

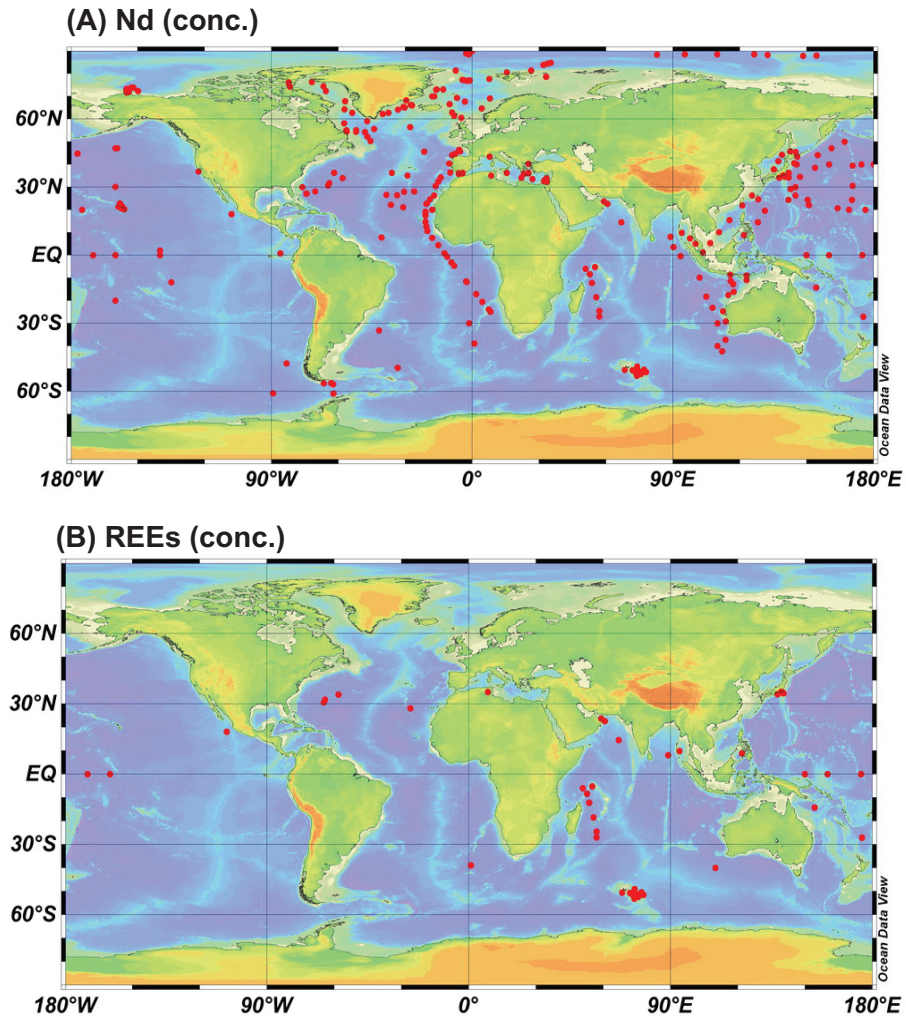

Figure 1.6 (A) Stations having published seawater Nd concentrations, including those having surface values only; (B) Stations having profiles of multiple REEs. (This compilation is a joint effort by X-Y Zheng, P. Scott and Y. Plancherel, and a full version of it, together with sources of the data, is available at http://climotope.earth.ox.ac.uk/data_compilations)

In addition to the use of Nd isotopes as a useful tracer, REEs as a group merit systematic investigation. According to observed oceanic distributions, trace metals in the ocean can be roughly categorized as five types: conservative-type, nutrient-type, scavenged-type, hybrid-type and mixed type (Bruland and Lohan, 2006). REEs are examples of the scavenged-type of trace metals. Studying their distribution, therefore, should provide information about the cycling of other scavenged-type trace metals, such as aluminum (Al). In addition, the behaviour of REEs in the ocean may help studies of trace metals that serve as micronutrients in the ocean. Recently, considerable efforts have been directed to study trace metals (such as Fe) that act as micronutrients in seawater. These trace metals play an important role in biogeochemical cycles that link different spheres of the earth, including the ocean, marine biosphere and atmosphere, into an integrated system. Taking Fe as an example, the lack of dissolved Fe in seawater has been linked to the existence of high-nutrient low-chlorophyll (HNLC) regions covering most of the Southern Ocean and part of the Pacific Ocean. Regional scale Fe fertilization experiments in HNLC regions have confirmed the importance of Fe for marine productivity (Boyd et al., 2007). Changes in the amount of Fe delivered to the ocean may affect biological productivity and hence the ocean uptake of CO_2 from atmosphere. The "Fe hypothesis" that invokes changes in the Fe supply to the ocean with time, especially the South Ocean, has been proposed to account for atmospheric CO_2 variations on glacial-interglacial timescales (Martin, 1990; Sigman and Boyle, 2000). Because Fe (and other similar metal-micronutrients) is a hybrid-type trace element in the ocean (Bruland and Lohan, 2006), its involvement in both biological uptake and abiotic processes, such as particle scavenging, makes studies of its marine cycle difficult. In contrast, REEs are generally not involved in biological processes in the ocean, but

affected by abiotic processes that also affect Fe. Inferences gained through REEs may therefore help to untangle the two processes that affect Fe and other similar metals in seawater. A further motivation to study the REEs is to better understand the redox cycling of Ce, and the potential of this element as a tracer of redox processes in the modern and past ocean.

The above motivations for study of seawater REEs are explored by study of dissolved REEs across a full-depth, zonal section sampled by the CoFeMUG cruise (chief scientist: Mak Saito, WHOI) in the South Atlantic along ~12°S. Compared to previous studies of REEs in seawater which have focused on a small number of oceanographically discrete profiles, this study adopted a section approach that places oceanic distributions of REEs in a well-constrained oceanographic context, making separation of underlying hydrographic and local processes possible. This approach is clearly advantageous for studying marine cycling of REEs themselves. More importantly, a study on other trace metals (including Fe, Mn and Co) from the same section has revealed several features that are of great interest for the study of REEs, including metal inputs from shelf sediments, redox cycling of trace metals in the oxygen minimum zone, and hydrothermal inputs of trace metals (Noble et al., 2012). Comparison between REEs and existing Fe, Mn and Co data allows an exploration of the use of REEs to help in understanding cycling of micronutrient trace metals.

1.2 Reconstructions of Cretaceous ocean circulation with Nd isotopes

1.2.1 Nd isotopes as a tracer for ocean circulation

An excellent example of successful development of REEs and their isotopes as oceanographic tracers is the use of Nd isotopes for reconstructions of ocean circulation in the past. This proxy has been used to explore changes in ocean

circulation during the Cretaceous, and the significance of these changes in relation to both rapid and secular variations in the global carbon cycle.

Neodymium has 7 isotopes – ^{142}Nd, ^{143}Nd, ^{144}Nd, ^{145}Nd, ^{146}Nd, ^{148}Nd and ^{150}Nd. ^{143}Nd is a radiogenic isotope that is produced by α-decay of ^{147}Sm with a half-life of 1.06×10^{11} years ($\lambda = 6.54\times10^{12}$). The use of the Sm–Nd isotopic system in geosciences was firstly envisaged in the 1970s, and initial applications of this system were intended to study high-temperature processes regarding mantle–crust evolution (DePaolo and Wasserburg, 1976; O'Nions et al., 1977). Because natural variability of ^{143}Nd/^{144}Nd ratios in terrestrial samples are very small as a result of the long half-life of ^{147}Sm, it is convenient to use the ε_{Nd}-notation that is defined as follows:

$$\varepsilon_{Nd} = \left(\frac{^{143}Nd/^{144}Nd_{sample}}{^{143}Nd/^{144}Nd_{CHUR}} - 1\right)\times10^{4}$$ (CHUR: chondritic uniform reservoir).

ε_{Nd} values vary with lithology and age of rocks, which can be schematically illustrated as in Figure 1.7. Because Sm is slightly more compatible than Nd as a result of its smaller ionic radius, it retains in the mantle (i.e. depleted mantle) during melting of the primitive silicate earth, and Nd is then preferentially partitioned in the melt (i.e. the crust). Consequently, more radiogenic ^{143}Nd is produced in the mantle because of its higher initial Sm/Nd ratios, leading to positive ε_{Nd} values of the mantle (and mantle-derived rocks) when compared to the CHUR. In contrast, crustal rocks have negative ε_{Nd} values because of their lower initial Sm/Nd ratios inherited when being fractionated from the bulk earth.

Shortly after the inception of the use of the Sm-Nd isotopic system in terrestrial rocks, a series of pioneering studies on ^{143}Nd/^{144}Nd ratios of seawater in major ocean basins found clear distinctions of ε_{Nd} values between different watermasses (e.g. Piepgras and Wasserburg, 1980; Piepgras and Wasserburg, 1982;

Piepgras et al., 1979). These findings ignited surges of studies on Nd isotopes in the ocean in the following few decades, in the hope of developing Nd isotopes as a robust tracer for ocean circulation. The principles of Nd isotopes in the ocean and their palaeoceanographic applications have been reviewed in several papers (Frank, 2002; Goldstein et al., 2003). Only a brief summary is given below.

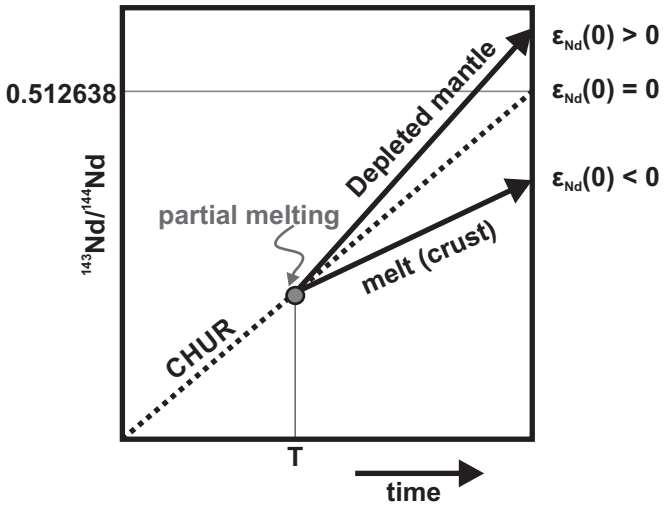

Figure 1.7 A schematic diagram that shows principles of the Sm–Nd isotope system. (After DePaolo and Wasserburg, 1976)

Nd isotopes in the ocean are predominantly controlled by weathering materials from continents, as demonstrated by negative ε_{Nd} values of seawater in most areas of the ocean. Watermasses are tagged with ε_{Nd} values of surrounding continents, which may vary from place to place due to varied lithology and age of constituent rocks of continents undergoing weathering. Characteristic ε_{Nd} values of different watermasses are not homogeneous throughout the ocean, and their identity can be maintained during circulation, because of the relatively short residence time of Nd in seawater (~1000 yr; e.g. Jeandel et al., 1995; Tachikawa et al., 1999a) compared to the average ocean mixing time of ~1500 yr. Intensive investigations of modern seawater Nd

isotopes reveal clear basinal variability: Pacific seawater has high ε_{Nd} values of ~ -4-0 caused by weathering of young volcanic materials around the Pacific basin, and Atlantic seawater generally has low values between ~ -13 and -10 resulting from weathering of Precambrian terrain, such as the Canadian shield and Greenland; and the Indian Ocean and Southern Ocean have intermediate values ranging from ~-9 to -6 (see a compilation of global data by Lacan et al., 2012). A tight coupling between water-column distribution of Nd isotopes and major watermasses identified by the conservative tracer of salinity in a N–W transect across the modern Atlantic provides one of the most convincing proofs of the quasi-conservative behaviour of Nd isotopes in the ocean (von Blanckenburg, 1999) (Figure 1.8).

The figure originally presented here cannot be made freely available via ORA because of copyright. The figure was sourced at Figure 1 in von Blanckenburg, 1999.

Figure 1.8 Compilations of water-column Nd-isotope profiles *versus* salinity distribution along a N–S transect across the modern Atlantic Ocean. (After von Blanckenburg, 1999)

1.2.2 Archives of Nd isotopes for reconstructions of past ocean circulation

Because direct measurement of Nd isotopes on ancient seawater is obviously impossible, reconstruction of past circulation has to rely on marine archives that can preserve ambient seawater Nd-isotope signals and survive diagenetic alteration.

Commonly used archives that can record seawater ε_{Nd} values include ferromanganese (Fe-Mn) crusts, sedimentary Fe-Mn oxides, foraminifera, deep-sea corals and fossil fish debris. Each of these archives has its own advantages and disadvantages regarding the interpretation of past seawater Nd isotopes, so choosing an appropriate archive, if possible, depends on the problem to be investigated.

Hydrogeneous Fe-Mn crusts are thought to precipitate directly from seawater, thus recording ambient seawater ε_{Nd} values without perceptible fractionation (e.g. Frank et al., 1999; Ling et al., 1997; Ling et al., 2005). Fe-Mn crusts contain Nd concentrations up to hundreds or thousands of ppm, and hence are resistant to diagenetic alterations. However, the low growth rates of Fe-Mn crusts (~mm/Ma) and restricted geographic distribution preclude their application as high-resolution chemostratigraphic archives. In addition, Fe-Mn crusts older than the latest Cretaceous are rarely found.

Dispersed Fe-Mn oxides leached from bulk marine sediments with reductive reagents may also record bottom-water ε_{Nd} values (e.g. Chen et al., 2012; Piotrowski et al., 2005), and ubiquitous presence of Fe-Mn oxides in marine sediments enables high-resolution chemostratigraphic research with minimum spatial constraints. However, the so-called “Fe-Mn oxides” are to some extent operationally defined, because their separation relies on chemical leaching of bulk sediments. Consequently, the resulting leachates are almost inevitably contaminated by components leached from other phases of sediments, although many efforts have been devoted to minimizing the contamination by improving leaching techniques (e.g. Bayon et al., 2002; Wilson et al., 2013). This difficulty is probably not a problem for many pelagic sediments that are composed of hydrogeneous components (such as foraminifera, authigenic Fe-Mn oxides) and detritus, but evidence clearly shows that Nd isotopes

from Fe-Mn leachates are heavily affected when sediments contain high contents of volcanic ash (Elmore et al., 2011), or pre-formed Fe-Mn oxides derived from rivers (Bayon et al., 2004; Kraft et al., 2013). A rule of thumb for the use of this archive is to compare its Nd isotopes with those preserved in other archives that are considered to be more reliable, such as fossil fish teeth.

Foraminiferal shells are thought to be recorders of seawater Nd isotopes (e.g. Burton and Vance, 2000; Vance and Burton, 1999; Vance et al., 2004). This archive permits generation of high-resolution Nd-isotope records. However, it is labour-intensive working with foraminifera to generate Nd-isotope data, because it involves picking a large amount of the microfossils that normally contain low concentrations (~ppb) of Nd, followed by tedious cleaning procedures. More importantly, the origin of Nd-isotope signals in foraminifera is controversial. Some early studies suggest that planktonic and benthic foraminifera may preserve surface- and bottom-water Nd isotopes respectively (Klevenz et al., 2008; Vance et al., 2004), but recent studies argue that seawater Nd-isotope signals in foraminifera are actually dominated by coatings of Fe-Mn oxides that are difficult to remove even after typical cleaning procedures. Both types of foraminifera, therefore, may largely reflect bottom-seawater/pore-water signals (e.g. Gourlan et al., 2008; Kraft et al., 2013; Piotrowski et al., 2012; Pomies et al., 2002). The later argument is supported by mapping Nd distribution in foraminiferal shells with Nano-SIMS, which revealed a close association of Nd with Fe-Mn oxides in shells (Tachikawa et al., 2013).

Similar to foraminifera, deep-sea corals that are also composed of calcium carbonates that can also preserve seawater Nd isotopes (e.g. Copard et al., 2010; van de Flierdt et al., 2010). The use of this method involves intensive cleaning steps as

well. An obvious advantage of corals is that they can be precisely dated by the U–Th method, but their growth only covers relatively short periods of time.

Fossil fish debris (i.e. phosphatic teeth and bones) is thought to be another archive that can record seawater Nd isotopes (e.g. Martin and Haley, 2000; Martin and Scher, 2004). Comparison of Nd isotopes recovered from fish debris and Fe-Mn crusts show nearly identical values, indicating the validity of skeletal phosphates in recording seawater Nd isotopes (Martin and Haley, 2000; Martin and Scher, 2004). Fish debris contains high concentrations of Nd (hundreds to thousands of ppm). Nd is incorporated rapidly into fish debris at the sediment-seawater interface during early diagenesis when they still have contact with seawater (Martin and Scher, 2004). Because teeth and bones of living fish contain only small amounts of Nd (hundreds of ppb), large post-mortem enrichment of Nd renders fish debris a faithful recorder of bottom-seawater Nd isotopes, independently of species or habitat of the fish. High Nd concentrations make fish debris very resistant to late diagenesis after burial. A shortcoming of fish debris is their spatially and temporally restricted presence in marine sediments.

1.2.3 Cretaceous ocean circulation and its significance to Cretaceous climate

In general, assessing the pattern of ocean circulation is of particular interest, because ocean circulation is an essential component of the climate system. It may affect local or global climate by changing heat/moisture distribution around the world; in turn, the circulation may shift to different modes in response to climate change (e.g. Rahmstorf, 2002). Studying ocean circulation in a world featuring different geographic and climatic conditions tests our current understanding as to how the

climatic system operates, and offers new insights that improve the current knowledge, leading to better prediction of changes in climate and environment in the future.

The Cretaceous environment was very different from the world in which we are living today. One obvious difference lies in the global land–sea distribution (Figure 1.9). The Pacific Ocean covered more surface area than it does today, and the Tethys Ocean existed at tropical latitudes. Accompanying the break up of the Gondwana continent during the Jurassic Period, South America and Africa separated during the early Cretaceous, the South Atlantic Ocean formed, and was subsequently connected with the North Atlantic in the mid-Cretaceous time. Climate in the Cretaceous was also noticeably different. The Cretaceous is deemed to have been one of the warmest periods in earth history, without permanent ice sheets at either pole (e.g. Barron, 1983; Jenkyns et al., 2004; Littler et al., 2011; Norris et al., 2002; Wilson et al., 2002). Modelled atmospheric CO_2 was ~2–8 times higher than its present level (Berner and Kothavala, 2001). This relatively warm interval was punctuated by several oceanic anoxic events (OAEs) characterized by widespread de-oxygenation of bottom waters (e.g. Jenkyns, 2003b; Jenkyns, 2010a; Leckie et al., 2002). These rapidly occurring oceanic anoxic events represent major perturbations of the global carbon cycle, and provide unique opportunities to understand the responses of the ocean and climate system to those events.

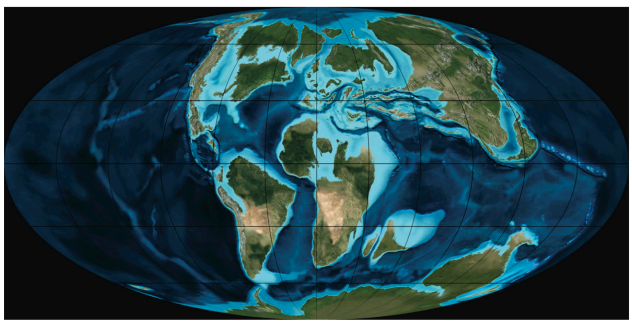

Figure 1.9 Palaeogeographic reconstructions of the middle Cretaceous. (From Ron Blakey, NAU Geology)

The study of Cretaceous ocean circulation can shed light on some fundamental questions on the Cretaceous climate and associated rapid changes. The first fundamental question is: how was heat distributed worldwide via ocean circulation under a warm climate? In the modern ocean, trade-winds and the equator–pole thermal gradients drive large-scale movements of watermasses (Rahmstorf, 2003), forming a conveyor belt that distributes heat when it circulates. However, the absence of ice-sheets at the two poles, and a reduced meridional thermal gradient during the Cretaceous, should have made a circulation system similar to that of today almost impossible (Hay, 2008), posing a major question as to how heat was distributed during the Cretaceous. The second question is: how did ocean circulation behave during rapid climatic changes in the Cretaceous, such as an anoxic event? Because ocean circulation is responsible for re-distributing nutrients in the ocean, and delivering dissolved oxygen from the surface to the ocean bottom, changes in ocean circulation have been frequently hypothesized as an important factor controlling or reacting to rapid climatic/environmental changes, including during OAEs (e.g. Arthur et al., 1987; Bralower and Thierstein, 1984; Schlanger and Jenkyns, 1976; Trabucho Alexandre et al., 2010). Answers to the above questions require a better understanding of Cretaceous ocean circulation.

Cretaceous ocean circulation has been poorly constrained to date, and many controversies remain unresolved. A consensus on even the general pattern of ocean circulation during the Cretaceous does not exist. Several prevailing, but controversial, ideas regarding Cretaceous ocean circulation are: (1) existence of a westward flowing circum-global current in the upper ocean at tropical latitudes as indicated by oceanographic experiments, biogeographic reconstructions, sedimentological evidence and modelling results (e.g. Barron and Peterson, 1989; Föllmi and

Delamette, 1991; Gordon, 1973; Luyendyk et al., 1972). However, the existence, direction and stability of this global current during the Cretaceous Period have been questioned by modelling results that suggest either the absence of this current or a more dynamic current system (Poulsen et al., 1998a). (2) Warm Saline Bottom Water (WSBW) may have formed at low-latitude marginal seas. It has been proposed that warm and saline water may have sunk oceanwards from low-latitude epicontinental shelf seas, and then formed deep waters that were responsible for heat distribution during the Cretaceous (e.g. Brass et al., 1982; Chamberlin, 1906). Evidence, albeit ambiguous, has been presented for the local presence of the WSBW at certain periods of the Cretaceous (e.g. Friedrich et al., 2008; Voigt et al., 2004). However, some modelling results contradict this notion, and claim that deep water can be formed at high latitudes in the Southern Ocean and North Pacific (e.g. Brady et al., 1998; Otto-Bliesner et al., 2002). (3) based on the formation of modern thermohaline circulation, which is driven by the equator–pole thermal gradient and a relatively stable wind system, a Cretaceous ocean filled with mesoscale eddies has been proposed, assuming that the lack of a stable trade-wind system due to Cretaceous warmth coupled with a restricted geographic configuration would not have supported a stable, and directionally moving, ocean circulation system (Hay, 2008).

The study of Cretaceous ocean circulation is largely constrained by availability of reliable proxies. Records, such as marine faunal or floral distribution, sedimentation patterns, marine trace metals, $\delta^{18}O$ or Mg/Ca ratios recovered from foraminifera etc., may provide some information about Cretaceous circulation patterns, but are also controlled by many other environmental or non-environmental variables, so commonly they cannot be similarly interpreted in terms of past circulation. Two relatively well-established and commonly used ocean circulation

proxies are $\delta^{13}C$ and Cd/Ca ratios in foraminifera, both of which mimic nutrient distribution in the ocean and can therefore be utilized to distinguish water masses with different nutrient contents (e.g. Boyle and Keigwin, 1985). Although these two tracers have been successfully applied to address issues related to ocean circulation in the Quaternary, applying them to the Cretaceous is difficult. Firstly, nutrient concentrations of possible end-member water masses in the Cretaceous ocean are not well known. Secondly, diagenesis of biogenic carbonate is more severe in Cretaceous samples than Quaternary samples. Thirdly, as with other proxies, these two tracers are controlled by factors in addition to ocean circulation that are sometimes difficult to assess for the Cretaceous (for example: temperature effects, biological processes, changes in the global carbon cycle etc.).

Recently, Nd isotopes have emerged as a promising tool to reconstruct ocean circulation during the Cretaceous. A growing body of seawater Nd-isotope data mainly recovered from fossil fish debris suggests that differences of Nd isotopes in different watermasses existed in the Cretaceous ocean (e.g. Martin et al., 2012; Moiroud et al., 2013; Murphy and Thomas, 2012; Pucéat et al., 2005; Robinson et al., 2010; Robinson and Vance, 2012; Voigt et al., 2013). This distinction in seawater Nd isotopes in different watermasses supports the application of this method to Cretaceous sediments. The published Nd-isotope data have provided new insights into general patterns of Cretaceous ocean circulation, and the significance of changes in ocean circulation in relation to the climate at that time. Building upon these previous studies on Nd isotopes in the Cretaceous, the second part of this thesis systemically investigated evolution of seawater Nd isotopes in the NW European shelf sea via two case studies. These studies aim at deconvolving the relationship between ocean circulation and climate during the Cretaceous.

1.2.4 Motivations of individual chapter on the study of Cretaceous ocean circulation

Chapter 4: This chapter reports a high-resolution Nd-isotope record from the NW European shelf sea (Chalk Sea) during OAE 2. High-resolution studies on seawater Nd isotopes during the Cretaceous are very rare. The only high-resolution Nd-isotope records across the OAE 2 interval were obtained from a depth transect on Demerara Rise in the tropical western North Atlantic. These records show a remarkable positive ε_{Nd} excursion of ~8 ε-units that happened coincidently with the positive $\delta^{13}C$ excursion characteristic of OAE 2 (MacLeod et al., 2008; Martin et al., 2012). The positive ε_{Nd} excursion observed during OAE 2 can either be explained by a change in ocean circulation, or as a record of volcanic input of Nd from eruptions of large igneous provinces (LIPs) (MacLeod et al., 2008; Martin et al., 2012). To constrain the geographic extent of the positive ε_{Nd} excursion, and ε_{Nd} values of a proposed source region for watermasses that may have affected the tropical western North Atlantic during OAE 2, seawater Nd isotopes preserved in fish debris in the English chalk (Eastbourne, UK) were studied. The new record from the English chalk favours a volcanic origin of the positive ε_{Nd} excursion observed at both Eastbourne and Demerara Rise during OAE 2, and suggests an intriguing correlation between a change in ocean circulation and a transient cooling episode during OAE 2 in the NW European shelf sea.

Chapter 5: This chapter reports preliminary results of a pilot study on seawater Nd isotopes in the Chalk Sea during the mid-Cenomanian Event. The study is a natural extension of the research reported in Chapter 4. Because the positive ε_{Nd} excursion during OAE 2 was either caused by volcanic inputs of radiogenic Nd, or a reorganization of ocean circulation, a possible way to test these theories is to study seawater Nd isotopes in a time interval when LIP-volcanism was not as intense as it

was during OAE 2. The mid-Cenomanian Event (MCE) is an ideal event for such a study, because, on the one hand, LIP volcanism was apparently less significant during MCE than during OAE 2; on the other hand, MCE resembles OAE 2 in many aspects, including being characterized by positive excursions in marine carbon isotopes (but with a smaller magnitude than that of OAE 2) and southward migrations of the similar species of boreal faunas as happened during OAE 2, apparently as a result of a climatic cooling. Apart from testing the origin of the positive ε_{Nd} excursions observed in both the tropical North Atlantic and NW European shelf sea during OAE 2, an additional purpose of the study was to test whether or not the observed tight coupling between a change in ocean circulation at Eastbourne in the Chalk Sea and the climatic cooling was a unique feature only confined to OAE 2.

1.3 The links between the two projects

Although the two projects of this thesis are focused on two seemingly different topics – trace-metal cycling in the modern ocean and ocean circulation during the Cretaceous, they are intrinsically linked. In general, the study of past oceans and climate stimulates the development and refinement of geochemical tracers through modern observations, and observations of the behaviour of geochemical tracers in modern seawater ensure realistic interpretations of the geochemical records preserved in geologic archives. Rare earth elements and their isotopes, particularly Nd isotopes, are potentially useful tracers for a wide range of processes that operated in past oceans, such as changing of ocean circulation and marine redox state, while reliable application of them for studying the past requires a comprehensive understanding of their behaviour in the modern ocean. This probably can be best illustrated by the case of Nd isotopes: increased observations of boundary exchange in

the modern ocean suggest that Nd isotopes are not a simple function of ocean circulation as thought previously, complicating the interpretation of palaeo-Nd-isotope records. As mentioned in the above sections (e.g. section 1.1), current knowledge on the cycling of REEs in seawater is not complete, and is constrained by a lack of large-scale observations. The first part of research in this thesis addresses this issue by providing the first full-depth ocean section of dissolved REE concentrations in seawater across the South Atlantic. With this new dataset, the first project aims to shed light on both the potential, and also the limitations, of applying REEs and their isotopes as tracers to reconstruct the past. This forms a basis of using Nd isotopes to reconstruct ocean circulation during the Cretaceous (i.e. the second project of this thesis), and of applications of REEs and their isotopes to extract useful information on past oceans in future studies.

Chapter 2

A new procedure for precise determination of rare earth elements (REEs) in seawater by desolvating nebulisation ICP-MS with isotope dilution and iron co-precipitation

NOTE: *A revised version of this chapter, co-authored with Jingjing Yang and Gideon M. Henderson, has been published in Geostandards and Geoanalytical Research, 39 (2015): 277–292 (http://dx.doi.org/10.1111/j.1751-908X.2014.00307.x).*

Abstract

This chapter reports a new procedure that permits high-precision determination of all 14 naturally occurring rare earth element (REE) concentrations, present at ppt (ng kg^{-1}) to sub-ppt, in ~100 ml of seawater. The procedure involves addition of a ^{142}Ce-^{145}Nd-^{171}Yb-enriched spike mixture, iron co-precipitation, REE purification with chromatographic separation and the use of a magnetic-sector-field ICP-MS (Element 2) coupled with a desolvating sample introduction system (Aridus 1). Critical steps within the procedure, including co-precipitation pH and matrix removal, have been optimized through a set of experiments reported in this chapter. Repeated analyses of two in-house seawater standards yielded precision typically <3% (1σ) for all REEs, using ~100 ml seawater. Two seawater standards (CASS-4 and NASS-5) were measured using this new procedure, and the results generally agree with published REE concentrations for these two standards. The method was further validated through participation in GEOTRACES intercalibration for seawater REE concentrations; results of the GEOTRACES intercalibration samples, measured using this new procedure, show good agreement with those reported by other participant laboratories. New REE results for additional intercalibration samples (SAFe and Arctic PS70) were also reported in this study. This procedure is straightforward, and can be routinely applied to determination of seawater REEs with relatively high sample throughput.

2.1 Existing approaches to the analysis of REE in seawater

Systematic variations in chemical properties of rare earth elements (REEs), coupled with the varying oxidation states of Ce and Eu, make them useful oceanic tracers (see reviews by Byrne and Sholkovitz, 1996; Elderfield et al., 1988; Nozaki, 2001b). Since pioneering work on REE distributions in the ocean in the 1960s (e.g. Goldberg et al., 1963; Høgdahl et al., 1968), the absolute concentrations of REEs, and their concentrations relative to one another (*i.e.* the REE pattern), have been used to trace a wide range of oceanic processes, such as mixing of different water masses, tracing of sources, assessment of internal cycling of trace metals in the ocean, and of hydrothermal and redox processes (e.g. Bau et al., 1997; Craddock et al., 2010; Hatta and Zhang, 2006; Sholkovitz et al., 1994; Zhang et al., 2008). Dissolved REEs have also been used as indicators of anthropogenic pollutants in rivers and coastal seas. For example, the presence of gadopentetic acid, which is a medical waste, can be traced by a characteristic positive Gd anomaly in river and sea waters (e.g. Bau and Dulski, 1996; Nozaki et al., 2000).

The desire to measure REEs in seawater is expected to increase in the future due to their potentially wide application, and the increasing interest in the study of oceanic trace-metal cycling to provide useful information on marine biogeochemical cycles associated with the climate. Such applications will be particularly stimulated and met through the recent GEOTRACES programme, which is an international research project aiming at studying trace elements and their isotopes in the global oceans (SCOR Working Group, 2007). A reliable procedure that enables the precise and accurate determination of REEs in easily collected volumes of seawater is therefore needed.

The determination of seawater REEs is challenging because of their low concentrations in seawater (sub-ppt to ppt). Instrumental neutron activation analysis (INAA) (e.g. De Baar et al., 1985; Goldberg et al., 1963; Høgdahl et al., 1968) and isotope-dilution thermal ionization mass spectrometry (ID-TIMS) (e.g. Elderfield and Greaves, 1983b; Greaves et al., 1989) represent two methods that were extensively applied to determine seawater REEs in early studies. The former has become less commonly used for seawater REE determination largely because it requires large sample sizes (10-30 L) and suffers from low sample throughput. The latter gives some of the best seawater REE results in terms of precision and accuracy, with quoted precision of <~5% for all REEs (e.g. Greaves et al., 1989). This technique has limitations, however, including: time-consuming sample pre-treatment, inability to determine mono-isotopic REEs (Pr, Tb, Ho, Tm), and relatively long data-acquisition time by TIMS. Furthermore, relatively large seawater sample sizes (~1 L) were used in most published work using the ID-TIMS method (e.g. German and Elderfield, 1990b; German et al., 1995). Methods based on inductively coupled plasma atomic emission spectrometry (ICP-AES) were also developed to measure REEs in natural waters (e.g. Liang et al., 2005; Pasinli et al., 2005), but detection limits of ICP-AES are normally on the ppb (ng g^{-1}) level for most elements, making it a poor instrument for the analysis of REEs in seawater, especially those from open-ocean surface seawater with typically concentrations < ~1 ng kg^{-1} for many REE elements. Currently, inductively coupled plasma mass spectrometry (ICP-MS) is the preferred instrument to measure seawater REEs because it allows rapid multi-elemental measurement, low detection limits and good precision.

Extraction of REEs from seawater is typically required to preconcentrate and separate them from the majority of matrix before the ICP-MS analysis. Techniques

developed for water samples include liquid-phase extraction (Chandrasekaran et al., 2012; Shabani et al., 1990) and solid-phase extraction by iron or magnesium co-precipitation (e.g. Bayon et al., 2011; e.g. Elderfield and Greaves, 1983b; Freslon et al., 2011; Greaves et al., 1989; Shaw et al., 2003), chelating and ion-exchange resins (e.g. De Baar et al., 1985; Fu et al., 2007; Karadaş et al., 2011; Rahmi et al., 2007; Willie and Sturgeon, 2001; Zhu et al., 2006), or other solid-phase sorbents (e.g. Bahramifar and Yamini, 2005; Liang et al., 2005). The solvent-extraction method developed by Shabani et al. (1990) and iron co-precipitation have been widely applied to generate seawater REE data in a large number of studies (e.g. Alibo and Nozaki, 1999; Elderfield and Greaves, 1983b; German et al., 1995; Greaves et al., 1989; Zhang and Nozaki, 1996).

Being able to reliably assess yields of REEs after the extraction is important to ensure accurate and precise analysis. Because quantitative recoveries of REEs from seawater samples are not generally possible, the extraction process may lead to internal fractionations of the REE group. Isotope dilution is the best way to overcome this issue, and provide a robust assessment of concentration independent of yield. An alternative approach is to add one of REEs, Tm, to samples to produce an artificial positive Tm anomaly. This method also permits REE recovery to be assessed after extraction (Bayon et al., 2011; Freslon et al., 2011), but relies on the assumption that the yield is equal for all REEs.

To obtain high-quality REE data, interferences on the ICP-MS also need to be taken into account. Isobaric interferences from other REEs can largely be avoided by careful selection of isotopes for analysis. Polyatomic interferences are more difficult to correct, and interferences of barium oxides on Eu, and oxides of light REEs on middle and heavy ones are examples of such interferences that must be considered

and corrected for (Chung et al., 2009). A traditional solution is to measure several suites of mixed standards separately to assess oxide formation rates, making the correction possible (e.g. Bayon et al., 2011; Freslon et al., 2011; Jenner et al., 1990). The desolvating sample introduction system significantly mitigates the problem of oxide formation, and provides an alternative approach. Desolvation converts sample liquid-droplets into dry aerosols through a heated membrane device (e.g. CETAC Aridus) before introducing them into the plasma, reducing oxide production to a negligible level. This method has proven useful to provide the interference-free determination of REEs in suspended marine particulates (Field and Sherrell, 1998).

Online- and coupled-systems have also been developed to allow preconcentration of REEs from seawater and direct analysis. These systems aim to reduce the labour required for the sample pre-treatment, and increase the sample throughput (e.g. Fu et al., 2007; Katarina et al., 2009; Zhu et al., 2009). Two such systems have been thoroughly tested with seawater or marine pore-water samples; one is a method using automated ion chromatography coupled with ICP-MS (Haley and Klinkhammer, 2003), and the other is a recent commercially available system called "seaFAST", produced by Elemental Scientific Inc. (Hathorne et al., 2012). These two systems have demonstrated high throughput and the ability to measure REEs in only a few millilitres of seawater, but the precision of analysis they offer is normally ~10% (1σ) or worse, somewhat less precise than that can be achieved by traditional off-line ICP-MS methods (<5% (1σ), e.g. Zhang and Nozaki, 1996).

A new analytical procedure is reported in this study. The new procedure takes advantage of both isotope dilution and the desolvating sample introduction system to precisely and accurately determine 14 REE concentrations (except for Pm that is not naturally occurring) in relatively small volumes of seawater (~100 ml), with

reasonably high sample throughput. This procedure was developed by combining approaches followed during ID-TIMS analysis of REEs (Elderfield and Greaves, 1983b; Greaves et al., 1989), with those used in ICP analysis (Field and Sherrell, 1998; Shaw et al., 2003). It involves addition of mixed ^{142}Ce-^{145}Nd-^{171}Yb-enriched spike solution to seawater samples, iron co-precipitation, a fast chromatographic column separation step, and analysis on a magnetic-sector-field ICP-MS with a desolvating sample introduction system. This procedure allows for analysis on easily-collectable volumes of seawater, and for relative fast throughput (32 samples can be analysed in 5 days with typical lab working-time of 1-3 hrs per day). The long-term reproducibility of this procedure, <3% (1σ) for all REEs, is comparable to that achieved by the slower ID-TIMS approach (e.g. Greaves et al., 1989).

2.2 Analytical details

2.2.1 Reagents and materials

The following reagents were used during the course of our experiments and analysis, unless otherwise specified: ultrapure de-ionized Milli-Q water (18.2 MΩ, Millipore), sub-boiling quartz-distilled HCl and HNO_3, trace-metal grade ammonia solution (~20-25%, BDH Aristar®, or Optima™), trace-metal grade sulfuric acid (98%, Optima™).

AG 1-X8 anion-exchange resin (100-200 mesh, Bio-Rad) was used for pre-purifying the iron(III) chloride solution for the co-precipitation, and for separation of REEs from $Fe(OH)_3$ precipitates. The resin was sequentially cleaned with 3 M HCl, Milli-Q water, 6 M HCl and Milli-Q water in a bottle. This cycle was repeated 5 times. The cleaned resin was stored in Milli-Q water prior to use.

Iron(III) chloride solution was prepared by dissolving high-purity iron powder (99.998%, Puratronic®, Johnson Matthey) in 10 M HCl at 80°C, followed by loading on a column with the AG 1-X8 resin to eliminate REE impurities. REEs were removed by elution with 10 M HCl, and Fe was subsequently eluted with Milli-Q water. This cleaning process was repeated two more times after drying down the eluted iron(III) chloride solution. Three column passes were required to remove initially high levels of REE impurities from the iron solution. The final purified iron(III) chloride solution was stored in Milli-Q water.

2.2.2 Sample pre-treatment environment and apparatus cleaning

The sample pre-treatment was performed in a metal-free clean laboratory that is overpressured with HEPA-filtered air, and any sample-handling was performed in class-100 laminar flow hoods. Polypropylene/polyethylene bottles (Nalgene), centrifuge tubes and pipette tips used in the procedure were acid-cleaned by soaking in cold reagent grade 7.5 M HNO_3 for >24 h, and then rinsed thoroughly with Milli-Q water before use. Teflon beakers (Savillex) were cleaned by a three-step sequential cleaning: reagent grade 16 M HNO_3, reagent grade 8 M HNO_3, and quartz-distilled 10 M HCl at 120°C for >24 h at each step, and rinsed thoroughly with Milli-Q water after each step.

2.2.3 Spike solution

A ^{145}Nd–^{171}Yb enriched spike mixture was initially prepared in 2007 by dissolving individually, and then mixing, certified ^{145}Nd-enriched Nd_2O_3 and ^{171}Yb-enriched Yb_2O_3 powders (CK Gas Products Ltd) with 16 M HNO_3. An additional ^{142}Ce-enriched spike solution was added to this ^{145}Nd–^{171}Yb spike in 2010 to improve

precision of Ce measurement. The ^{142}Ce solution was prepared by dissolving ^{142}Ce-enriched CeO_2 powder (CK Gas Products Ltd) with a few drops of 98% sulfuric acid at ~200°C. The isotopic composition of the spike mixture was checked on a multiple-collector ICP-MS (Nu Instruments) against natural Ce, Nd and Yb standard solutions (High-Purity^{TM} Standards). The spike mixture was then diluted to concentrations appropriate for seawater samples in 2% HNO_3, and the final concentrations were determined by reverse isotope dilution using gravimetrically prepared Ce, Nd and Yb standard solutions (High-Purity^{TM} Standards).

2.2.4 Seawater standards and samples

Currently there is no certified reference material for seawater REE concentrations. Two seawater standards (CASS-4 and NASS-5), released by the National Research Council of Canada are, however, commonly used to demonstrate the accuracy of the seawater REE analysis. Published REE concentration result for these two standards were compiled, and compared with new results obtained in this study.

The accuracy of the new analytical procedure was further tested via participation in the GEOTRACES laboratory intercalibration on seawater REEs. Two GEOTRACES inter-calibration samples (0.2μm-filtered seawater), KN193-6-Nd-533 and KN193-6-Nd-330, were measured in this study. These samples were collected at depths of 15 and 2000 m at the Bermuda Atlantic Time-Series Station (BATS) in the NW Atlantic in June-July 2008 during the KN193-6 cruise.

Two in-house seawater composites (SWC) were prepared by mixing unwanted seawater samples, and typically 1-3 aliquots of SWC of equal volume to samples were processed in parallel with all sample batches to assess the reproducibility of the

procedure. The first seawater composite (SWC-1) was mixed from a variety of open ocean seawater samples collected in the eastern equatorial Pacific during the "Biocomplexity Cruise" in September 2005 ranging from surface water to 300 m depth. The second seawater composite (SWC-2) was mixed from filtered seawater samples (upper 500 m) in the Drake Passage collected during the Blue Water Zone cruise in July-August 2006.

Additional intercalibration seawater samples, including two "SAFe" samples and two PS70 samples, were also measured for their REEs in this study. The two "SAFe" samples measured here, S1 and D2, were collected from the surface and 1000 m respectively at 30°N, 140°W during the Sampling and Analysis of Fe (SAFe) cruise (Johnson et al., 2007). PS70 intercalibration samples were collected at 2000 m in the Makarov Basin during the 2007 Polarstern ARK-XXII/2 cruise to the Arctic Ocean. Sample PS70/328/4 was collected from the ultra-clean CTD by Royal Netherlands Institute for Sea Research at 87°49.50' N 170°21.17' W, and sample PS70/328/6 was obtained by the normal CTD from Alfred Wegener Institute at 87°49.92' N 169°49.94' W.

A wide range of seawater samples collected from the Pacific and Atlantic during various cruises, including those from the CoFeMUG cruise presented in Chapter 3, have been analyzed using the analytical approach reported in this chapter since 2007.

2.2.5 Procedure of sample pre-treatment

Sample pre-treatment includes two main steps: Fe co-precipitation that preconcentrates REEs from seawater, and subsequent column separation that purifies REEs from the $Fe(OH)_3$ precipitates. A typical experimental batch comprised 16

samples (including blanks and at least one SWC). Two batches of samples can be processed in parallel and finished within 5 days with typical lab working-time of 1-3 hours per day. Details of the final procedure are described as follows.

Seawater samples stored in polypropylene or polyethylene bottles were acidified to pH<2 with 10 M HCl at least one week before the pre-treatment. Seawater (~100 ml) was weighed, and then the ^{142}Ce–^{145}Nd–^{171}Yb spike mixture added, together with the purified iron(III) chloride solution containing ~1 mg Fe. The mixture was shaken vigorously by hand, and left to stand for at least 24 hrs for seawater–spike isotope equilibrium. The equilibration is normally instantaneous, except for certain circumstances where water samples are rich in organics (Elderfield and Greaves, 1983b). $Fe(OH)_3$ co-precipitation was achieved by gradually adding ammonia solution to samples until the pH reached values of 7.5–8 (tested with pH strips). Samples were left to stand for >12 hrs for resulting precipitates to settle. The majority of supernatant liquid was then carefully decanted from sample bottles, and the remaining content was transferred to centrifuge tubes which were centrifuged to further separate the REE-bearing $Fe(OH)_3$ precipitates from the liquid. The precipitates were then thoroughly rinsed with Milli-Q water to remove residual salts. To prevent dissolution of the precipitates and internal fractionations among the REE series during this washing (see Section 2.3.2), Milli-Q water used for the wash was alkalified with a few drops of ammonia solution to ensure pH≥9 before use. The centrifuge tubes were shaken until precipitates were completely dispersed in water, and then centrifuged again to remove liquids. After a 5-time rinse, the precipitates were dissolved with a few drops of 10 M HCl, and transferred into Teflon beakers, and finally dried down at 120°C before dissolving in 0.5 ml 10 M HCl for subsequent column separation.

Column separation was adopted to purify REEs from Fe, using small Teflon columns (3.5-cm long, 0.15-cm inner diameter) with a resin reservoir of 0.25 ml. AG 1-X8 resin (100-200 mesh) was loaded and washed with 1 ml Milli-Q water, 1 ml 10M HCl, and 1 ml Milli-Q water in sequence, and then preconditioned by addition of 3 × 0.5ml 10M HCl. Samples, dissolved in 0.5 ml 10M HCl, were loaded onto columns. Because REEs have no adsorption on the AG 1-X8 resin under the 10 M HCl condition, they pass through the column directly and were collected directly into clean Teflon beakers, while Fe remains on the resin. A further 1 ml of 10 M HCl was added twice to ensure complete elution of REEs. Note that because yttrium (Y) and thorium (Th) did not stick to the resin, and can be eluted together with REEs, this procedure also separates Y and Th from Fe. The collected REE (+ Y, Th) solutions (2.5 ml in total) were dried down at 120°C. 50 µl 16 M HNO_3 was then added into each sample and dried down again to convert chlorides into nitrates, and to destroy potential organics eluted from the resin. Samples were finally dissolved in 1 ml 2% HNO_3 ready for introduction to the ICP.

2.2.6 Instrumentation

Analysis of REE concentrations was performed on a magnetic-sector-field ICP-MS (Element 2, Thermo) coupled with a desolvating nebulizer system (Aridus 1, CETAC) and an autosampler (ASX-100, CETAC) at the Department of Earth Sciences, University of Oxford. Typical instrument operation conditions, together with measured isotopes, are summarized in Table 2.1.

Table 2.1

Typical instrumental configurations and isotopes selected for the REE determination

ELEMENT 2 Parameters

Tune		*Scan*	
sample gas flow	0.8–1.18 L/min	resolution	low
auxiliary gas flow	1.0–1.8 L/min	detection mode	both
cooling gas flow	15 L/min	scan type	Escan
plasma power	1390–1480 W	mass window	20%
extraction	-2000 V	samples/peak	100
focus	-750 V	sample time	4 ms (Ce, Nd and Yb isotopes)
X-Deflection	-7.8 V		2 ms (the rest)
Y-Deflection	6.85 V	magnet settling time	300 ms (^{138}Ba)
shape	100 V		1 ms (the rest)
focus offset	5%	magnet mass	137.905

Aridus 1 Parameters

sweep gas flow	2.24–2.93 (L/min)	desolvator temp.	160 ºC
nitrogen flow	4–11 (ml/min)	spray chamber temp.	110 ºC

element	**mass measured** [a]	**element (cont.)**	**mass measured (cont.)** [a]
Ba	138	Tb	159
La	139	Dy	(161), 163
Ce	140, 142	Ho	165
Pr	141	Er	167
Nd	143, 145, 146	Tm	169
Sm	147	Yb	171, 172, 173
Eu	151, (153)	Lu	175
Gd	(157), 158		

[a] masses in brackets are measured on the MS, but are not used during data calculations.

Samples were introduced into the ICP-MS using the Aridus 1 to greatly increase instrument sensitivity and reduce oxide production. REE analysis on the Element 2 was performed at low mass resolution (M/ΔM >300) mode, rather than medium or high resolution, to take full advantage of high sensitivity and the flat-topped peaks that give high precisions on isotopic ratios. The Element 2 has two scanning modes: a magnetic scan and EScan mode. By default in the software, the faster EScan mode is limited to scan +15% from the current magnet mass by

automatically varying the acceleration voltage rather than the magnet field, and any mass differences larger than that are accommodated by magnet jumps. However, this default setting can be changed to accommodate a mass range of 30% in EScan mode. This is the approach used in our procedure, because it allows the full range of REEs plus Ba (a mass range of ~27%) to be analyzed without magnet jumps. This approach removes the need for long magnet settling times, thereby greatly increasing the scan speed. No detrimental effect of the increased EScan range was detected. A further increase in the scan speed was achieved by selecting a narrow mass window for every peak, comparable to the peak-hopping mode on Quadrupole instruments. All isotopes, except for Ba, were measured in counting mode (<5 million cps) to avoid any need for collector cross-calibration.

An in-house multi-element standard solution, "Coral Sea Standard", was prepared gravimetrically by mixing 14 individual lanthanide standard solutions (High-Purity™ Standards) to match the REE concentration ratios of average natural seawater in the Coral Sea (Sholkovitz et al., 1999; Zhang and Nozaki, 1996). This standard was measured periodically at a Ce concentration of ~0.5 ng ml^{-1} during each analysis session to monitor the mass bias and the response factor of specific REEs relative to Nd and Yb (see Section 2.2.7).

Each analysis session normally comprised 16 samples, with every four sample measurements bracketed by measurements of instrument memory (pure 2% HNO_3) and the Coral Sea Standard. A 100 ppb Ba standard solution (High-Purity™ Standards) was measured at the end of each session to monitor interferences resulting from Ba oxide on Eu.

2.2.7 Data calculation

Raw count rates for each mass analyzed on the ICP were first corrected for instrument memory. Nd and Yb concentrations were then calculated from $^{145}Nd/^{146}Nd$ and $^{171}Yb/^{172}Yb$ ratios using isotope dilution equations (Rodríguez-González et al., 2005). Ce concentrations were calculated from $^{140}Ce/^{142}Ce$ ratios after 2010, but were calculated as the other REEs using the method described below before 2010. Mass bias was monitored by periodic measurements (every 4 samples) of the Coral Sea Standard containing naturally occurring Nd and Yb throughout the analysis session, and corrections were applied to measured $^{145}Nd/^{146}Nd$ and $^{171}Yb/^{172}Yb$ ratios of all spiked samples using a linear law. ^{142}Ce was corrected for isobaric interference from ^{142}Nd by using measured ^{143}Nd intensities and the known abundance ratios of $^{142}Nd/^{143}Nd$ in nature and our spike solution.

The remaining REEs were calculated using Nd and Yb as internal standards. The principle is illustrated in equation (1) and (2), using Nd as the internal standard as an example:

$$\frac{C_{X\_CSS}}{C_{Nd\_CSS}} = f_{X/Nd} \times \left(\frac{I_{X\_CSS}}{I_{^{146}Nd\_CSS}}\right) \quad (1)$$

$$\frac{C_{X\_SW}}{C_{Nd\_SW}} = f_{X/Nd} \times \left(\frac{I_{X\_SW}}{I_{^{146}Nd\_SW}}\right) \quad (2)$$

where C represents concentration; X denotes a specific REE; CSS indicates the Coral Sea Standard; SW indicates a seawater sample; $f_{X/Nd}$ indicates the instrumental response factor of a specific REE relative to Nd; and I denotes signal intensity. In Eq. (1), C_{X_CSS}/C_{Nd_CSS} is the REE/Nd concentration ratio in the Coral Sea Standard, which was prepared gravimetrically, and therefore a known term. $I_{X\_CSS}/I_{^{146}Nd\_CSS}$ is the measured intensity ratio of a specific REE isotope relative to

^{146}Nd in the Coral Sea Standard. Both of above two terms are known, therefore an instrumental response factor, $f_{X/Nd}$, can be obtained. This value of $f_{X/Nd}$ is used in Eq. (2) so that the seawater concentration of a specific REE in samples, C_{X_SW}, is the only unknown that can be solved for. REE concentrations of each sample are calculated using the mean $f_{X/Nd}$ value averaged from the two measurements of the Coral Sea Standard that brackets this sample. The same rationale was also applied using Yb as the internal standard, thus two concentration results for each REE, based on Nd and Yb respectively, can be calculated. The final concentration was the average of the two results, using the following equation (3):

$$C_X = C_{X-Nd} \times \left(\frac{M_{Yb} - M_X}{M_{Yb} - M_{Nd}}\right) + C_{X-Yb} \times \left(\frac{M_X - M_{Nd}}{M_{Yb} - M_{Nd}}\right) \quad (3)$$

where C_{X-Nd} and C_{X-Yb} indicate the concentration of a specific REE calculated using Nd and Yb as the internal standard respectively; and M_X stands for atomic mass of a specific REE. Procedural blank was corrected from each sample on a batch-to-batch basis.

Oxide interferences were found to be negligible as a result of the use of the Aridus 1. The Ce oxide formation, representing LREE-oxide interference, was checked at the beginning of each analysis session with a high-purity Ce standard, and was found always to be <0.1% of total Ce signals. The Ba-oxide interference was monitored by measuring 100 ppb high-purity Ba standard solution at the end of each analysis session. Although final samples normally contain abundant Ba (~20 ng ml^{-1}) after pre-treatment, interferences of BaO^+ were observed to be constantly <1% of the total Eu^+ signal of each sample. Consequently, no corrections were applied.

2.3 Optimizing the preconcentration

2.3.1 Optimal pH for iron co-precipitation

An optimal pH for iron co-precipitation should avoid excessive recoveries of seawater major ions (such as Ba, Ca and Mg) that could lead to either interferences or matrix effects on the mass spectrometer, and also ensure that no fractionation within the REE series should occur during the co-precipitation. Previous work indicates that <0.2% of seawater Ba is recovered from seawater at pH of 8.4, but that enhanced recovery of Ca occurs at pH>8.5, and Mg starts to significantly precipitate as pH rises to between 9.3 and 9.5 (Greaves et al., 1989; Irving, 1926).

The co-precipitation pH of our procedure was optimized through a pH-control experiment, in which eight 200 g aliquots of an unfiltered seawater sample were precipitated at different pH ranging from 6.26 to 7.95, accurately measured by a pH meter, to determine their REE concentrations. Results suggest that all REEs in 8 aliquots displayed identical apparent concentrations in the tested pH range, except for La and Eu at pH 6.52 and 7.13 (Figure 2.1). The recommended co-precipitation pH in previous studies was 7.5 ± 0.5 (Greaves et al., 1989). Results in this study indicate, however, that precipitation at pH <7.5 may lead to fractionation between REEs (Figure 2.1), and suggest an optimal co-precipitation pH range between 7.5 and 8. This pH range is also low enough to avoid significant recovery of matrix elements.

2.3.2 An effective strategy for rinsing $Fe(OH)_3$ precipitates

The $Fe(OH)_3$ precipitates were thoroughly rinsed with Milli-Q water after the co-precipitation to further remove dissolvable salts recovered along with REEs from seawater. An effective rinse strategy should avoid fractionating individual REEs

within the group, and remove matrix elements to a minimum possible level at the same time.

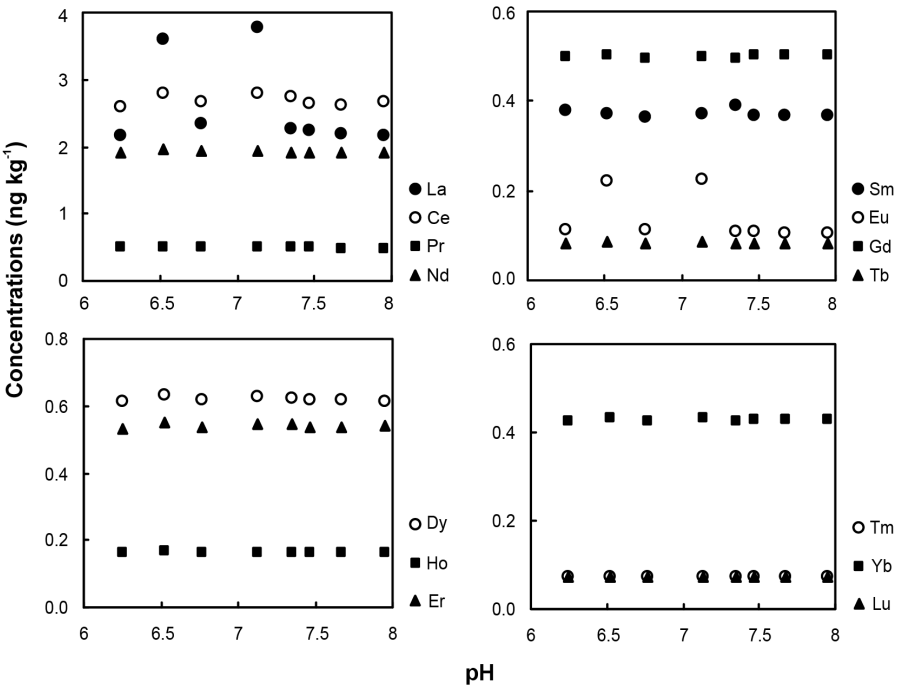

Figure 2.1 Results of the pH-control experiment that aims at determining the optimal co-precipitation pH. Eight aliquots for the same seawater were precipitated at different pH ranging from 6.26 to 7.95, and then analyzed for their REE concentrations. The results indicate that co-precipitation at pH between 7.5-8 can result in constant recoveries of all REEs from seawater samples.

Because the normal Milli-Q water is slightly acidic (pH *ca.* 5.6) due to the dissolution of ambient atmospheric CO_2, it may lead to dissolution of the $Fe(OH)_3$ precipitates, lowering yield and possibly fractionating REEs. Milli-Q water was therefore alkalified with a few drops of ammonia solution to ensure pH ≥9 prior to use. The effectiveness of this adjustment was demonstrated by a rinsing experiment. Six 200 ml aliquots were taken from the same seawater sample, and equally divided into two groups. One group was rinsed with normal Milli-Q water, and the other was rinsed with the alkalified Milli-Q water. One aliquot in each group was spiked before

iron co-precipitation to determine total REE concentrations, and the other two was spiked after the precipitate-rinsing step to assess the yields of REEs. The results showed that REE yields were ~85-93% for those rinsed with normal Milli-Q water, and ~90-92% for those rinsed with the alkalified Milli-Q (Figure 2.2). More importantly, rinsing with normal Milli-Q water tended to preferentially remove middle REEs from the precipitates, especially Eu, which had the lowest yield of 85%. Instead, rinsing with the alkalified Milli-Q water provided a stable recovery for the whole range of REEs. Rinsing with alkalified Milli-Q water is therefore suggested during preconcentration of REEs using Fe co-precipitation.

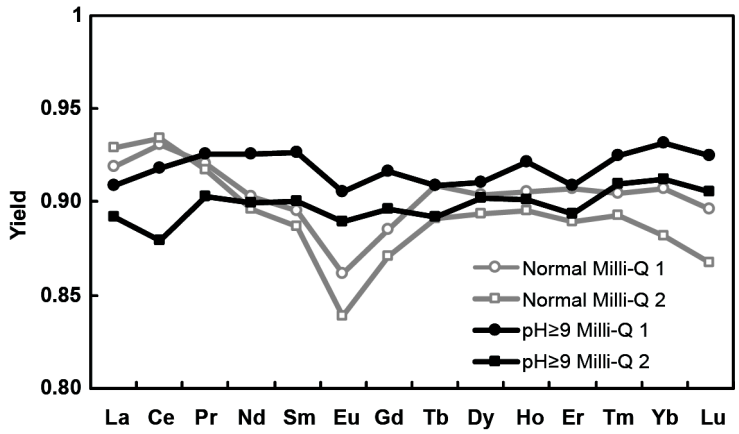

Figure 2.2 Yields of REEs in two groups of seawater aliquots that were rinsed with normal Milli-Q water and alkalified Milli-Q water (pH ≥ 9) respectively for 5 times after iron co-precipitation. The results indicate that rinsing with normal Milli-Q water tends to preferentially remove middle REEs from $Fe(OH)_3$ precipitates, and rinsing with alkalified Milli-Q water can ensure constant recoveries of REEs in individual samples.

The optimal number of rinses was determined by a consecutive rinse experiment. $Fe(OH)_3$ precipitates from two randomly selected 0.2 μm-filtered seawater samples (Test-1 and Test-2) were repeatedly rinsed with the alkalified Milli-Q water. Major matrix ions, including Na, Mg, K, Ca, Mn, Fe, Sr and Ba were

analyzed on each rinse on a Quadrupole ICP-MS (Perkin-Elmer Elan 6100 DRC) by adding In as an internal standard. The samples themselves were also analyzed after the fifth rinse. The results suggest significant removal of Na, Mg, K, Ca and Sr in the first three rinses, and a progressively decreased removal-efficiency towards the fifth rinse (Table 2.2). Ba was almost absent in the rinse-waters and samples. Fe and Mn concentrations remained at high levels in samples, probably due to Fe solution used in co-precipitation. A 5-rinse step is suggested during preconcentration to remove matrix ions.

Table 2.2

Matrix element concentrations in rinses and samples for a 5-rinse step

	[μg ml^{-1}]	Na	Mg	K	Ca	Mn	Fe	Sr	Ba
1st rinse-water	Test-1	11501	1458	488	446	0.006	5.5	7.73	< 0.002
	Test-2	10967	1392	462	417	0.005	7.9	7.48	< 0.002
2nd rinse-water	Test-1	9340	1178	394	380	0.005	5.2	6.27	< 0.002
	Test-2	9971	1279	425	426	0.006	4.7	7.08	< 0.002
3rd rinse-water	Test-1	510	67	21	21	0.004	2.6	0.37	< 0.002
	Test-2	506	66	21	20	0.008	2.4	0.36	< 0.002
4th rinse-water	Test-1	32	4.5	0.5	2	0.005	2.3	0.04	< 0.002
	Test-2	42	5.8	1	1.8	0.004	1.8	0.04	< 0.002
5th rinse-water	Test-1	3	0.4	<0.2	1.2	0.004	3.8	0.01	< 0.002
	Test-2	5	0.7	<0.2	2.3	0.013	3.5	0.02	0.004
sample	Test-1	2	2.1	40.6	12.6	46.4	24.7	0.001	0.005
	Test-2	1.2	0.9	2.4	16.4	142.8	34.3	0.001	0.004

2.4 Results and technique validation

2.4.1 Yield

Because Nd and Yb concentrations are determined by isotope dilution, 100% recoveries of REEs were not necessary, as long as all REEs have similar yields. The extraction yield of iron co-precipitation was investigated by applying the extraction procedure twice in succession to three samples: an aliquot of seawater standards, CASS-4 and NASS-5, and an in-house seawater composite, SWC-1. After co-precipitation, the supernatant liquids were treated as if they were dissolved samples,

and Fe co-precipitation repeated. REE masses removed in the second co-precipitation were only 2-3% of the mass removed in the first co-precipitation, suggesting high and constant extraction yields of ~97-98% for all REEs, except for Ce (Figure 2.3). Yields after the 5-rinse step were normally ~90-92% for all REEs (Figure 2.2), suggesting a ~1% loss of REEs during each rinse step. The Ce yield was somewhat less consistent, and as low as ~94% in the SWC-1 sample (Figure 2.3). This indicates that Ce extraction by iron co-precipitation may vary between samples, highlighting the advantage of adding a Ce spike in addition to Nd and Yb spikes.

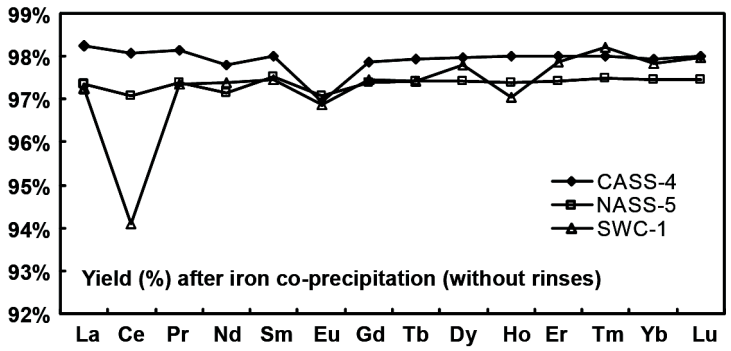

Figure 2.3 Yields of REEs after iron co-precipitation.

2.4.2 Total procedural blanks and detection limits

Procedural blanks were determined by applying the complete preconcentration approach to 100 ml of Milli-Q water. Sixty independent blank measurements, representing at least one determination per batch of samples run between 2010 and 2013, demonstrate procedural blanks <1% of the REE content of ~100 ml seawater, except for Ce, where blanks were as high as ~5% of the typical Ce content in an individual sample (Table 2.3). The detection limits of the analytical approach are also summarized in Table 2.3, based on 3 times the standard deviation of the procedural blanks.

Table 2.3

Procedural blank, detection limit, reproducibility of two in-house SWC

	Before 2010						After 2010				
	SWC-1			SWC-2			SWC-2			Blank (pg)	Detection Limit
	Mean (n=20) [a]	s [b]	RSD [c]	Mean (n=29) [a]	s [b]	RSD [c]	Mean (n=37) [a]	s [b]	RSD [c]	Mean (n=60)	(pg/kg)
La	1.03	0.03	2.8%	5.3	0.1	2.3%	5.25	0.08	1.5%	1.08	27.3
Ce	0.30	0.03	9.3%	1.2	0.1	8.8%	1.04	0.03	2.9%	5.28	55.7
Pr	0.168	0.006	3.5%	0.67	0.02	3.0%	0.63	0.02	2.6%	0.27	8.6
Nd	0.759	0.008	1.0%	2.68	0.01	0.5%	2.69	0.04	1.5%	1.22	33.7
Sm	0.157	0.003	1.8%	0.502	0.007	1.5%	0.502	0.006	1.1%	0.28	10.8
Eu	0.053	0.001	2.4%	0.150	0.007	4.8%	0.148	0.004	2.4%	0.05	2.6
Gd	0.261	0.007	2.7%	0.71	0.03	3.6%	0.74	0.01	1.6%	0.24	5.9
Tb	0.043	0.001	2.1%	0.117	0.002	1.3%	0.117	0.003	2.4%	0.05	4.2
Dy	0.357	0.007	1.9%	0.96	0.01	1.2%	0.96	0.01	1.3%	0.21	6.4
Ho	0.104	0.002	2.0%	0.272	0.004	1.5%	0.267	0.004	1.4%	0.05	3.2
Er	0.362	0.007	2.0%	0.98	0.02	1.6%	0.95	0.01	1.1%	0.09	2.1
Tm	0.052	0.001	1.8%	0.154	0.002	1.6%	0.149	0.003	1.7%	0.02	1.4
Yb	0.324	0.005	1.4%	1.08	0.02	1.5%	1.06	0.01	1.0%	0.11	3.1
Lu	0.055	0.001	2.4%	0.196	0.005	2.3%	0.186	0.003	1.4%	0.01	0.3

[a] unit: ng kg^{-1};
[b] 1 standard deviation (1σ);
[c] relative standard deviation (1σ).

2.4.3 Validation of the procedure

CASS-4 and NASS-5 were analysed to validate the accuracy of our procedure, and our results are listed in Table 2.4 and Table 2.5, together with the compiled literature REE data for these two standards. These are not certified reference materials, but have been measured in a range of previous studies. Previously published concentration data for these seawater standards show some variation, but values measured in this study are generally within the range of published values, except for Gd and Tm concentrations measured in CASS-4, which are slightly lower than literature values (Figure 2.4). Note that our measurements on CASS-4 and NASS-5 were made before addition of the Ce spike, so Ce data reported here were not determined by isotope dilution. The positive Sm anomalies observed for both reference seawaters were possibly caused by contamination during preparation of the reference materials (Lawrence and Kamber, 2007).

Table 2.4

REE concentrations (ng l^{-1}) of CASS-4 and the compilation of literature data

CASS-4 [a]	This Work (n=2)	Freslon *et al.*, 2011	Bayon *et al.*, 2011	Lawrence and Kamber, 2007	Zhu *et al.*, 2006
La	9.2 ± 0.2	9 ± 0.7	9.3 ± 0.2	9.34 ± 0.48	10.0 ± 0.4
Ce	4.3 ± 0.4	3.8 ± 0.1	3.85 ± 0.03	4.62 ± 0.94	6.1 ± 0.3
Pr	1.32 ± 0.04	1.27 ± 0.06	1.311 ± 0.005	1.4 ± 0.09	1.42 ± 0.04
Nd	4.65 ± 0.03	5.6 ± 0.4	5.51 ± 0.05	6.03 ± 0.54	5.5 ± 0.5
Sm	5.31 ± 0.07	5.6 ± 0.3	5.73 ± 0.04	5.73 ± 0.24	5.5 ± 0.5
Eu	0.229 ± 0.005	0.23 ± 0.03	0.21 ± 0.02	0.24 ± 0.01	0.19 ± 0.03
Gd	1.12 ± 0.02	1.31 ± 0.09	1.34 ± 0.06	1.34 ± 0.07	1.4 ± 0.2
Tb	0.170 ± 0.003	0.19 ± 0.02	0.189 ± 0.008	0.21 ± 0.01	0.17 ± 0.03
Dy	1.275 ± 0.008	1.4 ± 0.1	1.39 ± 0.04	1.49 ± 0.07	1.5 ± 0.2
Ho	0.336 ± 0.004	0.36 ± 0.03	0.368 ± 0.008	0.41 ± 0.04	0.35 ± 0.03
Er	1.11 ± 0.02	1.18 ± 0.06	1.202 ± 0.010	1.38 ± 0.12	1.1 ± 0.1
Tm	0.162 ± 0.001	-	-	0.22 ± 0.03	0.20 ± 0.05
Yb	1.064 ± 0.004	1.09 ± 0.07	1.15 ± 0.02	1.43 ± 0.4	1.2 ± 0.2
Lu	0.175 ± 0.002	0.185 ± 0.009	0.184 ± 0.002	0.25 ± 0.08	0.16 ± 0.03

[a] data are reported in the form of mean ± standard deviation (1σ)

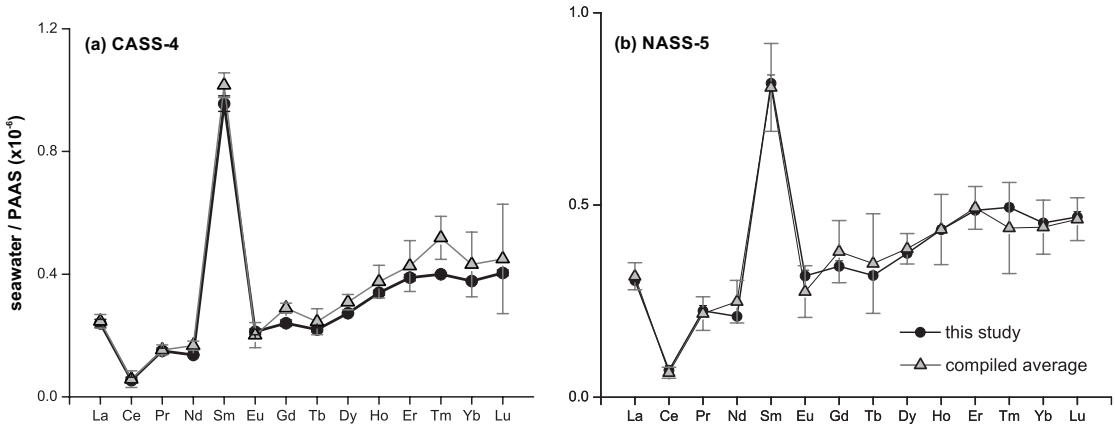

Figure 2.4 Comparison between our new REE results of CASS-4 (a), and NASS-5 (b) and literature values for the two standards in PAAS-normalized REE-pattern diagrams. Error bars in these figures indicates ± 2 standard deviations. Results of this study generally agree with values from the literature, except for Gd and Tm concentrations measured in CASS-4, which are lower than literature values. PAAS data are from McLennan, 1989 (Table 1.1).

Table 2.5

REE concentrations (ng l^{-1}) of NASS-5 and the compilation of literature data

NASS-5 [a]	This Work (n=2)	Freslon *et al.*, 2011	Bayon *et al.*, 2011	Zhu *et al.*, 2009	Rahmi *et al.*, 2007	Lawrence and Kamber, 2007	Zhu *et al.*, 2006	Shaw *et al.*, 2003	Willie and Sturgeon, 2001
La	11.6 ± 0.3	11.2 ± 0.9	13 ± 0.4	12.0 ± 0.3	11.8 ± 0.4	12.19 ± 1.14	11.1 ± 0.5	12.1 ± 0.5	12.8 ± 1.2
Ce	5.6 ± 0.5	5.4 ± 0.2	5.55 ± 0.11	5.26 ± 0.16	5.23 ± 0.05	5.72 ± 0.69	4.9 ± 0.3	4.5 ± 0.7	4.0 ± 0.6
Pr	1.98 ± 0.06	1.98 ± 0.07	2.11 ± 0.05	1.96 ± 0.02	1.84 ± 0.06	2.09 ± 0.19	1.9 ± 0.1	2.0 ± 0.2	1.5 ± 0.2
Nd	7.14 ± 0.05	8.4 ± 0.2	8.8 ± 0.3	8.7 ± 0.7	7.5 ± 0.1	8.43 ± 0.65	6.8 ± 0.5	8.9 ± 0.5	9.9 ± 1.8
Sm	4.53 ± 0.06	4.7 ± 0.2	4.84 ± 0.11	4.50 ± 0.14	4.5 ± 0.3	4.74 ± 0.34	4.0 ± 0.3	4.5 ± 0.2	4.0 ± 0.4
Eu	0.341 ± 0.008	0.32 ± 0.02	0.305 ± 0.014	0.27 ± 0.02	0.29 ± 0.02	0.33 ± 0.03	0.35 ± 0.01	0.27 ± 0.03	0.24 ± 0.05
Gd	1.59 ± 0.03	1.8 ± 0.1	1.9 ± 0.07	1.77 ± 0.09	1.59 ± 0.08	1.83 ± 0.15	2.1 ± 0.1	1.6 ± 0.08	1.53 ± 0.28
Tb	0.245 ± 0.004	0.27 ± 0.01	0.283 ± 0.006	0.37 ± 0.04	0.24 ± 0.02	0.27 ± 0.03	0.22 ± 0.01	0.21 ± 0.04	0.29 ± 0.05
Dy	1.75 ± 0.01	1.86 ± 0.05	1.93 ± 0.07	1.86 ± 0.05	1.8 ± 0.2	1.82 ± 0.2	1.8 ± 0.1	1.78 ± 0.07	1.61 ± 0.17
Ho	0.432 ± 0.005	0.47 ± 0.04	0.48 ± 0.02	0.44 ± 0.04	0.43 ± 0.02	0.47 ± 0.06	0.44 ± 0.02	0.37 ± 0.04	0.36 ± 0.05
Er	1.39 ± 0.02	1.47 ± 0.04	1.5 ± 0.03	1.49 ± 0.08	1.36 ± 0.08	1.43 ± 0.2	1.3 ± 0.1	1.37 ± 0.03	1.31 ± 0.21
Tm	0.200 ± 0.002	-	-	0.19 ± 0.02	0.18 ± 0.01	0.21 ± 0.04	0.19 ± 0.02	0.15 ± 0.03	0.15 ± 0.03
Yb	1.279 ± 0.005	1.26 ± 0.06	1.3 ± 0.03	1.40 ± 0.17	1.13 ± 0.07	1.29 ± 0.38	1.3 ± 0.1	1.2 ± 0.04	1.10 ± 0.24
Lu	0.203 ± 0.003	0.2 ± 0.01	0.204 ± 0.009	0.21 ± 0.02	0.20 ± 0.02	0.19 ± 0.06	0.22 ± 0.02	0.18 ± 0.02	0.20 ± 0.04

[a] data are reported in the form of mean ± standard deviation (1σ)

Participation in the GEOTRACES intercalibration effort for seawater REE concentrations further validates the method presented here. Results of measurements of two GEOTRACES intercalibration samples, KN193-6-Nd-533 (BATS, 15 m) and KN193-6-Nd-330 (BATS, 2000 m), made in 7 laboratories, were reported in van de Flierdt et al. (2012). Except for one participant laboratory that reported results significantly lower than those obtained from other laboratories, REE concentrations for the two intercalibration samples from the other 6 participant laboratories agreed within 10% (1σ) for most of REEs (van de Flierdt et al., 2012). REE concentration results obtained in this study for these two samples agree well with average results reported by 6 laboratories participating in the GEOTRACES intercalibration (Figure 2.5).

The precision of the method described here was demonstrated by repeated analyses of two in-house seawater composites, SCW-1 and SCW-2, aliquots of which were processed through the whole procedure with every batch of the chemistry. Twenty aliquots of SCW-1 were measured between 2007-2010 with the initial procedure, and sixty-six aliquots of SCW-2 were measured throughout the two phases of our procedure development. Results indicate that the precision is <3% (1σ) (commonly ~1%) for the REEs, except for Ce before 2010. The precision of Ce data improved from ~9% to 3% (1σ) after adding the ^{142}Ce spike into the procedure (Table 2.3).

REE concentrations measured in SWC-2 before and after addition of the Ce spike are in a good agreement, except for Ce, for which the mean of isotope-dilution concentrations were ~16% lower than the mean measured without isotope dilution before 2010 (Table 2.3 and Figure 2.6). The reasons for this offset are unclear, but

may relate to greater uncertainty for unspiked Ce concentrations, a higher blank for Ce, or a different yield.

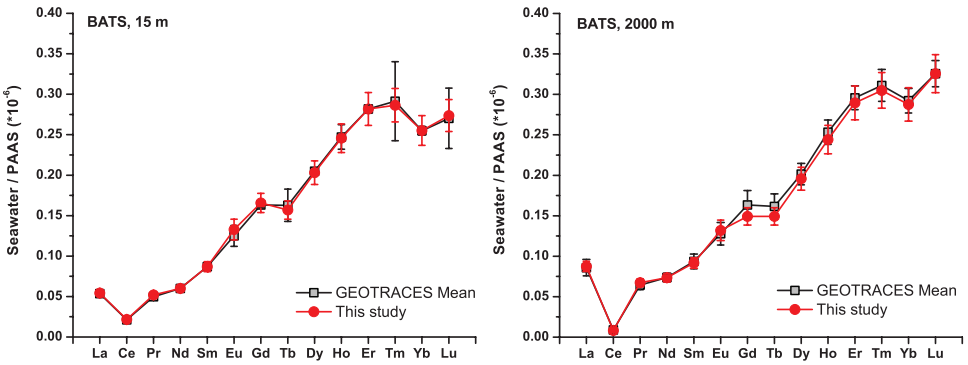

Figure 2.5 Results of REE concentrations for the two BATS seawater samples (KN193-6-Nd-533 and KN193-6-Nd-330) obtained in this study in comparison with respective mean results from 6 laboratories participating in the GEOTRACES inter-comparison on seawater REEs. Error bars indicate 2 standard deviations. PAAS data are from McLennan, 1989 (Table 1.1). Compilation of REE concentration results for the inter-comparison is available in van de Flierdt et al., (2012).

The accuracy of this analytical method was further tested by measuring solutions with known REE concentrations. Four aliquots of the Coral Sea Standards were diluted gravimetrically to concentrations typical of seawater, and measured as unknowns. The measured REE concentrations of these aliquots agree with the gravimetric "true values" of the Coral Sea Standard within ~4% (mostly ~1%) for all the REEs (Table 2.6).

Results of REE measurements on "SAFe" and PS70 intercalibration samples are reported in Table 2.7. Approximately 500 seawater samples, including those presented in Chapter 3, have been measured for their REE concentrations using this procedure at Oxford. The results are oceanographically consistent (i.e. vertical profiles are smooth, and the distributions are consistent with local hydrography), again suggesting good data-quality.

Table 2.6

Results of REE determination on aliquots of the Coral Sea standard with known REE concentrations (ng kg^{-1})

	Test-1 (1:10) [c]	Test-2 (2:10) [c]	Test-3 (3:10) [c]	Test-4 (4:10) [c]	Mean (n=4)	s (1σ) [d]	RSD	True Conc. [e]	Difference [f]
La	413	421	417	416	417	3	0.7%	410.71	1.44%
Ce (IS) [a]	535	529	522	518	526	7	1.4%	504.60	4.20%
Ce (ID) [b]	511	508	506	510	509	2	0.4%	504.60	0.83%
Pr	80.0	81.3	80.6	80.2	80.5	0.6	0.7%	79.07	1.82%
Nd	364.8	366.0	364.6	364.1	364.9	0.8	0.2%	366.84	-0.54%
Sm	73.5	73.8	73.0	73.0	73.3	0.4	0.5%	72.20	1.55%
Eu	22.6	22.9	22.9	22.5	22.7	0.2	0.8%	21.81	4.03%
Gd	128	124	124	123	125	2	1.8%	122.55	1.85%
Tb	20.9	21.2	21.3	21.1	21.1	0.2	0.8%	21.66	-2.49%
Dy	185	187	188	187	187	1	0.8%	187.66	-0.53%
Ho	49.9	50.4	50.6	50.2	50.3	0.3	0.6%	50.67	-0.76%
Er	169	171	172	170	170	1	0.8%	173.03	-1.68%
Tm	21.7	21.9	22.2	21.7	21.9	0.2	1.0%	21.66	0.96%
Yb	130.2	130.0	131.2	129.1	130.1	0.8	0.6%	129.72	0.31%
Lu	21.5	21.4	21.8	21.4	21.5	0.1	0.8%	21.65	-0.62%

[a] IS denotes Internal Standardization;

[b] denotes Isotope Dilution;

[c] the ratios in brackets are weight ratios of the Coral Sea standard to the spike

[d] standard deviation

[e] true concentrations are determined by weighing

[f] difference is defined as (mean - true conc.)/true conc.

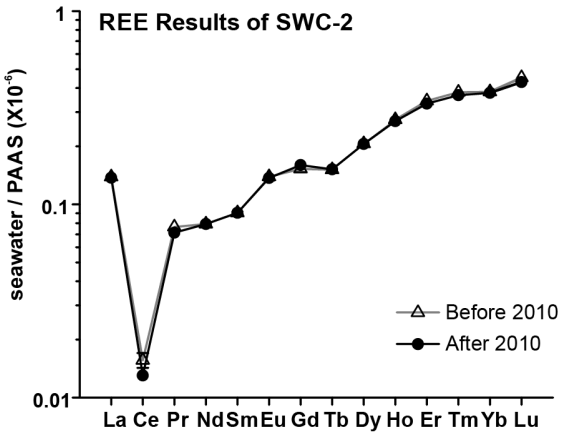

Figure 2.6 Results of mean REE concentrations determined on the same seawater composite (SWC-2) using the initial procedure before 2010 and the improved one after 2010. Error bars (1 standard deviation) are generally smaller than the symbols in the figure. Results obtained during these two periods are in excellent agreement. PAAS data are from McLennan, 1989 (Table 1.1).

Table 2.7

REE concentration results for 4 intercalibration samples

	SAFe-S1		SAFe-D2		PS70/328/4		PS70/328/6	
	MEAN (n=2) [a]	s [b]	MEAN (n=2)	s	MEAN (n=2)	s	MEAN (n=2)	s
La	0.729	0.02	4.702	0.127	2.293	0.062	2.558	0.069
Ce	0.454	0.042	0.466	0.043	0.309	0.029	0.548	0.051
Pr	0.136	0.005	0.601	0.021	0.423	0.015	0.477	0.017
Nd	0.615	0.006	2.61	0.027	1.849	0.019	2.044	0.021
Sm	0.122	0.002	0.495	0.009	0.403	0.007	0.446	0.008
Eu	0.039	0.001	0.155	0.004	0.118	0.003	0.128	0.003
Gd	0.206	0.006	0.802	0.022	0.592	0.016	0.625	0.017
Tb	0.034	0.001	0.126	0.003	0.097	0.002	0.101	0.002
Dy	0.271	0.005	1.036	0.019	0.766	0.014	0.795	0.015
Ho	0.076	0.001	0.301	0.006	0.204	0.004	0.209	0.004
Er	0.251	0.005	1.081	0.021	0.693	0.013	0.706	0.014
Tm	0.032	0.001	0.168	0.003	0.104	0.002	0.105	0.002
Yb	0.171	0.002	1.166	0.016	0.694	0.009	0.705	0.01
Lu	0.027	0.001	0.213	0.005	0.119	0.003	0.119	0.003

[a] unit: ng kg^{-1}

[b] 1 standard deviation (1σ)

2.5 Conclusions

This study presents a new procedure that permits simultaneous determination of all 14 REEs in ~100 ml seawater. The procedure was validated by measurement of two seawater standards (CASS-4 and NASS-5), the GEOTRACES inter-calibration samples (BATS) and a gravimetrically prepared multi-element standard containing all REEs. Concentrations measured on these samples agree with those reported from other laboratories, or with the known values. The procedure uses easily collectable volumes of seawater (~100 ml), and provides excellent precision of <3% (1σ) for all REEs. This is comparable with uncertainty from the much more time-consuming ID-TIMS analysis. Successful application of the new procedure to measure ~500 seawater samples from the Pacific and Atlantic suggests that this new method is reliable for routine measurement of REEs in a wide range of seawater samples.

Chapter 3

The cycling of dissolved rare earth elements in the tropical South Atlantic and implications for trace metal inputs and cycles

NOTE: *A revised version of this chapter, co-authored with Yves Plancherel, Mak A. Saito, Peter M. Scott and Gideon M. Henderson, has been published in Geochimica et Cosmochimica, 177 (2016): 217–237 (http://dx.doi.org/10.1016/j.gca.2016.01.018). X-Y Zheng preformed REE measurements, and developed MATLAB codes for the OMP model used in this study, and wrote the chapter with comments from all co-authors.*

Abstract

This chapter reports dissolved rare earth element (*d*REE) concentrations across a full-depth zonal section in the South Atlantic along ~12°S. The new dataset provides the first full ocean section of *d*REE concentrations, enabling systematic investigation of the REE cycling in the South Atlantic. Elevated *d*REE concentrations in surface waters are observed at coastal areas near the Angola coast, coinciding with high concentrations of other trace metals, including Fe, Mn and Co. This coastal trace-metal enrichment may result from reduction of Fe-Mn oxides, as suggested by changes of REE patterns. The variations in *d*Ce concentrations in surface waters suggest that this element may be controlled by both O_2-dependent Ce oxidation in surface seawater and input of REEs from external sources. The cycling of trivalent *d*REEs in the subsurface oxygen minimum zone (OMZ) at ~400 m off the African shelf is closely linked to the redox cycling of Fe and Mn under low oxygen conditions, and Ce is additionally controlled by its own redox behaviour.

An inverse model was developed to quantitatively deconvolve the relative importance of watermass mixing from non-hydrographic controls (particle scavenging and/or remineralization) in determining the observed distribution of *d*REE concentrations in deep waters (>1000 m). Results indicate that >80% of the *d*REE concentrations below ~1000 m represent preformed REE concentrations explained by watermass mixing. Analysis of the non-preformed concentration field reveals enhanced scavenging of dissolved light REEs above the mid-Atlantic ridge, and significant additions of *d*REEs at ~1500 m and below ~4000 m in the Angola Basin near the continental margin. Different Ce behaviour at the two depths probably indicates that different mechanisms may account for the observed *d*REE additions at the two depths. Although Ce and Mn typically have similar oceanic behaviour due to

their similar redox potential, unusual and unexplained decoupling of these elements is observed at intermediate water depths (~1500 m) near the African continental margin.

3.1 Introduction

The rare earth elements (REEs) consist of 14 naturally occurring elements with atomic numbers between 57 and 71. The filling of the 4f electron shell with increasing atomic number produces a progressive reduction of the ionic radii of REEs (i.e. the lanthanide contraction). This effect results in weak differences in bond strengths when REE interact with other atoms, which produces observable fractionation between the REEs and lead to distinctive patterns of REE concentrations. Spatio-temporal variations in these REE patterns in the ocean are controlled by source characteristics and by the geochemical environment (e.g. redox state, pH, particle interactions). As such, dissolved and particulate REE patterns and their evolution can be used to probe a variety of natural geochemical processes (e.g. metal-particle interactions, redox state, particle export, sediment-ocean and land-ocean exchange).

Motivated by the potential application of REEs as tracers for a wide range of oceanic processes, studies of REEs in the ocean bloomed in the 1980s–90s (e.g. Bertram and Elderfield, 1993; De Baar et al., 1985; Elderfield and Greaves, 1982; German and Elderfield, 1990b; Zhang and Nozaki, 1996), leading to understanding of the basics of their cycling in the ocean. These pieces of work indicated that the distributions of REEs in seawater are largely controlled by the competition between their complexation with ligands in seawater (mainly CO_3^{2-}) and ligands on marine particulate surfaces (e.g. Fe-Mn oxide coatings, organics) (e.g. Byrne and Sholkovitz, 1996; Elderfield et al., 1988). Light REEs (LREEs) are more particle-reactive than heavy REEs (HREEs) in seawater, because HREEs tend to form relatively more stable complexes with carbonate ions in seawater (e.g. Sholkovitz et al., 1994; Wood, 1990b). The resulting preferential scavenging of LREEs to particles leads to a

characteristic HREE-enriched *d*REE pattern in open-ocean seawater (e.g. Sholkovitz et al., 1994). Cerium (Ce) shows the strongest particle reactivity in the REE-group because, in addition to particle scavenging common for all trivalent REEs, Ce is also oxidatively removed from the water column via its redox transformation from soluble Ce^{3+} to insoluble Ce^{4+}. The extent of Ce oxidative removal is commonly expressed using the concept of the "Ce anomaly". The Ce-anomaly is calculated by comparing the dissolved Ce concentration to the theoretically predicted value, obtained by interpolation from its neighbouring elements. The ability to quantify the oxidative removal of Ce may provide a powerful tool to probe redox processes in the ocean.

The current understanding of marine cycling of REEs is far from complete. This is demonstrated by a lack of detailed knowledge of the REE fluxes near continental margins. Partial dissolution of atmospheric dust and rivers have been traditionally considered to be the major sources of REEs to the ocean (e.g. Goldstein and Jacobsen, 1988; Greaves et al., 1994). Recent studies, however, primarily based on Nd concentrations and Nd isotopes in seawater, suggest that Nd fluxes from continental margins may be larger than originally thought (e.g. Arsouze et al., 2009; Jeandel et al., 2007). Questions on the size and distribution of the flux of REEs at continental margins remain unanswered.

Recent studies of REEs in the ocean have increasingly focused on Nd and Nd isotopes alone (e.g. Carter et al., 2012; Grasse et al., 2012; Rickli et al., 2009; Singh et al., 2012; Stichel et al., 2012). The interest in Nd is primarily due to the successful use of Nd isotopes as a watermass tracer (e.g. Piotrowski et al., 2012; Roberts et al., 2010; Zheng et al., 2013). Studying REEs as a group, though, may provide valuable information on relevant oceanic processes, which are important in controlling REE

cycling (such as redox processes), but cannot be readily seen by the study of Nd (and its isotopes) alone.

In this study, we investigate the distribution of dissolved REE concentrations along a full-depth, zonal section at ~12°S in the South Atlantic. Concentration profiles of *d*REEs in the South Atlantic were only previously available at a single station at ~40°S in the Cape Basin (German et al., 1995), limiting our understanding on the cycling of REEs in the South Atlantic. In contrast to previous studies that focus on only a small number of oceanographically discrete REE profiles, this study constrains the distribution of *d*REEs across an entire ocean basin and sets these measurements in a well-constrained oceanographic context, making the separation of transport and local biogeochemical processes possible. It has been suggested that the distribution of *d*REE concentrations (and Nd isotopes) in the water column is controlled by both hydrographic processes resulted from advection/mixing of watermasses, and by non-hydrographic processes associated with particle scavenging and remineralization (e.g. Nozaki and Alibo, 2003; Siddall et al., 2008). A quantitative assessment of the relative importance of these conservative and non-conservative processes has not previously been realized. In this study, this goal was achieved by using inverse modeling of the new *d*REE data from the South Atlantic.

Previous studies of other trace metals, including dissolved Fe (*d*Fe) and Mn (*d*Mn), from the same section have revealed several features that are of great interest for the study of REEs. These features include large inputs of *d*Fe and *d*Mn in the subsurface oxygen minimum zone (OMZ) near the continental shelf, and significant hydrothermal input of these two metals as seen above the mid-Atlantic ridge (MAR) (Noble et al., 2012; Saito et al., 2013) (Figure 3.1). Study of *d*REEs along the same

section may help to improve the understanding of the cycling of these important micronutrient metals.

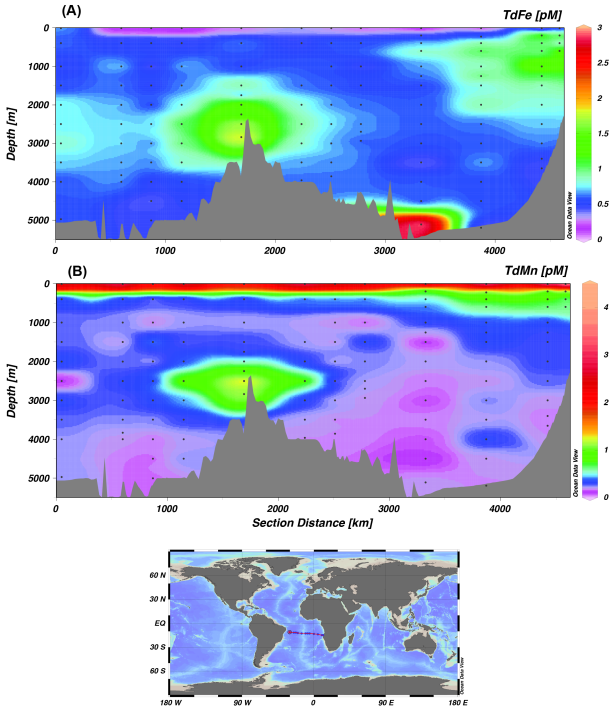

Figure 3.1 Cross-sections for *d*Fe (A) and *d*Mn (B) from the same ocean section analysed for *d*REE concentrations in this study. Dissolved Fe and Mn data from Noble et al. (2012).

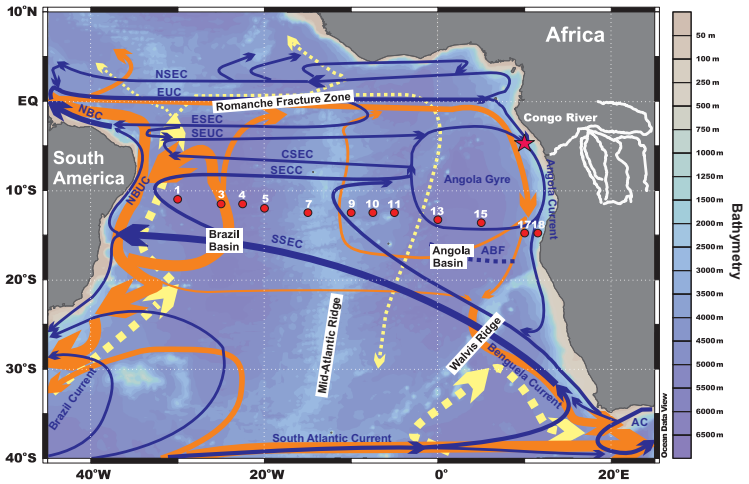

Figure 3.2 Map showing sampling locations of stations for dREE analysis from the CoFeMUG cruise (red circles), and a seawater sample with REE concentration data off the Congo River (red star; unpublished data from G. Bayon). The schematic flow patterns of major watermasses affecting the CoFeMUG section are also shown, from Stramma and England (1999). (Blue lines: upper ocean circulation; Orange lines: North Atlantic Deep Water (NADW); Yellow dashed lines: Antarctic Bottom Water (AABW)).

3.2 Regional hydrography

Seawater samples were collected at 12 stations during the CoFeMUG (KN195–2) cruise aboard the *R/V Knorr* from 16 November to 13 December 2007, along a full-depth east–west transect across the tropical South Atlantic, beginning at 11˚S, 330˚E, and ending at 14.75˚S, 12.2˚E (Figure 3.2).

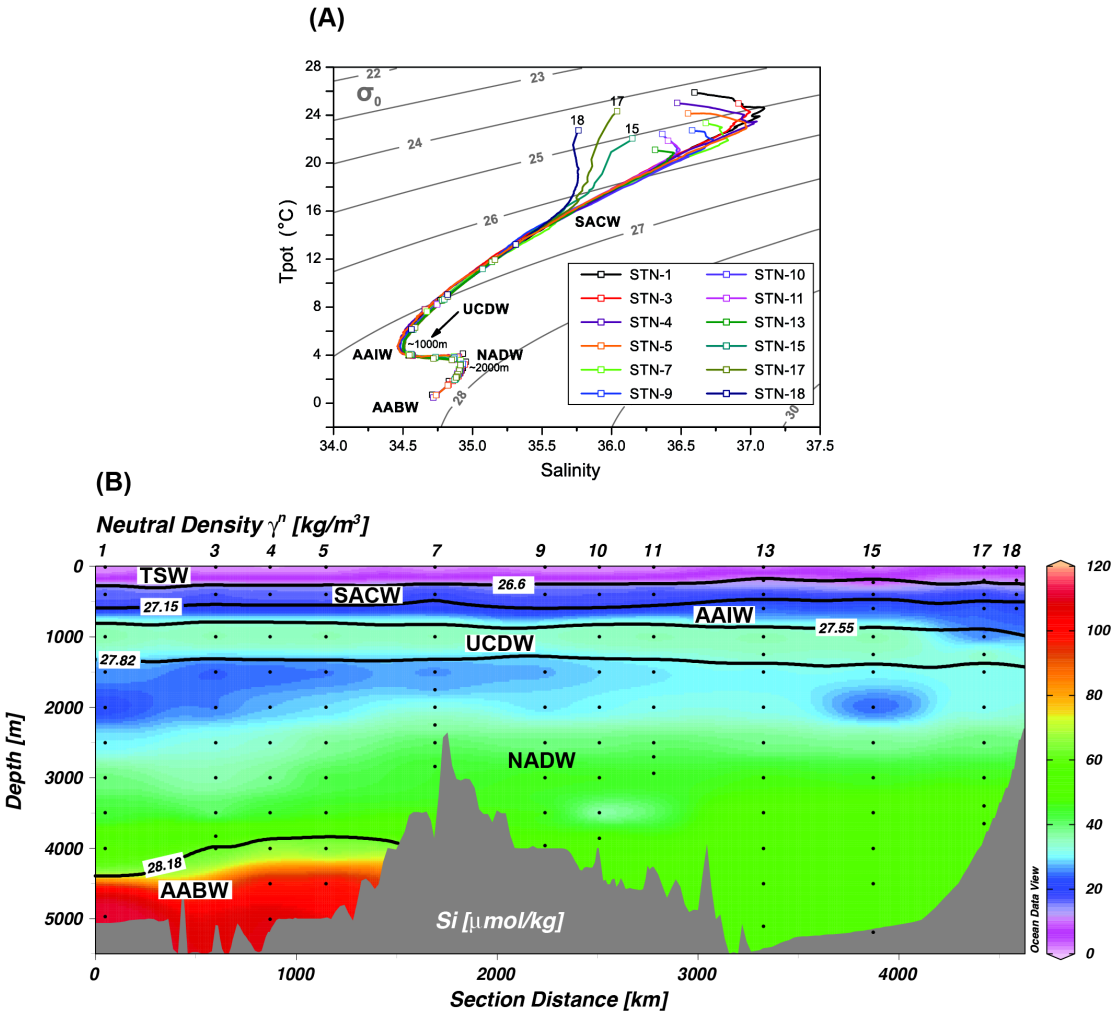

Figure 3.3 (A) T–S diagram for stations selected in this study from the CoFeMUG section; (B) The cross-section of dissolved silicate (*d*Si) from the CoFeMUG section (Noble et al., 2012), superimposed by depth ranges of major watermasses, according to characteristic neutral density surfaces defined after Vanicek and Siedler (2002). TSW–Tropical Surface Water; SACW–South Atlantic Central Water; AAIW–Antarctic Intermediate Water; UCDW–Upper Circumpolar Deep Water; NADW–North Atlantic Deep Water; AABW–Antarctic Bottom Water.

Hydrographic data (i.e. T–S and dissolved Si) are presented in Figure 3.3 to characterize the vertical distributions of the major water masses along the CoFeMUG section. Major watermasses can be approximately separated by the characteristic neutral density surfaces defined in Vanicek and Siedler (2002). The surface ocean is occupied by warm Tropical Surface Water (TSW) with typical mixed layer thickness of ~50 m. The uppermost samples were collected within this layer at ~10 m across the section. Below the mixed layer, South Atlantic Central Water (SACW) is found to ~500 m. SACW can be recognized on the T–S diagram by an approximately straight mixing line between surface waters and intermediate waters. One or two samples corresponding to SACW were measured at each station across the section. Antarctic Intermediate Water (AAIW), characterized by a salinity minimum, is found immediately below SACW, and extends to water depths of ~800 m. AAIW was sampled at only 4 stations (station 13–18) on the eastern side of the CoFeMUG section. Upper Circumpolar Deep Water (UCDW) is observed beneath AAIW, and is centred at ~1000 m. Although UCDW cannot be recognized by its T–S characteristics which fall on the mixing line of overlying AAIW and underlying North Atlantic Deep Water (NADW), the presence of this watermass at the CeFeMUG section is evidenced by its high nutrient signature (e.g. Si) centred at ~1000 m (Fig. 3.3b). One sample from the core of UCDW was measured at each station across the entire section. Beneath UCDW, NADW is found below ~1500 m. The NADW layer can be broadly separated as upper NADW (UNADW) and lower NADW (LNADW), or more sub-layers, based on detailed studies of tracer distributions (e.g. T, s, CFC) in the South Atlantic (e.g. Stramma and England, 1999). Many of the measured samples in this study are located in NADW. Antarctic Bottom Water (AABW) is found below ~4000 m in the Brazil Basin on the western side of the section, as indicated by high Si

content (Figure 3.3), whereas it is almost absent from the Angola Basin, because AABW is blocked by the Walvis Ridge at the southern border of the Angola Basin (Figure 3.2).

Major currents and the schematic flow-patterns of major watermasses, based on detailed large-scale hydrographic observations in the South Atlantic (e.g. Stramma and England, 1999; Stramma and Schott, 1999) are shown in Figure 3.2. The upper-ocean (~0–500 m) circulation at CoFeMUG section is influenced by the westward-flowing southern branch of the South Equatorial Current (SSEC), which is fed by the Benguela Current from the south, with the cyclonic Angola Gyre embedded at the eastern side of the section in the Angola Basin (Mercier et al., 2003; Stramma and England, 1999; Wienders et al., 2000). The Angola Gyre receives waters delivered by the southward-flowing Angola Current along the African coast, and is separated from the Benguela Current by the Angola–Benguela Front (ABF), located slightly south of our studied section at ~16°S (John et al., 2004; Lass and Mohrholz, 2008; Lass et al., 2000). A prominent oxygen minimum zone (OMZ), generated due to high productivity and low ventilation (Lass and Mohrholz, 2008; Mohrholz et al., 2008), is observed at water depths between ~100 m and ~600 m (centred at ~400 m) off the Angolan coast, and laterally extends into the interior of the Angola Basin with decreased thickness (Figure 3.4).

At intermediate depths, both AAIW and UCDW spread northwards, but they have different source regions in the south (Stramma and England, 1999). In the deep South Atlantic, the NADW is mainly transported by a southward-flowing Deep Western Boundary Current into the Brazil Basin. Part of NADW also flows southward along a weaker path near the eastern boundary of the South Atlantic into the Angola Basin with cyclonic recirculation (Arhan et al., 2003; Larqué et al., 1997;

Stramma and England, 1999). AABW spreads northward into the Brazil Basin, but is largely blocked from entering the Angola Basin from the south by the Walvis Ridge. A small amount of AABW can enter the Angola Basin from the north due to eastward deflection of its northward transport through the Romanche Fracture Zone at the equator, but this tongue of AABW gradually thins and loses its identity via mixing with NADW during its southward transport into the Angola Basin (Larqué et al., 1997; Stramma and England, 1999; Warren and Speer, 1991).

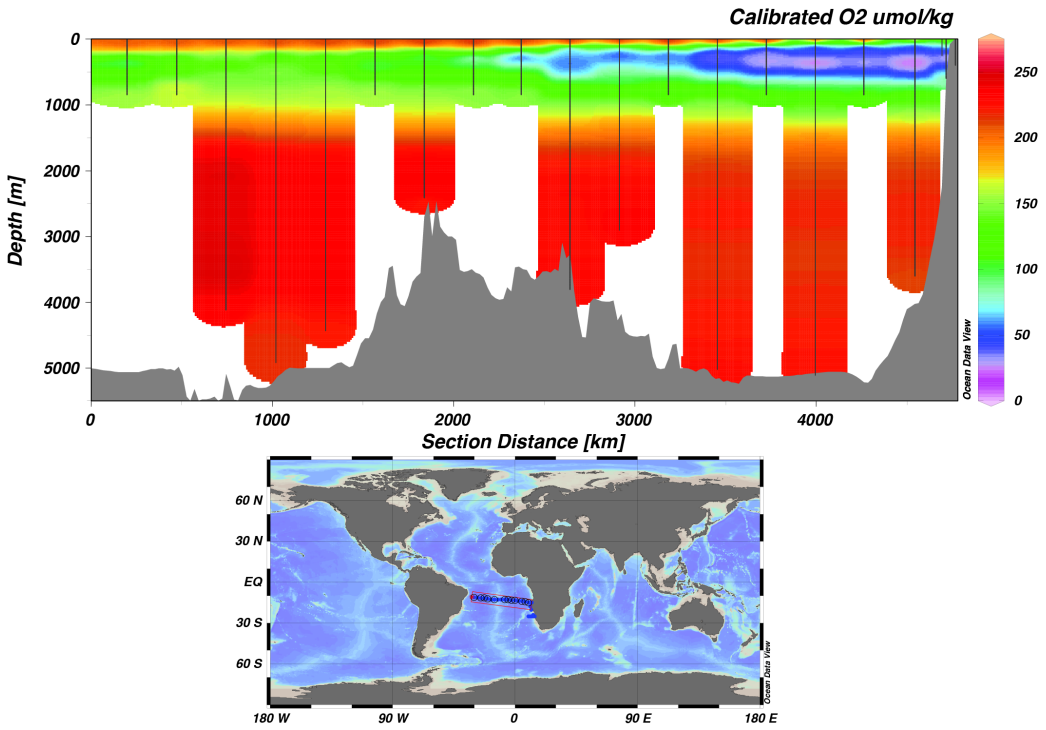

Figure 3.4 Dissolved O_2 distribution at the CoFeMUG section, which shows a prominent OMZ centred at ~400 m off the Angola shelf.

3.3 Material and methods

3.3.1 Sample collection

119 seawater samples from 12 stations of the CoFeMUG section along ~12°S were analyzed for *d*REEs (Figure 3.2). Samples were collected with a trace metal

sampling protocol: Teflon-coated X–Niskin sampling bottles (Ocean Test Equipment) were deployed on an epoxy-coated CTD rosette (Sea-Bird Electronics) attached to a non-metallic line, and were programmed to trip at pre-determined depths. Immediately following collection, seawater was filtered through a 142-mm 0.4-μm polycarbonate plastic sandwich filter (Geotech Environmental Equipment) in a class–100 laboratory. All bottles, tubing and filters were acid-cleaned before use. Samples intended for the measurement of *d*REEs were acidified to a pH of 1.7 using high-purity HCl (Seastar) within 6 months of sampling.

3.3.2 Analytical procedure for dissolved REEs

Sample pre-treatment and measurement was carried out at the Department of Earth Sciences, University of Oxford. A new procedure for analyzing *d*REEs in seawater using a reasonably small sample (~100 ml) was developed based mainly on methods of Elderfield and Greaves (1983a) and Field and Sherrell (1998). The procedure permits simultaneous determination of all 14 naturally occurring REEs at a precision comparable to that achieved by traditional isotope dilution methods (~ 3% (1σ); e.g. Greaves et al., 1989). The details and full validation of the procedure are provided in Chapter 2.

REEs were analyzed on a magnetic sector field ICP–MS (Element 2, Thermo), with a desolvating nebulizer system (Aridus 1, CETAC). The use of the Aridus desolvating nebulizer system eliminated oxide interferences on REEs during these analyses. Cerium oxide, typifying LREE-oxide that can interfere on HREE measurements, was checked at the beginning of each analysis session with a high-purity Ce standard, and was generally <0.1% of total Ce signals. The interference of

barium oxide on Eu was also monitored for each sample, and found negligible (typically <1% of total Eu signals).

Procedural blank, typically ~8% of sample mass for Ce and <1% for all other REEs, was measured with each batch of ~12 samples and corrected batch by batch. Repeated analyses of an in-house seawater composite standard yielded an external reproducibility of <3% (1σ, n=19) on all REEs. Accuracy of the analysis is estimated to be <4% for all REEs, based on four repeated analyses of a gravimetrically prepared standard containing all REEs.

3.3.3 CTD, nutrients and other trace metal (dFe, dMn) data

Salinity (s), potential temperature (T) and dissolved oxygen (dO_2) were measured *in-situ* with CTD-mounted sensors. CTD data were not available at several water-depths (mostly ≥1000 m) at a few stations (i.e. 1, 7, 9 and 18) due to malfunction of the sensors during the cruise, s and T data were, therefore, extracted from the World Ocean Atlas 2009 (WOA09) seasonal (October–December) hydrographic dataset from the same water-depths and locations as substitutes for the missing data points. The validity of using these substitute s and T data was demonstrated by good agreement between the WOA09-extracted values and existing *in-situ* data (≥1000 m) collected during the cruise. The WOA09-extracted T and s substitutes fitted the existing dataset in an oceanographically consistent fashion (Figure 3.3), validating their use in this study. Dissolved O_2 data extracted from the WOA09 were, on the other hand, less consistent with existing *in-situ* ones, they were therefore not adopted to fill gaps in the dO_2 data.

Nutrients (i.e. silicate and phosphate), *d*Fe, and *d*Mn concentrations were measured during the CoFeMUG cruise. Analytical details and significance of these

datasets are presented in Noble et al. (2012), and the full datasets can be retrieved from the online data repository (BCO–DMO, http://bcodmo.org).

3.3.4 Data analysis – an inverse model

The oceanic distribution of *d*REEs is controlled by both conservative mixing between different watermasses, and non-conservative processes, such as scavenging and remineralization. To separate these processes, an inverse model was developed to separate non-conservative behaviour from observed *d*Nd and *d*Yb at the CoFeMUG section. The inverse model used here was modified from the standard Optimum Multiparameter (OMP) analysis. OMP is a commonly used analytical method that simultaneously takes account of multiple parameters (i.e. hydrographic tracers) to calculate both mixing fractions of pre-defined end-member water types and remineralization terms of the chosen macro-nutrients for a given water parcel (e.g. Hupe and Karstensen, 2000; Karstensen and Tomczak, 1998; Tomczak and Large, 1989). Similar modelling approaches have been previously applied to analyze oceanic distributions of tracers other than macronutrients, such as ^{3}He in the Atlantic (Rüth et al., 2000), and, more recently, *d*Nd and Nd isotopes in the Indian Ocean (Singh et al., 2012).

A brief description of the inverse model used in this study is given below. Mixing of conservative and non-conservative tracers in seawater, together with mass conservation, can be mathematically formulated with following equations:

$$\sum_{i=1}^{n} f_i \times x_i^j = x_{obs}^j \quad \text{(Eq. 1)}$$

$$\sum_{i=1}^{n} f_i \times x_i^j + \Delta x^j = x_{obs}^j \quad \text{(Eq. 2)}$$

$$\sum_{i=1}^{n} f_i = 1 \quad \text{(Eq. 3)}$$

where n represents numbers of end-member water types; f_i represents the fraction of the end-member water type i; x_i^j represents the characteristic value of the chosen oceanic tracer j in the pre-defined end-member water type i; and Δx^j represents the non-conservative component of the tracer j during mixing. Eq. (1) and (2) are general representations for the conservative and non-conservative tracers respectively. The numbers of chosen tracers in the model sets the number of versions of Eq. (1) and/or Eq. (2) that needs to be solved. Eq. (3) denotes mass conservation. In this study, the chosen conservative tracers are potential temperature (θ) and salinity (s), and non-conservative tracers are silicate (Si), phosphate (PO_4), *d*Nd and *d*Yb.

Eqs. (1)–(3) can be written in a matrix form: $Ax = x_{obs}$ (Eq. 4)

where A is the design matrix containing pre-defined characteristics of all chosen tracers for all end-member water types; x is a vector containing all unknowns that need to be solved (i.e. mixing fractions and non-conservative terms); and x_{obs} is a vector containing measured values for all chosen tracers in each sample. Consequently, a solution for x in Eq. (4) gives the most probable (in a least-squares regression sense) mixing fractions of each end-member water type, and non-conservative terms for the chosen non-conservative tracers at a given sampling point.

Two approaches were adopted in this study to avoid solving an underdetermined system (i.e. a system in which the number of the unknowns is larger than the number of equations), whose solution may be unstable or oceanographically unrealistic due to insufficient constraints imposed by observations. Firstly, the analysis was limited to samples below water depths of ~1000 m to avoid complications of defining end-members in the shallow ocean, where local processes

are likely to be more important than mixing, as reflected by large regional/seasonal variability in tracer-distributions. Given the well-constrained hydrography in the region (see Section 3.2), 4 end-member water types, namely UCDW, UNADW, LNADW and AABW, were defined to account for mixing processes occurring below ~1000 m at the CoFeMUG section. Secondly, a $\Delta Si / \Delta PO_4$ ratio of 40, based on previously observed and modelled results (e.g. Hupe and Karstensen, 2000; Takeda, 1998), was used in the model to reduce one unknown (i.e. ΔSi). Consequently, a just-determined system, which includes 7 equations (i.e. based on θ, s, Si, PO_4, *d*Nd, *d*Yb and mass conservation) and 7 unknowns (i.e. ΔPO_4, ΔNd, ΔYb and $f_1 - f_4$ i.e. the fraction of each of the four water types in the sample), was solved in this study.

MATLAB scripts, based on those of the extended OMP analysis (e.g. Hupe and Karstensen, 2000; see more details on http://omp.ifm-geomar.de), were adjusted to incorporate *d*Nd and *d*Yb (Appendix B). Equations were firstly standardized to make parameters in different units directly commensurable, and then weighed accordingly, following the methods of Hupe and Karstensen (2000); Tomczak and Large (1989). The original algorithm of the extended OMP analysis adopted a non-negative least-squares regression method to find the most probable non-negative solutions for non-conservative terms (Hupe and Karstensen, 2000), but this method is not suitable for non-conservative terms of *d*Nd and *d*Yb (i.e. ΔNd and ΔYb), whose values may be either negative (i.e. removal) or positive (i.e. addition). Hence, the original algorithm was replaced by the conjugate gradient method (Tarantola, 2005) that does not enforce solutions of the two terms to be positive values in this study.

Table 3.1

Tracer characteristics in the 4 end-member water types

	UCDW	NADW		AABW
		UNADW	LNADW	
pot-T (°C)	3.97 ± 0.53	4.36 ± 0.39	2.85 ± 0.42	-0.02 ± 0.33
s	34.60 ± 0.11	35.06 ± 0.05	34.94 ± 0.04	34.67 ± 0.01
Silicate (µmol/L)	38.42 ± 8.14	18.65 ± 4.41	33.31 ± 8.01	118.38 ± 7.92
Phosphate (µmol/L)	2.19 ± 0.10	1.27 ± 0.16	1.35 ± 0.20	2.21 ± 0.06
***d*Nd (pmol/kg)**	15.9 ± 1.5	16.8 ± 0.8	19.8 ± 1.0	39.0 ± 1.4
***d*Yb (pmol/kg)**	6.3 ± 1.3	4.7 ± 0.1	5.1 ± 0.4	8.5 ± 0.2

Characteristics of the chosen tracers for each of the 4 end-member water types (i.e. UCDW, UNADW, LNADW and AABW) need to be pre-defined to perform the analysis, and the pre-defined end-member values are summarized in Table 3.1. End-member values of θ, s, Si and PO_4 and associated natural variability for the 4 water types were obtained using historical observations from the World Ocean Circulation Experiment (WOCE) at corresponding neutral-density ranges near respective source regions or on their main transport paths upstream of the CoFeMUG section. The neutral-density ranges for each end-member followed the previous separation (Vanicek and Siedler, 2002). Characteristic values for *d*Nd and *d*Yb and their variability in each end-member were also attained through referring to observational data near respective source regions, or on the main transport paths upstream of the CoFeMUG section if data near source regions are not available (Elderfield and Greaves, 1982; German et al., 1995; Lacan and Jeandel, 2005a; Piepgras and Wasserburg, 1987) (Figure 3.5).

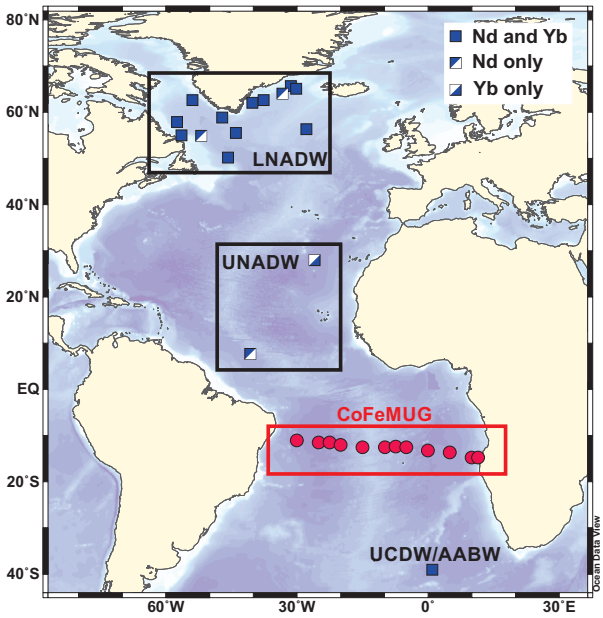

Figure 3.5 Locations of historical observations that were used to define Nd and Yb concentrations of the four end-member water types.

Because there is natural variability associated with the end-member values of the chosen tracers in each selected water type, and also analytical error associated with the measured data, robustness of the modelled results was tested by numerical perturbation experiments. Uniformly distributed random noise, assessed from natural variability observed near source regions (Table 3.1), was imposed on the pre-defined end-member values of corresponding tracers (i.e. matrix A in Eq. 4). Simultaneously, random noise, associated with analytical precision, was also added to the measured data (i.e. vector x_{obs} in Eq. 4). A total of 250,000 random combinations of perturbed source-water matrix A and observed data vector x_{obs} were generated to calculate solutions. The ranges of perturbed end-member values and perturbed observational data are displayed in property–property figures (Figure 3.6). Mean results of mixing fractions, ΔNd and ΔYb from 250,000 perturbation experiments are presented in the Results Section 3.4.2.

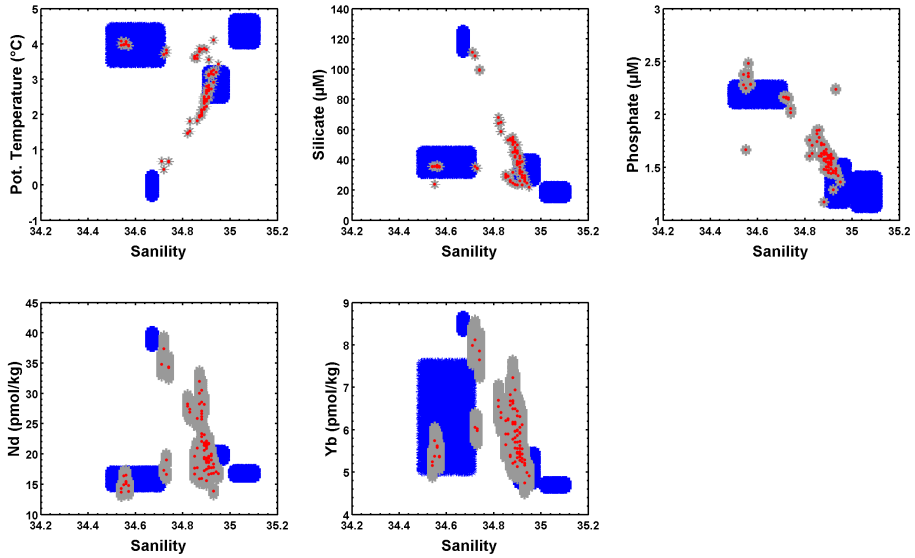

Figure 3.6 Property–property diagrams showing the ranges of random noise imposed on both pre-defined end-members and measured data during all perturbation experiments in this study (Blue regions: perturbed end-member ranges; Grey regions: perturbed observational data ranges; Red dots: measured data)

3.4 Results

3.4.1 Dissolved REEs

The results of *d*REE measurements are reported in Table 3.2 (Appendix C). Mean REE patterns for surface samples, and samples every 1000 m across the CoFeMUG section are shown in Figure 3.7. To simplify visualization of the results, *d*Nd is used to typify the *d*LREEs (i.e. La to Dy), and *d*Yb is used to represent and *d*HREEs (i.e. Ho to Lu). This is reasonable given the systematic change observed (and expected) in behaviour of the REEs in seawater. The results of *d*Ce concentrations are presented separately because this element behaves differently due to its unique redox properties. General features of *d*REE profiles at individual station are first described (Figure 3.8), followed by presentations of the *d*REE concentration distributions in cross-sections (Figure 3.9).

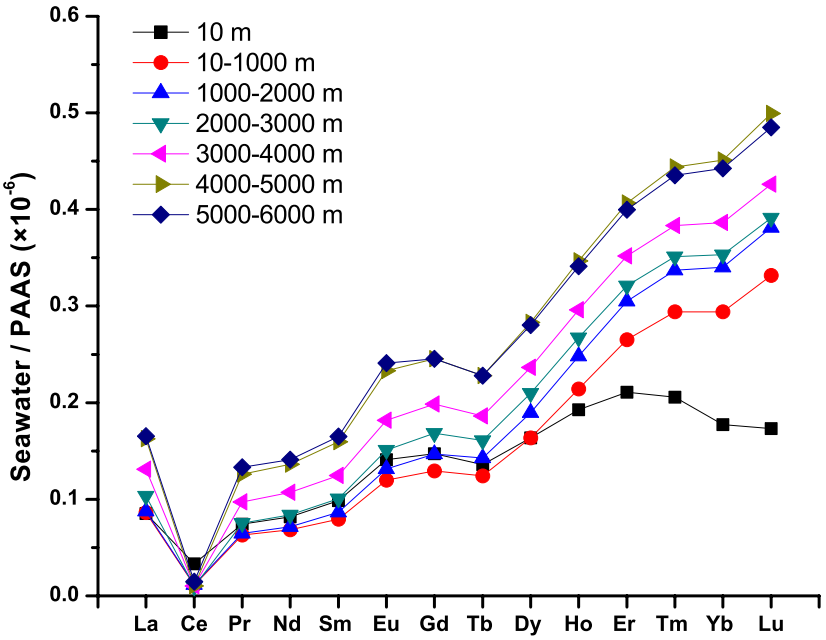

Figure 3.7 Average REE patterns (surface and every 1000 m) of the CoFeMUG section.

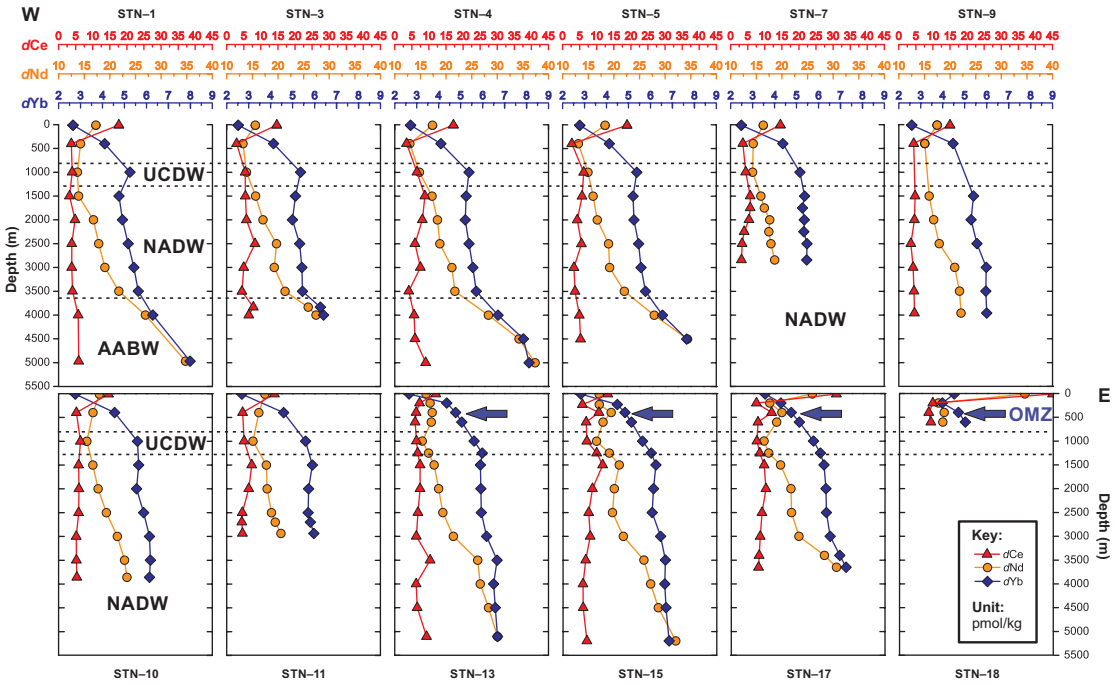

Figure 3.8 Profiles of *d*Nd, *d*Yb and *d*Ce at each sampling station (numbered STN-1 to STN-18) across the CoFeMUG section.

The *d*LREE-profiles (exemplified by *d*Nd) are broadly characterized by a decrease in concentrations from the surface (~10 m) to water depths between ~400 m and ~1000 m, followed by a continuous increase with depth towards the bottom (Figure 3.8). For stations 1, 3, 4 and 5 in the Brazil Basin where the AABW is present below ~3500 m, the increase of *d*LREE-concentrations is more pronounced in the AABW than in the overlying water column. A notable exception to the general shape of *d*LREE-profiles, as described above, is observed at stations that are affected by a subsurface OMZ off the western Angola shelf (e.g. stations 13–17), where secondary maxima in *d*LREE-concentrations develop at water depths of ~400 m coincident with the core of the OMZ (Figure 3.4 and Figure 3.8).

The *d*HREE-profiles (exemplified by *d*Yb) are typically characterized by a pronounced increase in concentrations from the surface to water depths between ~1000 m and ~1500 m (e.g. a ~2-fold increase for *d*Yb), followed by a weaker increase with depth towards the bottom (e.g. a <~25% increase for *d*Yb), except for the profiles in the Brazil Basin, which show a more pronounced increase below ~3500 m where AABW is present. Secondary concentration-maxima at ~1000 m, coincident with water depths of the UCDW, can be recognized from the *d*HREE-profiles in stations 1, 3, 4 and 5 within the Brazil Basin, but they are less apparent in other stations. In contrast to the apparent *d*LREEs enrichment in profiles at ~400 m within the OMZ (e.g. stations 13–17), *d*HREE at the same stations do not show perceptible increases compared to concentrations in the underlying and overlying water column.

The concentration-profiles of *d*Ce display surface maxima at all stations, and then decrease rapidly towards water depths of ~400 m, except for stations 15 and 17 where secondary maxima in *d*Ce concentrations are also found at ~400 m within the

OMZ. Despite moderate variations at some stations, *d*Ce concentrations remain approximately constant at each station below ~400 m.

Cross sections of *d*Nd, *d*Yb and *d*Ce concentrations are presented in Figure 3.9. The distribution of the Ce anomaly (Ce/Ce^*), which is defined as $Ce/Ce^* = \frac{2 \times Ce_{SN}}{La_{SN} + \mathrm{Pr}_{SN}}$ (REE_{SN} indicates PAAS-normalized values), is presented in the same figure. Although major water masses are present at similar depths at each station across the section (Figure 3.3), lateral variability in *d*REE concentrations at similar depths across the section (i.e. equivalent to approximately along different neutral density surfaces) is clear.

Surface-water *d*REE concentrations are enriched close to the western Angola coast, and decrease offshore from station 18 to station 17 before reaching relatively constant values at the remaining stations in the open-ocean regions of the section. In contrast, except for high *d*Ce concentrations in surface waters near the Angolan coast, surface *d*Ce concentrations show a gradual increase towards the west across the section, which is accompanied by a gradual decrease in seawater dO_2 (Figure 3.10).

High *d*LREE (including *d*Ce) concentration plumes are observed at water depths of ~400 m off the western Angola shelf. The metal plumes coincide with the subsurface OMZ, and extend laterally into the interior of the Angola Basin, resulting in an E–W *d*REE concentration gradient. Although individual *d*HREE profiles do not show a perceptible increase at this depth, the cross section of *d*Yb shows that an E–W *d*HREE concentration gradient, albeit small, does exist. The plumes of *d*REEs at this water depth coincide with elevated Ce anomaly values (Figure 3.9).

The E–W concentration gradients for both *d*LREEs and *d*HREEs, with higher values in the Angola Basin, persist between ~1500 m and ~4000 m. This contrasts

with observations in the deep waters of the Brazil Basin which exhibit relatively low *d*REE concentrations at these depths, but a marked increase of concentration below 4000 m (for both *d*LREEs and *d*HREEs).

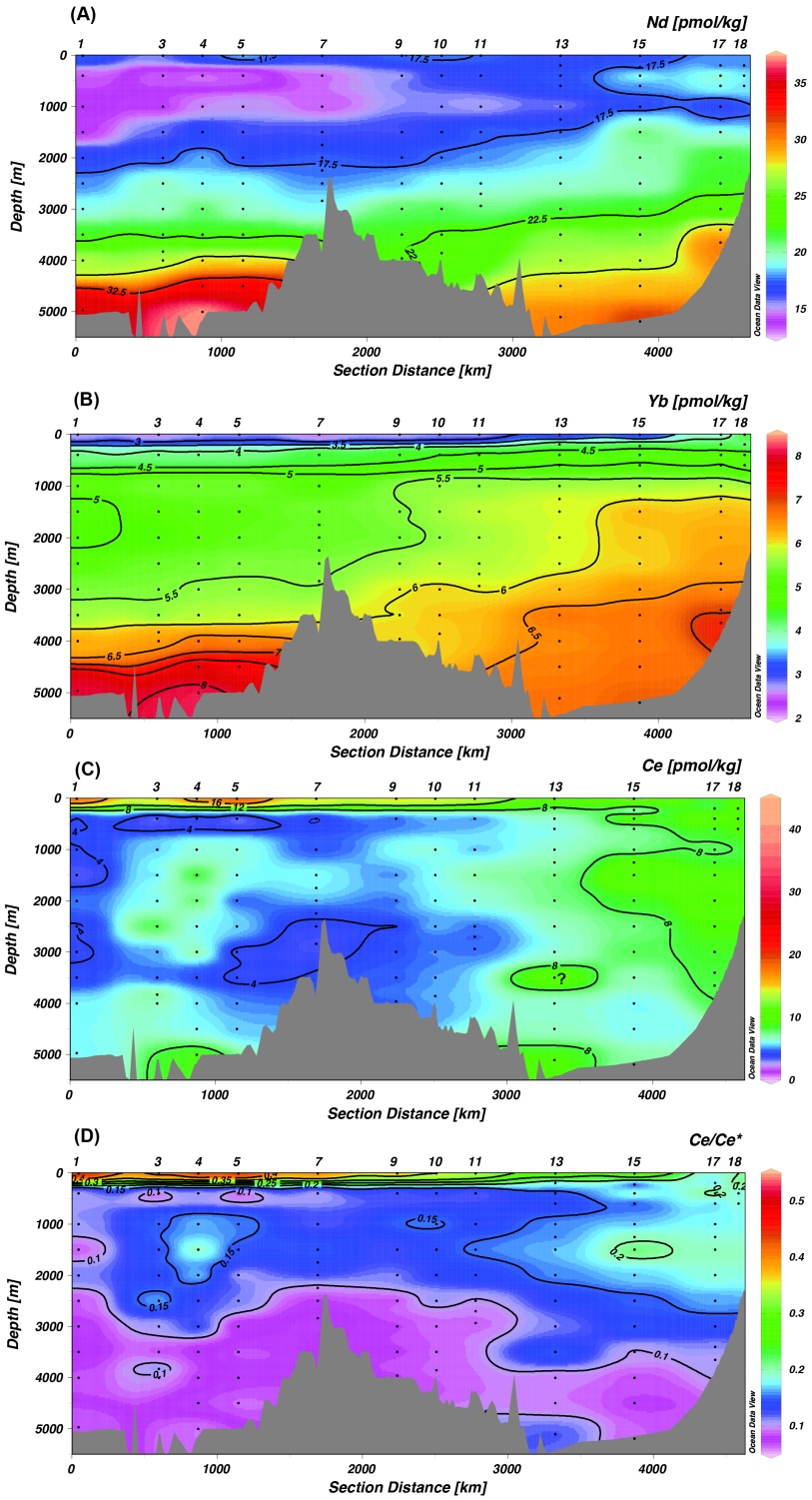

Figure 3.9 Cross-sections of *d*Nd, *d*Yb, *d*Ce and Ce anomaly (Ce/Ce*) for the CoFeMUG section

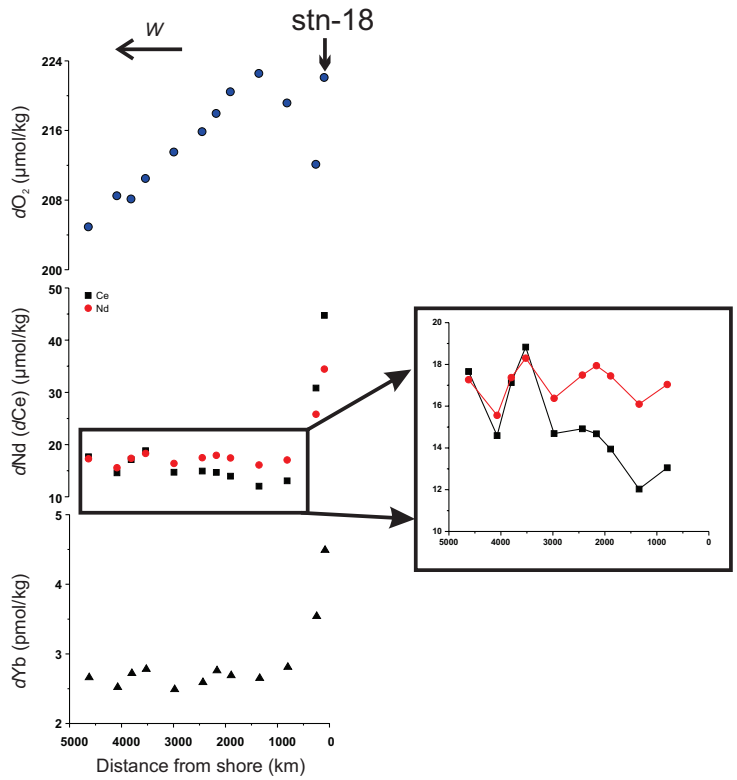

Figure 3.10 Variations of dO_2 and *d*REE concentrations in surface waters across the section. Distance is given from the eastern African shore.

A pronounced plume of elevated *d*Ce concentrations is seen near the African continental margin between ~1500 m and ~4000 m in the Angola Basin (Figure 3.9). A plume of Ce anomaly with elevated values is also found near the African continental margin, despite at more restricted water depths (~1500-2000 m) than the *d*Ce plume. No consistent pattern of *d*Ce or Ce anomaly is observed in the deep Brazil Basin and Angola Basin below ~4000 m.

3.4.2 Results of the inverse model

3.4.2.1 Results of mixing fractions of end-member watermasses

The contribution to each sample from four water types was calculated, but the similarity in properties for UNADW and LNADW makes it more appropriate to combine these two components into a single NADW. The results of modelled mixing

fractions for the three watermasses, namely UCDW, NADW and AABW, across the CoFeMUG section (>~1000 m) are illustrated in Figure 3.11.

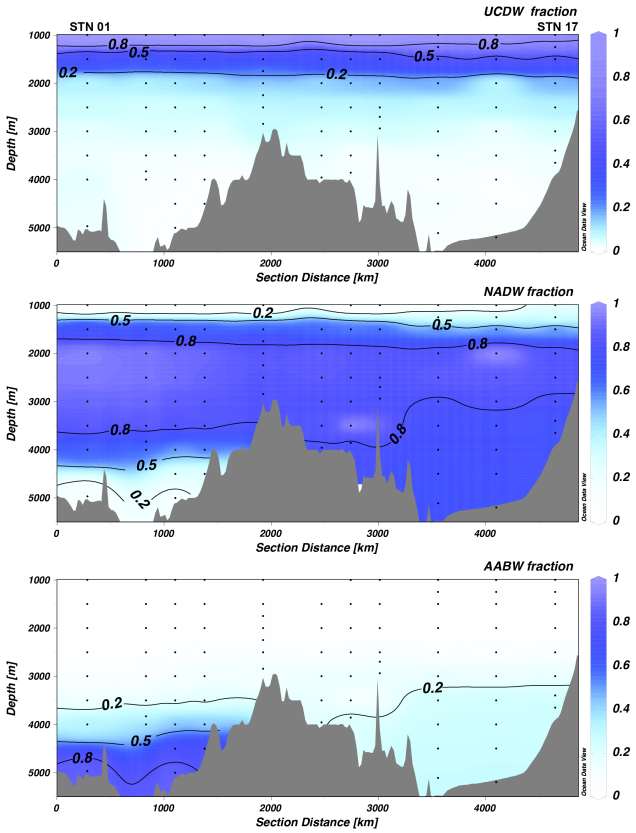

Figure 3.11 Results of modelled mixing fractions of UCDW, NADW and AABW across the CoFeMUG section. There results are the average of 250,000 realisations of the deconvolution to account for uncertainty in the end-member compositions.

The fraction of UCDW reaches its maximum (i.e. ~100%) at ~1000 m, and gradually decreases to <20% at ~2000 m. The diminished UCDW fraction with depth is balanced by the increasing influence of NADW, which dominates the section between ~2000 m and ~3500 m with a fraction of >80%. Below ~3500 m, the fraction of NADW progressively declines to <20% near the seafloor in the Brazil Basin, while AABW fraction increases from <20% to >80% at the same depth range of the same basin. In contrast, the fraction of NADW remains at ~80% in the deep Angola Basin, and the fraction of AABW remains low there (i.e. ~20%).

The modelled mixing fractions of the three end-member watermasses across the studied section are consistent with extensive hydrographic observations and previous modelling results for the South Atlantic (e.g. Larqué et al., 1997; Stramma and England, 1999), validating the inverse model used in this study.

3.4.2.2 The non-conservative contribution to *d*Nd and *d*Yb concentrations

Deviations of *d*Nd and *d*Yb from those expected by conservative mixing of the watermasses in each sample are denoted as ΔNd and ΔYb. The patterns of ΔNd and ΔYb are shown in Figure 3.12, and percentages of ΔNd and ΔYb relative to total *d*Nd and *d*Yb concentrations are calculated and shown in Figure 3.13. The distributions of ΔNd and ΔYb show significantly different patterns across the CoFeMUG section (>~1000 m). It is notable how the watermass mixing calculation draws out pronounced features in the Nd and Yb sections not directly visible in the data (Figure 3.9).

The strongest removal of *d*Nd (i.e. ΔNd <-2 pmol/kg) was observed in waters above the Mid-Atlantic Ridge (MAR), with this ΔNd signal representing >10% of total *d*Nd concentrations. High removal of *d*Nd ($\Delta Nd \approx$ ~2 pmol/kg) was also found at depth between ~1000 m and 3000 m in the west part of the section. Two plumes of *d*Nd addition were found in the Angola Basin at water depths of ~1500 m and below ~4000 m respectively, with ΔNd values becoming higher when closer to the continental margin of Angola. The *d*Nd addition below ~4000 m, with ΔNd values of up to ~6 pmol/kg, accounts for up to ~20% of the total *d*Nd concentrations, and is stronger than that seen at ~1500 m, where ΔNd values are ~2 pmol/kg. In contrast, neither removal nor addition of *d*Nd (i.e. $\Delta Nd \approx 0$) was found in the deep Brazil Basin (>~4000 m).

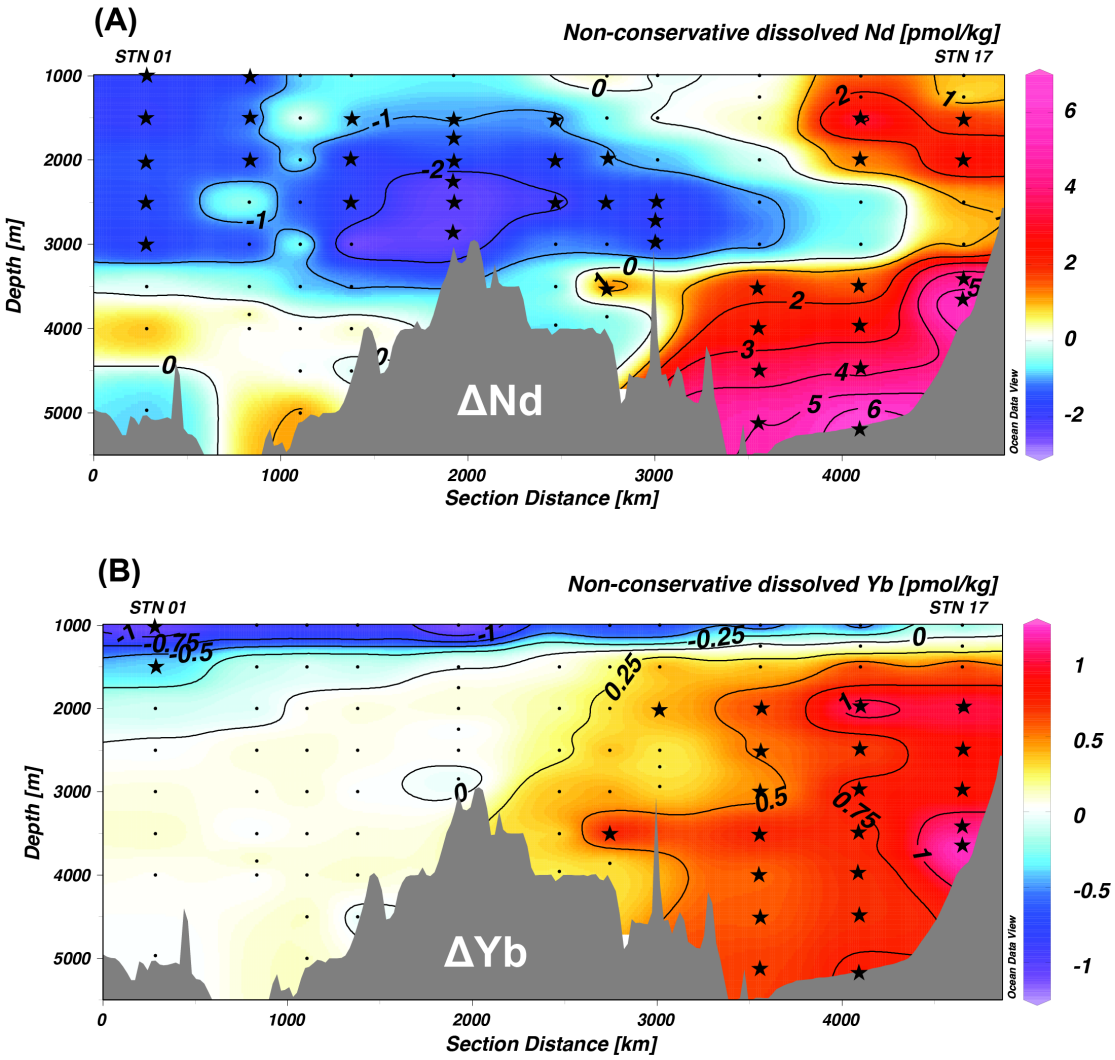

Figure 3.12 Modelled ΔNd (A) and ΔYb (B) across the CoFeMUG section. Positive values reflect addition of Nd or Yb, while negative values reflect removal. Stars denote modelled values that are considered as to be statistically stable, see text for details.

For ΔYb, addition of *d*Yb of up to ~1 pmol/kg was observed in the Angola Basin, but ΔYb shows almost ubiquitous additions of *d*Yb throughout the basin, rather than the two-plume additions as seen for *d*Nd in the same basin. The *d*Yb addition (i.e. ΔYb) in the Angola Basin accounts for a maximum of ~15% of the total *d*Yb concentrations. Neither addition nor removal of *d*Yb (i.e. $\Delta Yb \approx 0$) was found in most areas of the Brazil Basin, or above the MAR where removal of *d*Nd is strong. Removal is seen, however, in waters at depths of ~1000 m, corresponding to UCDW.

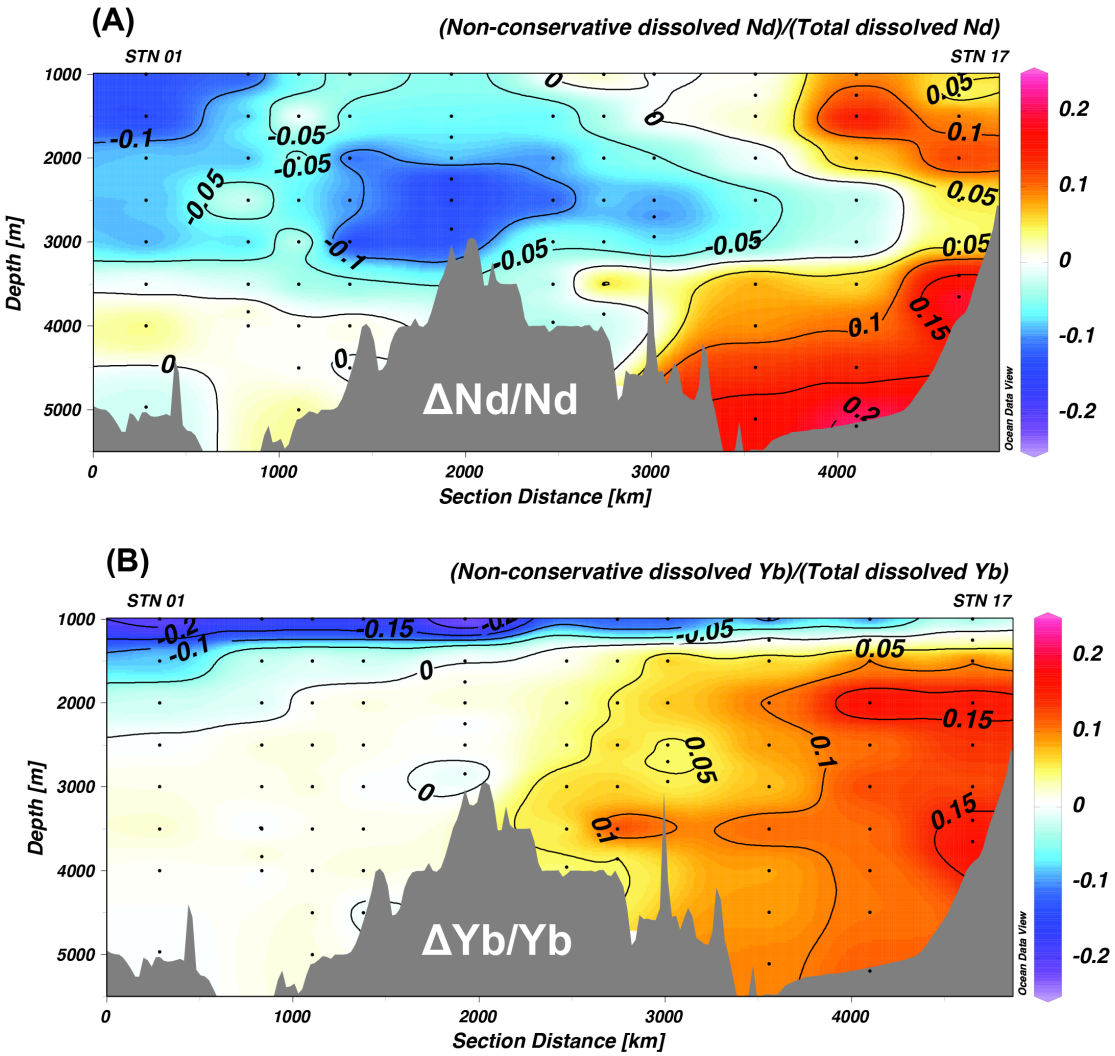

Figure 3.13 Modelled ΔNd (A) and ΔYb relative to respective total dissolved concentrations. Positive values reflect addition of Nd or Yb, while negative values reflect removal.

3.4.2.3 Robustness of the ΔNd and ΔYb results

The robustness of the mean ΔNd and ΔYb results can be demonstrated by the level of agreement obtained from the 250,000 perturbation experiments (Figure 3.12). Reliability of calculated values of ΔNd and ΔYb for each sample is assessed from the standard deviation of results obtained from 250,000 experiments relative to the mean (i.e. relative standard deviation). For some samples, ΔNd and ΔYb values differ significantly between experiments, indicating that the ΔNd and ΔYb values for

these samples are sensitive to the selection of end-member values. Samples whose ΔNd or ΔYb results from all perturbation experiments have a relative standard deviation smaller than 1 are labelled by stars in Figure 3.12, and values of ΔNd or ΔYb for these samples are considered to be relatively insensitive to the choices of pre-defined end-member values. It can be seen that samples with relatively reliable ΔNd and ΔYb values cover areas that show prominent non-conservative features, including the strong removal of *d*Nd above the MAR, and addition of *d*Nd and *d*Yb in the Angola Basin (Figure 3.12).

The broad pattern of ΔNd and ΔYb across the CoFeMUG section is even more robust than suggested by the above analysis. This is because, for any particular end-member composition selected, it is likely to move calculated ΔNd and ΔYb values for many samples in the same sense. One way to assess the robustness of the pattern is by rank analysis. If removal of *d*Nd (or ΔYb) is clear for a particular sample, that sample should always have one of the lowest ΔNd (or ΔYb) values amongst all samples in the section. Similar, if addition is clear, the ΔNd (or ΔYb) values should always be amongst the highest.

Rank analysis was performed by sorting ΔNd (or ΔYb) results of all samples in the section ascendingly by their values for each perturbation experiment, and determining the rank of ΔNd (or ΔYb) result for each sample in the sorted results. If the rank of ΔNd (or ΔYb) consistently falls in the bottom 1/3 of the samples in the ranked list, ΔNd (or ΔYb) is consistently low and removal of *d*Nd (or *d*Yb) is implicated. Similarly, if the rank consistently in the top third in the ranked list, ΔNd (or ΔYb) is high, and addition of *d*Nd (*d*Yb) is inferred. The probability of a sample falling in the bottom third or top third in the 250,000 perturbation experiments therefore provides assessment of the robustness of the results of the deconvolution.

The resulting probability distributions are presented in Figure 3.14. The probability of ΔNd results that fall in the bottom third was the highest (>0.7) in areas above the MAR and between ~1000-3000 m at station 1, where ΔNd values are low (Figure 3.14a), and the lowest (<0.1) at the two depths of ~1500 m and below ~4000 m near the continental margin in the Angola Basin. Mirroring this distribution, the probability of ΔNd results falling in the top third was lowest (<0.1) in areas above the MAR and between ~1000-3000 m at station 1, and the highest (>~0.5-0.9) at the two depths of ~1500 m and below ~4000 m near the continental margin in the Angola Basin (Figure 3.14c). The probability distributions of ΔNd (Figure 3.14a, c) are highly consistent with patterns of ΔNd results (Figure 3.12a), indicating that the modelled ΔNd distributions are statistically stable. Similarly, good agreement was observed between the probability distributions of ΔYb (Figure 3.14b, d) and ΔYb results (Figure 3.12b), suggesting that the modelled ΔYb distributions are also robust.

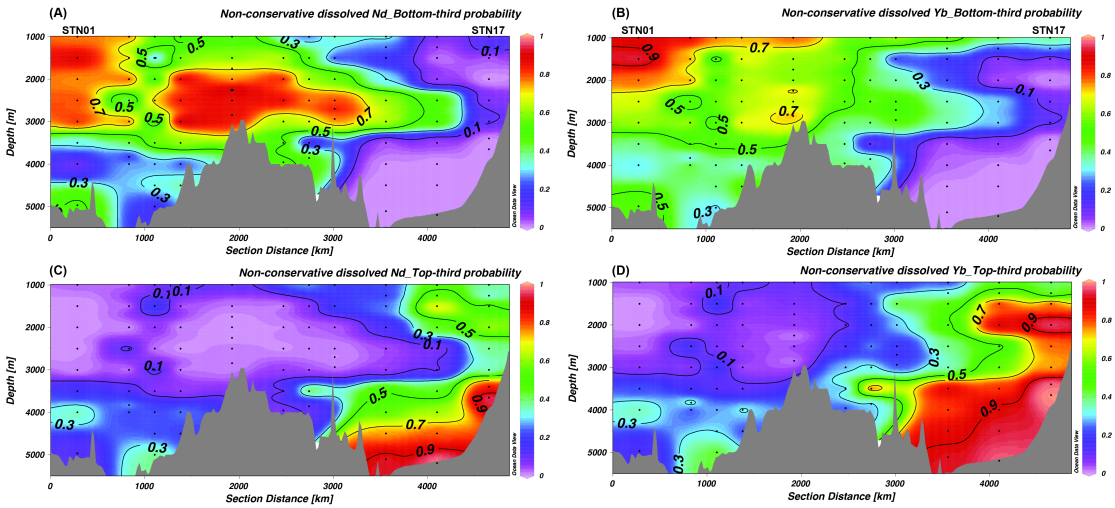

Figure 3.14 Probability distribution that characterizes the stability of the modelled ΔNd and ΔYb patterns seen on the section, see details in text.

3.5 Discussion

3.5.1 Dissolved REEs in surface waters

3.5.1.1 Sources of *d*REEs in surface waters near the Angolan coast

Stations near the western Angolan coast (i.e. 17 and 18) show higher *d*REE concentrations in surface waters than elsewhere (Figure 3.10). This coastal *d*REE enrichment in surface waters coincides with high concentrations of several other trace metals, including *d*Fe, *d*Mn and *d*Co (Noble et al., 2012), indicating the presence of local sources of trace metals. Dissolved REEs can help to improve constraints on the sources and processes responsible for the observed trace-metal enrichment in coastal surface waters.

Possible coastal sources of *d*REEs in this region include:

(1) Atmospheric dust from Southern Africa. Dust deposition is generally low (< ~0.5 g m^{-2} yr^{-1}) in the open-ocean regions of the CoFeMUG section (stations 1–15), but models suggest that it is higher (~1-2 g m^{-2} yr^{-1}) near the Angola coast (Mahowald et al., 2005), due to dust input from adjacent arid areas in Southern Africa (e.g. the Namib and Kalahari Desert). This is supported by back-trajectories for air masses over stations 17 and 18 using the HYSPLIT model (Draxler and Rolph, 2013). The higher dust fluxes near western Angola may account for high *d*REEs in surface waters near the coast;

(2) Advected *d*REEs transported by the southward-flowing Angola Current (Fig. 3.2). High *d*REE concentrations were observed in the surface ocean close to the Congo River (4°45'36"S, 9°56'35'E; unpublished data from Germain Bayon) (Fig. 3.2). These high values probably reflect local input of *d*REEs from the Congo River, whose tributaries are enriched in *d*REEs by several orders of magnitude relative to seawater (Dupré et al., 1996). The southward-flowing Angola Current along the

African coast might, therefore, bring seawater containing high *d*REEs to coastal surface waters at the CoFeMUG section. Low surface-water salinity observed at stations 17 and 18 indicates local intrusion of the Angola Current, which is affected by fresh water input from the Congo River (Figure 3.3);

(3) Local regeneration of *d*REEs from particulates and/or shelf sediments;

(4) Upwelling of intermediate waters with higher *d*REE concentrations.

Several pieces of evidence imply that dust is not the dominant source responsible for the observed elevation of *d*REEs in surface waters near the Angolan coast. A surface *d*Nd concentration of ~34 pmol/kg at station 18, the highest among all measured stations, is comparable to, or even higher than, those observed at the eastern tropical North Atlantic (~30 pmol/kg), where dust input dominates surface *d*Nd concentrations (Rickli et al., 2010), whereas dust deposition at station 18 is estimated to be at least 5 times lower (e.g. Mahowald et al., 2005). As revealed by this latitudinal comparison, the high surface *d*Nd concentration at station 18 is disproportional to local dust fluxes, indicating locally reduced *d*REE removal rates, or enhanced dissolution of dust, or presence of other REE sources in this region. The former two possibilities are unlikely, based on evidence from shale-normalized seawater REE patterns. Because REE patterns of seawater reflect the balance between those inherited from sources, and modification by particle scavenging that results in progressive enrichment of HREEs over LREEs in water, either reduced REE removal rates by scavenging or increased dust solubility should shift the balance towards the source, causing shale-normalized REE patterns of seawater close to those of dust (i.e. relatively flat patterns; e.g. Bayon et al., 2004; Greaves et al., 1994; Rickli et al., 2010). Despite comparable REE-concentrations, shale-normalized REE patterns of surface waters at stations 17 and 18 at ~12°S are not as flat as those observed under

high-dust regions in the tropical North Atlantic (Elderfield and Greaves, 1982) (Figure 3.15), arguing against a strong influence of atmospheric dust on *d*REEs in coastal surface waters at the CoFeMUG section. This conclusion is further supported by Nd-isotope compositions in surface waters near the Angolan coast at ~12°S (ε_{Nd} = ~-15), which are more negative than those of South African dust (ε_{Nd} = ~-12 to -3) (Rickli et al., 2010).

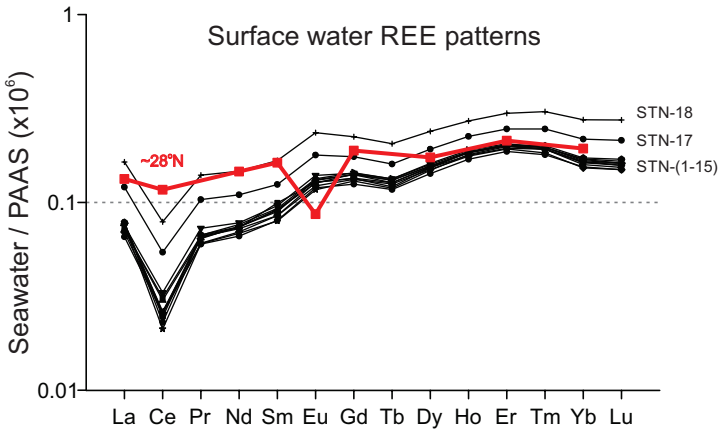

Figure 3.15 Comparison of shale-normalized REE patterns in surface seawater under high-dust flux regions in the tropical eastern North Atlantic (Elderfield et al., 1982) and at stations of the CoFeMUG section.

Southward advection of *d*REEs via the Angola Current is also an unlikely source, based on comparison of *d*REE patterns in seawater samples collected off the Congo River and the Angolan coast. This is illustrated by normalizing station 17 and 18 data against the mean surface-water *d*REE concentrations averaged across all open-ocean stations (i.e. stations 1–15) at the CoFeMUG section (Figure 3.16). This normalization scheme allows a better characterization of differences in seawater REE patterns than shale normailzation. The seawater-normalized REE pattern in the sample collected from the surface ocean off the Congo River shows a slight depletion in *d*LREEs between La and Nd, relative to the rest of REEs, which are almost flat

(Bayon, unpublished). If surface-water *d*REEs were advected southward by the Angola Current, the seawater REE pattern would show a stronger depletion in *d*LREEs over *d*HREEs further downstream the transport path (i.e. closer to the two coastal stations at the CoFeMUG section), due to continuous particle scavenging that preferentially removes *d*LREEs (e.g. Sholkovitz et al., 1994; Wood, 1990b). This is, however, obviously not the case, because the REE patterns in surface waters at stations 17 and 18 show prominent enrichment in *d*LREEs (particularly in *d*Ce) compared to *d*HREEs.

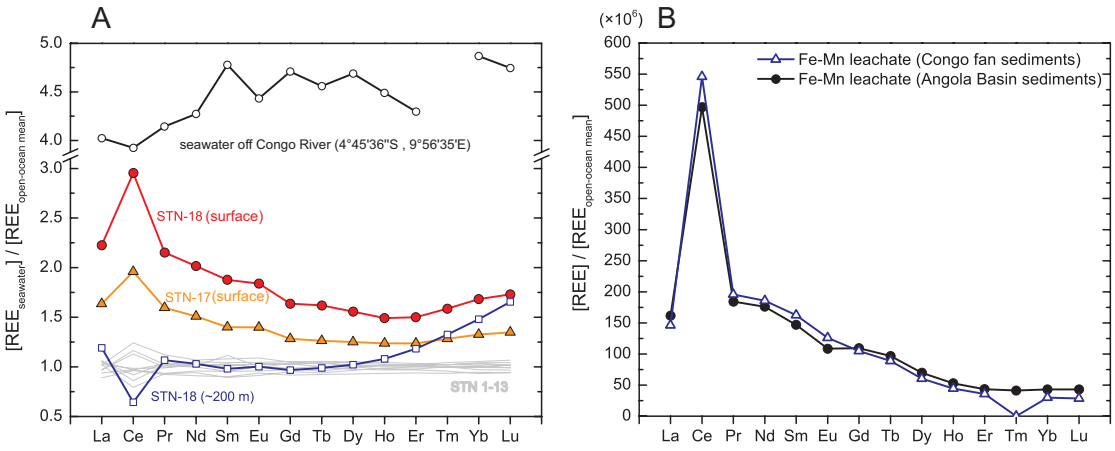

Figure 3.16 REE patterns of seawater samples and leachates of Fe-Mn oxides. All data are normalized against the average of REE concentrations observed in stations 1-15 of this study to more clearly indicate differences between samples. REE data for Fe-Mn leachates are from Bayon et al. (2004). Note that the REE pattern of surface waters from station 17 and 18 neither look similar to those of deep waters from the same site, nor seawater close to the Congo River. Rather, surface-water patterns are well explained by dissolution of Fe-Mn oxides from marine particles or sediments.

It has been suggested that local reduction of Fe-Mn oxides on marine particles in the water column or in shelf sediments is the major source for elevated *d*Nd concentrations observed in surface waters near the Angola coast at ~12°S (Rickli et al., 2010). This supposition is confirmed by evidence of REE patterns in this study.

Seawater-normalized REE patterns in surface waters at stations 17 and 18 exhibit prominent enrichment in *d*LREEs, particularly in *d*Ce, relative to *d*HREEs (Figure 3.16). These patterns are consistent with desorption of REEs from Fe-Mn coatings, which are typically LREE enriched with a large positive Ce anomaly (e.g. Sholkovitz et al., 1994; Tachikawa et al., 1999b), and are remarkably similar to seawater-normalized REE patterns in Fe-Mn oxides leached from sediments on the Congo Fan and in the Angola Basin (Figure 3.16) (Bayon et al., 2004). The evidence of seawater REE patterns suggests that regeneration of *d*REEs from reduction of Fe-Mn oxides on particles or in sediments, is the most probable source for the observed *d*REE elevation in surface waters near the Angolan coast. The conclusion is supported by high coastal surface *d*Fe and *d*Mn concentrations at the same location (Noble et al., 2012).

Upwelling occurs at coastal regions of the CoFeMUG section (Noble et al., 2012), but this process plays a negligible role in increasing *d*REE concentrations in surface waters, based on two pieces of evidence. Firstly, at station 18, seawater at deeper-than-the-surface depths (e.g. ~200 m) has *d*REE concentrations lower than those in surface waters; Secondly, although the seawater-normalized REE pattern in surface waters at station 18 shows weak enrichment in *d*HREEs from Er to Lu, which is to some extent similar to the *d*HREE-enriched patterns in samples from deeper water depths at the same station, the *d*LREE enrichment, especially the large *d*Ce enrichment, in surface waters clearly cannot be derived from deep-water, which are characterized by nearly a flat line REE patterns across the LREEs with an obvious deficiency in *d*Ce in its REE pattern (Figure 3.16).

3.5.1.2 Dissolved Ce in surface waters at the CoFeMUG section

Dissolved Ce concentrations in surface waters of the studied section show a linear correlation with dO$_2$. In contrast to nearly uniform concentrations of other dREEs in open-ocean surface waters, dCe concentrations show a gradual increase towards the west, which is in concert with a decrease in dO$_2$ in surface waters (Figure 3.10), possibly implying a redox control of Ce concentrations due to its redox properties. Dissolved Ce concentrations are inversely correlated with dO$_2$ in open-ocean surface waters ($R^2 = 0.65$), whereas other trivalent dREEs do not correlate with dO$_2$ ($R^2 < 0.1$) (Figure 3.17). Ce anomalies in open-ocean surface waters show a strong negative correlation with ambient seawater dO$_2$ (i.e. $[Ce/Ce^*] = -0.0084 \times [dO_2] + 2.18$, $R^2 = 0.90$) (Figure 3.17). Compared to the linear relationship between dCe concentrations and dO$_2$ (i.e. $R^2 = 0.65$), a more significant relationship between the Ce anomalies and ambient seawater dO$_2$ is not surprising, given that Ce anomalies only characterize the oxygen-dependent removal of Ce due to oxidation of Ce^{3+} into insoluble Ce^{4+} (e.g. Byrne and Sholkovitz, 1996; Elderfield et al., 1988), but dCe concentrations reflect a consequence of combined oxidative and non-oxidative (i.e. scavenging) removal.

A simple explanation of the observed dCe–dO$_2$ relationship in surface waters in the CoFeMUG section is due to a coincidence, rather than a causal relationship. The studied section transects a large-scale dO$_2$ gradient in surface waters within the South Atlantic subtropical/subequatorial gyre systems that transport high dO$_2$ surface waters from upwelling regions near the southern Africa to the west. This large-scale hydrographic feature in distributions of dO$_2$ concentration in surface waters may coincide with a gradient in REE input that is higher at coastal areas, either due to the Southern African dust or other sources from the coast (e.g. rivers), than interior of the

gyre. Consequently, the highest *d*Ce concentrations (and Ce anomaly values) are found in surface waters at coastal stations (i.e. stations 17 and 18), and lower *d*Ce concentrations (and Ce anomaly values) are observed at the rest of open-ocean stations. A piece of compelling evidence that precludes a causal link between *d*Ce–dO_2 relationship in surface waters comes from the sharp contrast observed between ranges of changes in Ce anomaly across dO_2 gradients in surface waters and the OMZ at ~400 m. Ce anomaly values change by 0.2 unit (i.e. from 0.5 to 0.3) across a surface dO_2 gradient of only ~18 μM (i.e. from ~203 μM to ~225 μM), whereas their values only change by 0.1 unit (i.e. from 0.1 to 0.2) across the OMZ at ~400 m that poses a much larger dO_2 gradient of over 100 μM along the studied section. The larger range of change in Ce anomaly across a smaller dO_2 gradient in surface waters, compared to changes occurred across the OMZ at ~400 m, either precludes a causal relationship between the two in the surface, or indicates multiple controls on the observed linear *d*Ce–dO_2 relationship.

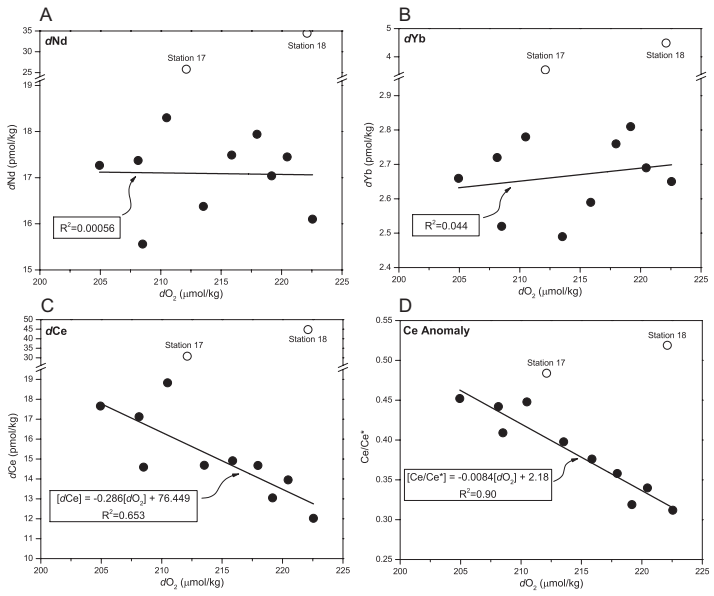

Figure 3.17 Dissolved Nd, Yb, Ce concentrations and Ce anomaly plotted against dissolved O_2 for surface waters of the CoFeMUG section. Note that neither LREEs (e.g. *d*Nd) nor HREEs (e.g. *d*Yb) exhibit any relationship with *d*O2, while *d*Ce concentration clearly shows a negative relationship, particularly when expressed as Ce anomaly.

However, if the observed inverse correlation between *d*Ce and dO_2 in the surface open-ocean regions does have a causal connection, a possible mechanism that partly contributes to the observed correlation is the kinetics of *d*Ce oxidation. Higher dO_2 content in seawater may cause an enhanced oxidation rate of Ce, leading to stronger oxidative removal of *d*Ce from the water column. Although detailed studies on changes of Ce oxidation rates in response to changes in dissolved oxygen content in seawater are not available so far, the hypothesis proposed above is generally consistent with previous incubation experiments, which observed a ~2-fold increase in the Ce oxidation rate in air saturated seawater compared to that in 5% air saturated samples (Moffett, 1994b).

In addition, it has been proposed that the Ce oxidation in the water column is microbially mediated, as for Mn (Moffett, 1990; Moffett, 1994a; Moffett, 1994b). If this is the case, the strong *d*Ce–dO_2 correlation observed in open-ocean surface waters in this study may suggest that microbial redox reactions of Ce also have a strong O_2-dependence, and O_2 is, therefore, likely to be the terminal electron acceptor in the oxidative step of such microbially mediated redox reactions.

Ce anomalies in surface waters near the Angolan coast deviate from the linear Ce-anomaly–dO_2 relationship observed in the open-ocean stations of the studied section (Figure 3.17). Ce-anomalies in surface waters at station 17 and 18 are higher than those at comparable dO_2-levels in open-ocean stations, indicating weakened oxidative removal of Ce^{3+} at the near-coast region. This deviation may suggest an input effect in which the removal of *d*Ce is competing against active addition of Ce, such as that from reduction of Fe-Mn oxides (Section 3.5.1.1). This would suggest that the observed Ce-anomaly–dO_2 correlation, given by surface-water results from

the open-ocean stations of the CoFeMUG section, indicates low *d*REE inputs, and/or inputs with a relatively uniform Ce anomaly.

The linear Ce-anomaly–dO_2 correlation observed in this study may not hold in other parts of the global ocean where the balance between oxidative removal of *d*Ce and REE input is different. This may challenge the use of Ce anomalies as a tracer to reconstruct redox conditions in the past oceans (e.g. Loope et al., 2013). In the CoFeMUG section, Ce anomalies are not only controlled by dO_2, but also by REE inputs. Besides other potential complications summarized by German and Elderfield (1990a), our observation implies that caution should be exercised when using Ce anomaly alone as a tracer to reconstruct water-column oxygen content in the past.

3.5.2 The cycling of dREEs in the subsurface Oxygen Minimum Zone (OMZ)

The cycling of *d*REEs in the water column under low-oxygen/anoxic conditions has been studied in many anoxic basins, such as the Black Sea and Cariaco Trench (e.g. Chen et al., 2013; de Baar et al., 1988; German and Elderfield, 1989; German et al., 1991; Schijf et al., 1995; Sholkovitz et al., 1992). Large enrichment of strictly trivalent *d*REEs is commonly found above the oxic/anoxic interface in the suboxic portion of the water column, and is attributed to REE-desorption associated with reductive dissolution of Fe-Mn oxides. In addition to this process, substantial enrichment of *d*Ce has been attributed to reduction of Ce oxides. Similar recycling of *d*REEs, albeit with a much smaller magnitude, has also been observed previously in the OMZs more typical of the open ocean (i.e. NW Indian Ocean) (German and Elderfield, 1990b).

Increased concentrations of *d*REEs in the OMZ of the western Angola slope are also closely related to the redox cycling of Fe and Mn. This is demonstrated at the

water depth of ~400 m, which is a quasi-isopycnal layer (density: ~27.0-27.1) transecting the central depth of the OMZ in the east, but being unaffected by the OMZ in the west. A sharp contrast in correlation between *d*REEs and the two trace metals was observed at stations within and outside the OMZ at this depth. The statistical significance of linear relationships between *d*REEs and *d*Fe or *d*Mn at this layer increases noticeably in stations (i.e. stations 10–18), which are influenced by the OMZ (i.e. dO_2 < ~60 μM), compared to that for stations 1-9 within the oligotrophic gyre (Figure 3.18). Dissolved REEs are positively correlated with *d*Fe and *d*Mn in the OMZ. The Ce anomaly, which characterizes the extent of oxidative removal of Ce associated with redox changes, is also positively correlated with *d*Fe and *d*Mn in the OMZ, suggesting reduced Ce oxidative removal with increased *d*Fe and *d*Mn.

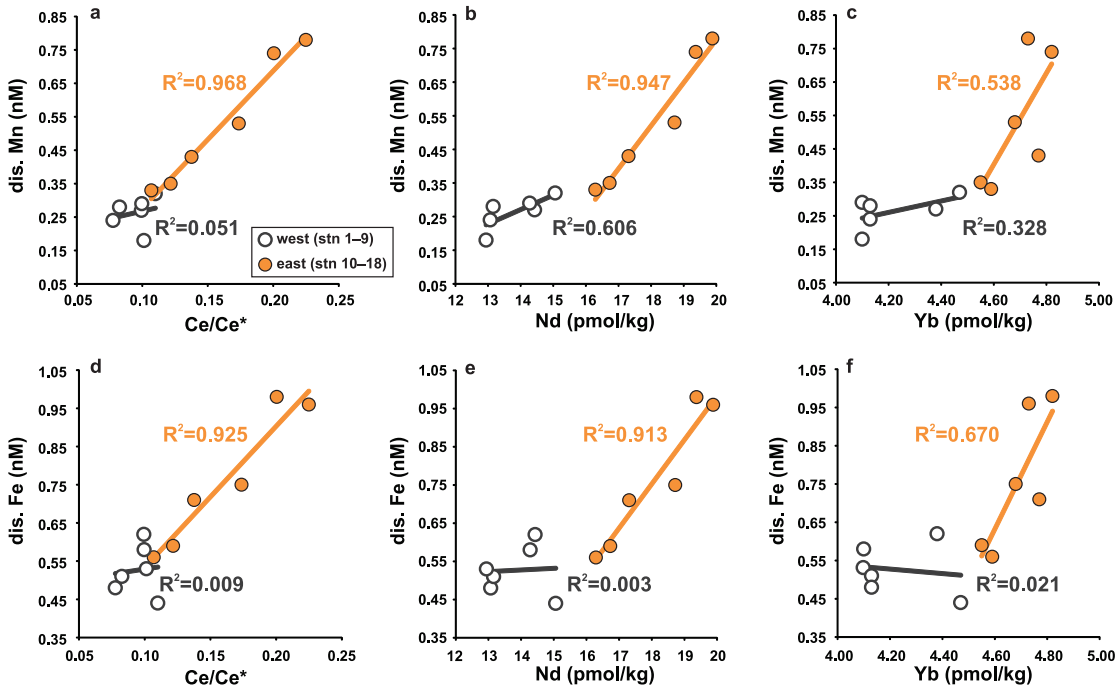

Figure 3.18 *d*REE (Ce anomaly)–*d*Fe (*d*Mn) correlations at ~400 m across the section. Significant linear relationships between *d*REEs and *d*Fe or *d*Mn were observed within the OMZ.

REE patterns at ~400 m depth provide further evidence supporting recycling of *d*REEs associated with reduction of Fe-Mn oxides in the OMZ. Seawater samples at ~400 m were normalized to mean *d*REE concentrations averaged across samples at ~1000 m to make small variations in *d*REE patterns clear. Compared to seawater outside the OMZ (i.e stations 1–9), seawater influenced by the OMZ (i.e. stations 10–18) shows unique REE patterns characterized by pronounced *d*LREE enrichment, and weak negative Ce anomalies or positive Ce anomalies. These features support inputs of REEs from reduction of Fe-Mn oxides, which possess *d*LREE-enriched REE patterns with prominent excesses in *d*Ce (Figure 3.19).

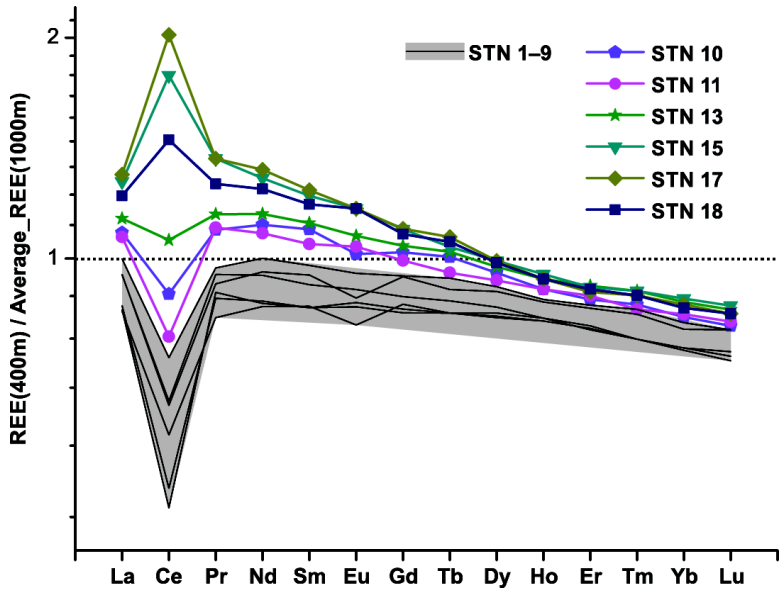

Figure 3.19 Seawater-normalized *d*REE patterns at ~400 m across the section. LREEs are more enriched in stations 15 and 17 than station 18, suggesting *in-situ* regeneration of *d*REEs in the water column. Ce anomaly in the two stations is more pronounced than that observed at station 18, indicating *in-situ* reduction of Ce oxides in the water column.

The observed linear relationships between *d*REEs and *d*Fe (and *d*Mn) at ~400 m in the OMZ may result from two processes (Figure 3.18): (1) lateral advection of trace metals, including *d*REEs, *d*Fe and *d*Mn, from reduced sediments on the African

shelf via westward-flowing subsurface currents; and/or (2) a dO_2-dependent *in-situ* reduction of Fe-Mn oxide coatings in the water column in response to a westward-decreased dO_2 gradient off the Angola shelf (Figure 3.4).

Although the coincidence of the westward-flowing currents and a westward increase in seawater dO_2 makes a definite separation of the two processes difficult, lateral variations in seawater REE patterns along ~400 m indicate that *in-situ* regeneration of *d*REEs must have occurred in the water column at a few stations in the OMZ. Assuming that *d*REE fluxes only result from westward advection of metals from reducing sediments on the shelf, a continuous depletion in *d*LREEs relative to *d*HREEs in REE patterns with an increasing distance from the shore would be predicted. But enrichment of *d*LREEs observed at stations 15 and 17 is more pronounced than that observed at station 18 (Figure 3.19), suggesting *in-situ* regenerations of *d*LREEs probably due to reduction of Fe-Mn coatings at the two stations. This trend is more obviously seen in Ce; a seawater-normalized negative Ce anomaly is observed at station 18, but a positive Ce anomaly is found at stations 17 and 15 (Figure 3.19), indicating *in-situ* reduction of Ce oxides at the two stations. A dissolved O_2 concentration of ~25 μM at stations 17 and 15, therefore, is a threshold that enables Ce reduction. This dO_2 concentration is slightly higher than that observed at the OMZ in the NW Indian Ocean (dO_2 < ~15 μM) (German and Elderfield, 1990b).

3.5.3 The cycling of dREEs in deep waters (>1000 m)

3.5.3.1 The hydrographic control on *d*REEs in deep waters

Results from the inverse model (Figure 3.12 and Figure 3.13) represent the first quantitative estimate on the relative importance of the hydrographic (i.e. mixing)

and non-conservative controls (e.g. particle scavenging and remineralization) on the distribution of *d*REEs in a major ocean basin. Although discernable fractions of total *d*REE concentrations across the CoFeMUG section below ~1000 m are explained by non-conservative processes, the majority of *d*REE concentrations (>80%) can be attributed to a hydrographic control due to watermass mixing (Figure 3.13). The dominance of hydrographic control on *d*REE distribution in deep waters across the section explains its general resemblance to watermass distribution. For example, higher *d*REE concentrations in the deep Brazil Basin (>~4000 m) than those observed in the deep Angola Basin are apparently related to the presence of AABW in the Brazil Basin (Figure 3.3 and Figure 3.9).

In contrast to the obvious addition of *d*Nd and *d*Yb in the Angola Basin, a hydrographic control on *d*REEs is significant in the deep Brazil Basin. Almost 100% of the observed *d*Yb, and ~90-100% of *d*Nd, is explained by watermass mixing (Figure 3.13). A higher percentage of preformed *d*Yb than that of preformed *d*Nd is consistent with REE behaviour in the ocean, which suggests LREEs are more particle-reactive than HREEs (e.g. Wood, 1990b). The strong hydrographic control on *d*REEs in deep Brazil Basin predicts that *d*REE should correlate well with other conservative or quasi-conservative tracers in seawater, such as *d*Si, which has been demonstrated to behave almost conservatively in the deep South Atlantic due to negligible opal dissolution (e.g. Broecker et al., 1991; Sarmiento et al., 2007). This is indeed the case, as can be illustrated by a linear *d*REE–*d*Si relationship at the mixing range of NADW and AABW (i.e. >~2000 m) in the Brazil Basin (Figure 3.20). This explanation precludes a direct link between the REE cycle and Si cycle in this region, although the two cycles may be linked locally, such as in the Atlantic sector of the Southern Ocean (Stichel et al., 2012).

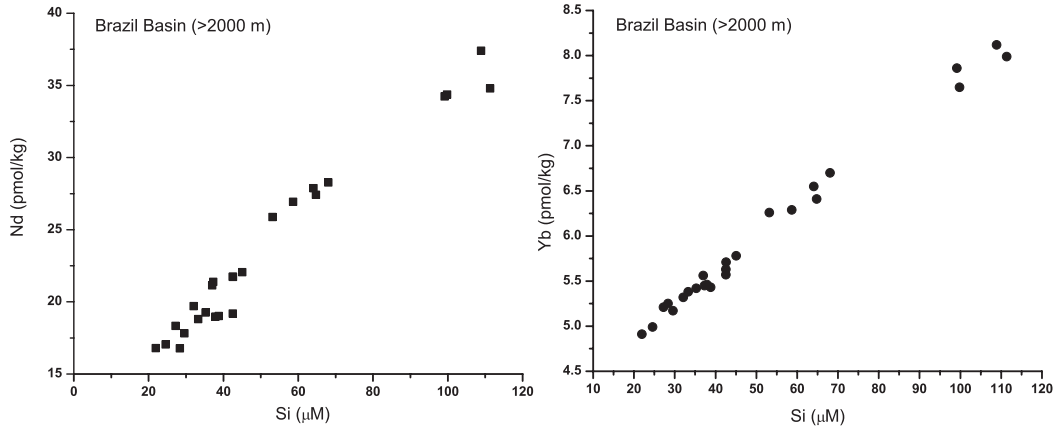

Figure 3.20 Linear deep-water (>2000 m) *d*REE–*d*Si relationship in the Brazil Basin.

3.5.3.2 Addition of *d*REEs in the deep Angola Basin near the continental margin

The modelled results suggest prominent addition of Nd and Yb near the continental margin in the Angola Basin. Margin addition of Nd appears to occur at two depths – ~1500 m and below ~4000 m – but addition of Yb is almost ubiquitous at all water depths below ~1500 m near the margin (Figure 3.12). These modelled features are robust, as suggested by relatively small variability in the calculated ΔNd and ΔYb values in samples at these areas during the perturbation experiments (stars in Figure 3.12).

The different distribution of ΔNd and ΔYb may result from distinct particle reactivity between Nd and Yd. Because Yb is less particle-reactive than Nd in seawater (e.g. Wood, 1990b), additional Yb from a source would stay longer in the water column, and hence be likely to be re-distributed by advection and diffusion processes; in contrast, additional Nd is more quickly scavenged by particles, so signals of Nd addition would expect to be more-restricted near the source of addition. Alternatively, the two plumes of *d*Nd addition at ~1500 m and below ~4000 m near the continental margin in the Angola Basin may be caused by eastward advection of

upper NADW, which is characterized by noticeable scavenging of *d*Nd (ΔNd <-1 pmol/kg), between ~2000 m and ~3000 m. The eastward intrusion of upper NADW at this depth in the Angola Basin can be inferred from the *d*Si cross-section of the CoFeMUG section that shows features of eastward advection of low–*d*Si upper NADW (Figure 3.3).

Identification of a specific cause for the REE addition at the two depths is tentative. Two processes may play a role: (1) *in-situ* regeneration of *d*REEs due to remineralization of particulates in the water column. Particle production near the African coast at the Angola Basin is relatively high, because of high upwelling-promoted surface productivity (Henson et al., 2012). Remineralization of particles would therefore lead to desorption of REEs that are scavenged in the upper water column; or (2) advection of *d*REEs from reducing sediments on the continental margins.

Remineralization of particles may not explain the shallow REE addition at ~1500 m, but may cause the deep REE addition. Strong dissolution of silicate- and carbonate-based particles, namely diatom and aragonite, occurs at water depths above ~1000 m in the Angola Basin (Feely et al., 2004; van Bennekom and Berger, 1984). These depths may be too shallow to cause the REE addition at ~1500 m. However, the calcite saturation depth (CCD) develops at ~4000 m in the Angola Basin (Feely et al., 2004), roughly coincident with the upper limit of the deep REE addition. Remineralization of calcite-based particles in the water column below this depth, or in bottom sediments, would lead to release of the scavenged REEs, resulting in an REE addition.

The shallow REE addition may result from advection of trace metals from reducing sediments on the continental margin. Several pieces of evidence suggest that

the addition of REEs at ~1500 m is related to redox processes. Firstly, the shallower plume of ΔNd at ~1500 m coincides with a plume of shale-normalized Ce anomaly with relatively high values (Figure 3.9 and Figure 3.12). In addition, high *d*Fe concentrations are also found at this depth (Figure 3.1) (Noble et al., 2012). In contrast, no consistent patterns of Ce anomalies, or other trace metal concentrations, are associated with the REE addition below ~4000 m (Figure 3.9 and Figure 3.12). The close association of the REE addition at ~1500 m and enrichment of redox-sensitive elements (i.e. Ce and Fe) supports a redox-related origin. Because the water column at ~1500 m in stations 15 and 17 is well-oxygenated (O_2 > 100 μM), the observed REE addition at this depth are likely to reflect an advected signal from sedimentary sources on continental margins.

Although there is ambiguity as to exact mechanisms for *d*REE enrichment found in the Angola Basin below ~1000 m, it appears that continental margins play an important role in inputting REEs to ambient seawater. These REE additions may explain anomalously low seawater Nd-isotope compositions observed in intermediate and deep waters in the Angola Basin (Rickli et al., 2009).

3.5.3.3 Decoupled behaviour of *d*Ce and *d*Mn near continental margins at ~1500 m

The absence of enrichment in *d*Mn at ~1500 m, where a plume of Ce anomaly is observed, suggests a decoupled behaviour of the two metals at this depth (Figure 3.1 and Figure 3.9). This decoupling is unique in marine environments, because Ce and Mn are typically considered as chemical twins during redox processes, due to their similar redox potentials (e.g. Moffett, 1994b). Similar decoupling of Ce and Mn, but in a much smaller magnitude, was previously observed in the NW Indian Ocean (German and Elderfield, 1990b). It has been proposed that such decoupling of Ce and

Mn may result from a delicate environment with O_2 concentrations sufficiently high to allow the occurrence of oxidative precipitation of Mn, but insufficient to cause oxidative removal of Ce (German and Elderfield, 1990b). In principle, this model can explain the observed plume of Ce and the absence of Mn signal in the water column, but cannot explain the observed high *d*Fe. Because the standard redox potential of Fe is lower than Mn (Lu et al., 2010), Fe should have already been oxidized at the O_2 level at which Mn is oxidized. As a consequence, it is unlikely to see *d*Fe enrichment in the water column without *d*Mn enrichment, if both of these metals indeed result from advected signals diffused out of reducing sediments.

Alternatively, it has been suggested that the redox cycling of Ce in seawater is mediated by bacteria (Moffett, 1990; Moffett, 1994a; Moffett, 1994b). It is well understood that Mn-oxidizing bacteria are a main controller for the formation of Mn oxides in marine environments (Tebo et al., 2004). If Ce is oxidized in the same way as Mn, but mediated by a different group of Ce-oxidizing bacteria, it is possible to explain the decoupled Ce and Mn behaviour observed at the CoFeMUG section by the selected presence of Mn-oxidizing bacteria, but absence of Ce-oxidizing bacteria, in reducing sediments, which leads to oxidative removal of Mn, but allow diffusion of reduced Ce out the sediments into seawater. This explanation clearly needs further validation.

3.5.3.4 Absence of hydrothermal inputs of *d*REEs to seawater

Hydrothermal fluids are typically enriched in *d*REEs by several orders of magnitude compared to ambient seawater (e.g. Bau and Dulski, 1999; Craddock et al., 2010; Douville et al., 1999; Klinkhammer et al., 1994; Mitra et al., 1994; Schmidt et al., 2010), but it is commonly believed that *d*REE-fluxes brought by hydrothermal

venting into seawater are negligible, due to nearly quantitative removal of hydrothermally derived *d*REEs via intense scavenging mainly by Fe- and/or Mn-oxide particles within hydrothermal plumes (e.g. Bau and Dulski, 1999; German et al., 1990; Mitra et al., 1994).

However, significant hydrothermal input has been recently observed for several other trace metals that were previously believed to undergo nearly complete removal within hydrothermal plumes, for example Fe (e.g. Klunder et al., 2012; Nishioka et al., 2013; Saito et al., 2013), due to their binding with organic ligands in hydrothermal fluids (e.g. Bennett et al., 2008; Sander and Koschinsky, 2011; Sander et al., 2007; Toner et al., 2009). Although influence of organic ligands on *d*REEs under hydrothermal environment is still largely unknown, recent laboratory experiments have revealed the potential importance of organic ligands (i.e. siderophore) in controlling concentrations and relative fractionation of *d*REEs in river water and seawater (Bau et al., 2013; Christenson and Schijf, 2011). Given the above new observations, the traditional view that hydrothermal fluxes of *d*REEs are negligible clearly requires further confirmation.

The CoFeMUG section permits direct observations to assess the significance of hydrothermal *d*REE-input to seawater. High *d*Fe and *d*Mn concentrations above the mid-Atlantic ridge at water depths between ~2000 and 3000 m at the CoFeMUG section have been attributed to hydrothermal inputs (Noble et al., 2012; Saito et al., 2013) (Figure 3.1). In contrast, both *d*REE concentrations and REE patterns do not suggest hydrothermal input of *d*REEs.

Firstly, in contrast to the plumes of *d*Fe and *d*Mn above the MAR, no plume of *d*REEs is found (Figure 3.21). Secondly, this conclusion is supported by REE patterns. Because *d*REEs in hydrothermal fluids are strongly fractionated by fluid–

mineral interactions and physical/chemical properties of fluids (Allen and Seyfried Jr, 2005; Craddock et al., 2010; Douville et al., 1999; Klinkhammer et al., 1994; Schmidt et al., 2010), they exhibit distinct chondrite-normalized REE (REE_{CN}) patterns, which are characterized by LREE enrichment with prominent Eu positive anomalies (Figure 3.21). It is, therefore, expected that REE_{CN} patterns of seawater should shift towards those of hydrothermal fluids, if seawater is affected by hydrothermal *d*REEs. However, REE_{CN} patterns of seawater samples within the *d*Fe- and *d*Mn-plume in the CoFeMUG section are almost identical to those observed in seawater at similar depths away from the plume. In addition, Eu_{CN} anomalies remain nearly constant and seawater-like (<1) in plumes waters that show high *d*Fe and *d*Mn (Figure 3.21). The above observations support the absence of hydrothermal input of *d*REEs in the CoFeMUG section.

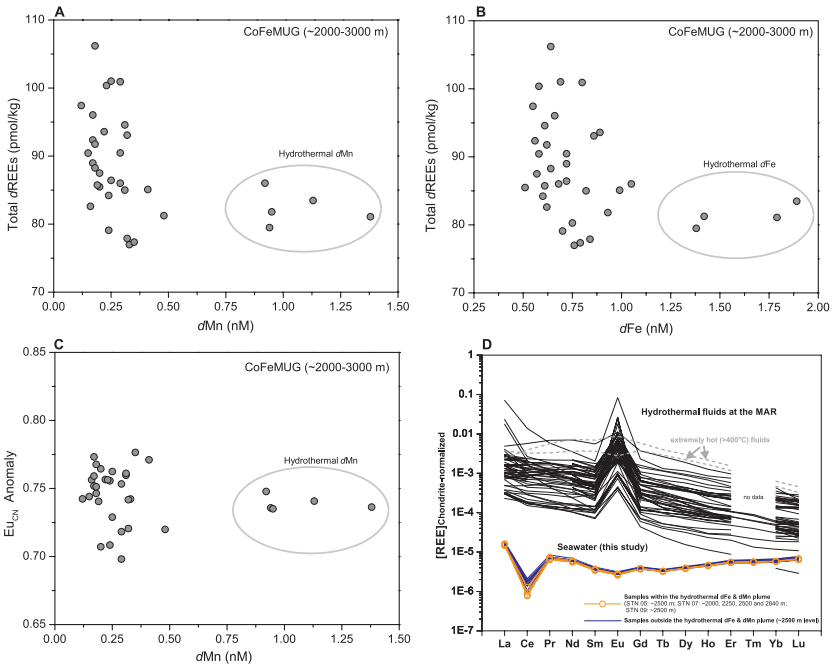

Figure 3.21 (A–B) Absence of elevation in total *d*REE concentrations in hydrothermal plume waters where *d*Fe and *d*Mn concentrations are high; (C) Absence of positive Eu anomaly in hydrothermal plume waters above the MAR; (D) Typical seawater REE patterns shown in hydrothermal plume waters. REE data of hydrothermal fluids at the MAR are from Klinkhammer et al. (1994); Mitra et al. (1994); Bau and Dulski (1999); Douville et al. (1999), Schmidt et al. (2010).

3.5.3.5 Scavenging of *d*REEs above the Mid-Atlantic Ridge

The results of ΔNd and ΔYb from the inverse model suggest enhanced removal for *d*Nd, but not for *d*Yb, above the MAR (Figure 3.12). This result is in good agreement with previous studies on particulate REEs in hydrothermally derived Fe-Mn particles above the MAR in the North Atlantic, which showed continuous scavenging of seawater REEs onto Fe-Mn particles during their dispersion in the neutrally buoyant plume, with a preferential uptake of LREEs over HREEs (German et al., 1990; Mitra et al., 1994; Rudnicki and Elderfield, 1993).

3.6 Conclusions

This study presents the first full-depth, zonal section of all *d*REE concentrations along ~12°S in the tropical South Atlantic, permitting a relatively comprehensive investigation of REE cycling in the ocean.

High concentrations of *d*REEs in surface waters near the Angola coast are likely to result from local reduction of Fe-Mn oxides on marine particles in the water column or in shelf sediments. An observed linear relationship between *d*Ce and dO_2 in surface waters at the studied section may be either due to a coincidence, or controlled by both redox processes and REE inputs from local sources.

The cycling of *d*REEs in the subsurface OMZ off the African shelf is closely linked to the redox cycling of Fe and Mn, as well as the direct redox behaviour of Ce. Enrichment of *d*REEs in the OMZ may result from advected REEs from reducing sediments on the African shelf, and/or their *in-situ* regeneration associated with reduction of Fe-Mn coatings in the water column. The later process must occur at a few stations in the section, based on evidence of seawater REE patterns. The O_2

threshold for Ce reduction is ~25 μM at the studied section, higher than previous observations in an OMZ in the Indian Ocean.

Dissolved REE data from the studied section below ~1000 m were analyzed by an inverse model. The modelling results, for the first time, provide quantitative estimates on the relative importance on the hydrographic (i.e. watermass mixing) and non-conservative (e.g. scavenging, remineralization) controls on the distribution of *d*REEs in the deep tropical South Atlantic. Although discernable fractions of the total *d*REE concentrations in deep waters across the studied section are explained by non-conservative processes, over 80% of the total *d*REE concentrations can be explained by watermass mixing. Significant addition of *d*REEs occurs at two depths, ~1500 m and below ~4000m, in the Angola Basin near African continental margins, as revealed by the modelling results. Despite large hydrothermal inputs of *d*Mn and *d*Fe above the MAR at ~12°S, there is no hydrothermal input of *d*REEs. Instead, enhanced scavenging of *d*Nd above the MAR is demonstrated by our modelling results, probably reflecting continuous scavenging of seawater *d*Nd onto hydrothermally derived Fe-Mn particles during their dispersion.

Chapter 4

Changing ocean circulation and hydrothermal inputs during Ocean Anoxic Event 2 (Cenomanian–Turonian): Evidence from Nd-isotopes in the European shelf sea

NOTE: *A slightly modified version of this chapter, co-authored with Hugh C. Jenkyns, Andrew S. Gale, David J. Ward and Gideon M. Henderson, has been published in Earth and Planetary Science Letters, 375 (2013): 338–348 (http://dx.doi.org/10.1016/j.epsl.2013.05.053). All authors contributed to sample collection in the field. David Ward helped to pick fish debris from bulk rocks. X-Y Zheng preformed all Nd-isotope/elemental analysis, and wrote the manuscript with inputs from all co-authors.*

Abstract

Nd isotopes of fish debris collected from the English Chalk at Eastbourne (Sussex, UK) are used to reconstruct the history of ocean circulation in the NW European shelf sea during Oceanic Anoxic Event 2 (OAE 2, Cenomanian–Turonian). The Eastbourne ε_{Nd} record exhibits a 1-unit negative excursion (decreasing from ~-9 to ~-10), immediately followed by a 3-unit positive excursion reaching ~-7. The onset of the negative ε_{Nd} excursion lags the global $\delta^{13}C$ rise characteristic of OAE 2, suggesting stable patterns of ocean circulation in the NW European shelf sea at this time. Both negative and positive Nd-isotope excursions took place during a transient cooling episode within OAE 2. The negative ε_{Nd} excursion is interpreted as due to a change in ocean circulation with northerly sourced water masses becoming the dominant bottom waters at Eastbourne. The positive excursion is best explained by the transport of radiogenic Nd derived from a volcanic source, possibly the High Arctic or Caribbean large igneous province (LIP). An input of volcanic Nd may reconcile the Eastbourne record with coeval ε_{Nd} records on Demerara Rise in the western tropical Atlantic. The broad synchroneity of high ε_{Nd} values (~-7) registered at both sites suggests a possible period with efficient oceanic mixing between the tropical Atlantic and the NW European shelf sea during the cooling episode. The Eastbourne ε_{Nd} record of OAE 2, together with coeval temperature reconstructions, provides evidence for the coincidence of changes in ocean circulation and transient climatic cooling, implying a tight coupling between the two phenomena during this interval.

4.1 Introduction

The globally recognized oceanic anoxic event 2 (OAE 2), which occurred at the Cenomanian–Turonian boundary, represents a major perturbation of the global carbon cycle (e.g. Jenkyns, 2010). High rates of organic-carbon burial under conditions of bottom-water anoxia/euxinia during OAE 2 led to increased seawater $\delta^{13}C$ values, producing a characteristic geochemical signature for this event. OAE 2 was associated with a late Cenomanian warming trend with a relative thermal maximum in the early Turonian (e.g. Jenkyns et al., 1994; Huber et al., 2002; Norris et al., 2002; Wilson et al., 2002). The warming was punctuated by a period of cooling in the North Atlantic and European shelf sea during OAE 2 (Gale and Christensen, 1996; Voigt et al., 2006; Forster et al., 2007; Sinninghe Damsté et al., 2010), probably in response to a drawdown of atmospheric pCO_2 due to high rates of organic-carbon burial and/or continental weathering (Barclay et al., 2010; Blättler et al., 2011; Jarvis et al., 2011; van Bentum et al., 2012).

Possible processes invoked to explain the widespread bottom-water anoxia/euxinia during OAE 2 include: (1) elevated nutrient supply, due to either enhanced continental weathering and/or upwelling, that would have stimulated primary plankton productivity, with the resulting rain of organic matter depleting seawater oxygen during decomposition in deep water (e.g. Schlanger and Jenkyns, 1976; Arthur et al., 1987; Trabucho Alexandre et al., 2010); (2) sluggish or stratified ocean circulation that would have prevented the deep ocean from replenishing oxygen from the surface (e.g. Schlanger and Jenkyns, 1976; Bralower and Thierstein, 1984; Arthur et al., 1987); (3) intense volcanism, associated with the formation of large igneous provinces (LIPs), that would have emitted not only large quantities of CO_2 to the atmosphere, leading to a warm climate, but also produced a large amount of

reduced metals and sulfides that could have consumed seawater oxygen during their oxidation, and fertilized the ocean as micro-nutrients (e.g. Sinton and Duncan, 1997; Kerr, 1998; Snow et al., 2005).

Ocean circulation has been hypothesized as an essential component in processes driving the significant changes associated with OAE 2, especially through its role in heat transport and nutrient delivery (e.g. Hay, 2008; Jiménez Berrocoso et al., 2010; Trabucho Alexandre et al., 2010). Previous studies of Cretaceous ocean circulation are available based on varied evidence, including sedimentology and palaeontology (e.g. Föllmi and Delamette, 1991), geochemical proxies (e.g. Barrera et al., 1997; van Bentum et al., 2009), and modelling (e.g. Poulsen et al., 1998; Trabucho Alexandre et al., 2010), but high-resolution reconstructions of changes in ocean circulation for OAE 2 remain sparse, so that deciphering their role in the oceanic anoxic event remains challenging.

Seawater Nd isotopes, expressed as ε_{Nd} (representing parts per 10^4 variation of $^{143}Nd/^{144}Nd$ ratio relative to the bulk Earth), are useful tracers for ocean circulation. Water masses are imprinted with Nd-isotope signatures of surrounding continents in source regions, and can then maintain their characteristic signatures along flow paths (e.g. Frank, 2002). Fish debris (phosphatic teeth and bones) are robust archives to preserve bottom-water Nd isotopes, because they acquire abundant neodymium from ambient seawater on the seafloor at the time of deposition, and are resistant to late diagenetic alteration (Martin and Scher, 2004). A limited number of Cretaceous records have revealed resolvable contrasts in seawater ε_{Nd} between different ocean basins, with values of ~-4 in the Pacific and ~-6 to -10 in the Atlantic and proto-Indian Ocean (e.g. Frank et al., 2005; Pucéat et al., 2005; Soudry et al., 2006; Robinson et al., 2010; Martin et al., 2012; Murphy and Thomas, 2012; Robinson and

Vance, 2012; Voigt et al., 2013). These observations have confirmed the potential usefulness of Nd isotopes as tracers for Cretaceous ocean circulation.

High-resolution ε_{Nd} records across OAE 2 have been reported recently and demonstrate significant changes across the event (MacLeod et al., 2008; Martin et al., 2012). These published records are from a depth transect recovered from shallow to intermediate water depths on Demerara Rise in the western tropical Atlantic. Low (i.e. non-radiogenic) ε_{Nd} values of ~-17 to -14 persisted for most of the mid- and late Cretaceous interval at Demerara Rise, probably reflecting the formation of locally derived Demerara Bottom Water that was imprinted with Nd isotopic signatures of the surrounding Precambrian Guyana Shield (MacLeod et al., 2008; Jiménez Berrocoso et al., 2010; MacLeod et al., 2011; Martin et al., 2012). The low background ε_{Nd} values were rapidly replaced by relatively high (i.e. radiogenic) values of ~-7 during OAE 2, forming a ~8 ε-unit positive excursion (MacLeod et al., 2008; Martin et al., 2012). This large ε_{Nd} positive excursion has been interpreted either as a signal of LIP-related volcanism, or a process in which Demerara Bottom Water was replaced by shallow waters from the Tethys or North Atlantic (MacLeod et al., 2008; Martin et al., 2012). The lack of high-resolution ε_{Nd} records spanning OAE 2 from other parts of the ocean limits knowledge both about relevant water-mass end-members, and about the spatial extent of this ε_{Nd} excursion, making unequivocal interpretation of Demerara Rise records difficult at present.

Here we report a new ε_{Nd} record spanning the Cenomanian–Turonian boundary from a chalk section at Eastbourne in southern England. This high-resolution record offers a direct reconstruction of changes in ocean circulation in the NW European shelf sea during OAE 2, and also provides additional insights into the

significance of the coeval ε_{Nd} positive excursion found at Demerara Rise (MacLeod et al., 2008; Martin et al., 2012).

4.2 Stratigraphic and palaeoceanographic setting

The study was conducted on a ~25-m thick chalk section that crops out at beach level below Holywell Pinnacle at Eastbourne in southern England. The section comprises alternations of chalks and marls that are composed of nannofossil-rich carbonate with variable amounts of clay (< 20%) (Paul et al., 1999; Gale et al., 2000, 2005). The Holywell section can be correlated, at a bed-by-bed scale, with the more extensively studied Gun Gardens section situated ~3 km to the south-west (e.g. Gale et al., 2005). Well-constrained bio- and chemo-stratigraphy in chalk sections at Eastbourne permits detailed stratigraphic correlation with other sections recording OAE 2 around the globe (e.g. Tsikos et al., 2004). The expression of OAE 2 in chalk sections at Eastbourne is clearly recognizable based on a positive $\delta^{13}C$ excursion, but organic content is low (0.1–0.3 wt.% TOC) throughout the section (Tsikos et al., 2004), suggesting a dominantly oxic water column at this locality during OAE 2. Chalk facies are pelagic in nature but were deposited in an epicontinental sea with water depths estimated as a few hundred metres (Hancock, 1975). The locality was connected with the Boreal Sea to the north, the Tethys to the south and the North Atlantic to the west during the mid-Cretaceous (Figure 4.1).

4.3 Materials and methods

4.3.1 Fish debris and detritus preparation

Bulk chalk (~10–20 kg per sample) was collected in the field as ~10-cm thick samples, and then was treated with calcium-formate-buffered formic acid (~7.5%,

v/v) with a pH of ~3.2 to dissolve carbonates. Depending on the weight and clay concentration of chalk, this step normally took ~1–3 days. Fish debris was then handpicked from acid-treated residues under a binocular microscope: material was collected and measured from 30 stratigraphic levels across the interval recording OAE 2. Fish teeth were used for most of the studied stratigraphic levels in this study, but bones, or mixed bones and teeth, were used for levels where fish teeth were not yielded, or insufficiently abundant for the Nd-isotope measurement. Different physical properties of teeth and bones, such as crystal size and porosity, could potentially lead to different geochemical signals, so teeth and bones from 7 stratigraphic levels were analyzed separately to compare ε_{Nd} values.

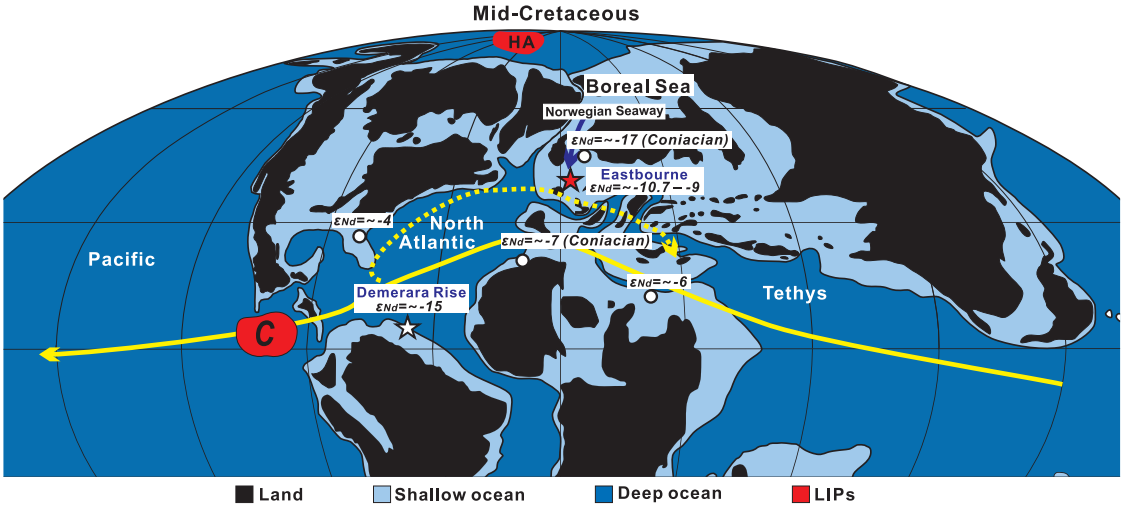

Figure 4.1 Palaeogeographic reconstruction at 90 Ma (map from R.C. Blakey, NAU Geology), showing localities and relevant $\varepsilon_{Nd}(t)$ data mentioned in the text. The listed $\varepsilon_{Nd}(t)$ data are from the Cenomanian–Turonian interval, except for those with estimated ages indicated in brackets (Pucéat et al., 2005; Soudry et al., 2006; Bourbon, 2008; Martin et al., 2012 and this study). Only background $\varepsilon_{Nd}(t)$ values from Demerara Rise and Eastbourne are listed, and high values found during OAE 2 are not indicated on the figure. Yellow arrow indicates the Tethys Circumglobal Current (TCC) (e.g. Bush, 1997), and yellow dashed arrow indicates another possible pattern of TCC (Poulsen et al., 1998). Blue arrow indicates boreal currents. C–Caribbean LIP; HA–High Arctic LIP.

Fish debris was cleaned by a set of physical (i.e. ultrasound) and chemical (i.e. reductive/oxidative) cleaning steps to remove attached clays and Fe–Mn oxides (Boyle, 1981; Boyle and Keigwin, 1985; Rosenthal et al., 1997), and then dissolved in 6 M HCl at ~120°C. Aqua regia was used where needed to ensure complete dissolution. Dissolved samples were split into two aliquots for isotopic and elemental analysis.

Detrital materials were extracted from bulk chalk from 5 stratigraphic levels where fish debris were measured. Bulk samples (~5 g) were first dissolved in 10% (v/v) acetic acid at room temperature for at least 2 days to remove carbonate fractions, and then in H_2O_2 for at least 2 days to remove organic content, and finally in 2 M HCl for 1 day to remove Fe-Mn oxides. ~100 mg residues after the sequential dissolution were taken and rinsed with Milli-Q water, and then fully dissolved with a mixture of HF and HNO_3 at ~120°C. The dissolved detrital materials were split into two aliquots for elemental and Nd-isotope analysis.

4.3.2 Nd-isotope and elemental analysis

Neodymium was separated by a two-stage ion-exchange chromatographic separation. The first stage separated rare earth elements (REEs) from major cations using AG 50W–X12 resin (Bio-Rad, 200–400 mesh) with HCl as an eluent, and the second stage separated Nd from other REEs using AG 50W–X4 resin (Bio-Rad, 200–400 mesh, ammonium form) with α–hydroxyisobutyric acid as an eluent. The total blank of column separation was negligible (~50 pg Nd), compared to typical sample size (>120 ng Nd).

Nd isotopes were analysed on an MC-ICP-MS (Nu Plasma) in the Department of Earth Sciences, University of Oxford. Mass bias was corrected by using

$^{146}Nd/^{144}Nd = 0.7219$ with an exponential law. Samples were measured by bracketing with the JNdi-1 Nd-isotope standard, and the instrument drift was corrected by normalizing $^{143}Nd/^{144}Nd$ ratios of the bracketing JNdi-1 to a reference value of 0.512115 (Tanaka et al., 2000). Measurements on the bracketing JNdi-1 standard during the course of this study yielded $^{143}Nd/^{144}Nd = 0.512099 \pm 0.000015$ (2σ, n = 90), which is equivalent to an external reproducibility of ±0.3 ε-unit (2σ).

Our reported $\varepsilon_{Nd}(t)$ values were corrected for radiogenic in-growth of ^{143}Nd. To this end, Sm/Nd ratios were determined on a HR-ICP-MS (Element 2). La/Sm ratios were determined simultaneously because of their potential indication for the degree of diagenesis (see discussion 4.5.1). Repeated analyses on a gravimetrically prepared multi-element standard containing all REEs suggest that accuracy is <1% for Sm/Nd ratios, and <3% for La/Sm ratios. Repeated analyses on a fish-bone composite gave a precision <1% (1σ) for Sm/Nd ratios, and ~3% (1σ) for La/Sm ratios. The age used for the in-growth correction of each sample was assigned based on the age model described in section 3.4.

4.3.3 Bulk carbon- and oxygen-isotope analysis

At the same levels where fish debris were sampled and measured, $\delta^{13}C_{carb}$ and $\delta^{18}O_{carb}$ were determined on bulk chalk using a VG Isogas Prism II mass spectrometer with an on-line VG Isocarb common acid bath preparation system. Reproducibility of replicated standards is <0.1‰ (1σ) for $\delta^{13}C_{carb}$ and $\delta^{18}O_{carb}$.

4.3.4 Age model

Numerical ages were assigned for each sample for the sole purpose of radiogenic in-growth corrections on Nd isotopes. The age model is based on an

astronomically tuned timescale developed by Voigt et al. (2008). Briefly, there are 38 precession cycles (~21 kyr) from the base of the *M. geslinianum* Zone to approximately the base of the *M. nodosoides* Zone, spanning a duration of ~798 kyr. This time span is represented by ~20.2 m of stratigraphic thickness in the Holywell section (Figure 4.2), yielding an average sedimentation rate of ~2.5 cm/kyr. This average sedimentation rate is then applied to calculate ages for each sample, with the Cenomanian–Turonian boundary tied to 93.55 Ma. Use of an average sedimentation rate ignores possible short-term variations in this parameter by a factor of 2 (Voigt et al., 2008), but $\varepsilon_{Nd}(t)$ values calculated with an average sedimentation rate differ from ones calculated with a 2× sedimentation rate by less than 0.1%, which is negligible.

4.4 Results

Bulk-chalk $\delta^{13}C_{carb}$ and $\delta^{18}O_{carb}$ data are reported in Table 4.1 (Appendix C). The $\delta^{13}C_{carb}$ positive excursion of OAE 2 from Holywell, derived from the same samples that yielded fish debris, displays features identical with those from the Gun Gardens section (e.g. Tsikos et al., 2004). According to the terminology commonly used in previous studies (e.g. Paul et al., 1999), this excursion can be sub-divided into 4 segments rising from a background of ~2.75‰ in the preceding upper Grey Chalk Member (Figure 4.2): an increase marking the onset of OAE 2 from the base of the Plenus Marls ("first build-up stage"); a decrease towards background values ("trough interval") from upper Bed 3 of the Plenus Marls to Bed 4; a subsequent increase ("second build-up stage") to top of Bed 8; and, finally, a plateau with values of ~4.5‰ in the Ballard Member and lower Holywell Member. $\delta^{13}C_{carb}$ then declines to background values of ~3.5‰. The overall trend of $\delta^{18}O_{carb}$ shows a gradual decrease from ~-3.0‰ to -4.0‰ from bottom to top of the studied section, interrupted by some

short-term fluctuations with amplitudes of ~0.5‰ (Figure 4.2). A ~1‰ positive excursion in $\delta^{18}O_{carb}$, defined by 6 consecutive data points, occurs between Bed 2 and 5 of the Plenus Marls.

Nd-isotope data obtained from fish debris and detritus, together with North American Shale Composite (NASC; values from Gromet et al., 1984) normalized La/Sm ratios (La_N/Sm_N) of fish debris, are reported in Table 4.2 (Appendix C). Fish teeth and bones from the same stratigraphic level show nearly identical $\varepsilon_{Nd}(t)$ values (Figure 4.3), which suggests that both fossil types record the same seawater Nd-isotopic compositions. Agreement of $\varepsilon_{Nd}(t)$ from replicates from 7 stratigraphic levels suggests that contamination from detrital materials and other phases during sample preparation is insignificant (Figure 4.2 and Figure 4.3). La_N/Sm_N ratios for the fish debris range between 0.7 and 1.5.

Fish-debris $\varepsilon_{Nd}(t)$ values range from -10.7 to -7.5 across the Cenomanian–Turonian boundary, and exhibit well-resolved excursions, first to relatively low and then relatively high values (Figure 4.2). The $\varepsilon_{Nd}(t)$ shows constant values of ~-9 during the pre-OAE 2 interval, and remains steady at the onset of the $\delta^{13}C_{carb}$ rise, then declines by ~1 ε_{Nd} unit starting between Bed 2 and 3 of the Plenus Marls. Following a minimum of ~-10 in Bed 3 (at the same depth that $\delta^{13}C_{carb}$ reaches its first maximum), $\varepsilon_{Nd}(t)$ recovers rapidly and continues to rise during the $\delta^{13}C_{carb}$ trough interval and second increase to reach a maximum of -7.5 in Bed 6. Overall, ε_{Nd} values peak 3 units above background values before decreasing gradually above Bed 6 and during the $\delta^{13}C_{carb}$ plateau stage. Values finally stabilize at ~-10.5 at the level of Holywell Marl 3 in the lower Turonian. Detrital $\varepsilon_{Nd}(t)$ values range between ~-12 and ~-11, and are consistently lower than fish-debris $\varepsilon_{Nd}(t)$ values from the same stratigraphic levels.

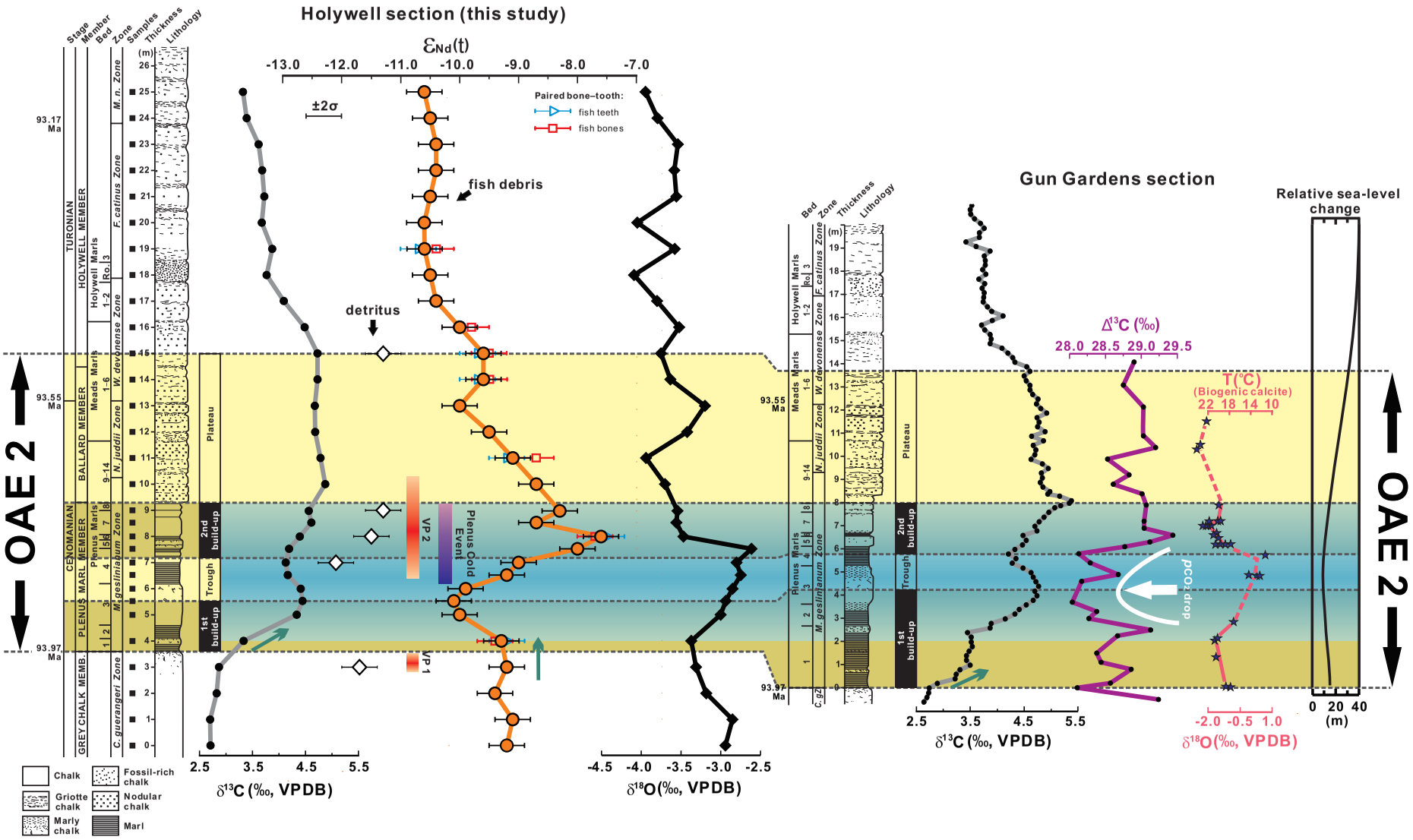
Holywell section (this study)
εNd(t)
-13.0 -12.0 -11.0 -10.0 -9.0 -8.0 -7.0
±2σ
Paired bone–tooth:
fish teeth
fish bones
fish debris
detritus
Stage
Member
Bed
Zone
Samples
Thickness
Lithology
TURONIAN
HOLYWELL MEMBER
BALLARD MEMBER
CENOMANIAN
PLENUS MARL MEMBER
GREY CHALK MEMB.
Holywell Marls
Meads Marls
Plenus Marls
M. n. Zone
F. catinus Zone
W. devonense Zone
N. juddii Zone
M. geslinianum Zone
C. guerangeri Zone
93.17 Ma
93.55 Ma
93.97 Ma
OAE 2
Plateau
2nd build-up
Trough
1st build-up
VP 2
VP 1
Plenus Cold Event
2.5 3.5 4.5 5.5
δ13C (‰, VPDB)
-4.5 -4.0 -3.5 -3.0 -2.5
δ18O(‰, VPDB)
Chalk
Fossil-rich chalk
Griotte chalk
Nodular chalk
Marly chalk
Marl
Gun Gardens section
Δ13C (‰)
28.0 28.5 29.0 29.5
T(°C)
(Biogenic calcite)
22 18 14 10
pCO2 drop
2.5 3.5 4.5 5.5
δ13C (‰, VPDB)
-2.0 -0.5 1.0
δ18O(‰, VPDB)
Relative sea-level change
0 20 40
(m)

Figure 4.2 Results of $\varepsilon_{Nd}(t)$, $\delta^{13}C_{carb}$ and $\delta^{18}O_{carb}$, plotted against the stratigraphic log from the Holywell section. Also shown are records of $\delta^{13}C_{carb}$ (Tsikos et al., 2004), $\Delta^{13}C$ (Gale et al., 2005) and $\delta^{18}O$ from biogenic calcites, along with the relative sea-level change reconstruction (Voigt et al., 2006), taken from the Gun Gardens section. Mean $\varepsilon_{Nd}(t)$ values of fish debris (closed orange circles) are plotted when more than one measurement from the same stratigraphic levels is available. Empty white diamonds indicate detrital $\varepsilon_{Nd}(t)$ values. Results of $\varepsilon_{Nd}(t)$ from paired bone–tooth are also plotted (empty blue triangles and empty red squares). The shaded area with alternating light and dark yellow bands indicates 4 segments of the $\delta^{13}C_{carb}$ rise characteristic of OAE 2, and key levels of $\delta^{13}C$ stratigraphy in the two sections are correlated by horizontal dashed lines (grey). The blue band represents the inferred cooling episode. The two vertical red bars indicate inferred volcanic pulses (VP 1 and VP 2). VP 1 is drawn based on evidence from Os isotopes (Turgeon and Creaser, 2008), and VP 2 is based on trace metal anomalies found at Eastbourne (Orth et al., 1993). The purple bar indicates the Plenus Cold Event as defined by the presence of boreal faunas at Eastbourne. The three green arrows indicate different trends of $\delta^{13}C_{carb}$ and $\varepsilon_{Nd}(t)$ at the onset of OAE 2. An atmospheric pCO_2 drop (white arrow) centered at the level of Bed 3 of the Plenus Marls is suggested by the $\Delta^{13}C$ data from the Gun Gardens section (Jarvis et al., 2011).

4.5 Discussion

4.5.1 Integrity of Nd isotopes recorded in fish teeth as bottom-water signatures at Eastbourne

Fish debris acquire Nd from seawater at the sediment–water interface during early diagenesis, and can generally preserve bottom-water signals under varied depositional conditions due to their high Nd concentrations, typically hundreds to thousands of ppm (Staudigel et al., 1985; Martin and Haley, 2000; Martin and Scher, 2004). Some studies, however, suggest that exchange of Nd in fish debris may occur during late diagenesis (Kocsis et al., 2010; Herwartz et al., 2011).

Several lines of evidence argue against significant late diagenetic alteration of seawater ε_{Nd} preserved in fish debris from Eastbourne. Firstly, background $\varepsilon_{Nd}(t)$ values of -10.7 to -9 at Eastbourne during the studied Cenomanian–Turonian interval

(except for within OAE 2) agree with published $\varepsilon_{Nd}(t)$ data from nearby coeval shallow shelf-sea sites in France (Pucéat et al., 2005). Secondly, although processes associated with REE-uptake in biogenic apatites, including fish debris, are not yet fully understood (e.g. Byrne et al., 1996; Lécuyer et al., 1998), thermodynamic calculations suggest that the La_N/Sm_N ratio in marine biogenic apatites can indicate the degree of diagenesis. In the model of Reynard et al. (1999), quantitative incorporation, adsorption and substitution are three proposed mechanisms that control the uptake of REEs into biogenic apatites. Because the former two mechanisms are responsible for incorporation of seawater REEs into bio-apatites, samples influenced only by these mechanisms should record pristine signals of seawater. However, the third mechanism – substitution – involves intense chemical–crystal interactions between bio-apatites and ambient fluids during late diagenesis, so that pristine seawater signals could be compromised. The former two mechanisms have little or no effect on fractionating the La_N/Sm_N ratio, allowing bio-apatites to inherit La_N/Sm_N ratios of seawater, but substitution could considerably lower the ratio to <0.3. Our measured La_N/Sm_N ratios in fish debris from Eastbourne are all higher than 0.3 (0.7 to 1.5; Table 4.2 in Appendix C), and are close to those of seawater (0.6–1.6; Reynard et al., 1999), indicating negligible late diagenetic effects.

Thirdly, fish bones are likely to be more susceptible to diagenesis than teeth due to the relatively open histological structure and smaller crystal size in bones (e.g. Kocsis et al., 2010). Diagenesis is therefore expected to impart different ε_{Nd} to fish teeth and bones. However, this is not observed for the samples from Eastbourne, where fish teeth and bones show nearly identical $\varepsilon_{Nd}(t)$ values (Figure 4.3). Furthermore, the low detrital content in chalk sections at Eastbourne (Paul et al., 1999; Gale et al., 2000, 2005) reduces the likelihood of major contamination of ε_{Nd} in

fish debris by any terrigenous signal. This supposition is supported by the observation that changes in the Holywell $\varepsilon_{Nd}(t)$ record do not co-vary with lithology, or calcite/detritus ratios in the Plenus Marls at Eastbourne (Keller et al., 2001). In summary, there are a number of arguments that indicate that our $\varepsilon_{Nd}(t)$ data from fish debris from Eastbourne faithfully reflect bottom-water values.

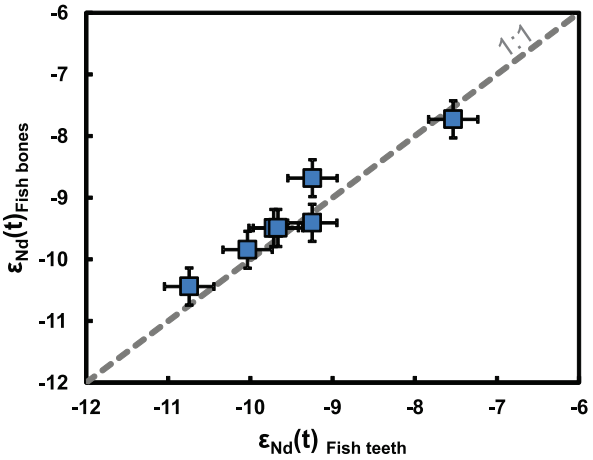

Figure 4.3 Comparison of $\varepsilon_{Nd}(t)$ between fish teeth and bones from the same stratigraphic levels.

4.5.2 Constraints on relevant water masses at Eastbourne

Interpreting the Eastbourne $\varepsilon_{Nd}(t)$ record in terms of changes in ocean circulation requires knowledge of regional circulation patterns and constraints on the ε_{Nd} of relevant water masses. Possible influences on ε_{Nd} at Eastbourne are shallow Tethys–Atlantic throughflow, and/or currents from the Boreal Sea (Figure 4.1).

A stable westward-flowing Tethys Circumglobal Current (TCC), facilitated by the lack of geographic barriers, has been hypothesized as a prominent feature of tropical upper-ocean circulation during the Cretaceous (Figure 4.1), and is supported by both field evidence and modelling results (e.g. Föllmi and Delamette, 1991; Bush,

1997). The stability and direction of the TCC, however, may have varied considerably in response to palaeogeographic changes. Some modelling results show a clockwise gyre in the Mediterranean Tethys, with a narrow westward flow into the North Atlantic along the south Tethyan margin, and an eastward flow returning to the Tethys across NW Europe (e.g. Poulsen et al., 1998) (Figure 4.1). Despite uncertainties regarding the precise flow of the TCC, shallow waters from either the Tethys or North Atlantic could have flowed over the mid-latitudinal passage connecting these two oceans during the Cenomanian–Turonian interval, and affected bottom waters at Eastbourne.

Tethys–Atlantic throughflow was probably characterized by relatively high $\varepsilon_{Nd}(t)$ values of ~-6 to -4, based on limited Cenomanian–Turonian data from shallow-water sites (<1000 m) in the mid-latitudinal Tethys and North Atlantic (Figure 4.1). Values of ~-6 were obtained from the southern margin of the Tethys (Soudry et al., 2006), and of ~-4 from Blake Nose in the NW Atlantic (Bourbon, 2008; Martin et al., 2012). One observation from Morocco indicates an $\varepsilon_{Nd}(t)$ value of ~-7 during the Coniacian (Pucéat et al., 2005), which is similar to the Cenomanian–Turonian values recorded at the southern margin of the Tethys. Although very low $\varepsilon_{Nd}(t)$ values of -17 to -14 were found at Demerara Rise in the western tropical Atlantic during the Cenomanian–Turonian boundary interval, the influence of this water mass was likely to be regional (Martin et al., 2012). It is noteworthy that shallow and intermediate waters in the equatorial Pacific generally have $\varepsilon_{Nd}(t)$ values higher than ~-6 during the Cretaceous (e.g. ~-6 to -3; Murphy and Thomas, 2012). Although lower $\varepsilon_{Nd}(t)$ values observed in the southern margin of the Tethys (~-7), compared to those observed at Blake Nose in the NW Atlantic (~-4), may result from the influence of local continental sources (Soudry et al., 2006), $\varepsilon_{Nd}(t)$ values found in the two locations

generally approach those of Cretaceous Pacific seawater, seemingly supporting the transport of Pacific waters by the TCC into the Tethys and Atlantic at that time.

The Boreal Sea (Figure 4.1) was connected to NW Europe through the Norwegian seaway during the Cretaceous (Gradstein et al., 1999). Boreal seawater may, therefore, have also contributed to bottom waters at Eastbourne. Cenomanian–Turonian $\varepsilon_{Nd}(t)$ data from the Boreal Sea are unavailable, but its shallow waters most likely had very negative $\varepsilon_{Nd}(t)$ values, receiving weathering products from surrounding old continental crust whose ε_{Nd} values could have been as low as -30 (Jeandel et al., 2007). A single data point of -17 from the lower Campanian of Sweden (Pucéat et al., 2005) supports the non-radiogenic nature of boreal seawater during at least part of the Cretaceous.

The Cenomanian–Turonian $\varepsilon_{Nd}(t)$ values of -10.6 to -7.6 observed at Eastbourne plot between the inferred $\varepsilon_{Nd}(t)$ value of the Tethys–Atlantic throughflow and that of boreal seawater, probably reflecting mixing between these two end-members. The temporal variability in the mixing of these water masses provides a viable mechanism to drive changes in $\varepsilon_{Nd}(t)$ values recorded at Eastbourne.

4.5.3 Significance of the Eastbourne ε_{Nd} record across OAE 2

4.5.3.1 Pre-excursion

The prominent features of the Eastbourne ε_{Nd} record are two excursions, first to low and subsequently to high values during OAE 2 (Figure 4.2). Relatively constant $\varepsilon_{Nd}(t)$ values at Eastbourne are observed at the onset of the $\delta^{13}C_{carb}$ rise that starts from the base of the Plenus Marls. The onset of the initial negative $\varepsilon_{Nd}(t)$ excursion lags the $\delta^{13}C_{carb}$ rise by at least 40 cm in the stratigraphy (Figure 4.2), representing a ~20 kyr duration (based on the timescale of Voigt et al. 2008). This

observation suggests that no major change in patterns of upper ocean circulation occurred in the NW European shelf sea at the initiation of OAE 2.

4.5.3.2 Coincidence of the double excursions and climatic cooling during OAE 2

The two ε_{Nd} excursions fall entirely within a cooling episode recorded at levels between upper Bed 1 and Bed 8 of the Plenus Marls during OAE 2, as defined by a synthesis of temperature proxies recovered from Eastbourne (Figure 4.2). The cooling episode, which likely resulted from a drawdown of atmospheric CO_2 caused by elevated rates of organic-carbon burial and/or silicate weathering, is supported by evidence from various sections covering OAE 2 (e.g. Jarvis et al., 2011; van Bentum et al., 2012). At Eastbourne, the initial decline of $\varepsilon_{Nd}(t)$ values coincides with an inferred drawdown in atmospheric pCO_2 (Figure 4.2). This putative pCO_2 drop is based on records of paired inorganic and organic-carbon isotopes ($\Delta^{13}C$) from both Eastbourne and other European sections at comparable stratigraphic levels (Jarvis et al., 2011). Although the use of $\Delta^{13}C$ as a pCO_2 proxy requires *a priori* assumptions that are not always straightforward to test (e.g. Jarvis et al., 2011), the $\Delta^{13}C$-inferred pCO_2 drop from Eastbourne is supported by an independent leaf stomatal record from the Western Interior Seaway in mid-continent North America (Barclay et al., 2010), correlated with European sections via $\delta^{13}C$ chemostratigraphy (Tsikos et al., 2004). Approximately coeval with the inferred pCO_2 drop, the positive shift in $\delta^{18}O_{carb}$ from Bed 2 of the Plenus Marls at Holywell suggests the onset of seawater cooling in the European shelf sea (Figure 4.2). This shift in $\delta^{18}O_{carb}$ (Figure 4.2) is consistent with $\delta^{18}O$ trends in well-preserved biogenic calcite (belemnites, bivalves and brachiopods) from the Gun Gardens section (Voigt et al., 2006) and $\delta^{18}O_{carb}$ records from several European sections (Jarvis et al., 2011), thereby implying a strong climatic control.

The subsequent increase in $\varepsilon_{Nd}(t)$ values is contemporaneous with the so-called Plenus Cold Event, which is characterized by an invasion of boreal index faunas, including a belemnite, two bivalves and serpulid worms, into mid-latitudes including Eastbourne and areas to the south in the Anglo–Paris Basin (Gale and Christensen, 1996). These distinctive faunas, demonstrated to have a northern origin and associated with cool waters (Jefferies, 1962), spread southward from the Arctic region, probably along the line of the Norwegian Sea. Comparable faunas, albeit of different ages, found in Manitoba, Canada, and central Greenland also originated in the Arctic (Jefferies, 1962; Gale and Christensen, 1996).

The stratigraphic range of boreal faunas in Bed 4–8 of the Plenus Marls at Eastbourne does not necessarily illustrate the exact duration of the cooling episode inferred from geochemical evidence. As faunal migration may have taken place only when cooling reached a certain threshold, the initial appearance of boreal faunas in Bed 4 may well have lagged the onset of temperature decline. Similarly, the complete disappearance of boreal faunas in Bed 8 was apparently preceded by a recovery of temperature recorded in underlying beds, as suggested by the negative shift of $\delta^{18}O$ data in bulk chalk and well-preserved biogenic calcite (Voigt et al., 2006). Bulk-chalk $\delta^{18}O_{carb}$ from the Holywell section shows a rapid recovery to warmer temperatures ending by Bed 5 time (Figure 4.2), but the $\delta^{18}O$ of well-preserved biogenic calcite from the Gun Gardens section shows a later recovery ending at Bed 7 time, which is followed by a small positive shift (i.e. cooling) at Bed 8 time (Voigt et al., 2006). These differences may reflect local diagenetic overprints on $\delta^{18}O_{carb}$ of bulk chalk (Voigt et al., 2006); thus we take the level of Bed 8, where the boreal faunas completely disappear, to indicate the end of the inferred cooling episode. The Plenus Cold Event, together with coeval TEX_{86} records from the tropical and mid-latitudinal

North Atlantic (Forster et al., 2007; Sinninghe Damsté et al., 2010), indicate an overall cool period with some fluctuations in temperature over the European shelf sea and adjacent North Atlantic during this interval.

4.5.3.3 Possible causes for the negative ε_{Nd} excursion

Despite the coincidence of ε_{Nd} excursions and climatic cooling, different mechanisms are required to explain the two excursions shifting $\varepsilon_{Nd}(t)$ in opposite directions. The initial negative excursion is not seen on Demerara Rise (MacLeod et al., 2008; Martin et al., 2012), and is a newly observed feature that could have been caused by: (1) a change in weathering; (2) boundary exchange control of seawater Nd-isotopes; or (3) a change in ocean circulation.

Enhanced weathering, introducing more non-radiogenic Nd from surrounding Precambrian continents into seawater, could have caused a ε_{Nd} negative excursion. It is generally believed that continental weathering increased significantly before OAE 2, due to warming caused by volcanic outgassing, and the resulting increase in nutrient supply boosted marine primary productivity, leading to the initiation of OAE 2 (e.g. Jenkyns, 2010). A warming is supported by a leaf-stomata record that indicates an increase in atmospheric pCO_2 right before the onset of the global $\delta^{13}C$ rise (Barclay et al., 2010). Probably in response to the warming, a transient pulse in continental weathering occurred before, or coincident with, the onset of the $\delta^{13}C$ rise, as indicated by evidence of Sr, Ca and Li isotopes recorded at carbonate sections in Italy and Eastbourne respectively (Frijia and Parente, 2008; Blättler et al., 2011; Pogge von Strandmann et al., 2013). However, either a reduced residence time of Sr, or a very large (threefold) increase in continental weathering is required to explain the observed short-term fluctuations registered by these records. The inferred large

incease in intensity of continental weathering at the onset of the $\delta^{13}C$ rise corresponds to constant ε_{Nd} values in the Holywell section, suggesting that the ε_{Nd} change was not associated with preferential weathering or delivery of materials with distinct ε_{Nd} values into seawater of the shelf sea at Eastbourne during OAE 2. To be explained by changes in weathering, the ε_{Nd} negative excursion would require a rapid weathering pulse after the onset of the $\delta^{13}C$ rise. This is later than the Sr, Ca and Li isotope evidence for weathering increase, and instead concurrent with cooling, which is expected to lead to reduced weathering. Changes in continental weathering, therefore, do not seem likely to be a major control on the observed ε_{Nd} excursion.

Boundary exchange, a process involving exchange of Nd between seawater and shelf sediments, is an important pathway by which bottom waters acquire their Nd-isotope signatures (e.g. Lacan and Jeandel, 2004a, 2004b). Given generally low ε_{Nd} values (~-14 – -17) on present-day NW European continental margins (Jeandel et al., 2007), stronger boundary exchange should have led to a negative $\varepsilon_{Nd}(t)$ excursion in bottom waters. Factors that affect boundary exchange are poorly constrained, but presumably the composition of sea-floor sediments should play a role, given that the process involves sediment–seawater interactions. Changes in boundary exchange are, therefore, most likely to have occurred when compositions of sea-floor sediments changed. A significant transition in lithology, from clay-poor chalks to clay-rich marls, occurs at the base of the Plenus Marls (Paul et al., 1999; Gale et al., 2000), but this transition clearly predates the $\varepsilon_{Nd}(t)$ negative excursion (Figure 4.2), implying either a lack of significant changes in boundary exchange, or negligible influence of boundary exchange on the $\varepsilon_{Nd}(t)$ record.

A change in the mixture of water-masses on the NW European continental margin appears the most likely explanation for observed changes in $\varepsilon_{Nd}(t)$ in bottom

waters. An increase in the fraction of boreal seawater, with low $\varepsilon_{Nd}(t)$ values, relative to the Tethys–Atlantic throughflow with high values, could explain the ε_{Nd} negative excursion. This explanation is consistent with obliquity amplification expressed in three sedimentary records in the mid- to low latitudinal North Atlantic during OAE 2, which was explained by an influence of high-latitude processes, most likely changes in ocean circulation, propagating into low latitudes at that time (Meyers et al., 2012). The coincidence in timing of this change in ocean circulation and the inferred pCO_2 drawdown supports a tentative causal link, as hypothesized by previous studies (Forster et al., 2007; Jarvis et al., 2011); an increased latitudinal thermal gradient caused by a drop in pCO_2 during OAE 2 (Sinninghe Damsté et al., 2010) could have produced thermal instability in the ocean and strengthened wind systems, ultimately leading to a change in circulation.

4.5.3.4 Possible causes for the ε_{Nd} positive excursion

The 3-unit positive ε_{Nd} excursion, which closely follows the negative excursion, requires either (1) a change in continental weathering and/or boundary exchange; (2) reorganization of ocean circulation; or (3) a sudden input of radiogenic Nd from a new source.

Whatever mechanism is invoked, a ε_{Nd} positive excursion that reaches values of ~-7 requires introduction of more radiogenic Nd into seawater that affects the shelf sea at Eastbourne during OAE 2. In the modern ocean, ε_{Nd} values of ~-8 to -7, similar to peak values of the Eastbourne record, are observed in seawater flowing between Greenland and Norway due to boundary exchange with basalt-rich sediments that have ε_{Nd} values of > ~7 (Lacan and Jeandel, 2004a, 2004b). However, those basaltic margins are related to the formation of the North Atlantic igneous province that first

developed in the late Cretaceous or early Paleogene (e.g. Storey et al., 2007; Hansen et al., 2009), and would not therefore have existed during the Cenomanian–Turonian interval. This is supported by the Nd-isotope results obtained from detrital materials in this study; all measured detrital materials at Eastbourne have very negative $\varepsilon_{Nd}(t)$ values of ~-11.5, even at stratigraphic levels where the positive $\varepsilon_{Nd}(t)$ excursion was registered in fish debris. The detrital data suggests that the local sources of sediment during OAE 2 had relatively unradiogenic ε_{Nd} values and therefore weathering or exchange with these materials would not have resulted in a 3-unit ε_{Nd} positive excursion reaching relatively radiogenic values of ~-7 in seawater at Eastbourne.

An increase in the relative strength of the Tethys–Atlantic throughflow could have produced the positive ε_{Nd} excursion. We cannot exclude this possibility, but it would be surprising that a southward migration of boreal faunas (i.e. Plenus Cold Event) corresponded to a period of a stronger southerly sourced water mass at Eastbourne, and it is also difficult to explain why such a reorganization in circulation, reversing the processes that led to the ε_{Nd} negative excursion, suddenly took place during continued climatic cooling. Modelling results suggest that small tectonic movements can alter patterns of upper-ocean circulation in the European shelf sea during the mid-Cretaceous (Poulsen et al., 1998). However, because tectonic movements are usually slow and irreversible, they are not a likely explanation for the rapid and subsequently reversed positive shift in ε_{Nd}. Model experiments also predict that sea-level rise can strengthen westward-flowing water masses from the Tethys (Poulsen et al., 1998). Although the increase in $\varepsilon_{Nd}(t)$ values at Eastbourne occurred during a major transgression (Voigt et al., 2006), the fall in $\varepsilon_{Nd}(t)$ values during continuous sea-level rise obviously contradicts this theory (Figure 4.2).

Introduction of Nd from submarine volcanism could produce a positive excursion without invoking any change in circulation patterns, because of the high ε_{Nd} values (~+10) of basalts. Formation of LIPs has been credited with triggering OAE 2 (Sinton and Duncan, 1997; Kerr, 1998; Snow et al., 2005; Turgeon and Creaser, 2008). Although hydrothermal Nd is rapidly immobilized by Fe–Mn oxides near vent sites in the modern ocean (e.g. Mitra et al., 1994), it could have dispersed more easily during OAEs because of possible destabilization of Fe–Mn oxides under anoxic/euxinic conditions (MacLeod et al., 2008; Jenkyns, 2010). Trace-metal enrichments recognized at similar stratigraphic levels in marine sections across the North Atlantic are interpreted as possible signals of LIP-related volcanism (Orth et al., 1993; Snow et al., 2005). The stratigraphic position of these trace-metal enriched layers, lying slightly above the last appearance of *R. cushmani* and below the lowermost *N. juddii* Zone at Eastbourne (Orth et al., 1993) (the red bar "VP 2" in Figure 4.2), is coeval with the ε_{Nd} positive excursion. In addition, the peak of the ε_{Nd} positive excursion coincides with a possible volcanically derived Cr/Al peak in Bed 6 (Pearce et al., 2009). Concurrence of an inferred volcanic pulse and the ε_{Nd} positive excursion supports the idea of transport of magmatic Nd to the NW European shelf sea.

The relatively oxic nature of the water column at Eastbourne would have prohibited any local reduction of Fe–Mn oxides during OAE 2. Radiogenic Nd must therefore have overprinted original seawater ε_{Nd} signatures at volcanic source regions under anoxic/euxinic conditions, and then been carried to Eastbourne by oceanic circulation. Both the High Arctic and Caribbean LIP had major eruptions close to the time of the Cenomanian–Turonian (Snow et al., 2005; Tegner et al., 2011) (Figure 4.1). The lack of outcrop makes eruption history of the High Arctic LIP rather poorly

constrained, but volcanic Nd derived from this LIP could have been transported to Eastbourne by boreal seawater, considering the geographic proximity of the two locations. The Caribbean LIP provides an alternative source of radiogenic Nd, but over a much longer distance than between the Arctic region and Eastbourne.

4.5.3.5 Post-excursion

Values of $\varepsilon_{Nd}(t)$ decrease after the peak in Bed 6 (Figure 4.2), suggesting less supply of radiogenic Nd and weakened volcanism. Values of $\varepsilon_{Nd}(t)$ finally stabilize at ~-10.5 before the fall in $\delta^{13}C$ values characteristic of the termination of OAE 2. The post-excursion $\varepsilon_{Nd}(t)$ values are ~1-unit lower than pre-excursion values, possibly reflecting long-term enhanced continental weathering due to the general warming trend during the late Cenomanian. Alternatively, because the post-excursion $\varepsilon_{Nd}(t)$ reached values similar to minimum values of the ε_{Nd} negative excursion, a circulation pattern with stronger influence of boreal-sourced water masses may have persisted after the onset of the cooling episode.

4.5.4 Reconciling the Eastbourne ε_{Nd} with coeval records observed on Demerara Rise

A positive ε_{Nd} excursion was recorded on Demerara Rise during OAE 2, and comprises two "spikes" (S1 and S2 in Figure 4.4), with the first one before or at the onset of the $\delta^{13}C$ rise, and the second one after the first maximum of the $\delta^{13}C$ rise (Martin et al., 2012). The first ε_{Nd} spike is not seen at Eastbourne, but the second spike can be approximately correlated with the positive ε_{Nd} excursion at Eastbourne based on $\delta^{13}C$ stratigraphy (Erbacher et al., 2005): both reached similar peak ε_{Nd} values of ~-7 (Figure 4.4).

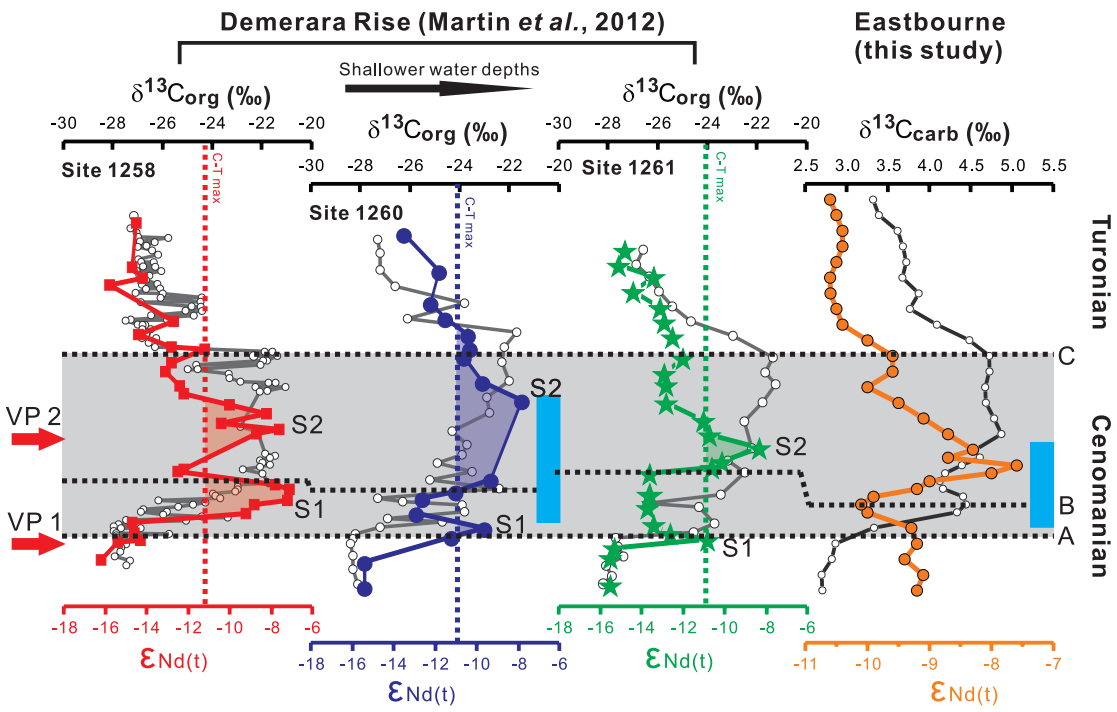

Figure 4.4 Comparison of $\varepsilon_{Nd}(t)$ records from Eastbourne (this study) and from a depth transect on Demerara Rise, western tropical Atlantic (Martin et al., 2012). Grey area marks OAE 2. Stratigraphic correlation is based on the characteristic $\delta^{13}C$ stratigraphy (open circles), after Erbacher et al., (2005) and Forster et al., (2007). A, B and C indicate the onset, first maximum and the end of the $\delta^{13}C$ rise respectively. VP 1 and VP 2 indicate the two volcanic pulses, and are drawn as in Fig. 4.2. Vertical dashed lines on the records from Demerara Rise indicate maximum $\varepsilon_{Nd}(t)$ values of each site during the Cenomanian–Turonian, except for OAE 2 (Martin et al., 2012). S1 and S2 indicate the two $\varepsilon_{Nd}(t)$ spikes. Colour-shaded areas on the $\varepsilon_{Nd}(t)$ records from the Demerara Rise indicate time intervals when local seawater was potentially influenced by the input of radiogenic Nd from the two volcanic pulses (VP 1 and VP 2). The two vertical blue bars indicate the inferred cooling episode. The stratigraphic position of the cooling episode at Site 1260 is based on the TEX_{86} record from this site (Forster et al., 2007); the cooling episode from Eastbourne is drawn as in Fig. 4.2. The two red arrows are inferred volcanic pulses.

The broad synchroneity of the second ε_{Nd} spike on Demerara Rise and the ε_{Nd} positive excursion at Eastbourne, each with similar peak ε_{Nd} values, could suggest a common process/source affecting both localities during this interval. The modelled clockwise circulation in the North Atlantic during the mid-Cretaceous offers a possible oceanic connection to propagate the radiogenic Nd (Figure 4.1; Poulsen et

al., 1998). Martin et al. (2012) invoked a change in local bottom waters with either decreased Demerara Bottom Water ($\varepsilon_{Nd}(t)$ = ~-16) or increased waters from the Tethys/North Atlantic ($\varepsilon_{Nd}(t)$ = ~-8 to -6) to explain the ε_{Nd} positive excursion on Demerara Rise. A decrease in the influence of Demerara Bottom Water is unable to explain the ε_{Nd} positive excursion at Eastbourne where bottom waters were not affected by this water-mass. Although increased supply of Tethyan or North Atlantic waters could have led to more elevated ε_{Nd} values in both localities, this is less likely to have been the case for Eastbourne, where the evidence implies a volcanic signal (as discussed in 4.5.3.4). Instead, an input of volcanic Nd at this time can reconcile the ε_{Nd} rise at both localities.

The two ε_{Nd} spikes on Demerara Rise are closely associated with two inferred volcanic pulses. The first ε_{Nd} spike corresponds well to an initial magmatic pulse during the onset of OAE 2, which is suggested by Os isotopes (Turgeon and Creaser, 2008) ("VP 1" in Figure 4.2 and Figure 4.4), and the second spike can be roughly correlated with a second volcanic pulse because of its synchroneity with the ε_{Nd} positive excursion at Eastbourne (Figure 4.2 and Figure 4.4). Peak values ranging from ~-10 to -7 on Demerara Rise during OAE 2 may also suggest a volcanic origin, because local seawater $\varepsilon_{Nd}(t)$ values never exceeded ~-11 during most of the Cenomanian–Turonian interval (Figure 4.4), even during the mid-Cenomanian when increased influence of Tethyan/North Atlantic waters was thought to have affected local bottom waters repeatedly (Jiménez Berrocoso et al., 2010; Martin et al., 2012).

Martin et al., (2012) excluded volcanism as a cause for the ε_{Nd} positive excursion on Demerara Rise based on three arguments: (1) the onset of the ε_{Nd} positive excursion preceded anoxic conditions required for the dispersion of volcanic Nd, taking the $\delta^{13}C$ rise as an indicator of bottom water anoxia; (2) anoxic conditions

required for the transport of magmatic Nd on Demerara Rise were not persistent during the ε_{Nd} positive excursion; (3) volcanic Nd could have been removed during the re-precipitation of Fe–Mn oxides in suboxic/oxic waters. However, the possibility of a volcanic input may still stand. Firstly, the onset of the $\delta^{13}C$ rise does not necessarily indicate the beginning of bottom-water anoxia. Instead, the start of anoxia, at least locally, should have predated the global $\delta^{13}C$ rise (Jenkyns, 2010). Indeed, organic geochemical evidence does indicate that oxygen at Demerara Rise had already become depleted in bottom waters before the $\delta^{13}C$ rise (van Bentum et al., 2009); hence a volcanically derived positive ε_{Nd} excursion predating the $\delta^{13}C$ rise is possible. Secondly, the release of magmatic Nd depends on redox conditions at the volcanic source region, rather than where the signals are registered; therefore it is not surprising that high ε_{Nd} values could have persisted even when local redox conditions fluctuated on Demerara Rise. Thirdly, once the radiogenic Nd derived from volcanism had been sufficiently mixed into anoxic seawaters as a dissolved phase, rapid removal of REEs by co-precipitation with formation of Fe-Mn oxides, as observed within hydrothermal plumes in the modern ocean (e.g. Mitra et al., 1994), might no longer have existed. Presumably re-precipitation of Fe–Mn oxides in suboxic/oxic waters cannot preferentially remove all volcanic Nd; the volcanic signal, therefore, can be transported by ocean circulation.

If the interpretation of a volcanic input of Nd is correct, it is noteworthy that the second volcanic pulse was recorded at both Demerara Rise and Eastbourne. This coincidence in timing may imply efficient mixing between the tropical Atlantic and the mid-latitudinal NW European shelf sea, which permitted transport of volcanic Nd to both localities, or a common source for both watermasses. Interchange of water-masses during this interval is consistent with a coeval bottom-water re-oxygenation

event in the North Atlantic, which possibly implies enhanced seawater mixing (e.g. Friedrich et al., 2006; van Bentum et al., 2009; Jarvis et al., 2011). The initial volcanic pulse that occurred before the inferred climate cooling associated with possible changes in ocean circulation was only registered on Demerara Rise, and is absent from Eastbourne (VP 1, Figure 4.4). This difference can be tentatively explained by a lack of oceanic connection to transport volcanic Nd between the tropical Atlantic and the NW European shelf sea at the time. It can be suggested that a more geographically restricted pattern of ocean circulation changed to one with more extensive latitudinal transport, probably triggered by the cooling episode.

4.6 Conclusions

Several lines of evidence indicate that Nd isotopes of fish debris from Eastbourne chalk reflect bottom-water ε_{Nd}, rather than diagenetic artefacts. The ε_{Nd} values are steady at the onset of the $\delta^{13}C$ rise characteristic of OAE 2, suggesting a stable ocean circulation in the NW European shelf sea. Excursions to low and then high values occurred during OAE 2, and fall entirely in a transient cooling episode that probably resulted from a drawdown of atmospheric CO_2 due to enhanced organic-carbon burial and/or continental weathering. Different mechanisms are required to account for the ε_{Nd} excursions in opposite directions. Enhanced continental weathering or boundary exchange does not readily explain the initial ε_{Nd} negative excursion. Instead, a change in ocean circulation with increased influence of boreal seawater can best explain the observed decrease. This change in ocean circulation coincides with the onset of the cooling episode, strongly supporting previous hypotheses that predicted a cooling-induced change in circulation. The coincidence of the subsequent ε_{Nd} positive excursion and an inferred volcanic pulse

(VP 2) during OAE 2 suggests that the positive ε_{Nd} excursion at Eastbourne can be interpreted as due to transport of radiogenic Nd from a volcanic source, most likely the High Artic LIP via boreal seawaters, or the Caribbean LIP via other routes. This explanation does not require changes in patterns of ocean circulation at this time, but changes in ε_{Nd} values in end-member watermasses at the areas of origin.

The only other high-resolution ε_{Nd} records across OAE 2 are from Demerara Rise in the western tropical Atlantic where a positive ε_{Nd} excursion is also developed. An input of volcanic Nd may also explain this positive ε_{Nd} excursion. The excursion on Demerara Rise comprises two ε_{Nd} "spikes" that could correspond to two inferred volcanic pulses. The second, later spike is broadly synchronous with the ε_{Nd} positive excursion at Eastbourne, and both reach similar peak values of ~-7. These observations suggest either a common source of watermasses or water exchange between the tropical Atlantic and NW European shelf sea that permitted the transport of volcanic Nd between these two sites at this time.

Chapter 5

Transient reorganizations in ocean circulation during the mid-Cenomanian: Nd-isotope evidence from the NW European shelf sea

NOTE: *A revised version of this chapter, co-authored with Hugh C. Jenkyns, Andrew S. Gale, David J. Ward and Gideon M. Henderson, has been published in Geology, 44 (2016): 151–154 (http://dx.doi.org/10.1130/G37354.1). All authors contributed to sample collection in the field. David Ward helped to pick fish debris from bulk rocks. X-Y Zheng preformed all Nd-isotope/elemental analysis, and wrote the manuscript with inputs from all co-authors.*

Abstract

The mid-Cenomanian Event I (MCE I, ~95.8 Ma), characterized by a double-peak positive excursion in marine $\delta^{13}C$, was associated with prominent climatic, marine environmental and biotic changes. Although ocean circulation has been commonly hypothesized as an essential component in processes that led to these significant changes, detailed reconstructions of ocean circulation during this event remains sparse. In this study, changes in ocean circulation in the NW European shelf sea (English Chalk: Folkestone, southern UK) across MCE I were tracked with Nd isotopes. The new high-resolution ε_{Nd} record displays two rapid 1-unit negative ε_{Nd} excursions, dropping from background values of ~-9 to minimum values of ~-10, during MCE I, which are interpreted as due to transient reorganizations in ocean circulation with increased boreal influence in the bottom waters of the NW European shelf sea. The two ε_{Nd} negative excursions coincided with the intrusion of boreal faunas into the mid-latitudes during this time, providing the first direct evidence for a close association between circulation and southward spread of these characteristic faunas. A climatic control (i.e. cooling) can tentatively explain the inferred changes in ocean circulation. This new ε_{Nd} record, together with previous evidence, indicates that MCE I was associated with periods of general reorganization in ocean circulation, leading to enhanced nutrient availability in surface waters, and promoted organic carbon burial and the observed $\delta^{13}C$ positive excursion characteristic of this event. The absence of a ε_{Nd} positive excursion in the European shelf sea and tropical North Atlantic during MCE I is in sharp contrast to a previously reported ε_{Nd} positive excursion observed in both locations during OAE 2, suggesting either a volcanic origin of the ε_{Nd} positive excursion during OAE 2, or an unresolved mechanism responsible for different patterns of ocean circulation during these two events.

5.1 Introduction

The generally warm Cretaceous period witnessed a series of rapid (i.e. duration of several hundred thousand years) climate fluctuations associated with prominent marine environmental and biotic changes (e.g. Jenkyns, 2003a). Notable examples of such changes include oceanic anoxic event 2 (OAE 2), which occurred at the Cenomanian–Turonian boundary (~93.9 Ma, Meyers et al., 2012), and a preceding event named Mid-Cenomanian Event I (MCE I; ~95.8 Ma, Gale et al., 2008) (Figure 5.1). OAE 2 was associated with extensive bottom-ocean anoxia/euxinia, as evidenced by widespread deposition of organic-rich black shales and large extinction of benthic species (e.g. Kaiho and Hasegawa, 1994; Schlanger et al., 1987). This event is best signified by a positive excursion in marine $\delta^{13}C$ isotopes registered in coeval sections around the globe, suggesting globally enhanced organic-carbon burial (e.g. Jenkyns, 2010b). Prior to OAE 2, the MCE I, characterized by a double-peak $\delta^{13}C$ positive excursion with a smaller magnitude than that of OAE 2, has been widely observed in marine sections around the North Atlantic, Tethys and Boreal realm (e.g. Ando et al., 2009; Coccioni and Galeotti, 2003; Friedrich et al., 2009; Li et al., 2006; Paul et al., 1994; Voigt et al., 2004). MCE I was only associated with regional deoxygenation in the ocean, inferred by sporadic deposition of black shales and local changes in benthic foraminifera (Coccioni and Galeotti, 2003; Friedrich et al., 2009). Although the influence of MCE I as a rapid climatic/carbon-cycle event was not as significant as that of OAE 2, it represents the onset of a period of gradual evolution in the atmosphere–ocean system that led up to the abrupt global change at the Cenomanian–Turonian boundary. MCE I has hence been considered as a precursor of OAE 2 (Coccioni and Galeotti, 2003; Friedrich et al., 2009; Jarvis et al., 2006).

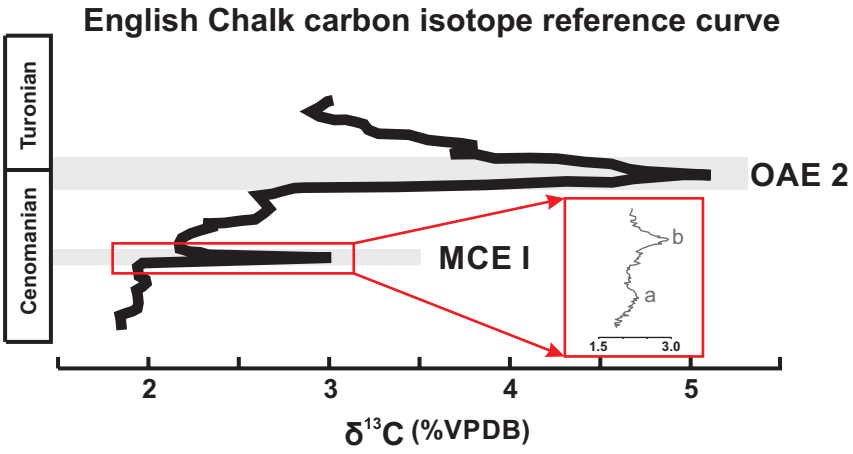

Figure 5.1 The carbon isotope reference curve from English Chalk (Jarvis et al., 2006), showing positive $\delta^{13}C$ excursions characteristic of MCE I and OAE 2. A close-up of the positive $\delta^{13}C$ excursions of MCE I show the double-peak feature (Paul et al., 1994).

Ocean circulation has been often invoked as an essential component in feedbacks that have driven these rapid climatic fluctuations and associated marine environmental/biotic changes during the Cretaceous (e.g. Friedrich et al., 2009; Voigt et al., 2004), due to its important role in distributing heat, nutrients and dissolved oxygen within the ocean (e.g. Hay, 2008). However, deconvolving the exact role of ocean circulation in relation to these changes is still hindered by the limited ability of most palaeoceanographic proxies to address this problem.

Nd isotopes have emerged as a promising tool to address the above question (e.g. Jiménez Berrocoso et al., 2010; MacLeod et al., 2008; Martin et al., 2012; Zheng et al., 2013). In the modern ocean, different watermasses are imprinted with ε_{Nd} values of surrounding continental rocks, and then can maintain their characteristic ε_{Nd} values along flow paths, which makes Nd isotopes a powerful tracer of ocean circulation (e.g. Frank, 2002). Fish debris (i.e. bioapatite) can normally record bottom-water ε_{Nd} values robustly, due to its rapid post-mortem scavenging of Nd from ambient seawater during early diagenesis on the seafloor (e.g. Martin and Scher, 2004).

High-resolution Nd-isotope records are sparse for the Cretaceous Period. A few studies, relying on high-resolution Nd-isotope records (MacLeod et al., 2008; Martin et al., 2012; Zheng et al., 2013), have attempted to reconstruct ocean circulation in the western tropical North Atlantic (Demerara Rise) and the NW European shelf sea (Eastbourne) during the OAE 2 interval (Figure 5.2 and Figure 5.3). These studies resulted in two intriguing observations. Firstly, an ε_{Nd}-inferred change in ocean circulation with stronger influence of boreal seawater in the NW European shelf sea has been found to be coincident with a transient cooling episode during OAE 2 (Zheng et al., 2013). This tight coupling between changes in ocean circulation and climate (i.e. pCO_2) was not expected from modelling results, which suggested an insensitive pattern of upper-ocean circulation to changes in atmospheric pCO_2 during the mid-Cretaceous (Poulsen et al., 2001). Secondly, the records from both localities show a rapid ε_{Nd} positive excursion during OAE 2, which has been interpreted as due to either a change in ocean circulation (Martin et al., 2012), or dispersion of radiogenic Nd introduced by an intense volcanic pulse under prevailing anoxic/euxinic conditions (Zheng et al., 2013). These observations give rise to two major questions: (1) whether the inferred change in ocean circulation, and its tight coupling with a cooling episode during OAE 2, is a unique phenomena only linked to this event; (2) how to interpret the observed ε_{Nd} positive excursion during OAE 2.

In this study, we investigated the evolution of seawater ε_{Nd} in the NW European Chalk shelf sea during MCE I, not only aiming to constrain variations of ocean circulation across MCE I in this area, but also to gain insights into the above two questions, raised by the high-resolution ε_{Nd} records from OAE 2. The two events are to some extent analogous, because both events are characterized by a marine $\delta^{13}C$ positive excursion, suggesting enhanced organic-carbon burial in some parts of the

globe, and were punctuated by short-lived southward migrations of boreal faunas, interpreted as indications of transient cooling episodes (e.g. Gale and Christensen, 1996; Paul et al., 1994). The absence of any evidence for major volcanic pulses during MCE I, in contrast to OAE 2, also permits a better understanding of the origin of the ε_{Nd} positive excursion observed in both NW European shelf sea and tropical North Atlantic during OAE 2 (MacLeod et al., 2008; Martin et al., 2012; Zheng et al., 2013).

5.2 Stratigraphic and palaeoceanographic background

The mid-Cenomanian chalk section exposed in Folkestone in southern England offers a thick (~11 m) sedimentary record with well-constrained litho-, bio- and cyclostratigraphy (e.g. Gale et al., 1999; Paul et al., 1994) (Figure 5.3), which greatly facilitates the high-resolution study of MCE I. Our samples were collected from the outcrop at Lydden Spout (51.103°N, 1.260°E). The section mainly consists of alternations of chalk–marl beds, variably rich in nannofossils and planktonic foraminifera (e.g. Paul et al., 1994). Rhythmic chalk–marl beds developed in basinal settings across Europe during the Cenomanian stage. Each alternation of chalk–marl bed (i.e. a couplet) was numbered in previous studies, and was considered to be controlled by the ~20 kyr-precession cycle (e.g. Gale et al., 1999). The section studied in this study is between couplets B33 and C8 (Figure 5.3). The expression of MCE I in this area can be recognized through a well-resolved double-peak $\delta^{13}C$ positive excursion, as previously demonstrated by a high-resolution $\delta^{13}C$ curve collected from the outcrop at Abbot's Cliff (Paul et al., 1994) (Figure 5.3), situated ~200 m away from our studied outcrop. Organic-matter contents are consistently low (<0.5 wt% TOC) with weak increases at the same stratigraphic levels containing the two peaks of

the $\delta^{13}C$ positive excursion of MCE I (Paul et al., 1994). The section comprises two discrete beds that enclose unusual faunas; the lower of these beds at the basal couplet B41, named the *arlesiensis* Bed, contains bivalves *L. (A.) arlesiensis* and *O. seminudum*, and the upper one, at the basal of couplet C1 and named the Cast Bed, contains the bivalve *O. seminudum* and belemnite *L. (A.) primus* (Paul et al., 1994). These faunas can be widely traced at the same stratigraphic levels in the Anglo–Paris Basin and other European basins (e.g. Paul et al., 1994; Wilmsen, 2003). The same or similar species appeared in Bed 4–6 of the Plenus Marls higher in the Chalk sequence of the NW European shelf sea. Because these faunas were demonstrated to have a boreal origin, thereby signifying the presence of relatively cold seawaters, their presence during OAE 2 around the Cenomanian–Turonian boundary interval represents a specific cold event, termed as the Plenus Cold Event (Gale and Christensen, 1996; Jefferies, 1962). The section was deposited in the shallow pelagic shelf sea of NW Europe, connecting the Boreal Sea to the north, Tethys to the south and North Atlantic to the west during the mid-Cenomanian (Figure 5.2).

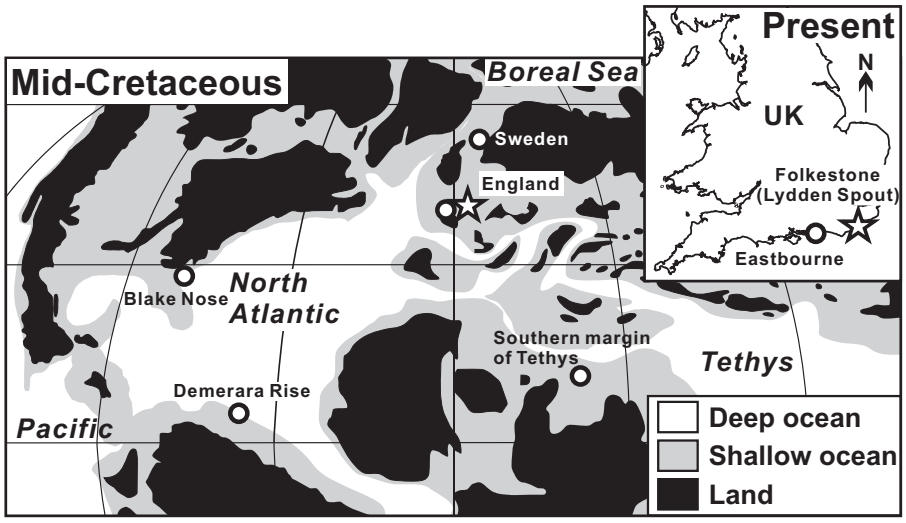

Figure 5.2 Palaeo-map shows sampling location of this study (Lydden Spout) and locations mentioned in the text.

5.3 Materials and methods

Two sets of bulk-chalk samples were collected from the Lydden Spout section. One set, intended for a high-resolution bulk-carbonate $\delta^{13}C$ curve, was collected by taking small samples (i.e. several grams each) every ~5 cm from the section, and the other one, intended for picking fish debris, comprised large samples (i.e. ~5-10 kg each) collected every ~50 cm from the section with stratigraphic thickness of individual samples <10 cm.

Extraction of fish debris followed a method described in Chapter 4. Briefly, bulk samples were dissolved with buffered formic acid to remove carbonate fractions, and fish debris was then handpicked from the de-carbonated residues. Fish debris was cleaned by a reductive–oxidative protocol to remove Fe-Mn oxides and attached fine clays (Boyle, 1981; Boyle and Keigwin, 1985; Rosenthal et al., 1997), followed by dissolution in 6 M HCl at ~120°C. Dissolved fish-debris samples were split into two aliquots for isotopic and elemental analysis.

Carbonate fractions of bulk chalk from several stratigraphic levels were also measured for Nd isotopes to increase temporal resolution of the ε_{Nd} record across MCE I. Large chunks of chalk (> 10 g) were ground into powder using an agate mortar and pestle. About 5 g of powder was leached using 10% (v/v) distilled acetic acid at room temperature for ~2 h before being centrifuged, and supernatant was then taken for elemental and Nd isotopic analysis. Bulk carbonate fractions were measured from 8 stratigraphic levels where fish debris was measured to test whether the two archives preserve the same Nd isotopes.

Rare-earth elements (REEs) of fish debris and bulk carbonate fractions were measured on an HR-ICP-MS (Element 2) with indium as an internal standard. Nd isotopes were measured on an MC-ICP-MS (Nu plasma) after purification of Nd with

a two-stage ion-exchange chromatographic separation. Further details on sample preparations and MS configurations are given in Zheng et al. (2013). Analytical precision for REEs, Nd isotopes and bulk-chalk $\delta^{13}C$ is < ~5% (1σ), ~0.3-ε_{Nd} (2σ) and ~0.1‰ (1σ) respectively. All ε_{Nd} values reported here were corrected for radiogenic in-growth of ^{143}Nd. The age model was based on cyclostratigraphy that considers each chalk–marl couplet to be controlled by a 20 kyr-precession cycle (e.g. Gale et al., 1999), and the base of the *C. inerme* Zone was tied to 96.50 Ma according to the Geological Time Scale (GTS) 2012 (Gradstein et al., 2012).

5.4 Results

The bulk-carbonate $\delta^{13}C$ results from the Lydden Spout section are presented in Table 5.1 (Appendix C), part of which were previously reported in Gale et al. (2008). The bulk-carbonate $\delta^{13}C$ record exhibits a ~0.6‰ positive excursion with two peaks, which permits the unambiguous placement of MCE I on a bed scale in the studied section (Figure 5.3). Bulk-carbonate $\delta^{13}C$ remained at relatively constant values of ~1.9‰ in the upper *M. dixoni* Zone during the lower Cenomanian, and then started to rise from the basal *C. inerme* Zone (the upper chalk–marl couplet B38) during the middle Cenomanian, gradually reaching peak values of ~2.4‰ at stratigraphic levels of the couplets B41–B42. From the upper couplet B42, $\delta^{13}C$ gradually decreased to values of ~2‰ towards the couplet B43, and then increased again from the base of couplet C1 until reaching peak values of ~2.5‰ in the upper couplet C1 and lower couplet C2. Finally, the $\delta^{13}C$ decreased from the upper couplet C2 upwards in section, and stabilized at values of ~2.2‰. The stratigraphic levels of major shifts in the $\delta^{13}C$ record at Lydden Spout, as described above, are consistent with those observed at the nearby outcrop at Abbot's Cliff (Paul et al., 1994) (Figure

5.3), although a slight offset in absolute $\delta^{13}C$ values exists between the two outcrops, presumably reflecting slightly different primary lithology of the two locations and/or local diagenetic effects.

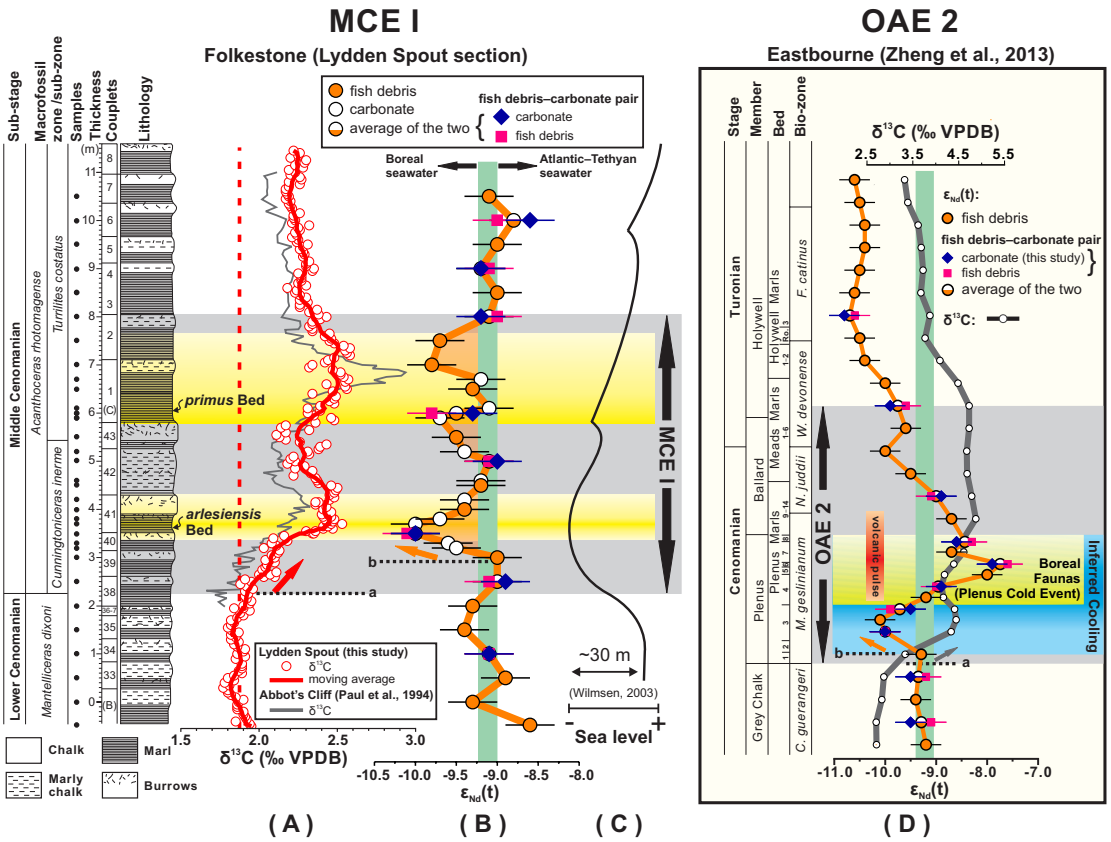

Figure 5.3 $\delta^{13}C$ and ε_{Nd} results plotted against the stratigraphic column of the Lydden Spout section across the MCE I interval. (A) red circles = bulk-carbonate $\delta^{13}C$; thick red line = 10-point moving average that brings out key features of the $\delta^{13}C$ record; vertical red dashed line = pre-MCE $\delta^{13}C$ values; gray line = carbonate $\delta^{13}C$ from nearby Abbot's Cliff (Paul et al., 1994); red arrow = the initial $\delta^{13}C$ rise of MCE I; gray band = MCE I, defined by a double-peak $\delta^{13}C$ positive excursion. (B) thick orange line = the composite ε_{Nd} curve, which comprises data from fish debris (orange circles), carbonates (open black circles), and mean values (half-filled orange circles) where paired εNd results (fish debris = pink squares; carbonates = blue diamonds) are available; green vertical bar = typical ε_{Nd} mid-Cretaceous background values; orange arrow = the onset of the first ε_{Nd} decrease. (C) black curve = sea-level reconstruction (Wilmsen, 2003). Graded yellow bands = levels of boreal faunas with darker yellow indicating the two faunal beds (the arlesiensis and primus Bed) where boreal faunas are abundant (Paul et al., 1994). (D) the ε_{Nd} record (orange) from the chalk section at Eastbourne across the OAE 2 interval (grey band), together with the $\delta^{13}C$ curve (grey), is shown for comparison (Zheng et al., 2013). Green vertical bar = pre-OAE ε_{Nd} values; red bar = an inferred volcanic pulse, coincident with the positive ε_{Nd} excursion; yellow band = levels of boreal faunas (the Plenus

Marl Beds 4–8; i.e. Plenus Cold Event); blue bar = a transient cooling phase inferred from combined geochemical and faunal evidence from the Eastbourne section (Chapter 4). Dashed lines “a” and “b” in (A) (B) and (D) mark the onset of the $\delta^{13}C$ positive excursion and the beginning of reorganization of circulation, respectively.

Nd-isotope results of fish debris and carbonate fractions of bulk samples are reported in Table 5.2 (Appendix C). Fish debris and carbonate fractions of bulk samples from the same stratigraphy levels show almost identical ε_{Nd} values (Figure 5.4), indicating that carbonate fractions also record bottom-water Nd-isotope compositions in the Chalk section at the studied section during the mid-Cenomanian.

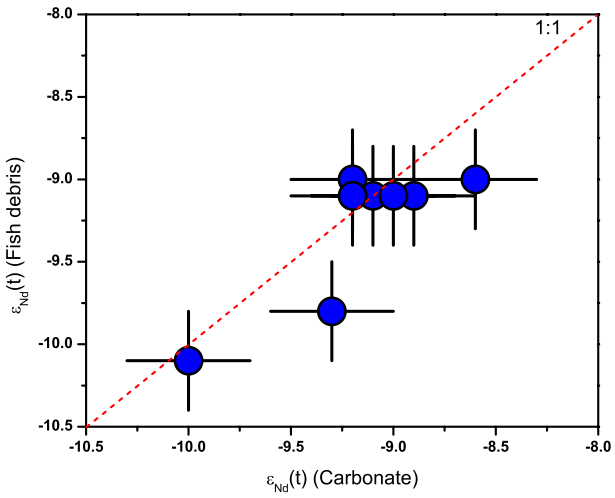

Figure 5.4 Comparison of ε_{Nd} results in fish debris and bulk-carbonate fractions from the same stratigraphic levels.

The ε_{Nd} record that is composed of Nd-isotope results obtained from both fish debris and bulk carbonate show background values of ~-9 before and after MCE I during the mid-Cenomanian. These background values are nearly identical to pre-OAE 2 values (Figure 5.3). Superimposed on this background, three resolvable negative excursions were observed during MCE I (Figure 5.3). ε_{Nd} is largely constant at the base of the sequence at values of ~-9 (Figure 5.3), followed by an abrupt ~1 ε-

unit negative excursion reaching values of ~-10 at the base of couplet B41, slightly before the first peak of the $\delta^{13}C$ positive excursion that is developed in the upper part of the same couplet. ε_{Nd} then recovers to background values of ~-9 from the upper couplet B41 towards the couplet B42, then displays another ~1 ε-unit negative excursion reaching a minimum value of ~-10 at the lower part of couplet C1. Again, minimum values of the ε_{Nd} negative excursion are registered before the $\delta^{13}C$ reached its second peak at the upper couplet C1. It appears that minimum values of the two negative ε_{Nd} excursions are not developed at the exact same stratigraphic levels as the two peaks in the $\delta^{13}C$ are observed, but coincide with the presence of distinct boreal faunas in the two marker beds, the *arlesiensis* Bed and Cast Bed, at basal couplet B41 and C1 respectively. Above minimum values of the second negative ε_{Nd} excursion in lower part of couplet C1, the ε_{Nd} record rapidly recovers to background values of ~-9 in upper couplet C1, and then decreases again, reaching minimum values of ~-10 at couplet C2, and then finally recovers to background values of ~-9 from couplet C3.

The results of rare earth element (REE) concentrations in fish debris are presented in Table 5.3 (Appendix C). Nd concentrations in fish debris are high, ranging ~60-3700 ppm. The shale-normalzied La/Sm ratios in fish debris from the Lydden Spout section range 0.5-0.8. The shale-normalized REE patterns of fish debris show a similar shape, which is characterized by small enrichments in middle REEs with weak Ce anomalies (Figure 5.5).

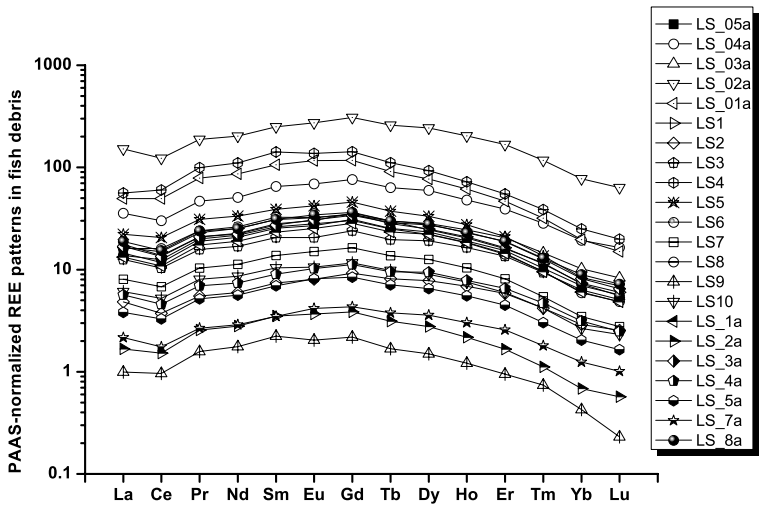

Figure 5.5 The REE-patterns of fish debris measured in this study

5.5 Discussion

5.5.1 Assessment of diagenetic effects on the ε_{Nd} record from Lydden Spout

The observed excursions in the ε_{Nd} record, defined by a composite of Nd-isotope data from both fish debris and bulk carbonate fractions from Lydden Spout, are unlikely to be caused by late diagenesis. For fish debris, firstly, its high Nd concentrations at Lydden Spout (mostly several hundred ppm, Table 5.3 in Appendix C), together with relatively low clay content (<20%) throughout the section (Paul et al., 1994), should have minimized the likelihood of diagenetic alteration of fish-debris ε_{Nd} values. This supposition is supported by the observations that changes in ε_{Nd} values do not co-vary with lithology, namely, the rhythmic alternations of relatively clay-rich marls and clay-poor chalks. Secondly, thermodynamic modelling has suggested that intense bioapatite–fluid exchanges during late diagenesis could decrease shale-normalized La/Sm ratios in fish debris to <0.3 (Reynard et al., 1999). All measured samples have La/Sm ratios >0.3 (i.e. 0.5-0.8) (Table 5.2 in Appendix C), which suggests that intense diagenetic effects can be precluded. Furthermore,

because detrital materials typically display relatively flat shale-normalized REE patterns (e.g. Charbonnier et al., 2012), severe diagenetic alterations due to REE-exchange with detrital materials are expected to shift REE-patterns of fish debris towards flatter shapes. However, all fish-debris samples show highly similar patterns with moderate enrichments in middle REEs and weak Ce anomalies (Figure 5.5), suggesting negligible exchange of REEs with detrital materials. For carbonate fractions, similar ε_{Nd} values obtained from this archive, compared to those retrieved from fish debris collected from the same stratigraphic levels, suggest that bulk carbonate can record pristine bottom-water Nd isotopes without significant post-burial alteration. The reason as to why carbonate fractions can reflect bottom-water signals is not entirely clear, but presumably it relates to the composition of chalk that is dominated by seawater-originated carbonates (i.e. calcareous nanofossil-rich carbonate), and comprises low detrital content (e.g. Paul et al., 1994). This composition leads to preservation of seawater Nd isotopes in carbonate fractions, and minimizes the likelihood of alteration of seawater ε_{Nd} values in carbonates due to detrital contamination after burial. Alternatively, Nd isotopes in leachates of bulk chalk may be dominated by Fe-Mn oxide fractions due to their high Nd concentrations with respect to carbonate fractions. A similar leaching approach as used by this study, which dissolves bulk sediments in acetic acids, has proven to be able to extract bottom-water Nd-isotope signals from Quaternary sediments with high non-carbonate content (30-40%) in previous studies (e.g. Gourlan et al., 2008), and this may be also the case for chalk samples used in this study. Nonetheless, given the above considerations, the ε_{Nd} record from Lydden Spout is considered to reflect seawater ε_{Nd} values, with no diagenetic overprint.

5.5.2 Interpretation of the ε_{Nd} record at Lydden Spout across MCE I

Although observations of the modern ocean have suggested that boundary exchange, involving seawater–sediment interactions, is an important process that may affect seawater ε_{Nd} signatures (e.g. Lacan and Jeandel, 2005b), the factors that control this process are still largely unknown, and, presumably, the composition of sediment plays an important role. Despite alternations of chalks and marls in the mid-Cenomanian interval, lithology does not change significantly throughout the studied section, including the two marker beds, so boundary exchange would be expected to have imposed relatively similar, or cyclic, effects on the ε_{Nd} record, rather than selectively affecting it only during the two specific periods when boreal faunas were migrating. Elevated continental weathering, which delivers more non-radiogenic Nd from surrounding Precambrian continents to seawater, may have resulted in a ε_{Nd} negative excursion in seawater, but enhanced continental weathering during MCE I is not supported by temperature reconstructions that show either a cooling (Huber et al., 2002; Voigt et al., 2004), or relatively constant temperatures (Ando et al., 2009; Forster et al., 2007a; Moriya et al., 2007) during this interval.

A change in patterns of ocean circulation in the NW European shelf sea can explain the observed ε_{Nd} negative excursions during MCE I. Water masses that may affect the studied site during the mid-Cenomanian include the through-flow connecting the Tethys and North Atlantic, and flows from the Boreal Sea via the Norwegian seaway (Figure 5.2). However, accurate constraints on ε_{Nd} values of these potential end-member watermasses during the mid-Cenomanian are yet not known and geographical ε_{Nd} data for this period are sparse. Around the Cenomanian–Turonian boundary, Tethys–Atlantic through-flow was probably characterized by ε_{Nd} values of ~-6 to -4 (Bourbon, 2008; Martin et al., 2012; Soudry et al., 2006). This

possibly reflects advection of Pacific seawater with high ε_{Nd} values (>~-6, Murphy and Thomas, 2012) at low- and mid-latitudes, where no geographic barrier, at least at shallow-water depths, was present during the Cretaceous (Pucéat et al., 2005). Because major tropical seaways were open during the mid-Cenomanian, relatively high ε_{Nd} values of the Tethys–Atlantic through-flow may have persisted during this interval. This suggestion is supported by low-resolution shallow-water (<1000 m) ε_{Nd} values between ~-3 and -6 observed at Blake Nose in the mid-latitudinal North Atlantic throughout the Cenomanian interval (Bourbon, 2008; Martin et al., 2012). Although shallow-water ε_{Nd} at the "southern margin of Tethys" reportedly remained at low values of ~-11 from the Hauterivian to the mid-Cenomanian (Soudry et al., 2006), nearly all measured samples for this interval in that study were actually collected further north in the NW European shelf seas, so they may not represent seawater ε_{Nd} values in the low-latitude Tethys. In contrast to the Tethys–Atlantic through-flow, boreal seawater probably had relatively low ε_{Nd} values, because of introduction of weathered materials from surrounding continents characterized by extremely low ε_{Nd} values (i.e. ~ -17 to -30, Jeandel et al., 2007). The only existing data point from the Boreal realm comes from the Sweden has an ε_{Nd} value of ~-17, supporting the non-radiogenic nature of boreal seawater during at least part of the Cretaceous (Pucéat et al., 2005). Assuming the above constraints imposed on the potential end-member water masses are correct for the mid-Cenomanian interval, the ε_{Nd} values observed in the NW European shelf sea can be explained as due to mixing of the two end-member watermasses. The observed two negative ε_{Nd} excursions across MCE I, therefore, reflect transient increased influence of boreal seawater from the north in the NW European shelf sea. This interpretation is consistent with the

cold-water fauna observed at the same stratigraphic levels as the negative ε_{Nd} excursions.

5.5.3 Implications of the ε_{Nd} record from Lydden Spout

The coincidence between the two ε_{Nd} negative excursions and the presence of boreal faunas in two discrete beds at Lydden Spout during MCE I is striking. The southward migration of boreal faunas to the NW European shelf sea has long been considered as an indication of relatively cool seawater in the context of general Cretaceous warmth (e.g. Gale and Christensen, 1996; Jefferies, 1962), but the faunal evidence alone does not distinguish whether their migration to the south was caused by an overall cooling in the global ocean without any change in circulation patterns, or by the local intrusion of relatively cold boreal seawater to the mid-latitudes, or by a combination of the two processes. Although our ε_{Nd} record at Lydden Spout does not invalidate the first process, it confirms that the migrations of boreal index faunas were accompanied by physical changes in circulation patterns with stronger influence of boreal seawater in the NW European shelf sea during MCE I.

Incursion of the same, or similar, boreal faunas to the NW European shelf sea is also seen during OAE 2 (i.e. Plenus Cold Event, see Chapter 4), and seems to be closely associated with a period of reorganization in ocean circulation, supported by a high-resolution ε_{Nd} record obtained from Eastbourne across OAE 2 (Zheng et al., 2013), and other evidence from the North Atlantic (e.g. Friedrich et al., 2006; van Bentum et al., 2009). In contrast to the coincidence between the boreal faunas and ε_{Nd} negative excursions found during MCE I, the presence of boreal faunas was synchronous with a ε_{Nd} positive excursion in seawater during OAE 2 at Eastbourne, immediately following a nearly identical 1-unit ε_{Nd} negative excursion reaching

values of ~ -10 (Zheng et al., 2013). Because the ε_{Nd} positive excursion can be explained as an overprint of seawater ε_{Nd} values by a volcanic pulse during OAE 2 (Zheng et al., 2013), it is possible that the preceding ε_{Nd} negative excursion would have persisted into the levels containing boreal faunas if volcanism had not taken place. If this were the case, the Plenus Cold Event during OAE 2 was also associated with increased influence of boreal seawater in the NW European shelf sea, similar to the processes that occurred during MCE I.

The driving forces for the circulation changes during MCE I are uncertain, compared to the evidence showing the reorganization in ocean circulation. Modelling results suggest that upper-ocean circulation was sensitive to tectonically induced changes in palaeogeography during the mid-Cretaceous (Poulsen et al., 1998b), but tectonic movements, which are unusually slow and irreversible, are difficult to reconcile with the two rapid and reversible ε_{Nd} negative excursions. Similarly, sea-level changes have also been proposed to have affected ocean circulation during the mid-Cenomanian (Mitchell and Carr, 1998; Poulsen et al., 1998b), but the stepwise transgression from deposition of the base of couplet B41 upsection does not seem to provide a viable forcing factor that could lead to the two short-lived changes in ocean circulation (Figure 5.3).

The recurrent association between a reorganization in ocean circulation, marked by shifts in seawater ε_{Nd}, and migrations of boreal faunas during both MCE I and OAE 2 may suggest a common driving force (Figure 5.3). For OAE 2, the synchroneity of the ε_{Nd}-inferred circulation change, and an inferred atmospheric pCO_2 drop, probably resulted from enhanced organic carbon burial and continental weathering (e.g. Arthur et al., 1988; Blättler et al., 2011; Pogge von Strandmann et al., 2013). This implies that climatic cooling drove circulation changes during OAE 2

(Zheng et al., 2013). This inference is consistent with previous conjectures that an increased latitudinal thermal gradient resulted from the transient cooling during OAE 2 would have caused instability in the ocean, leading to reorganization of ocean circulation (Forster et al., 2007b; Sinninghe Damsté et al., 2010). In principle, similar mechanisms may have operated during MCE I to drive changes in ocean circulation, because the event was also associated with enhanced organic carbon burial, evidenced by the positive $\delta^{13}C$ excursion, which may have caused a transient cooling through sequestrating CO_2 from the atmosphere.

However, this climatic control on ocean circulation during MCE I is tentative, as the causes and consequences of MCE I are less well-understood than the extensively studied OAE 2 interval. A transient cooling episode during MCE I has been proposed, based on evidence of boreal faunal migrations (Paul et al., 1994), and marine $\delta^{18}O$ records from the North Atlantic and European sections (Huber et al., 2002; Stoll and Schrag, 2000; Voigt et al., 2004). However, contradictory evidence based on $\delta^{18}O$ and TEX_{86} suggest relatively stable temperatures across MCE I (Ando et al., 2009; Forster et al., 2007a; Moriya et al., 2007). Further studies are required to constrain the factors that drove MCE I, before a firm conclusion on the cause of a circulation change can be drawn.

Regardless of the driving forces, it is noted that evidence of changes in ocean circulation has also been found in other parts of the ocean during MCE I. Enhanced upwelling or downwelling has been inferred over Blake Nose in the North Atlantic, based on the observation of a reduced planktonic–benthic gradient in foraminiferal $\delta^{13}C$ (Ando et al., 2009). A change in ocean circulation on Demerara Rise in the western tropical North Atlantic has been inferred based on regional changes in seawater ε_{Nd} (Jiménez Berrocoso et al., 2010). Together with the new Nd-isotope

evidence, it seems that MCE I was accompanied by periods of general reorganization in ocean circulation that favoured intensified ventilation and vertical mixing over large areas in the North Atlantic and adjacent shelf seas. These circulation changes may have led to increased nutrient availability in the upper ocean, which may have, at least partly, promoted the development of $\delta^{13}C$ positive excursion through increasing primary production and subsequent enhanced deposition of organic matter.

A ε_{Nd} positive excursion reaching values of ~ -7, immediately following an ε_{Nd} negative excursion, was observed at Eastbourne in the NW European shelf sea during OAE 2 (Zheng et al., 2013). This ε_{Nd} positive excursion was also registered on Demerara Rise in the western tropical North Atlantic, and was explained as either due to a change in ocean circulation (Martin et al., 2012), or dispersion of volcanism-induced radiogenic Nd under anoxic conditions (Zheng et al., 2013). Because MCE I was associated with climatic/environmental changes similar to those associated with OAE 2, but with no evidence for major volcanic pulses such as that which punctuated OAE 2 (e.g. Snow et al., 2005; Turgeon and Creaser, 2008), it is expected that the NW European shelf sea would have undergone similar changes in ocean circulation during MCE I. Such changes would have led to local registration of ε_{Nd} records with similar variations to those registered during OAE 2, if the inferred volcanic pulses around the Cenomanian–Turonian time did not affect seawater ε_{Nd}. The nearly identical ε_{Nd} negative excursions closely associated with the presence of boreal faunas in the NW European shelf sea during both events partly suggests analogous behaviour of ocean circulation in this region during the two events. In contrast to the ε_{Nd} negative excursions, no ε_{Nd} positive excursion was observed in the NW European shelf sea during MCE I. Similarly, no ε_{Nd} positive excursion was observed on Demerara Rise in the equatorial western North Atlantic during MCE I (Jiménez

Berrocoso et al., 2010). The absence of ε_{Nd} positive excursions during MCE I could suggest either that the ε_{Nd} positive excursions observed during OAE 2 had a volcanic origin, as argued by Zheng et al. (2013), or that there are unresolved mechanisms responsible for the different behaviour in ocean circulation during the two events.

5.6 Conclusions

The high-resolution ε_{Nd} record from Lydden Spout in the NW European shelf sea exhibits three negative excursions across MCE I, two of which coincide with southward migration of boreal faunas. The ε_{Nd} excursions are interpreted as due to increased influence of boreal seawater in the NW European shelf sea, and provide the first direct evidence for changes in ocean circulation during MCE 1, with the invasion of boreal faunas into more southerly latitudes. The reorganization of ocean circulation during MCE I is tentatively explained as due to a climatic cooling that affected the ocean and wind system. Similar observations of changes in seawater ε_{Nd} in this area during OAE 2 (Zheng et al., 2013) support a relationship between circulation change and the cooling. Together with other evidence from the North Atlantic and Tethys, the ε_{Nd} record suggests that MCE I was associated with periods of general reorganization in ocean circulation, which may have led to the enhanced nutrient availability in surface waters during the event. The absence of a ε_{Nd} positive excursion in the European shelf sea and tropical North Atlantic during MCE I – a period with similar climatic and environmental changes to those during OAE 2, but probably weaker volcanism – is in contrast to a prominent ε_{Nd} positive excursion observed in both locations during OAE 2. These relationships are consistent with a volcanic origin of the ε_{Nd} positive excursion during OAE 2.

Chapter 6

Summary and outlook

6.1 Summary of this thesis

A new analytical protocol was developed to enable highly precise and accurate determination of seawater REE concentrations, using only relatively small (~100 ml) samples. The method was successfully applied to measure dissolved REE concentrations from a full-depth transect in the tropical South Atlantic along ~12°S. This new set of dissolved REE concentration data significantly fill the gap in study of the REE cycling in the South Atlantic and, for the first time, allows systematic investigation of all *d*REEs on the basis of an oceanographic section. Hydrographic and non-hydrographic controls on the distribution of *d*REE concentrations in the tropical South Atlantic were studied quantitatively using an inverse model. Our results suggest a large hydrographic control (>80%) on the distribution of dissolved REE concentrations. Addition of *d*REEs in the deep Angola Basin (>1000 m) is apparent at two water depths, namely ~1500 m and >~4000 m, near the continental margin of Africa. The shallower *d*REE addition may result from advected metal-rich waters from reducing sediments on the margin, and the deeper addition is more likely to be caused by remineralization of particles *in-situ* in the water column, or in bottom sediments. Ce shows intriguing features from the section. Ce concentrations (and Ce anomalies) in surface waters are possibly controlled by a dynamic balance between O_2-dependent Ce oxidation and a REE-input effect. At depth (~1500 m), a prominent decoupling of the marine cycling in Ce and Mn was observed, although the cause of this phenomenon remains unknown.

Reconstruction of ocean circulation with Nd isotopes preserved in fossil fish debris from the English chalk during two rapid climatic events, the mid-Cenomanian Event at the middle Cenomanian and oceanic anoxic event 2 (OAE 2) at the Cenomanian–Turonian boundary, indicates a coupling of changes in ocean circulation and transient climate cooling in both cases. An advected volcanic signal during OAE 2, probably from either the High Arctic large igneous province (LIP) or the Caribbean LIP, was captured by the Nd-isotope record from the NW European shelf sea, probably suggesting a period with enhanced ocean ventilation/mixing during a transient cooling episode within OAE 2.

6.2 Implications of cycling of REEs in the modern ocean to palaeo-studies

The observations of dissolved REEs along the CoFeMUG section (Chapter 3) have three major implications to the study of past oceans that uses REEs and their isotopes to trace varied marine processes, including reconstructions of ocean circulation during the Cretaceous using Nd isotopes (Chapter 4 and 5).

Firstly, addition of REEs near continental margins (or boundary exchange) is an important process that must be considered when interpreting Nd-isotope records, especially in an oceanic basin where ocean circulation is relatively sluggish, because changes in seawater Nd isotopes may be affected by this process without any change in circulation patterns. This is particular the case for the Cretaceous when many available marine records were retrieved from relatively shallow marginal seas, and ocean circulation may be sluggish. Secondly, seawater REEs scavenged by Fe-Mn oxides indeed become remobilized under low oxygen conditions (i.e. OMZ), and are released back to seawater. This observation supports the assumption made in Chapter 4, which assumed that LIP-induced Nd may be liberated into seawater due to

destabilization of Fe-Mn oxides under anoxic conditions during anoxic events. Thirdly, Ce anomaly in seawater is controlled by both input and dissolved oxygen content, so reconstructions of seawater redox history using Ce anomaly should consider the possible input effect. In addition, redox of Ce in seawater does not necessarily occur only under anoxic conditions, but can also occur under suboxic conditions that may contain dissolved O_2 as high as 25 μM.

6.3 Future directions

The methodology and results of this thesis open doors to many possible directions for future research. For the study of the cycling of REEs in modern seawater, a natural extension of this thesis is to couple data from other trace metals, such as Fe and Mn, from the CoFeMUG section into the inverse model. This would allow a quantitative examination of the relationship of *d*REE regeneration, together with *d*Fe (and *d*Mn) regeneration throughout the water column, providing an opportunity to explore inter-elemental connections of trace-metal cycling in the ocean. Several difficulties exist for implementation of this idea. Firstly, there are fewer tracer data available to accommodate additional unknowns in the model. This difficulty can be alleviated by addition of O_2 data into the analysis. Although dissolved O_2 data are missing from several depths at a few stations across the CoFeMUG section, substitutes can be taken from historical hydrographic datasets, such as WOA-09. However, potential model bias resulting from the discrepancies between historical O_2 data and *in-situ* measurements would need to be evaluated. Secondly, definition of characteristic values of *d*Fe and *d*Mn in end-member watermasses may prove difficult, because of the active involvement of the two elements in local biogeochemical cycles.

Another direction for research of immediate interest is the fate of additional *d*REEs that are released into seawater in the Angola Basin. It has been found that the unique signal of water-column Nd isotopes in the Angola Basin does not seem to extend to other basins in the Atlantic (Rickli et al., 2009), suggesting a process that acts locally to confine and/or remove the Nd excess in the Angola Basin. Such a mechanism is not understood yet. In addition, the prominent decoupling of Ce and Mn in their cycling at a water-depth of ~1500 m near the Angolan margin merits further exploration. Detailed geochemical work of the sediments is required, if the addition of metals at this depth in this basin is indeed due to a sedimentary source.

The study of dissolved REE distribution on a full-depth oceanic section collected during the CoFeMUG cruise highlights the advantage of using such an approach in studying distributions of trace metals in the ocean. This section approach is currently implemented in the ongoing GEOTRACES programme, which seeks to study the cycling of a suite of trace metals and isotopes, including REEs and Nd isotopes, in the global ocean. Among planned sections that have been sampled, two sections of particular interest to this study are: the US GEOTRACES section in the North Atlantic and the UK GEOTRACES section in the south Atlantic. Measurement of dissolved REE concentrations across the UK GEOTRACES section is close to complete at Oxford, and similar datasets are also expected to come out soon for the US GEOTRACES section. The modelling developed in this thesis can potentially be applied to REE datasets from these two sections, and the results would then provide information on meridional variations in non-conservative terms of *d*REEs along major circulation flow-paths in the Atlantic.

For the study of the Cretaceous ocean and climate, more Nd-isotope data are needed to give a fuller picture of the general distribution of Nd isotopes in different

parts of the Cretaceous ocean, and secular changes in their distribution with time. As demonstrated by the two case studies in this thesis, a tight coupling existed between shallow ocean circulation and climate forcing during rapid climatic events during the Cretaceous. The underlying mechanism of this coupling requires further investigations. Recent developments in regional circulation models for the Cretaceous would be of particular interest (Topper et al., 2011), because they provide an approach to test the effect of various forcing (e.g. CO_2, tectonic) on ocean circulation and associated tracer distributions at a regional scale. Attempts to reproduce the observed circulation–climate coupling in the NW European shelf sea, based on the Nd-isotope evidence presented in this thesis, with these new models would advance current understanding of ocean–climate feedbacks during the Cretaceous.

Appendix A

The Method of Nd-isotope analysis

This section gives details on the cleaning and dissolution protocol for fish debris, the procedure that was developed to measure Nd isotopes during the course of relevant projects reported in this thesis, and validation of the Nd-isotope analysis with respect to precision and accuracy. Nd-isotope results of several reference materials, including JNdi-1, BCR-1, BHVO-2 and a fish-bone composite, are also reported here for the purpose of inter-laboratory calibration.

A.1 Cleaning protocol for fish debris and sample dissolution

All fish-debris samples were cleaned with a reductive–oxidative cleaning protocol, based on Boyle, (1981), Boyle and Keigwin (1985) and Rosenthal et al. (1997), to remove attached clays and Fe-Mn oxides before sample dissolution.

Fish-debris samples, typically several to hundreds of mg, were put in 2 ml centrifuge tubes during the cleaning. Firstly, fish debris was alternately cleaned with Milli-Q water (×3 times) and methanol (×2 times) in an ultrasonic bath for ~2 min at each step to remove fine clay grains adhering to the surface of samples. Secondly, samples were soaked in a reductive solution, which was made by mixing 240 mg citric acid crystal, 625 µl 31 M hydrous hydrazine and 10 ml ammonium solution, in a hot water bath at ~80°C for ~30 min to remove Fe-Mn oxide coatings. Centrifuge tubes containing samples were ultrasounded in an ultrasonic bath every ~5 min for a duration of ~1 min each time, and then put back in the hot water bath. Samples were rinsed with Milli-Q water after the reductive cleaning step. Thirdly, fish-debris

samples were cleaned by an oxidative solution, which was made by mixing 30 ml of 0.1 M NaOH with 300 µl of ~30% (v/v) H_2O_2, in a hot water bath at ~80°C for ~20 min, and ultrasounded for a duration of ~1 min every 5 min. Samples were rinsed with Milli-Q water after the oxidative cleaning step, and then cleaned by 0.003 M distilled HNO_3 in an ultrasonic bath for ~5 min to remove any re-adsorbed ions. Finally, samples were rinsed with Milli-Q water before dissolution.

Cleaned fish-debris samples were weighed, and dissolved in 6 M HCl at ~120°C for >12 h. Most of samples were dissolved quickly (normally within half an hour). For samples that did not dissolve completely in 6 M HCl after 2 h, aqua regia was added to destroy organic matter to ensure complete dissolution. Samples dissolved with aqua regia were dried down after complete dissolution, and converted to chloride form by re-dissolution with 6 M HCl. All samples were then dried down, and dissolved in 3 M HCl. Small aliquots were taken from the final solution for the elemental analysis, and the remaining solution was ready for the subsequent separation of Nd.

A.2 Column chemistry for Nd separation

A two-stage ion-exchange chromatographic separation (i.e. column chemistry) was set-up to separate Nd from interfering matrix before isotopic analysis on a multi-collector ICP-MS (Nu plasma). The first stage separated rare earth element (REEs) as a group from major cations using AG 50W–X12 resin (Bio-Rad®, 200-400 mesh, hydrogen form) with quartz-distilled HCl as an eluent, and the second stage separated Nd from other REEs using AG 50X–X4 resin (Bio-Rad®, 200-400 mesh, ammonium form) with α–hydroxyisobutyric acid (α–HIBA) as en eluent.

A.2.1 α–Hydroxyisobutyric acid (α–HIBA) preparation

α–HIBA crystal was purchased from Sigma-Aldrich (Aldrich®, 99%, product NO.: 323594-100G). α–HIBA of ~100 g was first dissolved in ~300 ml Milli-Q water (18 MΩ), and then passed through a big column with an AG 50W–X4 (Bio-Rad®, 200–400 mesh, hydrogen form) resin bed (~4 cm long × 1.5 cm diameter) to remove any particulate impurities. The resulting solution was then diluted to ~1400 ml with Milli-Q water, and sequentially passed through two columns, each of which was filled with an AG 50W–X4 (Bio-Rad®, 200–400 mesh, hydrogen form) resin bed (~8 cm long × 1.5 cm diameter), to remove REEs and other cation impurities. The molarity of solution after column purification was determined by titration against a NaOH standard solution (Normadose™), and the solution was then buffered to a pH of 4.7 with aqueous ammonia solution (BDH Aristar®, ~25% NH_3). The pH of the solution was determined with a clean pH meter. The volume of the solution after buffering was measured by an acid-cleaned 2L measuring cylinder. From the molarity determined by titration and the volume measured by the measuring cylinder, two stock α–HIBA solutions with concentrations of 0.15 M and 0.225 M respectively were prepared by diluting with Milli-Q water. Variations in pH during final dilution were negligible, and both stock solutions had pH values between 4.7 and 4.8.

A.2.2 Specifications of columns

The first-stage separation used a commercially available Bio-Rad® polypropylene column with a resin-bed volume of 2 ml and a sample volume of 10 ml. The second-stage separation used a homemade quartz column that was constructed from a 30 cm long × 0.3 inner diameter glass tubing, with a porous

polyethylene frit tightly installed immediately above the drip tip at one end, and a 10 ml glass reservoir fused to the other end.

A.2.3 AG 50X–X4 resin conversion

The Bio-Rad® AG 50X–X4 (200-400 mesh, hydrogen form) resin needed to be converted to the ammonium form before used for the second-stage column separation. New resin was repeatedly cleaned, in a batch, with alternating 3 M HCl, 6 M HCl and Milli-Q water in a bottle before the conversion. The resin conversion was achieved by eluting the resin in a big column with ammonium solution (BDH Aristar®, ~8-10 M) until the eluate became alkaline, as checked with pH papers. The converted resin was then washed with Milli-Q water until the eluate became neutral, and finally equilibrated with 0.15 M α–HIBA solution before being stored in 0.15 M α–HIBA in an acid-cleaned polypropylene bottle.

A.2.4 Column calibration and the final recipe of column-separation for Nd

The first set of columns was calibrated with an artificially prepared solution that contained elements of prime interest for our study (e.g. Ca, Sr, Rb, Fe, Ba and REEs) with concentrations similar to those in fossil fish teeth, and a Cretaceous fish-tooth sample to determine elution curves. Two-millilitre AG 50W–X4 resin (Bio-Rad®, 200–400 mesh, hydrogen form) was loaded into each column at the beginning of the separation, and then preconditioned with 5 ml 3 M distilled HCl. One-millilitre of the artificial solution and the dissolved fish-tooth solution, both in 3 M HCl, was then put onto the resin beds. The resin was then eluted with 30 ml 3 M HCl, and the eluate was collected in a series of 1.5 ml aliquots. After 3 M HCl in columns dripped out, 21 ml 6 M HCl was added into each column to further elute the resin. Again, the

eluate was collected in aliquots of 1.5 ml. The collected eluate was measured on a HR-ICP-MS (Element 2) to determine relative elemental concentrations. The elution curves for both the artificial solution and real fish-tooth sample were found to be similar, and illustrated in Figure A.1.

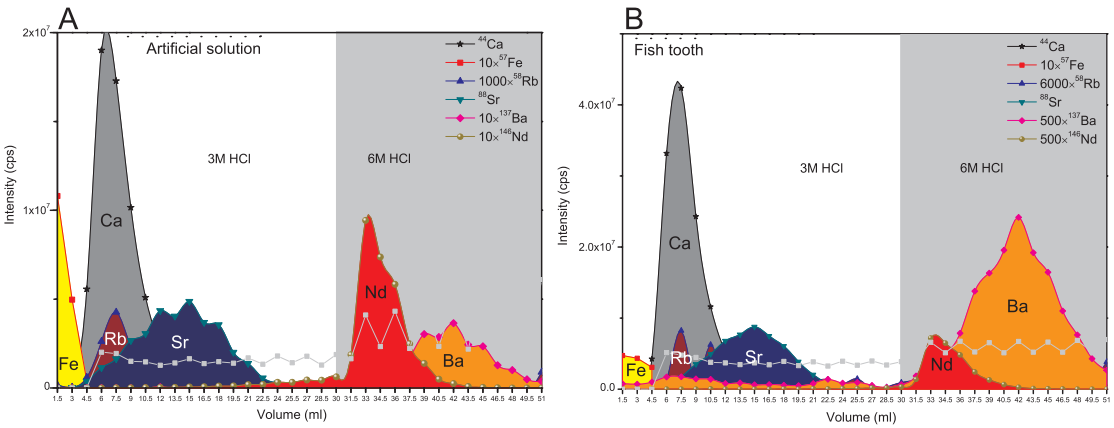

Figure A.1 Calibration results for the first set of columns using both an artificial solution (A) and a real fish-tooth sample (B). By selecting only the portion of eluate from 30ml to 40ml, Nd can be separated from Fe, Ca, Sr, Rb and part of Ba. Note that the Fe curve after 4.5ml is plotted in light grey because the Fe signal suffered interference. Most of the Fe is believed to be eluted within the first 4.5ml as indicated by the gradually fading of the yellow colour of the eluents. Intensities of different elements have been amplified appropriately in order to put them in the same panel.

The second set of columns was calibrated with another artificially prepared solution that contained all naturally occurring REEs, and the combined fish-tooth REE-cut that was collected during the calibration of the first set of columns. AG 50X–X4 resin in ammonium form was added into the resin-bed tubing of the second column until it reached the height of ~28 cm from the frit, and then preconditioned with 200 µl Milli-Q water. The artificial solution and the fish-tooth solution of 400 µl, both in 0.1 M HCl, was then loaded onto the resin beds. A further 200 µl Milli-Q water was added into the columns, and the eluate was collected. The resin beds were then eluted with 3 ml 0.15 M α–HIBA, and the eluate was collected in 0.5 ml aliquots.

After 0.15 M α–HIBA in columns dripped out, 8 ml of 0.225 M α–HIBA was added into columns, and the eluate was collected in 0.4 ml aliquots. The collected eluate was measured on a HR-ICP-MS (Element 2) to determine relative elemental concentrations. The elution curves for the second column were illustrated in Figure A.2, which shows a good separation between Nd and Sm, the major interfering element, for both the artificial solution and fish-tooth sample. Ce and La, both of which were not collected in the eluate during our calibration, should be still bound with the resin, because the sequence of REEs eluted from the resin by our method was generally in a reverse order from Lu to La.

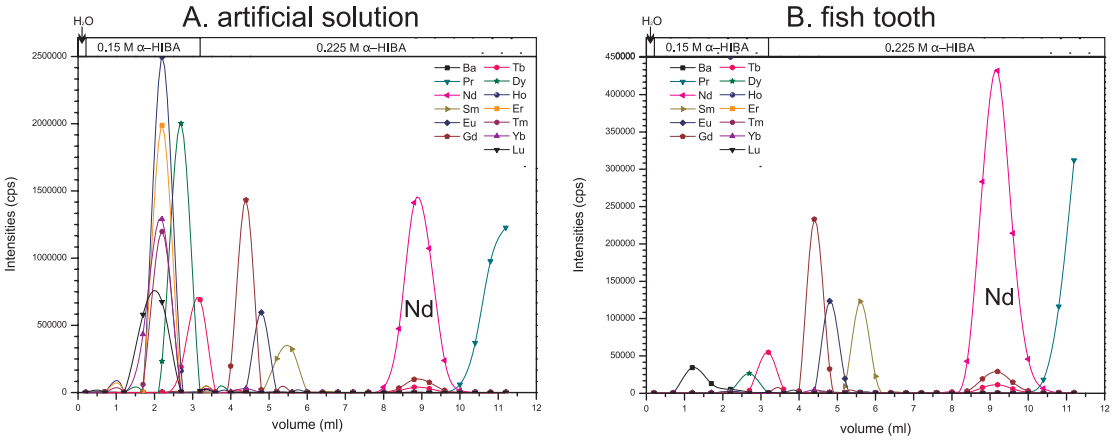

Figure A.2 Calibration results for the second set of columns using both an artificial solution (A) and a real fish-tooth sample (B).

Based on the results of our column calibrations, the final recipe of the two-stage ion-exchange chromatographic separation for Nd is given in Table A.1. This recipe was adopted throughout the relevant projects reported in this thesis.

Table A.1

Recipe for Nd-isotope column chemistry

Step	Reagent/Condition	Volume
1st column		
Resin loading	Bio-Rad AG50W-X12 (200-400 mesh, H form)	2 ml
Pre-condition	3M HCl	5 ml
Sample loading	sample in 3M HCl	1 ml
Elute	3M HCl (30ml in total)	1 ml
		1 ml
		1 ml
		2 ml
		5 ml
		5 ml
		5 ml
		5 ml
		5 ml
Collect REEs	6M HCl (12 ml in total)	4 ml
		4 ml
		4 ml
Dry down	150℃	
2nd column		
Resin loading	Bio-Rad AG50W-X4 (200-400 mesh, NH4+ form)	
Pre-condition	Milli-Q	200 µl
Sample loading	sample 0.1M HCl	400 µl
Elute	Milli-Q	200 µl
	0.15M α–HIBA	3 ml
	0.225M α–HIBA	1.6 ml
		1.6 ml
		1.6 ml
Collect Nd	0.225M α–HIBA	2.4 ml
Dry down	150℃	
Re-dissolution	concentrated HNO_3 + HCl	~100 µl
Dry down	150℃	

A.3 Instrumental configurations and acquisition of Nd-isotope data

Nd isotopes were measured on a MC-ICP-MS (Nu plasma), connected with a DSN–100 desolvating nebuliser system, in the Department of Earth Sciences, University of Oxford. The design of the instrument has been described in detail in the

literature (e.g. Belshaw et al., 1998). The configuration of Faraday collectors and isotopes selected for the Nd-isotope measurement were summarised in Table A.2. Data acquisition of each measurement took ~6 min with a sample uptake rate of 100 μl/min, and ~60-120 ng Nd was required for each measurement that comprised one-hundred5-s integrations. Mass bias was corrected by using $^{146}Nd/^{144}Nd = 0.7219$ with an exponential law.

Although a previous study suggested that normalization with the $^{145}Nd/^{142}Nd$ ratio could provide better results of corrected $^{143}Nd/^{144}Nd$ ratios in terms of precision and accuracy compared to those obtained with the $^{146}Nd/^{144}Nd$-normalization (Vance and Thirlwall, 2002), the use of the two normalization schemes was found to have resulted in negligible difference on the corrected $^{143}Nd/^{144}Nd$ ratios during this study.

An in-house Nd-isotope standard, which was made of an Aldrich® Nd standard solution (2002), was measured during the method set-up stage, and yielded $^{143}Nd/^{144}Nd = 0.512136 \pm 0.000016$ (2σ, n = 60). Two international Nd-isotope standards, La Jolla and JNdi-1, were used in subsequent measurement on samples. Repeated analysis of the La Jolla standard yielded $^{143}Nd/^{144}Nd = 0.511846 \pm 0.000015$ (2σ, n = 103), and repeated analysis of the JNdi-1 standard yielded $^{143}Nd/^{144}Nd = 0.512099 \pm 0.000016$ (2σ, n = 289). Both results were consistent within analytical errors with recommended values of 0.511858 (± 7) and 0.512115 (± 7) respectively (Tanaka et al., 2000), and gave an external precision of ~±0.3 ε_{Nd}-unit. The $^{143}Nd/^{144}Nd$ ratios of samples were measured with a standard-bracketing method on the MC-ICP-MS, and corrected for instrumental drift by normalizing the bracketing standards to the recommended values.

Table A.2

Collector configuration and selected masses for the measurement

	High mass						AXIAL			Low mass
Collectors	DVM1	gap	DVM2	DVM3	DVM4	DVM5	DVM6	DVM7	DVM8	DVM9
Mass	150		148	147	146	145	144	143	142	140

DVMs are Faraday collectors

A.4 Comparison of the La Jolla and JNdi-1

Due to near exhaustion of the La Jolla standard, the JNdi-1 is increasingly used as an Nd-isotope standard in many laboratories worldwide today. Because the JNdi-1 standard was made of purified Nd-oxide (Nd_2O_3) powders, and then sub-split into small bottles, each of which contains ~1 g Nd_2O_3 powders (Tanaka et al., 2000), it is important to make sure the homogeneity of $^{143}Nd/^{144}Nd$ ratios in each powder aliquot. In addition, a good characterization of $^{143}Nd/^{144}Nd$ ratios of the JNdi-1 relative to that of the La Jolla standard is useful to ensure the consistency between new Nd-isotope data and historical ones.

Given the above considerations, the JNdi-1 and La Jolla standards were measured alternately to characterize the $^{143}Nd/^{144}Nd$ ratio in our JNdi-1 standard relative to that in the La Jolla standard. Our JNdi-1 Nd_2O_3 powder was provided by Dr. Hikari Kamioka at the Geological Survey of Japan, and labeled as Split 1, Position 140. The JNdi-1 Nd_2O_3 powder of ~56 mg was dissolved in a clean Teflon beaker with 2 ml distilled concentrated HNO_3 at ~120°C on a hotplate for >24 h, and then diluted with 130 ml 2% distilled HNO_3 as the stock solution. Further dilution from the stock JNdi-1 solution to ~0.1-0.2 ppm was performed before it was measured on the instrument. The results of alternate measurements on the La Jolla and JNdi-1 standards are reported in Table A.3. The factor (F) of $^{143}Nd/^{144}Nd$ values

of JNdi-1 (A) relative to that of La Jolla (B) at the *n*th measurement was calculated as: $F_n = 2 \times A_n / (B_{n-1} + B_{n+1})$. The results gave F = 1.000498 ± 0.000012 (1 standard deviation), which is consistent with the reported value of 1.000503 ± 0.000015 (1 standard deviation) (Tanaka et al., 2000). Using the recommended $^{143}Nd/^{144}Nd$ value of 0.511858 and the F value obtained from my measurements, JNdi-1 has a $^{143}Nd/^{144}Nd$ value of 0.512113 relative to the La Jolla standard, which is indistinguishable from the value of 0.512115 ± 0.000007 (2σ) obtained from previous calibrations (Tanaka et al., 2000). This result suggests that our aliquot of JNdi-1 has an identical $^{143}Nd/^{144}Nd$ value to other aliquots measured by Tanaka et al. (2000), offering more confidence in replacing the La Jolla with this standard.

A.5 Validation of the procedure

Several reference materials that have well-characterized $^{143}Nd/^{144}Nd$ ratios have been passed through the whole procedure described above, including the column separation and instrumental analysis, to validate that the procedure can provide precise and accurate measurement of Nd isotopes. The standards that were used for the validation included rock (basalt) standards BCR-1, BHVO-2 and a fish-bone composite that was made of a ground mixture of Mesozoic fish bones from varied depositional environments (Chavagnac et al., 2007).

Rock standards were dissolved with a mixture of concentrated HNO_3 and HF (v/v = 1:4) at ~130°C for over 3 days. The fish-bone composite was dissolved with a two-stage sequential dissolution procedure recommended in Chavagnac et al. (2007). Briefly, it was dissolved with 3 M HNO_3 at ~130°C for 24 h, and then centrifuged to separate the supernatant and residues. The supernatant was dried down, and re-dissolved in 6 M HCl. The residues were rinsed with Milli-Q water, followed by

centrifuging to separate the rinsing water. The rinsing water was kept, and combined later with other dissolved components of the composite. The residues were dissolved with a mixture of concentrated HNO_3 and HF (1:3) at ~130°C for over 2 days, and finally converted to chloride form by re-dissolution in 6 M HCl after being dried down on a hotplate. All dissolved components of the fish-bone composite were finally combined together.

The Nd-isotope results of the three reference materials are reported in Table A.4. Results of BCR-1 gave $^{143}Nd/^{144}Nd$ = 0.512649 ± 0.000005 (2σ, n=8), and BHVO-2 gave $^{143}Nd/^{144}Nd$ = 0.512992 ± 0.000010 (2σ, n=7), both of which are consistent with previous results obtained from other laboratories (Figure A.3). The fish-bone composite was a direct analogue to fish-debris samples, which were of prime interest in this study, in terms of the similarity of their chemical compositions, so it served as the most relevant test for the method of Nd-isotope analysis. Although certified $^{143}Nd/^{144}Nd$ values are not available for the fish-bone composite, $^{143}Nd/^{144}Nd$ ratios have been reported by several laboratories. Our results yielded a $^{143}Nd/^{144}Nd$ value of 0.512363 ± 0.000012 (2σ, n=16), which is consistent with results from other laboratories (Figure A.3). The good agreement of our $^{143}Nd/^{144}Nd$ results for the three different reference materials with respective values reported in the literature suggests that the adopted procedure is robust for making precise and accurate measurement of Nd isotopes.

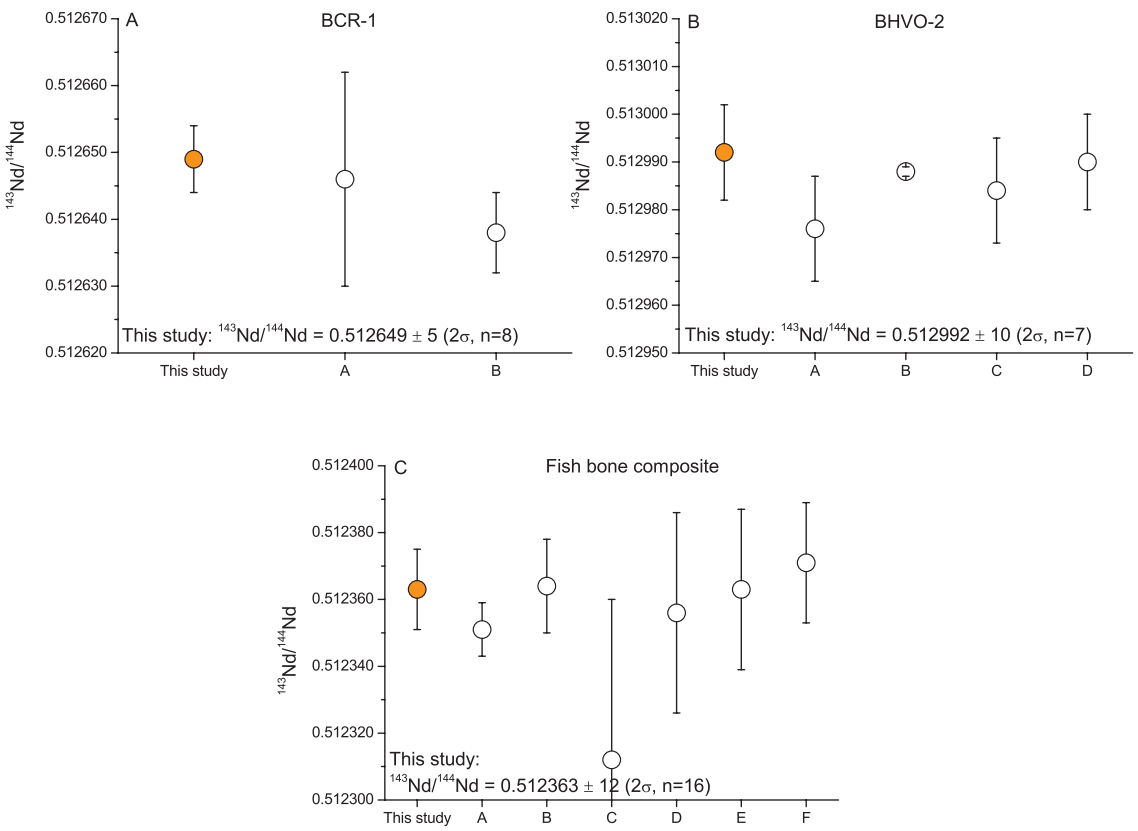

Figure A.3 Comparison of Nd-isotope results of three reference materials (orange closed circles), namely BCR–1 (A), BHVO–2 (B) and the fish-bone composite (C), with respective literature results (open circles). The letters on the *x*-axis of each figure indicate results from different laboratories/publications. The literature results for BCR–1 and BHVO–2 have been complied in Raczek et al. (2003); Weis et al. (2006); Weis et al. (2005). The literature results for the fish-bone composite have been compiled in Scher and Delaney (2010). Error bars in the figure indicate ±2σ.

Table A.3

Results of alternate measurements of the La Jolla and JNdi-1

La Jolla			JNdi-1		
*n**	$^{143}Nd/^{144}Nd$	2SE	*n**	$^{143}Nd/^{144}Nd$	2SE
1	0.511847	0.000010	2	0.512102	0.000005
3	0.511844	0.000010	4	0.512103	0.000007
5	0.511843	0.000008	6	0.512098	0.000007
7	0.511846	0.000010	8	0.512105	0.000006
9	0.511847	0.000009	10	0.512109	0.000006
11	0.511847	0.000009	12	0.512101	0.000007
13	0.511856	0.000009	14	0.512106	0.000006
15	0.511855	0.000009	16	0.512107	0.000007
17	0.511856	0.000009	18	0.512099	0.000007
19	0.511844	0.000010	20	0.512109	0.000007
21	0.511856	0.000009	22	0.512099	0.000007
23	0.511856	0.000009	24	0.512100	0.000006
25	0.511845	0.000009	26	0.512106	0.000007
27	0.511844	0.000008	28	0.512103	0.000007
29	0.511847	0.000009	30	0.512099	0.000007
31	0.511842	0.000010	32	0.512100	0.000007
33	0.511847	0.000008	34	0.512112	0.000007
35	0.511855	0.000009	36	0.512109	0.000007
37	0.511848	0.000009	38	0.512100	0.000007
39	0.511844	0.000009	40	0.512098	0.000007
41	0.511841	0.000008	42	0.512107	0.000007
43	0.511851	0.000010	44	0.512102	0.000007
45	0.511849	0.000008	46	0.512106	0.000007
47	0.511854	0.000009	48	0.512109	0.000008
49	0.511833	0.000013	50	0.512103	0.000009
51	0.511845	0.000010	52	0.512099	0.000008
53	0.511855	0.000008	54	0.512099	0.000008
55	0.511855	0.000009	56	0.512096	0.000006
57	0.511844	0.000009	58	0.512104	0.000006
59	0.511842	0.000009	60	0.512097	0.000006
61	0.511845	0.000008	62	0.512099	0.000006
63	0.511848	0.000008	64	0.512101	0.000006
65	0.511844	0.000008	66	0.512097	0.000007
67	0.511847	0.000009	68	0.512100	0.000007
69	0.511844	0.000009	70	0.512109	0.000008
71	0.511841	0.000007	72	0.512099	0.000007
73	0.511847	0.000009	74	0.512094	0.000008
75	0.511851	0.000008	76	0.512093	0.000007
77	0.511853	0.000009	78	0.512100	0.000006

79	0.511843	0.000008	80	0.512100	0.000007
81	0.511835	0.000009	82	0.512098	0.000007
83	0.511842	0.000009	84	0.512101	0.000007
85	0.511840	0.000009	86	0.512098	0.000007
87	0.511834	0.000008	88	0.512097	0.000007
89	0.511847	0.000008			

* *n* indicates the *n*th measurement

Table A.4

ε_{Nd} results of BCR–1, BHVO–2 and the fish-bone composite

	$^{143}Nd/^{144}Nd$	2σ
BCR–1	0.512649	0.000013
	0.512648	0.000010
	0.512650	0.000011
	0.512650	0.000017
	0.512646	0.000011
	0.512649	0.000011
	0.512646	0.000009
	0.512654	0.000008
Mean (n=8)	**0.512649**	**0.000005**
BHVO-2	0.512998	0.000010
	0.512986	0.000011
	0.512989	0.000009
	0.512988	0.000012
	0.512989	0.000011
	0.512999	0.000011
	0.512994	0.000011
Mean (n=7)	**0.512992**	**0.000010**
Fish-bone composite	0.512366	0.000006
	0.512359	0.000006
	0.512361	0.000006
	0.512363	0.000006
	0.512375	0.000012
	0.512367	0.000007
	0.512353	0.000010
	0.512356	0.000009
	0.512370	0.000007
	0.512362	0.000006
	0.512369	0.000009
	0.512362	0.000007
	0.512366	0.000008
	0.512357	0.000010
	0.512371	0.000009
	0.512359	0.000009
Mean (n=16)	**0.512363**	**0.000012**

Appendix B

The MATLAB code for the OMP analysis

Appendix B details the MATLAB code for OMP analysis that was used in Chapter 3. The code was modified to incorporate dissolved Nd and Yb into the analysis, based on the OMP package developed by Johannes Karstensen and Matthias Tomczak. The original OMP package with detailed descriptions regarding its usage can be found at http://omp.ifm-geomar.de. Only source code files that were modified during the study of Chapter 3 in this thesis are presented in this Appendix. The code presented below follows the MATLAB syntax, and the green lines after the "%" symbol are non-executive, explanatory notes for the code.

---
bigloop.m

```
%%  Configure numbers of perturbation experiments and start the analysis
%%  Call omp2auto.m
clear all;

%  select a depth range from which samples will be selected and analyzed
%  analysisRANGE=0; (depth between 960 and 2500 m);
%  analysisRANGE=1; (depth >2500 m)
%  analysisRANGE=2; (depth > 960 m)(used in this thesis)
analysisRANGE=2;


% set numbers of perturbation experiments;
% the total number of experiments will be: (EXPcount*count)
EXPcount=1;
count=1;


% initialize the condition number to a dummy value;
```

```
conditionNO=-999;


% beginning of the loop of perturbation experiments;
for EXP=1:EXPcount

for cycle=1:count

% run omp2auto.m file;
   omp2auto;

end
end
```

---

omp2auto.m

%% Main code–build the matrix containing end-member values

%% Use configuration file–*incontr3.m*, and call *omp2.m* when the matrix is built

```
% ######### OMP analysis main program version 3  ###################
%
%  The original version was prepared by Johannes Karstensen and Matthias Tomczak,
%  and can be downloaded from http://omp.ifm-geomar.de. This version incorporated
%  changes made by Xin-Yuan Zheng to analyze dissolved Nd and Yb in seawater.
%
%  This program is largely modified to analyze the REE dataset from the CoFeMUG
%  section, which is provided in Chapter 3 of this thesis. Any further application of
%  this code may require changes according to specific questions that need to be
%  solved.
%  Function files used: qwt2.m; qwt_tst.m; nansum.m.
%  sw_ptmp sw_dens0.m may be called for some data files
% The above files are from the Seawater Matlab library of Phil Morgan (CSIRO
%  Marine Research, Hobart, 12).
%  This library can be downloaded via anonymous ftp: ftp.ml.csiro.au
%  the files are in /pub/morgan/seawater.


% Screen display control
if EXP==1&&cycle==1
disp('  ')
disp('OMP Analysis version 2 (March 1999) - modified (Oct 2013)')
disp('  ')
EXPcounter=['Now Experiment:' num2str(EXP)];
counter=['This is cycle:' num2str(cycle)];
```

```
countd=count-cycle;
countdown=[num2str(countd) ' cycle(s) left in this experiment'];
countdownEXP=EXPcount-EXP;
countdownEXPERIMENT=[num2str(countdownEXP) ' experiment(s) left'];
disp('  ');
disp('************************************');
disp(EXPcounter);
disp(counter);
disp(countdown);
disp(countdownEXPERIMENT);

else
EXPcounter=['Now Experiment:' num2str(EXP)];
counter=['This is cycle:' num2str(cycle)];
countd=count-cycle;
countdown=[num2str(countd) ' cycle(s) left in this experiment'];
countdownEXP=EXPcount-EXP;
countdownEXPERIMENT=[num2str(countdownEXP) ' experiment(s) left'];
disp('  ');
disp('************************************');
disp(EXPcounter);
disp(counter);
disp(countdown);
disp(countdownEXPERIMENT);

end


% Loading the run parameters from the configuration file–incontr3.m
newfile='incontr3';
eval(newfile);
eval(['load ' dataset])

eex(1:11) = [1 1 1 1 1 0 0 0 0 0 1];   % index of available variables
esx(1:11) = [1 1 1 1 1 0 0 0 0 0 1];   % index of selected variables
                % 1: latitude
                % 2: longitude
                % 3: pressure
                % 4: salinity
                % 5: potential temperature
                % 6: silicate
                % 7: phosphate
                % 8: nitrate (replaced by dissolved Nd in this thesis)
                % 9: oxygen (replaced by dissolved Yb in this thesis)
                %10: potential vorticity
                %11: temperature

% NOTE: For historical reasons the two columns mass conservation and potential
% vorticity are swapped in the program so that mass conservation is always the last
%  column, after potential vorticity.
```

```
%  check parameters used for the analysis
%  NOTE: “ni” represents dNd, and “oxy” represents dYb in this thesis
if exist('temp')  == 0
   temp = sw_temp(sal,ptemp,press,0);
end

if exist('sal')   == 1 eex(4) = 1;  end
if exist('ptemp') == 1 eex(5) = 1;  end
if exist('si')    == 1 eex(6) = 1;  end
if exist('ph')    == 1 eex(7) = 1;  end
if exist('ni')    == 1 eex(8) = 1;  end
if exist('oxy')   == 1 eex(9) = 1;  end
if exist('pvort') == 1 eex(10) = 1;  end

% Check and if necessary calculate potential vorticity
if switchpot == 'y'
% Find top and bottom pressure for each station, calculate potential vorticity
   statind=[0 find(diff(press)<0)' length(press)];
   disp('gone through all right')
   vvort =[];
   pp = [];
      [bfrq,vort,p_ave] = sw_bfrq(sal,temp,press,lat);
      for i = 1:size(vort(:))
         vvort = [vvort vort(i)];
         pp    = [pp p_ave(i)];
      end
   vvort = 10E08*[vvort 0];
   pp    = [pp 10000];
   pvort = -999999*ones(size(press));
   for i = 2:size(statind(:))
      pvort(statind(i-1)+2:statind(i)-1) = ...
         interp1(pp(statind(i-1)+1:statind(i)-1),vvort(statind(i-1)+1:statind(i)-1),...
         press(statind(i-1)+2:statind(i)-1));
   end
   eex(10) = 1;
   clear bfrq
   clear vort
   clear vvort
   clear p_ave
   clear pp
   pvort = abs(pvort);
end


% Determine the number of variables used in this run:
nvar = 3;
if isi == 'y' nvar = nvar +1; esx(6) = 1; end
if iph == 'y' nvar = nvar +1; esx(7) = 1; end
if ini == 'y' nvar = nvar +1; esx(8) = 1; end
if iox == 'y' nvar = nvar +1; esx(9) = 1; end
```

```
if switchpot == 'y' nvar = nvar +1; esx(10) = 1; end

% Read the weight and Redfield ratio file
eval(['load ' weightset]);

%Check which weights are needed and reset the diagonal:
A = diag(Wx);
A1 = A(8);  % change order of weights so that mass conservation is last
A(8) = A(7);
A(7) = A1;
if esx(5) == 0 A(1) = 0;
   ratio(1) = -999; end          % no pot. temperature weight if not needed
if esx(4) == 0 A(2) = 0;
   ratio(2) = -999; end          % no salinity weight if not needed
if esx(6) == 0 A(3) = 0;
   ratio(3) = -999; end          % no silicate weight if no oxygen
if esx(7) == 0 A(4) = 0;
   ratio(4) = -999;  end         % no phosphate weight if no phosphate
if esx(8) == 0 A(5) = 0;
   ratio(5) = -999;  end         % no dNd weight if no nitrate
if esx(9) == 0 A(6) = 0;
   ratio(6) = -999;  end         % no dYb weight if no silicate
if esx(10) == 0 A(7) = 0;
   ratio(7) = -999;  end         % no pot. vorticity weight if not needed
statind = find(A>0);
Wx = diag(A(statind));
statind = find(ratio>-999);
redfrat = ratio(statind);    % Redfield ratio for selected variables only
disp('  ')
clear A
%  End of if statements for weights and Redfield ratio

% Read the water types, and build the matrix G1 that contains end-member values of
%  the defined water types
clear G1;
[G0,wmnames,i]=eval([swtypes '(qwt_pos,1)']);
wm_index = [];
wm_ind0  = [     ];
wm_ind1  = [     ];
j = 0;
tit_index = [];
for i = 1:length(qwt_pos)
   wm_ind1 = wmnames(5*(qwt_pos(i)-1)+1:5*(qwt_pos(i)-1)+5);
   k = strcmp(wm_ind0,wm_ind1);
   if k == 0
      j = j+1;
      tit_index = [tit_index wmnames(5*(qwt_pos(i)-1)+1:5*(qwt_pos(i)-1)+5)];
      end
   wm_ind0 = wm_ind1;
   wm_index = [wm_index j];
```

```
end
nr_of_wm = wm_index(length(wm_index));

i = 3;
clear G1;
G1(1,:) = G0(1,:);
G1(2,:) = G0(2,:);
if esx(6) == 1
   G1(3,:) = G0(3,:);
   i = i+1;
end
if esx(7) == 1
   G1(i,:) = G0(4,:);
   i = i+1;
end
if esx(8) == 1
   G1(i,:) = G0(5,:);
   i = i+1;
end
if esx(9) == 1
   G1(i,:) = G0(6,:);
   i = i+1;
end
if esx(10) == 1
   G1(i,:) = abs(G0(8,:));
   i = i+1;
end
G1(i,:) = G0(7,:);


%%  Code for perturbation experiments
%  use pre-defined end-member values for all water types in the first calculation
if EXP==1
  G1;

%   generate uniformly-distributed random noise for each pre-defined end-member
%    values, and build a new matrix A.
%   The noises are bound by the 2 standard deviations of the mean values of
%    corresponding parameters observed in nature
else
      [row,column]=size(G1);
      randG1=zeros(row,column);
      STDsource=[0.53 0.39 0.42 0.33; 0.11 0.05 0.04 0.01; 8.14 4.41 8.01 7.92; 0.10
0.16   0.2 0.06; 1.5 0.8 1.0 1.4; 1.3 0.1 0.4 0.2; 0 0 0 0];
     TwoSDsource=2*STDsource;

   for ppp=1:column
      for qqq=1:row
         randG1(qqq,ppp)=TwoSDsource(qqq,ppp)*rand;
      end
```

```
    end

G1=G1-STDsource+randG1;  % convert G1 to randomized G1

    end

end

close all

%  Call the "omp2.m" file that does the analysis
 omp2
```

---

omp2.m

%% Main code of OMP analysis–build vector of observed data, and perform
%% regression calculation for each data point

%% Use configuration file–*incontr3.m*

%% Use the function *cgls.m* for the regression calculation

```
%  Screen display
disp('  ')
disp(['OMP analysis now running. ' num2str(length(lat)) ' data points found.'])
disp('  ')
starttime = clock;
gap=0;


%  determine MATLAB version
vers=version;vers=vers(1);


%  select observed data within the depth range in the configuration file incontr3.m
%  set potential vorticity to positive values (independent of hemisphere) if required
%  Note that "ni" and "oxy" represent "dNd" and "dYb" respectively in this thesis
disp('Screening the data and reducing them to the selected range.')
disp('  ')
switch(switchpot)
case 'y'
    eval(['index=find(imag(pvort)==0&pvort<100&' selection ');'])
    pvort = abs(pvort);
otherwise
```

```
    eval(['index=find(' selection  ');'])
end
     lat=   lat(index)';
    press= press(index)';
     long=  long(index)';
      sal=   sal(index)';

    if exist('temp') == 1
        temp= temp(index)';
    end
    if ~isempty(switchpot) & switchpot == 'y'
        pvort=pvort(index)';
    end
     if exist('ptemp') == 1
        ptemp=ptemp(index)';
    else
          ptemp = sw_ptmp(sal,temp,press,0);
    end
    if exist('pdens') == 1
           pdens=pdens(index)';
    else
       pdens = sw_dens0(sal,temp) - 1000;
    end
    if esx(6)  == 1 oxy=  oxy(index)';  end
    if esx(7)  == 1 ph =   ph(index)';  end
    if esx(8)  == 1 ni =   ni(index)';  end
    if esx(9)  == 1 si =   si(index)';  end
clear index
disp(['OMP analysis now running. ' num2str(length(lat)) ' data points to be
analysed.'])
disp('  ')

[m,n]=size(G1); % n = number of water types, m = number of equations


%  normalize the source water matrix (get meanG, get stdG for weighting):
[G,mG,stdG]=norm_qwt(G1);


%  EXTENDED OMP switch (it can be configured in incontr3.m file, and the switch
was %  turned on in this thesis):
switch(OMP)
case 'ext'


    %  Adding Redfield ratio to the system, ratio comes from weight file
    G1(1:m,n+1)=[redfrat(1:m)]';

    %  normalization of the ratios:
    for rr=1:(m-1)
```

```
        G(rr,n+1)=redfrat(rr)*(max(G(rr,1:n))-min(G(rr,1:n)))...
            /(max(G1(rr,1:n))-min(G1(rr,1:n)));
    end
    G(m,n+1)=0;


  %  Adding dNd to the matrix G1
    addNd=[0 0 0 0 1 0 0];
    G1(1:m,n+2)=addNd';

    %  normalization of the ratios
    for rrr=1:(m-1)
        G(rrr,n+2)=addNd(rrr)*(max(G(rrr,1:n))-min(G(rrr,1:n)))...
            /(max(G1(rrr,1:n))-min(G1(rrr,1:n)));
    end
    G(m,n+2)=0;


    %  Adding dYb to the matrix G1
    addYb=[0 0 0 0 0 1 0];
    G1(1:m,n+3)=addYb';
    %  normalization of the ratios:
    for rrrr=1:(m-1)
        G(rrrr,n+3)=addYb(rrrr)*(max(G(rrrr,1:n))-min(G(rrrr,1:n)))...
            /(max(G1(rrrr,1:n))-min(G1(rrrr,1:n)));
    end
    G(m,n+3)=0;
end


%  weighing the matrix G1

%--------Weight Perturbation Experiment-----------
% purtbWx=[0.5 0.5 0.5 0.5 0.5 0.5 0.5]; %  randomly changing weights by 50%
% PURTB=diag(purtbWx);
% absPURTB=Wx*PURTB;
% randPURTB=2*absPURTB*rand;
% Wxnew=Wx-absPURTB+randPURTB;
% Wx=Wxnew;
%-----------------------------------------------------------

G2=Wx*G;


%  calculate condition number of normalized and weighed matrix G1–G
conditionNO=cond(G2);

gap=0;
```

```
% This is the main loop for each data point; k = point index
% First some initial settings. (NOTE: “ni” and “oxy” denote “dNd” and “dYb” here.)
   err=zeros(m,length(lat))-nan;

switch(OMP)
case 'ext';
  biogeo=zeros(3,length(lat))-nan;
end


A(1:wm_index(length(wm_index)),1:length(lat)) = ...
              zeros(wm_index(length(wm_index)),length(lat));
oxy_dat = [];
ph_dat  = [];
ni_dat  = [];
si_dat  = [];
pv_dat  = [];

btstall=zeros(length(lat),7); %  a matrix used for observed data compilation


%  vector of each datapoint (btst) is build here
for k=1:length(lat);
   %  selecting the correct parameters
    p_dat  = press(k);
    t_dat  = ptemp(k);
    s_dat  =   sal(k);
    if esx(6) == 1  si_dat =    si(k); end
    if esx(7) == 1  ph_dat =    ph(k); end
    if esx(8) == 1  ni_dat =    ni(k); end
    if esx(9) == 1  oxy_dat=    oxy(k); end
    if exist('pdens') == 1  pden_dat   = pdens(k); end
    if esx(10) == 1 pv_dat = pvort(k); end
    kon=1;

   btst= [t_dat,s_dat,si_dat,ph_dat,ni_dat,oxy_dat,pv_dat,kon];

%%  Code for perturbation experiments
%  use the original observed data in the first calculation
if cycle==1
   btst;

%  generating random noises that are bound by analytical error of each parameter, and
%  adding noises to the observed data vector
else
analytical_err=[0.0005 0.00005 0.002 0.004 0.03 0.03 0]; % define analytical error for
each parameter here!
STDobservation=[btst(1)*analytical_err(1) btst(2)*analytical_err(2)
btst(3)*analytical_err(3) btst(4)*analytical_err(4) btst(5)*analytical_err(5)
btst(6)*analytical_err(6) 0]; % define standard deviation of each observations
```

```
FourSD_STDobservation=4*STDobservation;
TwoSD_STDobservation=2*STDobservation;
STDobsLength=length(STDobservation);
randG1=zeros(1,STDobsLength);

 for STDobsINDEX=1:STDobsLength-1
         randG1(STDobsINDEX)=FourSD_STDobservation(STDobsINDEX)*rand;
 end


 RANDNbtst=btst-TwoSD_STDobservation+randG1;

btst=RANDNbtst; %convert btst to randomized btst
end


   if etime(clock,starttime) > 5
      disp([num2str(k) ' data points analysed so far.'])
      starttime = clock;
   end
%  looking for GAP (indicated through NaN):
  index1=find(~isnan(btst));
  index0=find(isnan(btst));

   cutit=n;

%  using extended OMP we need one parameter more
%  (because we have one unknown more!)
   if OMP(1:3)=='ext' cutit=n+1; end
   if length(index1) < cutit+1 %  if 1
%  insufficient parameters to do the regression
%  data point not successful analyzed
      disp(['ANALYSIS of the datapoint failed, not enough parameters available !!'])
         A(1:nr_of_wm,k) = nan;
         Dual(1:nr_of_wm,k) = nan;
      gap=gap+1;

   else
    %  new data without GAP:
      b1 = btst(index1);
      mG1=   mG(index1);
      stdG1= stdG(index1);

      btstall(k,:)=b1; %  compile observed data


%  normalize the data vector:
  for i=1:length(b1)-1
    b(i,1)=(b1(i)-mG1(i))/stdG1(i);
  end
```

```
   b(length(b1))=b1(length(b1));

%  add weights:
    b2=Wx(index1,index1)*b;

%  call cgls.m to do regression calculation with the conjugate gradient method
[x,resnorm] = cgls(G2(index1,:),b2,5000);


%  calculate residuals for individual parameters
    err(index1,k)= G1(index1,:)*x-btst(index1)';


%  add contributions from identically named water masses
    for i=1:n
        A(wm_index(i),k)    = A(wm_index(i),k) + x(i);
    end


%  in case of extended OMP analysis the biogeochemical part is stored
switch(OMP)
      case 'ext'

%  store results of non-conservative components in variable 'biogeo'
          for ttt=1:3
            biogeo(ttt,k) = x(4+ttt)*stdG(3+ttt)*((max(G(3+ttt,1:n))-
min(G(3+ttt,1:n)))/(max(G1(3+ttt,1:n))-min(G1(3+ttt,1:n))));
          end
 end
      end

    clear b
    end                %end of loop with enough data

end  % %end of data point loop


switch(OMP)
case 'ext'


%  clear up results and save to .mat files for each experiment
solution=A;
[Arow, Acolumn]=size(A);
biorowstat=Arow+1;
biorowend=Arow+3;
solution(biorowstat:biorowend,:)=biogeo;
if analysisRANGE==0
vname=strcat('EXP_',num2str(EXP),'_shallow_','cycle_',num2str(cycle));
save(['/Users/XYZheng/Documents/MATLAB/CoFeMUGresults/' vname '.mat']);
```

```
elseif analysisRANGE==1
vname=strcat('EXP_',num2str(EXP),'_deep_','cycle_',num2str(cycle));
save(['/Users/XYZheng/Documents/MATLAB/CoFeMUGresults/' vname '.mat']);
elseif analysisRANGE==2
vname=strcat('EXP_',num2str(EXP),'_all_','cycle_',num2str(cycle));
save(['/Users/XYZheng/Documents/MATLAB/CoFeMUGresults/' vname '.mat']);
end

end

if cycle==count&&EXP==EXPcount

disp(' ')
disp('E N D  O F  O M P  A N A L Y S I S');

end
```

---

incontr3.m

```
%%  This is the configuration file for the extended OMP analysis

%%  Used by omp2auto.m and omp2.m

%  Set type of OMP analysis by placing/deleting comment (%) sign:
%  OMP = 'cla'; % classical OMP analysis
 OMP = 'ext'; % extended OMP analysis

%  Define the file which contains the data:
dataset = 'CoFeMUG.mat';

%%%  define a specific range of data to be used:
if analysisRANGE==0
   selection='press>960&press<2500';
elseif analysisRANGE==1
   selection='press>=2500';
elseif analysisRANGE==2;
   selection='press>960';
end


%  Select/deselect potential vorticity by setting switchpot to 'y' or 'n':
switchpot = 'n';

%  Select/deselect variables by setting corresponding switches to 'y' or 'n':
iox = 'y';  %  dYb switch
```

```
iph = 'y';  %  phosphate switch
ini = 'y';  %  dNd switch
isi = 'y';  %  silicate switch

% Define the file which contains the weights:
weightset = 'testwght';

% Define the routine which contains the source water type definitions:
swtypes = 'qwt2';

% Set the total number of water masses to be included in the analysis
if analysisRANGE==2;
   wm = 3;
else wm = 3;
end

%  Select the water type numbers (row in the water type matrix)
% (The square brackets have to contain wm numbers):

if analysisRANGE==0
qwt_pos = [3 4 5];
elseif analysisRANGE==1
qwt_pos = [4 5 6];
elseif analysisRANGE==2
   qwt_pos = [3 4 5 6];
end
```

---

cgls.m

%% Function that performs regression with the conjugate gradient method

%% Called by *omp2.m*

```
%  itern:  number of iteration
function [X,rsq]=cgls(A,b,itern)


%---------initialization-------
sa=size(A);
X=zeros(sa(2),1);
X0=zeros(sa(2),itern);
Xerror = zeros(sa(2),itern+1);
s0=b-A*X; %s0: xi
g=A'*s0; %r0,p0
h=g; %r0,p0
```

```
rsq=zeros(itern,1);
%------------------------------
for iter=1:itern
   q=A*h; %xi=A*h
   anum=sum(g.*h);
   aden=q'*q;
   if aden==0
      disp('very singular matrix')
   end
   anum=anum./aden;

   X=X+anum.*h;

% ---------configure constraint of the regression  -------------
%      X(1:4) = abs(X(1:4)); % positive constraint for X(1:4)
%     X(X<0) = 0;
%     X(X(1:4)<0) = 0;
      X(X(1:5)<0) = 0; %  positive constraint for watermass fractions and dP
% ---------constraint end ----------------------------------------

   Xerror(:,iter+1) = anum.*h;
   X0(:,iter)=X;
 %-------------------------------------------------------------
   s=(A*X)-b;  %  xj=(A*X)-b;
   %  s=s0-anum*q;
   rsq(iter)=mean(abs(s).^2);
   %  rp=rsq;
   r=A'*s;  %  xi=A'*xj;
   gg=sum(g.^2);
   dgg=sum((r+g).*r);
   g=-r;
   h=g+dgg./gg.*h;
end
[m,n]=min(rsq);
X=X0(:,n);
return
%------------------End----------
```

Appendix C

Additional tables

Table 3.2 (Chapter 3)

Dissolved REE concentrations (pmol/kg)

Depth	La	Ce	Pr	Nd	Sm	Eu	Gd	Tb	Dy	Ho	Er	Tm	Yb	Lu
Station 1 (11°S, 330°E, 5300 m)														
10	19.62	17.66	4.16	17.27	3.67	0.91	3.99	0.62	4.41	1.07	3.31	0.46	2.66	0.40
400	21.32	3.76	3.47	14.28	2.58	0.76	3.41	0.54	4.24	1.15	3.97	0.61	4.10	0.69
999	20.94	3.99	3.32	13.68	2.55	0.77	3.60	0.58	4.70	1.33	4.76	0.76	5.25	0.92
1499	20.82	3.19	3.34	13.91	2.57	0.77	3.54	0.57	4.51	1.25	4.45	0.70	4.75	0.82
2000	23.68	4.86	4.01	16.79	3.26	0.95	4.52	0.71	5.45	1.44	4.85	0.73	4.91	0.82
2499	25.60	3.89	4.27	17.83	3.40	0.98	4.66	0.73	5.62	1.49	5.00	0.76	5.17	0.87
3000	27.64	3.85	4.58	19.02	3.56	1.05	4.83	0.75	5.80	1.54	5.24	0.80	5.43	0.92
3499	31.17	4.07	5.31	21.75	4.05	1.17	5.27	0.82	6.18	1.60	5.41	0.82	5.63	0.94
4000	38.24	5.78	6.68	26.94	4.97	1.39	6.26	0.95	7.11	1.82	6.08	0.92	6.29	1.05
4968	49.43	5.89	8.68	34.79	6.45	1.83	7.94	1.21	8.86	2.25	7.49	1.15	7.99	1.35
Station 3 (11.5°S, 335°E, 4400 m)														
9	18.05	14.59	3.76	15.56	2.96	0.85	3.71	0.57	4.10	1.02	3.18	0.43	2.52	0.37
399	19.37	2.86	3.22	13.16	2.40	0.73	3.28	0.52	4.12	1.14	3.99	0.61	4.13	0.71
999	21.19	5.38	3.37	13.84	2.57	0.79	3.65	0.59	4.77	1.35	4.89	0.77	5.36	0.94
1499	22.31	5.43	3.77	15.62	3.02	0.89	4.24	0.68	5.31	1.44	4.94	0.76	5.13	0.86
2000	24.25	5.70	4.00	17.06	3.32	0.92	4.57	0.73	5.59	1.47	4.92	0.75	4.99	0.82
2499	27.37	8.21	4.62	19.70	3.86	1.03	5.08	0.79	6.02	1.56	5.22	0.79	5.32	0.89
3000	27.40	4.93	4.47	19.27	3.68	1.04	4.98	0.78	5.95	1.56	5.25	0.80	5.42	0.90
3500	30.22	4.39	5.00	21.39	4.07	1.11	5.35	0.83	6.25	1.61	5.37	0.81	5.45	0.90
3832	36.10	7.75	6.16	25.88	4.92	1.32	6.24	0.96	7.10	1.81	6.02	0.92	6.26	1.04
3999	38.72	6.42	6.56	27.42	5.16	1.38	6.51	1.00	7.37	1.88	6.23	0.94	6.41	1.07
Station 4 (11.5°S, 337.5°E, 5100 m)														
10	19.69	17.13	4.06	17.37	3.39	0.90	4.20	0.64	4.49	1.11	3.44	0.47	2.72	0.40
399	19.02	3.38	3.03	12.94	2.41	0.68	3.33	0.52	4.16	1.15	4.02	0.61	4.10	0.69
999	22.19	6.41	3.48	14.80	2.82	0.82	3.92	0.62	4.99	1.39	4.95	0.78	5.38	0.93
1499	23.81	8.74	4.01	17.27	3.42	0.96	4.63	0.74	5.67	1.50	5.13	0.78	5.25	0.88
1999	25.40	8.02	4.30	18.34	3.58	0.98	4.83	0.77	5.81	1.52	5.10	0.77	5.21	0.86
2499	26.75	5.85	4.38	18.81	3.66	1.02	4.96	0.77	5.92	1.56	5.26	0.80	5.38	0.89
3000	29.23	7.45	5.38	21.15	4.04	1.16	5.18	0.81	6.04	1.57	5.29	0.80	5.56	0.92
3499	30.47	4.06	5.44	21.73	4.06	1.20	5.29	0.82	6.16	1.62	5.46	0.83	5.71	0.95
4000	39.17	5.60	7.17	28.28	5.27	1.50	6.57	1.00	7.40	1.90	6.34	0.97	6.70	1.12
4500	46.98	5.87	8.74	34.24	6.40	1.83	7.85	1.19	8.69	2.22	7.31	1.13	7.86	1.32
5002	50.82	8.99	9.72	37.40	7.06	2.02	8.31	1.27	9.15	2.29	7.52	1.15	8.12	1.36
Station 5 (12°S, 340°E, 4700 m)														
10	20.72	18.83	4.56	18.30	3.55	0.99	4.24	0.65	4.59	1.12	3.45	0.47	2.78	0.41
399	19.13	2.69	3.28	13.07	2.40	0.72	3.24	0.52	4.10	1.14	3.99	0.61	4.13	0.70
999	22.21	6.16	3.75	14.95	2.81	0.83	3.80	0.61	4.88	1.37	4.89	0.77	5.38	0.93
1500	22.61	5.66	3.94	15.94	3.09	0.92	4.23	0.67	5.32	1.44	4.95	0.76	5.21	0.88
1999	23.88	4.26	4.12	16.78	3.22	0.98	4.45	0.70	5.53	1.49	5.05	0.77	5.25	0.88
2499	26.87	5.52	4.73	18.98	3.63	1.04	4.80	0.75	5.80	1.54	5.19	0.79	5.46	0.91

2999	27.74	3.29	4.76	19.19	3.56	1.06	4.78	0.74	5.81	1.56	5.28	0.81	5.57	0.94
3499	31.12	3.61	5.15	22.06	4.11	1.16	5.40	0.85	6.36	1.65	5.57	0.85	5.78	0.96
4000	38.88	4.88	6.54	27.88	5.18	1.41	6.57	1.02	7.40	1.90	6.31	0.96	6.55	1.08
4502	47.52	5.25	8.16	34.36	6.39	1.74	7.87	1.21	8.74	2.21	7.28	1.11	7.65	1.27
Station 7 (12.5°S, 345°E, 2900 m)														
10	19.08	14.69	3.80	16.38	3.14	0.87	3.93	0.61	4.31	1.06	3.28	0.44	2.49	0.37
399	21.37	3.71	3.37	14.43	2.66	0.74	3.63	0.56	4.45	1.21	4.25	0.66	4.38	0.76
999	21.85	4.54	3.38	14.30	2.64	0.77	3.74	0.60	4.76	1.33	4.76	0.76	5.16	0.90
1499	22.42	5.86	3.68	15.93	3.12	0.90	4.35	0.70	5.46	1.48	5.11	0.79	5.37	0.90
1749	23.07	5.87	3.80	16.61	3.25	0.94	4.52	0.72	5.65	1.49	5.08	0.78	5.28	0.89
1999	24.77	5.48	4.09	17.65	3.42	0.96	4.68	0.75	5.72	1.53	5.16	0.79	5.36	0.90
2249	24.96	4.07	4.06	17.47	3.33	0.96	4.60	0.74	5.63	1.51	5.12	0.79	5.34	0.90
2500	26.04	3.49	4.14	17.90	3.39	0.98	4.70	0.74	5.77	1.53	5.21	0.80	5.48	0.92
2841	27.43	3.32	4.30	18.62	3.50	1.01	4.78	0.75	5.81	1.54	5.22	0.80	5.47	0.92
Station 9 (12.5°S, 350°E, 4100 m)														
9	20.79	14.92	4.02	17.49	3.35	0.93	4.16	0.64	4.51	1.10	3.41	0.46	2.59	0.38
399	22.43	4.31	3.54	15.06	2.74	0.80	3.64	0.58	4.52	1.22	4.29	0.67	4.47	0.76
1499	22.65	4.72	3.64	15.92	3.04	0.88	4.33	0.69	5.48	1.48	5.17	0.79	5.40	0.91
1999	24.07	4.51	3.83	16.80	3.22	0.92	4.55	0.72	5.67	1.50	5.16	0.78	5.29	0.88
2499	26.28	3.47	4.10	17.89	3.42	0.99	4.77	0.75	5.89	1.57	5.34	0.82	5.56	0.95
3000	30.58	4.12	4.81	20.92	3.91	1.12	5.25	0.83	6.30	1.68	5.69	0.88	5.98	1.02
3499	32.28	4.39	5.07	21.86	4.03	1.13	5.36	0.83	6.31	1.68	5.69	0.87	5.96	1.01
3959	32.40	4.55	5.16	22.14	4.07	1.14	5.35	0.83	6.31	1.68	5.70	0.88	6.00	1.02
Station 10 (12.5°S, 352.5°E, 3990 m)														
9	21.33	14.68	4.19	17.94	3.43	0.95	4.26	0.65	4.65	1.14	3.50	0.47	2.76	0.40
399	24.36	5.26	3.99	16.73	3.07	0.85	3.92	0.62	4.72	1.26	4.37	0.68	4.55	0.77
1000	22.53	6.46	3.75	15.50	2.89	0.89	3.94	0.63	5.00	1.41	5.02	0.80	5.59	0.97
1499	23.75	5.93	4.03	16.68	3.19	0.95	4.39	0.70	5.53	1.51	5.25	0.82	5.65	0.95
1999	25.07	6.03	4.29	17.72	3.39	1.00	4.64	0.73	5.71	1.53	5.22	0.81	5.55	0.93
2500	27.60	5.96	4.64	19.33	3.69	1.08	4.94	0.79	6.08	1.62	5.53	0.86	5.87	0.98
2999	31.07	5.23	5.15	21.47	3.98	1.18	5.27	0.82	6.33	1.69	5.79	0.89	6.14	1.04
3499	32.80	5.26	5.57	22.86	4.19	1.21	5.45	0.84	6.42	1.70	5.78	0.89	6.18	1.03
3859	33.49	5.42	5.70	23.35	4.26	1.22	5.47	0.84	6.36	1.69	5.77	0.89	6.14	1.03
Station 11 (12.5°S, 355°E, 3000 m)														
10	21.31	13.95	4.21	17.45	3.30	0.94	4.16	0.62	4.46	1.11	3.43	0.46	2.69	0.39
399	24.03	4.60	4.02	16.29	2.93	0.87	3.82	0.59	4.61	1.26	4.42	0.67	4.59	0.78
998	22.46	5.04	3.65	15.13	2.82	0.85	3.86	0.62	5.03	1.41	5.06	0.79	5.59	0.97
1499	25.08	7.29	4.32	17.75	3.41	0.97	4.63	0.73	5.82	1.59	5.54	0.86	5.90	1.00
1999	25.36	6.41	4.25	17.89	3.42	1.01	4.70	0.76	5.88	1.57	5.43	0.84	5.73	0.97
2500	27.37	4.55	4.49	18.75	3.52	1.02	4.85	0.77	5.91	1.58	5.42	0.84	5.71	0.97
2700	28.43	4.42	4.67	19.47	3.66	1.06	4.96	0.78	6.03	1.61	5.53	0.85	5.81	0.98
2936	30.12	4.56	4.93	20.59	3.85	1.11	5.10	0.80	6.18	1.64	5.62	0.87	5.97	1.01
Station 13 (13.25°S, 0°E, 5472 m)														
10	20.74	12.03	3.78	16.10	2.94	0.83	3.85	0.58	4.27	1.08	3.38	0.46	2.65	0.39
200	24.52	7.27	4.08	16.88	3.03	0.85	3.92	0.61	4.67	1.24	4.28	0.66	4.37	0.73
399	25.45	6.23	4.19	17.31	3.13	0.90	4.00	0.63	4.81	1.30	4.56	0.71	4.77	0.81
600	25.20	5.94	4.16	17.13	3.08	0.93	3.97	0.63	4.84	1.32	4.71	0.73	5.05	0.87
999	22.93	6.32	3.65	15.37	2.84	0.84	3.92	0.64	5.06	1.42	5.11	0.81	5.61	0.98
1249	24.33	6.69	3.93	16.61	3.07	0.92	4.26	0.70	5.54	1.53	5.48	0.86	5.98	1.03
1499	25.13	7.41	4.21	17.69	3.36	0.99	4.58	0.74	5.81	1.58	5.53	0.86	5.90	1.01
1999	26.01	7.39	4.38	18.57	3.53	1.05	4.81	0.77	6.02	1.61	5.57	0.86	5.92	1.00
2499	27.99	6.76	4.62	19.39	3.66	1.06	4.99	0.79	6.09	1.64	5.63	0.87	5.94	1.00

3000	31.46	6.28	5.08	21.44	3.96	1.13	5.27	0.82	6.36	1.70	5.80	0.90	6.18	1.04
3500	38.87	10.35	6.36	26.19	4.61	1.29	5.92	0.91	6.93	1.84	6.23	0.96	6.66	1.12
3999	37.85	6.26	6.45	26.68	4.74	1.35	6.03	0.93	6.96	1.81	6.13	0.95	6.50	1.09
4499	39.61	6.54	6.88	28.29	5.07	1.42	6.29	0.96	7.17	1.85	6.23	0.96	6.58	1.11
5106	41.79	9.27	7.39	30.06	5.38	1.49	6.56	1.00	7.37	1.90	6.36	0.98	6.68	1.10
Station 15 (13.6°S, 5°E, 5475 m)														
10	21.58	13.05	4.12	17.04	3.14	0.91	3.97	0.59	4.40	1.11	3.46	0.48	2.81	0.42
229	24.34	5.61	4.28	17.06	3.10	0.87	3.93	0.61	4.68	1.25	4.30	0.67	4.47	0.74
399	28.59	10.45	4.99	19.37	3.41	0.98	4.21	0.64	4.90	1.32	4.54	0.71	4.82	0.82
599	26.15	6.72	4.50	17.80	3.18	0.93	4.05	0.63	4.90	1.33	4.73	0.74	5.11	0.88
1000	24.06	6.95	4.13	16.53	3.03	0.92	3.99	0.63	5.04	1.41	5.07	0.80	5.62	0.97
1249	26.63	9.83	4.78	19.04	3.53	1.03	4.53	0.71	5.65	1.56	5.53	0.87	6.02	1.03
1499	28.35	11.59	5.26	20.97	3.97	1.14	5.03	0.79	6.19	1.67	5.80	0.91	6.23	1.05
1999	27.88	8.57	4.94	19.99	3.77	1.09	4.96	0.78	6.14	1.66	5.76	0.89	6.12	1.03
2500	28.01	7.46	4.79	19.64	3.69	1.09	4.92	0.77	6.13	1.64	5.67	0.88	6.06	1.02
2999	31.34	7.91	5.33	21.76	4.06	1.17	5.31	0.83	6.49	1.74	5.98	0.93	6.44	1.08
3499	38.02	6.62	6.43	25.77	4.61	1.31	5.84	0.89	6.89	1.83	6.23	0.96	6.66	1.12
3999	38.76	5.81	6.47	27.10	4.84	1.37	6.19	0.95	7.13	1.85	6.28	0.97	6.63	1.12
4499	40.40	5.86	6.98	28.58	5.16	1.46	6.40	0.98	7.28	1.89	6.33	0.97	6.69	1.13
5196	43.77	6.95	7.90	31.98	5.83	1.63	6.96	1.06	7.71	1.96	6.55	1.00	6.83	1.14
Station 17 (14.75°S, 10°E, 3830 m)														
10	33.20	30.84	6.49	25.81	4.60	1.27	5.19	0.78	5.53	1.35	4.19	0.59	3.54	0.53
200	24.86	7.44	4.35	17.50	3.19	0.87	3.97	0.62	4.66	1.23	4.20	0.64	4.26	0.71
399	29.22	11.87	4.99	19.88	3.47	0.98	4.22	0.66	4.90	1.30	4.47	0.70	4.73	0.80
600	27.48	7.89	4.70	18.86	3.35	0.96	4.15	0.65	4.96	1.35	4.73	0.74	5.10	0.87
999	24.22	7.56	4.00	16.39	3.04	0.90	4.01	0.65	5.14	1.45	5.17	0.82	5.74	1.00
1249	25.34	8.41	4.24	17.31	3.22	0.94	4.34	0.70	5.53	1.56	5.52	0.88	6.06	1.04
1500	27.03	9.67	4.67	19.62	3.57	1.04	4.76	0.77	6.01	1.65	5.76	0.90	6.22	1.05
1999	30.20	10.22	5.32	21.65	4.03	1.15	5.21	0.83	6.41	1.72	5.90	0.92	6.31	1.06
2500	31.16	9.08	5.32	21.77	4.04	1.17	5.25	0.83	6.44	1.73	5.92	0.92	6.33	1.07
3000	33.85	8.55	5.67	23.20	4.25	1.21	5.50	0.86	6.69	1.77	6.11	0.95	6.50	1.10
3400	41.54	8.24	7.00	28.18	5.01	1.40	6.22	0.96	7.27	1.92	6.52	1.01	6.94	1.16
3650	45.11	8.07	7.60	30.52	5.34	1.49	6.56	1.01	7.57	2.00	6.77	1.06	7.23	1.22
Station 18 (14.75°S, 11.5°E, 2660 m)														
10	45.18	44.76	8.75	34.47	6.17	1.67	6.63	1.00	6.88	1.63	5.08	0.73	4.49	0.68
200	24.20	9.74	4.34	17.60	3.22	0.91	3.92	0.61	4.52	1.18	4.00	0.61	3.95	0.65
399	27.33	8.53	4.61	18.72	3.32	0.98	4.15	0.65	4.87	1.30	4.51	0.70	4.68	0.80
599	27.42	9.13	4.60	18.44	3.27	0.94	4.10	0.65	4.92	1.33	4.69	0.74	5.00	0.86

Table 4.1 (Chapter 4)

$\delta^{13}C_{carb}$ and $\delta^{18}O_{carb}$ results of bulk chalk.

Sample	Height	Age[a]	Stable isotopes (‰$_{VPDB}$)[b]	
	(m)	(Ma)	$\delta^{13}C_{carb}$	$\delta^{18}O_{carb}$
HC1	0	94.13	2.708	-2.942
HC2	1	94.08	2.732	-2.886
HC2–replicate			2.668	-2.820
HC3	2	94.04	2.840	-3.269
HC3–replicate			2.805	-3.095
HC4	3	94.00	2.886	-3.341
HC4–replicate			2.848	-3.281
HC5	4	93.95	3.349	-3.469
HC5–replicate			3.317	-3.273
HC6	5	93.91	4.329	-2.909
HC6–replicate			4.341	-3.096
HC6a	5.5	93.89	4.384	-3.067
HC6a–replicate			4.505	-2.807
HC7	6	93.86	4.340	-2.924
HC7–replicate			4.481	-2.780
HC7a	6.5	93.84	4.148	-2.906
HC7a–replicate			4.184	-2.591
HC8	7	93.82	4.200	-2.856
HC8–replicate			4.055	-2.746
HC8a	7.5	93.80	4.248	-2.749
HC8a–replicate			4.134	-2.480
HC9	8	93.78	4.373	-3.568
HC9–replicate			4.413	-3.372
HC9a	8.5	93.76	4.603	-3.639
HC9a–replicate			4.621	-3.479
HC10	9	93.73	4.499	-3.540
HC10–replicate			4.625	-3.547
HC11	10	93.69	4.789	-3.722
HC11–replicate			4.956	-3.683
HC12	11	93.65	4.782	-3.992
HC12–replicate			4.786	-3.891
HC13	12	93.60	4.684	-3.423
HC14	13	93.56	4.710	-3.313
HC14–replicate			4.644	-3.086
HC15	14	93.52	4.728	-3.634
HC16	15	93.49	4.727	-3.752
HC17	16	93.45	4.561	-3.577
HC17–replicate			4.410	-3.469
HC18	17	93.41	4.091	-3.801
HC19	18	93.38	3.767	-4.091
HC20	19	93.34	3.873	-3.607

HC20–replicate			3.873	-3.550
HC21	20	93.31	3.675	-4.050
HC22	21	93.27	3.723	-3.559
HC23	22	93.24	3.687	-3.658
HC23–replicate			3.680	-3.510
HC24	23	93.20	3.616	-3.540
HC25	24	93.16	3.391	-3.795
HC26	25	93.13	3.320	-3.947

[a]Age model is based on Voigt et al. (2008), see details in 3.4. The same below.

[b]Where replicates are available, average values are plotted in Fig. 4.2 and 4.4.

Table 4.2 (Chapter 4)

ε_{Nd} and La_N/Sm_N of fish debris from Eastbourne.

Sample[a]	Height (m)	Age (Ma)	$^{143}Nd/^{144}Nd$	2*SE	$^{147}Sm/^{144}Nd$	$\varepsilon_{Nd}(0)$	$\varepsilon_{Nd}(t)$[b]	La_N/Sm_N[c]
FISH DEBRIS								
HC1	0	94.13	0.512124	0.000012	0.1261	-10.0	-9.2	0.89
HC2	1	94.08	0.512127	0.000008	0.1279	-10.0	-9.1	0.77
HC3	2	94.04	0.512111	0.000010	0.1219	-10.3	-9.4	0.89
HC4	3	94.00	0.512118	0.000012	0.1201	-10.2	-9.2	0.98
HC5	4	93.95	0.512121	0.000006	0.1259	-10.1	-9.2	0.73
HC5 – Teeth			*0.512121*	*0.000006*	*0.1259*	*-10.1*	*-9.2*	
HC5 – Bones			*0.512113*	*0.000006*	*0.1270*	*-10.2*	*-9.4*	
HC6	5	93.91	0.512081	0.000010	0.1218	-10.9	-10.0	0.82
HC6a	5.5	93.89	0.512076	0.000006	0.1236	-11.0	-10.1	0.98
HC7	6	93.86	0.512084	0.000011	0.1209	-10.8	-9.9	0.83
HC7a	6.5	93.84	0.512119	0.000007	0.1152	-10.1	-9.2	0.92
HC8	7	93.82	0.512129	0.000011	0.1160	-9.9	-9.0	0.90
HC8a	7.5	93.80	0.512185	0.000006	0.1226	-8.8	-8.0	0.78
HC9	8	93.78	0.512206	0.000009	0.1210	-8.4	-7.5	0.90
HC9 – Teeth			*0.512206*	*0.000009*	*0.1210*	*-8.4*	*-7.5*	
HC9 – Bones			*0.512195*	*0.000006*	*0.1203*	*-8.6*	*-7.7*	
HC9a	8.5	93.76	0.512145	0.000007	0.1221	-9.6	-8.7	1.00
HC10	9	93.73	0.512171	0.000011	0.1305	-9.1	-8.3	1.02
HC11	10	93.69	0.512148	0.000007	0.1198	-9.6	-8.7	0.88
HC12	11	93.65	0.512117	0.000012	0.1189	-10.2	-9.2	0.96
HC12 – Teeth			*0.512117*	*0.000012*	*0.1189*	*-10.2*	*-9.2*	
HC12 – Bones			*0.512144*	*0.000006*	*0.1160*	*-9.6*	*-8.7*	
HC13	12	93.60	0.512103	0.000011	0.1171	-10.4	-9.5	0.89
HC14	13	93.56	0.512080	0.000006	0.1194	-10.9	-10.0	0.98
HC15	14	93.52	0.512092	0.000006	0.1182	-10.7	-9.7	0.92
HC15 – Teeth			*0.512092*	*0.000006*	*0.1182*	*-10.7*	*-9.7*	
HC15 – Bones			*0.512102*	*0.000006*	*0.1166*	*-10.4*	*-9.5*	
HC16	15	93.49	0.512090	0.000016	0.1106	-10.7	-9.7	1.52
HC16 – Teeth			*0.512090*	*0.000016*	*0.1106*	*-10.7*	*-9.7*	
HC16 – Bones			*0.512100*	*0.000007*	*0.1124*	*-10.5*	*-9.5*	
HC17	16	93.45	0.512074	0.000008	0.1162	-11.0	-10.0	0.96
HC17 – Teeth			*0.512074*	*0.000008*	*0.1162*	*-11.0*	*-10.0*	
HC17 – Bones			*0.512089*	*0.000006*	*0.1247*	*-10.7*	*-9.8*	
HC18	17	93.41	0.512053	0.000006	0.1155	-11.4	-10.4	1.04
HC19	18	93.38	0.512053	0.000007	0.1196	-11.4	-10.5	0.87
HC20	19	93.34	0.512038	0.000007	0.1168	-11.7	-10.7	1.22
HC20 – Teeth			*0.512038*	*0.000007*	*0.1168*	*-11.7*	*-10.7*	
HC20 – Bones			*0.512054*	*0.000006*	*0.1174*	*-11.4*	*-10.4*	

HC21	20	93.31	0.512041	0.000006	0.1105	-11.6	-10.6	1.14
HC22	21	93.27	0.512048	0.000007	0.1143	-11.5	-10.5	1.08
HC23	22	93.24	0.512053	0.000006	0.1142	-11.4	-10.4	1.07
HC24	23	93.20	0.512055	0.000006	0.1149	-11.4	-10.4	0.99
HC25	24	93.16	0.512048	0.000006	0.1145	-11.5	-10.5	0.96
HC26	25	93.13	0.512044	0.000007	0.1138	-11.6	-10.6	1.02
DETRITUS								
HC4	3	94.00	0.511978	0.000007	0.1023	-12.9	-11.7	
HC8	7	93.82	0.511962	0.000005	0.1063	-13.2	-12.1	
HC9	8	93.78	0.511991	0.000007	0.1060	-12.6	-11.5	
HC10	9	93.73	0.512004	0.000007	0.1046	-12.4	-11.3	
HC16	15	93.49	0.512002	0.000012	0.1035	-12.4	-11.3	

[a]Results of fish tooh–bone pairs from the same stratigraphic levels are listed in Italics.

[b]All εNd(t) results from the same stratigraphic level are averaged and plotted in Fig. 2 and 4.

[c]North American Shale Composite (NASC) normalized values. NASC values are taken from Gromet et al. (1984).

Table 5.1 (Chapter 5)

Results of bulk-carbonate $\delta^{13}C$

Sample	Height (m)	$\delta^{13}C$ (‰$_{VPDB}$)	Sample	Height (m)	$\delta^{13}C$ (‰$_{VPDB}$)	Sample	Height (m)	$\delta^{13}C$ (‰$_{VPDB}$)
S99/0832	1.55	1.95	S99/0942	5.55	2.34	O99/1388	9.35	2.55
S99/0833	1.60	1.94	O99/1568	5.55	2.35	O99/1389	9.40	2.58
S99/0834	1.65	1.85	O99/1569	5.60	2.36	O99/1390	9.45	2.54
S99/0835	1.70	1.92	S99/0943	5.60	2.30	O99/1391	9.50	2.48
S99/0836	1.75	1.91	O99/1570	5.65	2.47	O99/1392	9.55	2.45
S99/0837	1.80	1.90	S99/0944	5.65	2.41	O99/1393	9.60	2.46
S99/0838	1.85	1.90	S99/0945	5.70	2.41	O99/1394	9.65	2.42
S99/0839	1.90	1.86	O99/1571	5.70	2.44	O99/1395	9.70	2.45
S99/0840	1.95	1.86	S99/0946	5.75	2.46	O99/1396	9.75	2.34
S99/0841	2.00	1.86	O99/1572	5.75	2.53	O99/1397	9.80	2.34
S99/0842	2.05	1.87	O99/1573	5.80	2.47	O99/1398	9.85	2.32
S99/0843	2.10	1.90	S99/0947	5.80	2.43	O99/1399	9.90	2.34
S99/0844	2.15	1.85	S99/0948	5.85	2.42	O99/1552	9.95	2.34
S99/0845	2.20	1.82	O99/1574	5.85	2.48	O99/1411	10.00	2.39
S99/0846	2.25	1.80	S99/0949	5.90	2.41	O99/1412	10.05	2.43
O99/1561	2.30	1.80	O99/1575	5.90	2.46	O99/1413	10.10	2.38
S99/0848	2.35	1.77	S99/0950	5.95	2.40	O99/1414	10.15	2.32
S99/0849	2.40	1.81	S99/0951	6.00	2.46	O99/1415	10.20	2.37
S99/0850	2.45	1.78	S99/0952	6.05	2.41	O99/1416	10.25	2.26
S99/0851	2.50	1.84	S99/0953	6.10	2.43	O99/1417	10.30	2.26
S99/0852	2.55	1.80	S99/0954	6.15	2.36	O99/1418	10.35	2.31
S99/0853	2.60	1.84	S99/0955	6.20	2.38	O99/1419	10.40	2.26
S99/0854	2.65	1.89	O99/1576	6.20	2.36	O99/1420	10.45	2.30
S99/0855	2.70	1.87	S99/0956	6.25	2.45	O99/1401	10.50	2.26
S99/0856	2.75	1.89	S99/0957	6.30	2.48	O99/1402	10.55	2.23
S99/0857	2.80	1.89	S99/0958	6.35	2.45	O99/1403	10.60	2.24
S99/0858	2.85	1.89	S99/0959	6.40	2.48	O99/1404	10.65	2.18
S99/0859	2.90	1.87	S99/0960	6.45	2.49	O99/1405	10.70	2.30
S99/0860	2.95	1.85	S99/0961	6.50	2.50	O99/1406	10.75	2.25
S99/0891	3.00	1.91	S99/0962	6.55	2.46	O99/1407	10.80	2.27
S99/0892	3.05	1.86	S99/0963	6.60	2.38	O99/1408	10.85	2.27
S99/0893	3.10	1.90	S99/0964	6.65	2.37	O99/1409	10.90	2.27
S99/0894	3.15	1.91	S99/0965	6.70	2.36	O99/1410	10.95	2.25
S99/0895	3.20	1.86	S99/0966	6.75	2.22	O99/1421	11.00	2.34
S99/0896	3.25	1.84	O99/1577	6.80	2.33	O99/1422	11.05	2.35
S99/0897	3.30	1.87	S99/0968	6.85	2.34	O99/1423	11.10	2.30
S99/0898	3.35	1.82	S99/0969	6.90	2.23	O99/1424	11.15	2.30
S99/0899	3.40	1.85	S99/0970	6.95	2.29	O99/1425	11.20	2.32
S99/0900	3.45	1.82	O99/1341	7.00	2.18	O99/1426	11.25	2.29
O99/1562	3.45	1.82	O99/1342	7.05	2.23	O99/1427	11.30	2.28
S99/0901	3.50	1.84	O99/1343	7.10	2.20	O99/1428	11.35	2.29
O99/1563	3.50	1.87	O99/1344	7.15	2.22	O99/1429	11.40	2.28
S99/0902	3.55	1.82	O99/1578	7.20	2.32	O99/1430	11.45	2.26
S99/0903	3.60	1.80	O99/1579	7.25	2.31	O99/1431	11.50	2.28
S99/0904	3.65	1.82	O99/1347	7.30	2.38	O99/1432	11.55	2.31
S99/0905	3.70	1.84	O99/1348	7.35	2.39	O99/1433	11.60	2.24
S99/0906	3.75	1.82	O99/1349	7.40	2.43	O99/1434	11.65	2.25
S99/0907	3.80	1.86	O99/1350	7.45	2.26	O99/1435	11.70	2.21
S99/0908	3.85	1.90	O99/1351	7.50	2.17	O99/1436	11.75	2.24

S99/0909	3.90	1.88	O99/1352	7.55	2.13	O99/1437	11.80	2.23
S99/0910	3.95	1.94	O99/1353	7.60	2.11	O99/1438	11.85	2.26
S99/0911	4.00	1.84	O99/1354	7.65	2.17	O99/1553	11.90	2.25
O99/1564	4.00	1.90	O99/1355	7.70	2.32	O99/1554	11.95	2.32
S99/0912	4.05	1.90	O99/1580	7.75	2.14	O99/1441	12.00	2.21
S99/0913	4.10	1.94	O99/1581	7.80	2.17	O99/1442	12.05	2.23
S99/0914	4.15	1.95	O99/1358	7.85	2.36	O99/1443	12.10	2.22
S99/0915	4.20	1.92	O99/1582	7.90	2.48	O99/1444	12.15	2.22
S99/0916	4.25	1.91	O99/1360	7.95	2.46	O99/1445	12.20	2.26
S99/0917	4.30	1.93	O99/1361	8.00	2.35	O99/1447	12.30	2.21
S99/0918	4.35	1.91	O99/1362	8.05	2.31	O99/1448	12.35	2.20
S99/0919	4.40	1.96	O99/1363	8.10	2.39	O99/1449	12.40	2.19
S99/0920	4.45	1.92	O99/1364	8.15	2.31	O99/1450	12.45	2.20
S99/0921	4.50	1.88	O99/1365	8.20	2.39	O99/1451	12.50	2.17
S99/0922	4.55	1.95	O99/1366	8.25	2.48	O99/1452	12.55	2.19
S99/0923	4.60	1.91	O99/1367	8.30	2.45	O99/1453	12.60	2.18
S99/0924	4.65	2.10	O99/1368	8.35	2.48	O99/1454	12.65	2.17
O99/1565	4.65	2.03	O99/1369	8.40	2.49	O99/1455	12.70	2.17
S99/0925	4.70	2.00	O99/1370	8.45	2.34	O99/1456	12.75	2.19
O99/1566	4.70	2.07	O99/1371	8.50	2.47	O99/1555	12.80	2.26
O99/1567	4.75	2.11	O99/1372	8.55	2.56	O99/1458	12.85	2.19
S99/0927	4.80	2.02	O99/1373	8.60	2.55	O99/1459	12.90	2.27
S99/0928	4.85	2.04	O99/1551	8.65	2.43	O99/1556	12.95	2.26
S99/0929	4.90	2.05	O99/1375	8.70	2.55	O99/1461	13.00	2.20
S99/0930	4.95	2.10	O99/1376	8.75	2.57	O99/1557	13.05	2.23
S99/0931	5.00	2.04	O99/1377	8.80	2.54	O99/1463	13.10	2.19
S99/0932	5.05	2.10	O99/1378	8.85	2.52	O99/1464	13.15	2.28
S99/0933	5.10	2.08	O99/1379	8.90	2.52	O99/1465	13.20	2.23
S99/0934	5.15	2.12	O99/1380	8.95	2.47	O99/1558	13.25	2.29
S99/0935	5.20	2.13	O99/1381	9.00	2.32	O99/1467	13.30	2.30
S99/0936	5.25	2.03	O99/1382	9.05	2.34	O99/1559	13.35	2.20
S99/0937	5.30	2.11	O99/1383	9.10	2.42	O99/1469	13.40	2.25
S99/0938	5.35	2.08	O99/1384	9.15	2.44	O99/1470	13.45	2.26
S99/0939	5.40	2.18	O99/1385	9.20	2.48	O99/1471	13.50	2.22
S99/0940	5.45	2.09	O99/1386	9.25	2.58			
S99/0941	5.50	2.16	O99/1387	9.30	2.56			

Table 5.2 (Chapter 5)

Results of ε_{Nd} and La_N/Sm_N in fish debris.

Sample	Height (m)	Age (Ma)	$^{143}Nd/^{144}Nd$ (0)	2σ	$^{147}Sm/^{144}Nd$ (0)	$\varepsilon_{Nd}(0)$	$\varepsilon_{Nd}(t)$[a]	La_N/Sm_N[b]
FISH DEBRIS								
LS05a	-0.5	96.59	0.512148	0.000005	0.1218	-9.6	-8.6	0.7
LS04a	0.0	96.58	0.512118	0.000010	0.1268	-10.1	-9.3	0.7
LS03a	0.5	96.56	0.512136	0.000009	0.1229	-9.8	-8.9	0.8
LS02a	1.0	96.54	0.512126	0.000006	0.1221	-10.0	-9.1	0.8
LS01a	1.5	96.53	0.512106	0.000009	0.1211	-10.4	-9.4	0.6
LS1	2.0	96.51	0.512116	0.000009	0.1208	-10.2	-9.3	0.7
LS2	2.5	96.49	0.512124	0.000010	0.1224	-10.0	-9.1	0.8
LS3	3.0	96.47	0.512128	0.000008	0.1205	-9.9	-9.0	0.8
LS4	3.5	96.46	0.512077	0.000007	0.1266	-10.9	-10.1	0.5
LS5	4.0	96.44	0.512107	0.000010	0.1154	-10.4	-9.4	0.7
LS6	4.5	96.42	0.512122	0.000008	0.1231	-10.1	-9.2	0.6
LS7	5.0	96.41	0.512124	0.000010	0.1204	-10.0	-9.1	0.7
LS8	5.5	96.39	0.512102	0.000009	0.1190	-10.4	-9.5	0.6
LS9	6.0	96.37	0.512092	0.000008	0.1259	-10.7	-9.8	0.5
LS10	6.5	96.36	0.512113	0.000011	0.1196	-10.2	-9.3	0.7
LS1a	7.0	96.34	0.512089	0.000007	0.1215	-10.7	-9.8	0.7
LS2a	7.5	96.32	0.512097	0.000006	0.1238	-10.6	-9.7	0.6
LS3a	8.0	96.31	0.512128	0.000008	0.1209	-9.9	-9.0	0.8
LS4a	8.5	96.29	0.512129	0.000011	0.1205	-9.9	-9.0	0.8
LS5a	9.0	96.27	0.512123	0.000007	0.1223	-10.1	-9.1	0.7
LS6a	9.5	96.26	0.512127	0.000008	0.1207	-10.0	-9.0	0.8
LS7a	10.0	96.24	0.512127	0.000007	0.1196	-10.0	-9.0	0.8
LS8a	10.5	96.22	0.512127	0.000007	0.1217	-10.0	-9.1	0.8
BULK CARBONATE								
LS02a_carb	1.0	96.54	0.512119	0.000006	0.1146	-10.1	-9.1	
LS2_carb	2.5	96.49	0.512125	0.000010	0.1034	-10.0	-8.9	
LSP6_carb	3.2	96.47	0.512100	0.000008	0.1127	-10.5	-9.5	
LSP7_carb	3.3	96.46	0.512089	0.000007	0.1091	-10.7	-9.6	
LS4_carb	3.5	96.46	0.512073	0.000009	0.1104	-11.0	-10.0	
LSP11_carb	3.7	96.45	0.512072	0.000008	0.1132	-11.0	-10.0	
LSP12_carb	3.8	96.45	0.512091	0.000008	0.1207	-10.7	-9.7	
LSP16_carb	4.2	96.43	0.512106	0.000008	0.1144	-10.4	-9.4	
LSP20_carb	4.6	96.42	0.512112	0.000008	0.1115	-10.3	-9.2	
LS7_carb	5.0	96.41	0.512121	0.000008	0.1092	-10.1	-9.0	
LSP25_carb	5.2	96.40	0.512107	0.000008	0.1177	-10.3	-9.4	
LSP31_carb	5.9	96.38	0.512084	0.000008	0.1084	-10.8	-9.7	
LS9_carb	6.0	96.37	0.512107	0.000009	0.1126	-10.3	-9.3	

LSP33_carb	6.1	96.37	0.512119	0.000008	0.1161	-10.1	-9.1
LSP39_carb	6.7	96.35	0.512109	0.000008	0.1050	-10.3	-9.2
LS3a_carb	8.0	96.31	0.512113	0.000007	0.1151	-10.2	-9.2
LS5a_carb	9.0	96.27	0.512108	0.000008	0.1061	-10.3	-9.2
LS7a_carb	10.0	96.24	0.512141	0.000008	0.1083	-9.7	-8.6

[a] $\varepsilon_{Nd}(t) = \{[^{143}Nd/^{144}Nd_{sample}(t) / {}^{143}Nd/^{144}Nd_{CHUR}(t)] - 1\} \times 10^4$; $^{143}Nd/^{144}Nd(t) = {}^{143}Nd/^{144}Nd(0) - {}^{147}Sm/^{144}Nd(0) \times [EXP(\lambda_{Sm} \times T) - 1]$; λ_{Sm} (decay constant of ^{147}Sm) = 6.54×10^{-12} yr^{-1}; T: age; $^{147}Sm/^{144}Nd_{CHUR}(0) = 0.1967$, $^{143}Nd/^{144}Nd_{CHUR}(0) = 0.512638$ (Patchett et al., 2004)

[b] North American Shale Composite (NASC) normalized values. NASC values are taken from Gromet et al. (1984).

Table 5.3

Results of REE-concentrations (ppm) in fish debris.

(ppm)	La	Ce	Pr	Nd	Sm	Eu	Gd	Tb	Dy	Ho	Er	Tm	Yb	Lu
LS_05a	553.7	931.9	167.6	701.2	141.4	29.0	144.8	19.6	109.2	18.9	43.8	4.2	19.6	2.5
LS_04a	1355.9	2394.4	412.2	1724.2	361.9	74.6	354.5	49.0	278.4	47.5	111.3	11.5	54.5	7.1
LS_03a	673.4	1092.8	185.1	765.8	155.8	32.7	166.6	23.1	131.9	24.3	58.4	5.9	28.7	3.6
LS_02a	5803.3	9782.1	1660.7	6875.3	1389.2	294.5	1432.7	200.1	1136.8	201.7	478.2	47.5	218.1	27.5
LS_01a	1895.5	3948.2	695.6	2929.6	587.3	126.2	547.3	70.7	361.0	60.9	133.0	12.9	55.4	6.5
LS1	632.4	1189.8	203.3	857.4	171.4	34.8	163.2	21.8	116.4	20.7	46.7	4.6	20.7	2.6
LS2	184.6	296.7	48.7	202.5	41.0	8.7	43.0	6.3	36.5	6.8	16.6	1.7	8.2	1.1
LS3	480.7	822.5	139.3	571.7	114.1	22.3	111.5	15.2	89.4	16.3	38.5	3.8	17.8	2.2
LS4	2148.0	4776.3	879.9	3756.5	786.9	148.1	662.8	86.3	435.4	71.5	157.1	15.7	70.7	8.6
LS5	848.8	1635.5	273.6	1132.5	216.3	45.5	213.8	28.8	155.8	27.3	59.9	5.5	23.5	3.0
LS6	613.3	1282.7	212.0	887.5	180.8	35.0	160.5	23.0	114.7	20.2	45.6	4.7	20.4	2.4
LS7	306.8	542.1	91.6	382.0	76.1	16.2	76.1	10.6	58.9	10.3	23.2	2.2	9.8	1.2
LS8	524.5	995.9	175.9	737.7	145.3	30.4	140.8	19.4	103.1	18.1	40.3	3.9	16.7	2.1
LS9	38.0	76.5	13.9	59.8	12.4	2.2	10.2	1.3	7.0	1.2	2.7	0.3	1.2	0.1
LS10	233.1	416.7	70.9	291.1	57.6	11.4	54.1	7.6	42.1	7.5	17.0	1.7	7.5	1.0
LS_1a	504.7	863.8	153.6	641.2	129.0	27.3	131.9	18.1	103.6	18.3	41.0	3.8	17.0	2.1
LS_2a	63.9	121.3	22.6	95.0	19.5	4.0	17.9	2.4	12.9	2.2	4.7	0.5	1.9	0.2
LS_3a	645.2	1070.0	184.7	756.8	151.4	33.2	157.7	22.3	128.1	23.1	53.4	5.1	23.0	2.8
LS_4a	216.5	364.0	61.3	251.3	50.1	11.1	52.2	7.4	44.2	7.8	18.6	1.9	8.9	1.1
LS_5a	145.6	262.0	45.6	190.6	38.6	8.8	39.4	5.5	30.5	5.5	12.8	1.2	5.8	0.7
LS_6a	not determined due to a weighing error													
LS_7a	82.7	139.4	23.5	97.6	19.3	4.5	20.1	2.9	16.7	3.0	7.3	0.7	3.5	0.4
LS_8a	720.8	1222.0	210.6	854.5	172.1	36.9	168.8	23.2	130.2	22.7	54.1	5.2	25.2	3.1

Bibliography

Akagi, T., 2013. Rare earth element (REE)–silicic acid complexes in seawater to explain the incorporation of REEs in opal and the "leftover" REEs in surface water: New interpretation of dissolved REE distribution profiles. Geochimica et Cosmochimica Acta, 113: 174–192.

Akagi, T., Fu, F.-f., Hongo, Y., Takahashi, K., 2011. Composition of rare earth elements in settling particles collected in the highly productive North Pacific Ocean and Bering Sea: Implications for siliceous-matter dissolution kinetics and formation of two REE-enriched phases. Geochimica et Cosmochimica Acta, 75: 4857–4876.

Alibo, D.S., Nozaki, Y., 1999. Rare earth elements in seawater: particle association, shale-normalization, and Ce oxidation. Geochimica Et Cosmochimica Acta, 63: 363–372.

Allen, D.E., Seyfried Jr, W.E., 2005. REE controls in ultramafic hosted MOR hydrothermal systems: An experimental study at elevated temperature and pressure. Geochimica et Cosmochimica Acta, 69: 675–683.

Ando, A., Huber, B.T., MacLeod, K.G., Ohta, T., Khim, B.-K., 2009. Blake Nose stable isotopic evidence against the mid-Cenomanian glaciation hypothesis. Geology, 37: 451–454.

Arhan, M., Mercier, H., Park, Y.-H., 2003. On the deep water circulation of the eastern South Atlantic Ocean. Deep Sea Research Part I: Oceanographic Research Papers, 50: 889–916.

Arsouze, T., Dutay, J.C., Lacan, F., Jeandel, C., 2009. Reconstructing the Nd oceanic cycle using a coupled dynamical - biogeochemical model. Biogeosciences, 6: 2829–2846.

Arthur, M., Schlanger, S.O., Jenkyns, H., 1987. The Cenomanian-Turonian Oceanic Anoxic Event, II. Palaeoceanographic controls on organic-matter production and preservation. Geological Society, London, Special Publications, 26: 401–420.

Arthur, M.A., Dean, W.E., Pratt, L.M., 1988. Geochemical and climatic effects of increased marine organic carbon burial at the Cenomanian/Turonian boundary. Nature, 335: 714–717.

Bahramifar, N., Yamini, Y., 2005. On-line preconcentration of some rare earth elements in water samples using C_{18}-cartridge modified with l-(2-pyridylazo) 2-naphtol (PAN) prior to simultaneous determination by inductively coupled plasma optical emission spectrometry (ICP–OES). Analytica Chimica Acta, 540: 325–332.

Balashov, Y.A., Khitrov, L., 1961. Distribution of the rare earths in the waters of the Indian Ocean. Geochem. Int, 9: 877–890.

Barrera, E., Savin, S.M., Thomas, E., Jones, C.E., 1997. Evidence for thermohaline-circulation reversals controlled by sea-level change in the lastest Cretaceous. Geology 25, 715–718.

Barron, E.J., 1983. A warm, equable Cretaceous: The nature of the problem. Earth-Science Reviews, 19: 305–338.

Barron, E.J., Peterson, W.H., 1989. Model Simulation of the Cretaceous Ocean Circulation. Science, 244: 684–686.

Bau, M., Dulski, P., 1996. Anthropogenic origin of positive gadolinium anomalies in river waters. Earth and Planetary Science Letters, 143: 245–255.

Bau, M., Dulski, P., 1999. Comparing yttrium and rare earths in hydrothermal fluids from the Mid-Atlantic Ridge: implications for Y and REE behaviour during near-vent mixing and for the Y/Ho ratio of Proterozoic seawater. Chemical Geology, 155: 77–90.

Bau, M., Möller, P., Dulski, P., 1997. Yttrium and lanthanides in eastern Mediterranean seawater and their fractionation during redox-cycling. Marine Chemistry, 56: 123–131.

Bau, M., Tepe, N., Mohwinkel, D., 2013. Siderophore-promoted transfer of rare earth elements and iron from volcanic ash into glacial meltwater, river and ocean water. Earth and Planetary Science Letters, 364: 30–36.

Bayon, G., Birot, D., Bollinger, C., Barrat, J.A., 2011. Multi-element determination of trace elements in natural water reference materials by ICP-SFMS after Tm addition and iron co-precipitation. Geostandards and Geoanalytical Research, 35: 145–153.

Bayon, G. et al., 2002. An improved method for extracting marine sediment fractions and its application to Sr and Nd isotopic analysis. Chemical Geology, 187: 179–199.

Bayon, G., German, C.R., Burton, K.W., Nesbitt, R.W., Rogers, N., 2004. Sedimentary Fe-Mn oxyhydroxides as paleoceanographic archives and the role of aeolian flux in regulating oceanic dissolved REE. Earth and Planetary Science Letters, 224: 477–492.

Bennett, S.A. et al., 2008. The distribution and stabilisation of dissolved Fe in deep-sea hydrothermal plumes. Earth and Planetary Science Letters, 270: 157–167.

Berner, R.A., Kothavala, Z., 2001. Geocarb III: A Revised Model of Atmospheric CO2 over Phanerozoic Time. American Journal of Science, 301: 182–204.

Bertram, C.J., Elderfield, H., 1993. The geochemical balance of the rare earth elements and neodymium isotopes in the oceans. Geochimica Et Cosmochimica Acta, 57: 1957–1986.

Blättler, C.L., Jenkyns, H.C., Reynard, L.M., Henderson, G.M., 2011. Significant increases in global weathering during Oceanic Anoxic Events 1a and 2 indicated by calcium isotopes. Earth and Planetary Science Letters, 309: 77–88.

Bourbon, É., 2008. Neodymium isotopes throughout the North Atlantic in the Late Cretaceous and across the Oceanic Anoxic Event 2. Thesis Thesis, University of Florida, 147 pp.

Boyd, P.W. et al., 2007. Mesoscale Iron Enrichment Experiments 1993-2005: Synthesis and Future Directions. Science, 315: 612–617.

Boyle, E.A., 1981. Cadmium, zinc, copper, and barium in foraminifera tests. Earth and Planetary Science Letters, 53: 11–35.

Boyle, E.A., Keigwin, L.D., 1985. Comparison of Atlantic and Pacific paleochemical records for the last 215,000 years: changes in deep ocean circulation and chemical inventories. Earth and Planetary Science Letters, 76: 135–150.

Brady, E.C., DeConto, R.M., Thompson, S.L., 1998. Deep Water Formation and Poleward Ocean Heat Transport in the Warm Climate Extreme of the Cretaceous (80 Ma). Geophys. Res. Lett., 25.

Bralower, T.J., Thierstein, H.R., 1984. Low productivity and slow deep-water circulation in Mid-Cretaceous oceans. Geology, 12: 614–618.

Brass, G.W., Southam, J.R., Peterson, W.H., 1982. Warm saline bottom water in the ancient ocean. Nature, 296: 620–623.

Broecker, W.S., Blanton, S., Smethie, W.M., Ostlund, G., 1991. Radiocarbon decay and oxygen utilization in the Deep Atlantic Ocean. Global Biogeochemical Cycles, 5: 87–117.

Bruland, K., Lohan, M., 2006. Controls of trace metals in seawater. The oceans and marine geochemistry. Elsevier: 23–47.

Burton, K.W., Vance, D., 2000. Glacial-interglacial variations in the neodymium isotope composition of seawater in the Bay of Bengal recorded by planktonic foraminifera. Earth and Planetary Science Letters, 176: 425–441.

Byrne, R.H., Kim, K.-H., 1990. Rare earth element scavenging in seawater. Geochimica et Cosmochimica Acta, 54: 2645–2656.

Byrne, R.H., Sholkovitz, E.R., 1996. Marine chemistry and geochemistry of the lanthanides. In: Gschneidner Jr., K.A., Eyring, L. (Eds.), Handbook on the physics and chemistry of rare earths. Elsevier, pp. 497–593.

Carter, P., Vance, D., Hillenbrand, C.D., Smith, J.A., Shoosmith, D.R., 2012. The neodymium isotopic composition of waters masses in the eastern Pacific sector of the Southern Ocean. Geochimica Et Cosmochimica Acta, 79: 41–59.

Chamberlin, T., 1906. On a possible reversal of deep-sea circulation and its influence on geologic climates. The Journal of Geology, 14: 363–373.

Chandrasekaran, K., Karunasagar, D., Arunachalam, J., 2012. Dispersive liquid-liquid micro-extraction for simultaneous preconcentration of 14 lanthanides at parts per trillion levels from groundwater and determination using a micro-flow nebulizer in inductively coupled plasma-quadrupole mass spectrometry. Journal of Analytical Atomic Spectrometry, 27: 1024–1031.

Charbonnier, G. et al., 2012. Reconstruction of the Nd isotope composition of seawater on epicontinental seas: testing the potential of Fe–Mn oxyhydroxide coatings on foraminifera tests for deep-time investigations. Geochimica et Cosmochimica Acta, 99: 39–56.

Chen, T.-Y., Frank, M., Haley, B.A., Gutjahr, M., Spielhagen, R.F., 2012. Variations of North Atlantic inflow to the central Arctic Ocean over the last 14 million years inferred from hafnium and neodymium isotopes. Earth and Planetary Science Letters, 353–354: 82–92.

Chen, T.-Y., Stumpf, R., Frank, M., Bełdowski, J., Staubwasser, M., 2013. Contrasting geochemical cycling of hafnium and neodymium in the central Baltic Sea. Geochimica et Cosmochimica Acta, 123: 166–180.

Christenson, E.A., Schijf, J., 2011. Stability of YREE complexes with the trihydroxamate siderophore desferrioxamine B at seawater ionic strength. Geochimica Et Cosmochimica Acta, 75: 7047–7062.

Chung, C.-H., Brenner, I., You, C.-F., 2009. Comparison of microconcentric and membrane-desolvation sample introduction systems for determination of low rare earth element concentrations in surface and subsurface waters using sector field inductively coupled plasma mass spectrometry. Spectrochimica Acta Part B: Atomic Spectroscopy, 64: 849–856.

Coccioni, R., Galeotti, S., 2003. The mid-Cenomanian Event: prelude to OAE 2. Palaeogeography, Palaeoclimatology, Palaeoecology, 190: 427–440.

Copard, K. et al., 2010. Nd isotopes in deep-sea corals in the North-eastern Atlantic. Quaternary Science Reviews, 29: 2499–2508.

Craddock, P.R. et al., 2010. Rare earth element abundances in hydrothermal fluids from the Manus Basin, Papua New Guinea: indicators of sub-seafloor

hydrothermal processes in back-arc basins. Geochimica et Cosmochimica Acta, 74: 5494–5513.

De Baar, H.J.W., Bacon, M.P., Brewer, P.G., 1983. Rare-earth distributions with a positive Ce anomaly in the Western North Atlantic Ocean. Nature, 301: 324–327.

De Baar, H.J.W., Bacon, M.P., Brewer, P.G., Bruland, K.W., 1985. Rare earth elements in the Pacific and Atlantic Oceans. Geochimica et Cosmochimica Acta, 49: 1943–1959.

de Baar, H.J.W., German, C.R., Elderfield, H., van Gaans, P., 1988. Rare earth element distributions in anoxic waters of the Cariaco Trench. Geochimica et Cosmochimica Acta, 52: 1203–1219.

DePaolo, D.J., Wasserburg, G.J., 1976. Nd isotopic variations and petrogenetic models. Geophysical Research Letters, 3: 249–252.

Douville, E. et al., 1999. Yttrium and rare earth elements in fluids from various deep-sea hydrothermal systems. Geochimica et Cosmochimica Acta, 63: 627–643.

Draxler, R.R., Rolph, G.D., 2013. HYSPLIT (HYbrid Single-Particle Lagrangian Integrated Trajectory) Model access via NOAA ARL READY Website (http://www.arl.noaa.gov/HYSPLIT.php). NOAA Air Resources Laboratory, College Park, MD.

Dupré, B., Gaillardet, J., Rousseau, D., Allègre, C.J., 1996. Major and trace elements of river-borne material: The Congo Basin. Geochimica et Cosmochimica Acta, 60: 1301–1321.

Elderfield, H., Greaves, M., 1983a. Determination of the rare earth elements in sea water. In: Wong, C.S., Boyle, E., Bruland, K.W., Burton, J.D., Goldberg, E.D. (Eds.), Trace Metals in Sea Water. Plenum Press, New York, pp. 427–445.

Elderfield, H., Greaves, M.J., 1982. The rare earth elements in seawater. Nature, 296: 214–219.

Elderfield, H., Greaves, M.J., 1983b. Determination of the rare earth elements in sea water. In: Wong, C.S., Boyle, E., Bruland, K.W., Burton, J.D., Goldberg, E.D. (Eds.), Trace metals in sea water. Plenum, New York, pp. 427–445.

Elderfield, H., Upstill-Goddard, R., Sholkovitz, E.R., 1990. The rare earth elements in rivers, estuaries, and coastal seas and their significance to the composition of ocean waters. Geochimica et Cosmochimica Acta, 54: 971–991.

Elderfield, H., Whitfield, M., Burton, J.D., Bacon, M.P., Liss, P.S., 1988. The oceanic chemistry of the rare-earth elements. Philosophical Transactions of the Royal Society A: Mathematical and Physical Sciences, 325: 105–126.

Elmore, A.C., Piotrowski, A.M., Wright, J.D., Scrivner, A.E., 2011. Testing the extraction of past seawater Nd isotopic composition from North Atlantic deep sea sediments and foraminifera. Geochemistry Geophysics Geosystems, 12: Q09008.

Feely, R.A. et al., 2004. Impact of Anthropogenic CO2 on the CaCO3 System in the Oceans. Science, 305: 362–366.

Field, M.P., Sherrell, R.M., 1998. Magnetic sector ICPMS with desolvating micronebulization: interference-free subpicogram determination of rare earth elements in natural samples. Analytical Chemistry, 70: 4480–4486.

Föllmi, K.B., Delamette, M., 1991. Model Simulation of Mid-Cretaceous Ocean Circulation - technical comments. Science, 251: 94–95.

Forster, A., Schouten, S., Baas, M., Sinninghe Damsté, J.S., 2007a. Mid-Cretaceous (Albian–Santonian) sea surface temperature record of the tropical Atlantic Ocean. Geology, 35: 919–922.

Forster, A., Schouten, S., Moriya, K., Wilson, P.A., Sinninghe Damsté, J.S., 2007b. Tropical warming and intermittent cooling during the Cenomanian/Turonian oceanic anoxic event 2: Sea surface temperature records from the equatorial Atlantic. Paleoceanography, 22: PA1219.

Frank, M., 2002. Radiogenic isotopes: tracers of past ocean circulation and erosional input. Reviews of Geophysics, 40.

Frank, M., Reynolds, B.C., O'Nions, R.K., 1999. Nd and Pb isotopes in Atlantic and Pacific water masses before and after closure of the Panama gateway. Geology, 27: 1147–1150.

Freslon, N., Bayon, G., Birot, D., Bollinger, C., Barrat, J.A., 2011. Determination of rare earth elements and other trace elements (Y, Mn, Co, Cr) in seawater using Tm addition and $Mg(OH)_2$ co-precipitation. Talanta, 85: 582–587.

Friedrich, O., Erbacher, J., Moriya, K., Wilson, P.A., Kuhnert, H., 2008. Warm saline intermediate waters in the Cretaceous tropical Atlantic Ocean. Nature Geosci, 1: 453–457.

Friedrich, O., Erbacher, J., Mutterlose, J., 2006. Paleoenvironmental changes across the Cenomanian/Turonian Boundary Event (Oceanic Anoxic Event 2) as indicated by benthic foraminifera from the Demerara Rise (ODP Leg 207). Revue de Micropaléontologie, 49: 121–139.

Friedrich, O., Erbacher, J., Wilson, P.A., Moriya, K., Mutterlose, J., 2009. Paleoenvironmental changes across the Mid Cenomanian Event in the tropical Atlantic Ocean (Demerara Rise, ODP Leg 207) inferred from benthic foraminiferal assemblages. Marine Micropaleontology, 71: 28–40.

Fu, Q., Yang, L., Wang, Q., 2007. On-line preconcentration with a novel alkyl phosphinic acid extraction resin coupled with inductively coupled plasma mass spectrometry for determination of trace rare earth elements in seawater. Talanta, 72: 1248–1254.

Gale, A., Christensen, W., 1996. Occurrence of the belemnite Actinocamax plenus in the Cenomanian of SE France and its significance. Bulletin of the Geological Society of Denmark, 43: 68–77.

Gale, A.S., Voigt, S., Sageman, B.B., Kennedy, W.J., 2008. Eustatic sea-level record for the Cenomanian (Late Cretaceous)—extension to the Western Interior Basin, USA. Geology, 36: 859–862.

Gale, A.S., Young, J.R., Shackleton, N.J., Crowhurst, S.J., Wray, D.S., 1999. Orbital tuning of Cenomanian marly chalk successions: towards a Milankovitch time-scale for the Late Cretaceous. Philosophical Transactions of the Royal Society of London. Series A: Mathematical, Physical and Engineering Sciences, 357: 1815–1829.

German, C.R., Elderfield, H., 1989. Rare earth elements in Saanich Inlet, British Columbia, a seasonally anoxic basin. Geochimica et Cosmochimica Acta, 53: 2561–2571.

German, C.R., Elderfield, H., 1990a. Application of the Ce anomaly as a paleoredox indicator: The ground rules. Paleoceanography, 5: 823–833.

German, C.R., Elderfield, H., 1990b. Rare earth elements in the NW Indian Ocean. Geochimica et Cosmochimica Acta, 54: 1929–1940.

German, C.R., Holliday, B.P., Elderfield, H., 1991. Redox cycling of rare earth elements in the suboxic zone of the Black Sea. Geochimica et Cosmochimica Acta, 55: 3553–3558.

German, C.R., Klinkhammer, G.P., Edmond, J.M., Mura, A., Elderfield, H., 1990. Hydrothermal scavenging of rare-earth elements in the ocean. Nature, 345: 516–518.

German, C.R., Masuzawa, T., Greaves, M.J., Elderfield, H., Edmond, J.M., 1995. Dissolved rare earth elements in the Southern Ocean: cerium oxidation and the influence of hydrography. Geochimica et Cosmochimica Acta, 59: 1551–1558.

Goldberg, E.D., Koide, M., Schmitt, R., Smith, R., 1963. Rare-earth distributions in the marine environment. Journal of Geophysical Research, 68: 4209–4217.

Goldstein, S.J., Jacobsen, S.B., 1988. Rare earth elements in river waters. Earth and Planetary Science Letters, 89: 35–47.

Goldstein, S.L., Hemming, S.R., Heinrich, D.H., Karl, K.T., 2003. Long-lived Isotopic tracers in oceanography, paleoceanography, and ice-sheet dynamics. In: Elderfield, H. (Ed.), Treatise on Geochemistry. Pergamon, Oxford, pp. 453–489.

Gordon, W., 1973. Marine life and ocean surface currents in the Cretaceous. The Journal of Geology, 81: 269–284.

Gourlan, A.T., Meynadier, L., Allegre, C.J., 2008. Tectonically driven changes in the Indian Ocean circulation over the last 25 Ma: Neodymium isotope evidence. Earth and Planetary Science Letters, 267: 353–364.

Gradstein, F.M., Ogg, J.G., Schmitz, M.D., Ogg, G.M., 2012. A geologic time scale 2012, Elsevier.

Grasse, P., Stichel, T., Stumpf, R., Stramma, L., Frank, M., 2012. The distribution of neodymium isotopes and concentrations in the Eastern Equatorial Pacific: Water mass advection versus particle exchange. Earth and Planetary Science Letters, 353–354: 198–207.

Greaves, M.J., Elderfield, H., Klinkhammer, G.P., 1989. Determination of the rare earth elements in natural waters by isotope-dilution mass spectrometry. Analytica Chimica Acta, 218: 265–280.

Greaves, M.J., Statham, P.J., Elderfield, H., 1994. Rare earth element mobilization from marine atmospheric dust into seawater. Marine Chemistry, 46: 255–260.

Haley, B.A., Klinkhammer, G.P., 2003. Complete separation of rare earth elements from small volume seawater samples by automated ion chromatography: method development and application to benthic flux. Marine Chemistry, 82: 197–220.

Halliday, A.N., Davidson, J.P., Holden, P., Owen, R.M., Olivarez, A.M., 1992. Metalliferous Sediments and the Scavenging Residence Time of Nd Near Hydrothermal Vents. Geophysical Research Letters, 19: 761–764.

Hanson, G.N., 1980. Rare earth elements in petrogenetic studies of igneous systems. Annual Review of Earth and Planetary Sciences, 8: 371–406.

Hathorne, E.C. et al., 2012. Online preconcentration ICP-MS analysis of rare earth elements in seawater. Geochemistry, Geophysics, Geosystems, 13: Q01020.

Hatta, M., Zhang, J., 2006. Possible source of advected water mass and residence times in the multi-structured Sea of Japan using rare earth elements. Geophysical Research Letters, 33: L16606.

Hay, W.W., 2008. Evolving ideas about the Cretaceous climate and ocean circulation. Cretaceous Research, 29: 725–753.

Henson, S.A., Sanders, R., Madsen, E., 2012. Global patterns in efficiency of particulate organic carbon export and transfer to the deep ocean. Global Biogeochemical Cycles, 26: GB1028.

Høgdahl, O.T., Melsom, S., Bowen Vaughan, T., 1968. Neutron activation analysis of Lanthanide elements in sea water. In: Baker, R.A. (Ed.), Trace inorganics in water. Advances in Chemistry. American chemical society, pp. 308–325.

Huber, B.T., Norris, R.D., MacLeod, K.G., 2002. Deep-sea paleotemperature record of extreme warmth during the Cretaceous. Geology: 123–126.

Hupe, A., Karstensen, J., 2000. Redfield stoichiometry in Arabian Sea subsurface waters. Global Biogeochemical Cycles, 14: 357–372.

Irving, L., 1926. The precipitation of calcium and magnesium from sea water. Journal of the Marine Biological Association of the United Kingdom (New Series), 14: 441–446.

Jarvis, I., Gale, A.S., Jenkyns, H.C., Pearce, M.A., 2006. Secular variation in Late Cretaceous carbon isotopes: a new $\delta^{13}C$ carbonate reference curve for the Cenomanian–Campanian (99.6-70.6 Ma). Geological Magazine, 143: 561–608.

Jeandel, C., Arsouze, T., Lacan, F., Téchiné, P., Dutay, J.-C., 2007. Isotopic Nd compositions and concentrations of the lithogenic inputs into the ocean: A compilation, with an emphasis on the margins. Chemical Geology, 239: 156–164.

Jeandel, C., Bishop, J.K., Zindler, A., 1995. Exchange of neodymium and its isotopes between seawater and small and large particles in the Sargasso Sea. Geochimica et Cosmochimica Acta, 59: 535–547.

Jefferies, R., 1962. The palaeoecology of the Actinocamax plenus subzone (lowest Turonian) in the Anglo-Paris Basin. Palaeontology, 4: 609–647.

Jenkyns, H.C., 2003a. Evidence for rapid climate change in the Mesozoic-Palaeogene greenhouse world. Philosophical Transactions of the Royal Society of London Series a-Mathematical Physical and Engineering Sciences, 361: 1885–1916.

Jenkyns, H.C., 2003b. Evidence for rapid climate change in the Mesozoic-Palaeogene greenhouse world. Philosophical Transactions of the Royal Society a-Mathematical Physical and Engineering Sciences, 361: 1885–1916.

Jenkyns, H.C., 2010a. Geochemistry of oceanic anoxic events. Geochemistry, Geophysics, Geosystems, 11: Q03004.

Jenkyns, H.C., 2010b. Geochemistry of oceanic anoxic events. Geochemistry Geophysics Geosystems, 11.

Jenkyns, H.C., Forster, A., Schouten, S., Damste, J.S.S., 2004. High temperatures in the Late Cretaceous Arctic Ocean. Nature, 432: 888–892.

Jenner, G.A., Longerich, H.P., Jackson, S.E., Fryer, B.J., 1990. ICP-MS – a powerful tool for high-precision trace-element analysis in Earth sciences: evidence from analysis of selected U.S.G.S. reference samples. Chemical Geology, 83: 133–148.

Jiménez Berrocoso, Á. et al., 2010. Nutrient trap for Late Cretaceous organic-rich black shales in the tropical North Atlantic. Geology, 38: 1111–1114.

John, H.C. et al., 2004. Oceanographic and faunistic structures across an Angola Current intrusion into northern Namibian waters. Journal of Marine Systems, 46: 1–22.

Johnson, K.S. et al., 2007. Developing standards for dissolved iron in seawater. Eos, Transactions American Geophysical Union, 88: 131–132.

Kaiho, K., Hasegawa, T., 1994. End-Cenomanian benthic foraminiferal extinctions and oceanic dysoxic events in the northwestern Pacific Ocean. Palaeogeography, Palaeoclimatology, Palaeoecology, 111: 29–43.

Karadaş, C., Kara, D., Fisher, A., 2011. Determination of rare earth elements in seawater by inductively coupled plasma mass spectrometry with off-line column preconcentration using 2,6-diacetylpyridine functionalized Amberlite XAD-4. Analytica Chimica Acta, 689: 184–189.

Karstensen, J., Tomczak, M., 1998. Age determination of mixed water masses using CFC and oxygen data. Journal of Geophysical Research: Oceans, 103: 18599–18609.

Katarina, R.K., Oshima, M., Motomizu, S., 2009. On-line collection/concentration and determination of transition and rare-earth metals in water samples using Multi-Auto-Pret system coupled with inductively coupled plasma-atomic emission spectrometry. Talanta, 78: 1043–1050.

Klevenz, V., Vance, D., Schmidt, D.N., Mezger, K., 2008. Neodymium isotopes in benthic foraminifera: Core-top systematics and a down-core record from the Neogene south Atlantic. Earth and Planetary Science Letters, 265: 571–587.

Klinkhammer, G.P., Elderfield, H., Edmond, J.M., Mitra, A., 1994. Geochemical implications of rare earth element patterns in hydrothermal fluids from mid-ocean ridges. Geochimica et Cosmochimica Acta, 58: 5105–5113.

Klunder, M.B., Laan, P., Middag, R., de Baar, H.J.W., Bakker, K., 2012. Dissolved iron in the Arctic Ocean: Important role of hydrothermal sources, shelf input and scavenging removal. Journal of Geophysical Research: Oceans, 117: C04014.

Kraft, S., Frank, M., Hathorne, E.C., Weldeab, S., 2013. Assessment of seawater Nd isotope signatures extracted from foraminiferal shells and authigenic phases of Gulf of Guinea sediments. Geochimica et Cosmochimica Acta, 121: 414–435.

Lacan, F., Jeandel, C., 2005a. Acquisition of the neodymium isotopic composition of the North Atlantic Deep Water. Geochemistry Geophysics Geosystems, 6.

Lacan, F., Jeandel, C., 2005b. Neodymium isotopes as a new tool for quantifying exchange fluxes at the continent-ocean interface. Earth and Planetary Science Letters, 232: 245–257.

Lacan, F., Tachikawa, K., Jeandel, C., 2012. Neodymium isotopic composition of the oceans: A compilation of seawater data. Chemical Geology, 300–301: 177–184.

Larqué, L., Maamaatuaiahutapu, K., Garçon, V., 1997. On the intermediate and deep water flows in the South Atlantic Ocean. Journal of Geophysical Research: Oceans, 102(C6): 12425-12440.

Lass, H.U., Mohrholz, V., 2008. On the interaction between the subtropical gyre and the Subtropical Cell on the shelf of the SE Atlantic. Journal of Marine Systems, 74: 1–43.

Lass, H.U., Schmidt, M., Mohrholz, V., Nausch, G., 2000. Hydrographic and Current Measurements in the Area of the Angola–Benguela Front. Journal of Physical Oceanography, 30: 2589–2609.

Lawrence, M.G., Kamber, B.S., 2007. Rare earth element concentrations in the natural water reference materials (NRCC) NASS-5, CASS-4 and SLEW-3. Geostandards and Geoanalytical Research, 31: 95–103.

Leckie, R.M., Bralower, T.J., Cashman, R., 2002. Oceanic anoxic events and plankton evolution: Biotic response to tectonic forcing during the mid-Cretaceous. Paleoceanography, 17.

Lee, J.H., Byrne, R.H., 1992. Examination of comparative rare earth element complexation behavior using linear free-energy relationships. Geochimica et Cosmochimica Acta, 56: 1127–1137.

Li, X. et al., 2006. Upper Cretaceous carbon- and oxygen-isotope stratigraphy of hemipelagic carbonate facies from southern Tibet, China. Journal of the Geological Society, 163: 375–382.

Liang, P., Liu, Y., Guo, L., 2005. Determination of trace rare earth elements by inductively coupled plasma atomic emission spectrometry after preconcentration with multiwalled carbon nanotubes. Spectrochimica Acta Part B: Atomic Spectroscopy, 60: 125–129.

Ling, H.F. et al., 1997. Evolution of Nd and Pb isotopes in Central Pacific seawater from ferromanganese crusts. Earth and Planetary Science Letters, 146: 1–12.

Ling, H.F. et al., 2005. Differing controls over the Cenozoic Pb and Nd isotope evolution of deepwater in the central North Pacific Ocean. Earth and Planetary Science Letters, 232: 345–361.

Littler, K., Robinson, S.A., Bown, P.R., Nederbragt, A.J., Pancost, R.D., 2011. High sea-surface temperatures during the Early Cretaceous Epoch. Nature Geosci, 4: 169–172.

Loope, G.R., Kump, L.R., Arthur, M.A., 2013. Shallow water redox conditions from the Permian–Triassic boundary microbialite: The rare earth element and iodine geochemistry of carbonates from Turkey and South China. Chemical Geology, 351: 195–208.

Lu, Z.L., Jenkyns, H.C., Rickaby, R.E.M., 2010. Iodine to calcium ratios in marine carbonate as a paleo-redox proxy during oceanic anoxic events. Geology, 38: 1107–1110.

Luyendyk, B.P., Forsyth, D., Phillips, J.D., 1972. Experimental Approach to the Paleocirculation of the Oceanic Surface Waters. Geological Society of America Bulletin, 83: 2649–2664.

MacLeod, K.G., Martin, E.E., Blair, S.W., 2008. Nd isotopic excursion across Cretaceous ocean anoxic event 2 (Cenomanian-Turonian) in the tropical North Atlantic. Geology, 36: 811–814.

Mahowald, N.M. et al., 2005. Atmospheric global dust cycle and iron inputs to the ocean. Global Biogeochemical Cycles, 19: GB4025.

Martin, E.E., Haley, B.A., 2000. Fossil fish teeth as proxies for seawater Sr and Nd isotopes. Geochimica Et Cosmochimica Acta, 64: 835–847.

Martin, E.E., MacLeod, K.G., Jiménez Berrocoso, A., Bourbon, E., 2012. Water mass circulation on Demerara Rise during the Late Cretaceous based on Nd isotopes. Earth and Planetary Science Letters, 327–328: 111–120.

Martin, E.E., Scher, H.D., 2004. Preservation of seawater Sr and Nd isotopes in fossil fish teeth: bad news and good news. Earth and Planetary Science Letters, 220: 25–39.

Martin, J.H., 1990. Glacial-Interglacial CO_2 Change: The Iron Hypothesis. Paleoceanography, 5: 1–13.

McLennan, S.M., 1989. Rare earth elements in sedimentary rocks; influence of provenance and sedimentary processes. Reviews in Mineralogy and Geochemistry, 21: 169–200.

Mercier, H., Arhan, M., Lutjeharms, J.R.E., 2003. Upper-layer circulation in the eastern Equatorial and South Atlantic Ocean in January–March 1995. Deep Sea Research Part I: Oceanographic Research Papers, 50: 863–887.

Meyers, S.R. et al., 2012. Intercalibration of radioisotopic and astrochronologic time scales for the Cenomanian-Turonian boundary interval, Western Interior Basin, USA. Geology, 40: 7–10.

Millero, F.J., 1992. Stability constants for the formation of rare earth-inorganic complexes as a function of ionic strength. Geochimica et Cosmochimica Acta, 56: 3123–3132.

Mitchell, S.F., Carr, I.T., 1998. Foraminiferal response to mid-Cenomanian (Upper Cretaceous) palaeoceanographic events in the Anglo-Paris Basin (Northwest Europe). Palaeogeography, Palaeoclimatology, Palaeoecology, 137: 103–125.

Mitra, A., Elderfield, H., Greaves, M.J., 1994. Rare earth elements in submarine hydrothermal fluids and plumes from the Mid-Atlantic Ridge. Marine Chemistry, 46: 217–235.

Moffett, J.W., 1990. Microbially mediated cerium oxidation in sea water. Nature, 345: 421–423.

Moffett, J.W., 1994a. A radiotracer study of cerium and manganese uptake onto suspended particles in Chesapeake Bay. Geochimica et Cosmochimica Acta, 58: 695–703.

Moffett, J.W., 1994b. The Relationship Between Cerium and Manganese Oxidation in the Marine Environment. Limnology and Oceanography, 39: 1309–1318.

Mohrholz, V., Bartholomae, C.H., van der Plas, A.K., Lass, H.U., 2008. The seasonal variability of the northern Benguela undercurrent and its relation to the oxygen budget on the shelf. Continental Shelf Research, 28: 424–441.

Moiroud, M. et al., 2013. Evolution of the neodymium isotopic signature of neritic seawater on a northwestern Pacific margin: new constrains on possible end-members for the composition of deep-water masses in the Late Cretaceous ocean. Chemical Geology, 356: 160–170.

Moriya, K., Wilson, P.A., Friedrich, O., Erbacher, J., Kawahata, H., 2007. Testing for ice sheets during the mid-Cretaceous greenhouse using glassy foraminiferal calcite from the mid-Cenomanian tropics on Demerara Rise. Geology, 35: 615–618.

Murphy, D.P., Thomas, D.J., 2012. Cretaceous deep-water formation in the Indian sector of the Southern Ocean. Paleoceanography, 27: PA1211.

Nishioka, J., Obata, H., Tsumune, D., 2013. Evidence of an extensive spread of hydrothermal dissolved iron in the Indian Ocean. Earth and Planetary Science Letters, 361: 26–33.

Noble, A.E. et al., 2012. Basin-scale inputs of cobalt, iron, and manganese from the Benguela-Angola front to the South Atlantic Ocean. Limnology and Oceanography, 57: 989–1010.

Norris, R.D., Bice, K.L., Magno, E.A., Wilson, P.A., 2002. Jiggling the tropical thermostat in the Cretaceous hothouse. Geology, 30: 299–302.

Nozaki, Y., 2001a. Rare earth elements and their isotopes. Encyclopedia of Ocean Sciences, 4: 2354–2366.

Nozaki, Y., 2001b. Rare Earth Elements and their Isotopes in the Ocean. In: John, H.S. (Ed.), Encyclopedia of Ocean Sciences. Academic Press, Oxford, pp. 2354–2366.

Nozaki, Y., Alibo, D.S., 2003. Importance of vertical geochemical processes in controlling the oceanic profiles of dissolved rare earth elements in the northeastern Indian Ocean. Earth and Planetary Science Letters, 205: 155–172.

Nozaki, Y., Lerche, D., Alibo, D.S., Tsutsumi, M., 2000. Dissolved indium and rare earth elements in three Japanese rivers and Tokyo Bay: evidence for anthropogenic Gd and In. Geochimica et Cosmochimica Acta, 64: 3975–3982.

O'Nions, R.K., Hamilton, P.J., Evensen, N.M., 1977. Variations in $^{143}Nd/^{144}Nd$ and $^{87}Sr/^{86}Sr$ ratios in oceanic basalts. Earth and Planetary Science Letters, 34: 13–22.

Oka, A., Hasumi, H., Obata, H., Gamo, T., Yamanaka, Y., 2009. Study on vertical profiles of rare earth elements by using an ocean general circulation model. Global Biogeochem. Cycles, 23.

Otto-Bliesner, B.L., Brady, E.C., Shields, C., 2002. Late Cretaceous ocean: Coupled simulations with the National Center for Atmospheric Research Climate System Model. J. Geophys. Res., 107.

Pasinli, T., Eroğlu, A.E., Shahwan, T., 2005. Preconcentration and atomic spectrometric determination of rare earth elements (REEs) in natural water samples by inductively coupled plasma atomic emission spectrometry. Analytica Chimica Acta, 547: 42–49.

Patchett, P.J., Vervoort, J.D., Söderlund, U., Salters, V.J.M., 2004. Lu–Hf and Sm–Nd isotopic systematics in chondrites and their constraints on the Lu–Hf properties of the Earth. Earth and Planetary Science Letters, 222: 29–41.

Paul, C.R.C. et al., 1994. Palaeoceanographic events in the Middle Cenomanian of Northwest Europe. Cretaceous Research, 15: 707–738.

Piepgras, D.J., Wasserburg, G.J., 1980. Neodymium isotopic variations in seawater. Earth and Planetary Science Letters, 50: 128–138.

Piepgras, D.J., Wasserburg, G.J., 1982. Isotopic Composition of Neodymium in Waters from the Drake Passage. Science, 217: 207–214.

Piepgras, D.J., Wasserburg, G.J., 1987. Rare earth element transport in the western North Atlantic inferred from Nd isotopic observations. Geochimica Et Cosmochimica Acta, 51: 1257–1271.

Piepgras, D.J., Wasserburg, G.J., Dasch, E.J., 1979. The isotopic composition of Nd in different ocean masses. Earth and Planetary Science Letters, 45: 223–236.

Piotrowski, A.M. et al., 2012. Reconstructing deglacial North and South Atlantic deep water sourcing using foraminiferal Nd isotopes. Earth and Planetary Science Letters, 357–358: 289–297.

Piotrowski, A.M., Goldstein, S.L., Hemming, S.R., Fairbanks, R.G., 2005. Temporal relationships of carbon cycling and ocean circulation at glacial boundaries. Science, 307: 1933–1938.

Pogge von Strandmann, P.A.E., Jenkyns, H.C., Woodfine, R.G., 2013. Lithium isotope evidence for enhanced weathering during Oceanic Anoxic Event 2. Nature Geosci, 6: 668–672.

Pomies, C., Davies, G.R., Conan, S.M.H., 2002. Neodymium in modern foraminifera from the Indian Ocean: implications for the use of foraminiferal Nd isotope compositions in paleo-oceanography. Earth and Planetary Science Letters, 203: 1031–1045.

Poulsen, C., Seidov, D., Barron, E., Peterson, W., 1998a. The impact of paleogeographic evolution on the surface oceanic. Paleoceanography, 13: 546–559.

Poulsen, C.J., Barron, E.J., Arthur, M.A., Peterson, W.H., 2001. Response of the mid-Cretaceous global oceanic circulation to tectonic and CO_2 forcings. Paleoceanography, 16: 576–592.

Poulsen, C.J., Seidov, D., Barron, E.J., Peterson, W.H., 1998b. The impact of paleogeographic evolution on the surface oceanic circulation and the marine environment within the mid-Cretaceous Tethys. Paleoceanography, 13: 546–559.

Pucéat, E., Lécuyer, C., Reisberg, L., 2005. Neodymium isotope evolution of NW Tethyan upper ocean waters throughout the Cretaceous. Earth and Planetary Science Letters, 236: 705–720.

Rahmi, D., Zhu, Y., Fujimori, E., Umemura, T., Haraguchi, H., 2007. Multielement determination of trace metals in seawater by ICP-MS with aid of down-sized chelating resin-packed minicolumn for preconcentration. Talanta, 72: 600–606.

Rahmstorf, S., 2002. Ocean circulation and climate during the past 120,000 years. Nature, 419: 207–214.

Rahmstorf, S., 2003. Thermohaline circulation: The current climate. Nature, 421: 699–699.

Rempfer, J., Stocker, T.F., Joos, F., Dutay, J.-C., Siddall, M., 2011. Modelling Nd-isotopes with a coarse resolution ocean circulation model: Sensitivities to model parameters and source/sink distributions. Geochimica Et Cosmochimica Acta, 75: 5927–5950.

Reynard, B., Lecuyer, C., Grandjean, P., 1999. Crystal-chemical controls on rare-earth element concentrations in fossil biogenic apatites and implications for paleoenvironmental reconstructions. Chemical Geology, 155: 233–241.

Rickli, J. et al., 2010. Hafnium and neodymium isotopes in surface waters of the eastern Atlantic Ocean: Implications for sources and inputs of trace metals to the ocean. Geochimica Et Cosmochimica Acta, 74: 540–557.

Rickli, J., Frank, M., Halliday, A.N., 2009. The hafnium-neodymium isotopic composition of Atlantic seawater. Earth and Planetary Science Letters, 280: 118–127.

Roberts, N.L., Piotrowski, A.M., McManus, J.F., Keigwin, L.D., 2010. Synchronous Deglacial Overturning and Water Mass Source Changes. Science, 327: 75–78.

Robinson, S.A., Murphy, D.P., Vance, D., Thomas, D.J., 2010. Formation of "Southern Component Water" in the Late Cretaceous: Evidence from Nd-isotopes. Geology, 38: 871–874.

Robinson, S.A., Vance, D., 2012. Widespread and synchronous change in deep-ocean circulation in the North and South Atlantic during the Late Cretaceous. Paleoceanography, 27: PA1102.

Rodríguez-González, P., Marchante-Gayón, J.M., García Alonso, J.I., Sanz-Medel, A., 2005. Isotope dilution analysis for elemental speciation: a tutorial review. Spectrochimica Acta Part B: Atomic Spectroscopy, 60: 151–207.

Rosenthal, Y., Boyle, E.A., Labeyrie, L., 1997. Last Glacial Maximum Paleochemistry and Deepwater Circulation in the Southern Ocean: Evidence From Foraminiferal Cadmium. Paleoceanography, 12: 787–796.

Rudnicki, M.D., Elderfield, H., 1993. A chemical model of the buoyant and neutrally buoyant plume above the TAG vent field, 26 degrees N, Mid-Atlantic Ridge. Geochimica et Cosmochimica Acta, 57: 2939–2957.

Rüth, C., Well, R., Roether, W., 2000. Primordial ^{3}He in South Atlantic deep waters from sources on the mid-Atlantic ridge. Deep Sea Research Part I: Oceanographic Research Papers, 47: 1059–1075.

Saito, M.A. et al., 2013. Slow-spreading submarine ridges in the South Atlantic as a significant oceanic iron source. Nature Geosci, 6: 775–779.

Sander, S.G., Koschinsky, A., 2011. Metal flux from hydrothermal vents increased by organic complexation. Nature Geosci, 4: 145–150.

Sander, S.G., Koschinsky, A., Massoth, G., Stott, M., Hunter, K.A., 2007. Organic complexation of copper in deep-sea hydrothermal vent systems. Environmental Chemistry, 4: 81–89.

Sarmiento, J.L. et al., 2007. Deep ocean biogeochemistry of silicic acid and nitrate. Global Biogeochemical Cycles, 21: GB1S90.

Schijf, J., De Baar, H.J.W., Millero, F.J., 1995. Vertical distributions and speciation of dissolved rare earth elements in the anoxic brines of Bannock Basin, eastern Mediterranean Sea. Geochimica et Cosmochimica Acta, 59: 3285–3299.

Schlanger, S.O., Arthur, M.A., Jenkyns, H.C., Scholle, P.A., 1987. The Cenomanian–Turonian oceanic anoxic event, I. Stratigraphy and distribution of organic carbon-rich beds and the marine $\delta^{13}C$ excursion. Geological Society, London, Special Publications, 26: 371–399.

Schlanger, S.O., Jenkyns, H.C., 1976. Cretaceous oceanic anoxic events: Causes and consequences. GEOLOGIE EN MIJNBOUW, 55: 179–184.

Schmidt, K., Garbe-Schönberg, D., Bau, M., Koschinsky, A., 2010. Rare earth element distribution in >400°C hot hydrothermal fluids from 5°S, MAR: The role of anhydrite in controlling highly variable distribution patterns. Geochimica et Cosmochimica Acta, 74: 4058–4077.

SCOR Working Group, 2007. GEOTRACES – An international study of the global marine biogeochemical cycles of trace elements and their isotopes. Chemie der Erde - Geochemistry, 67: 85–131.

Shabani, M.B., Akagi, T., Shimizu, H., Masuda, A., 1990. Determination of trace lanthanides and yttrium in seawater by inductively coupled plasma mass spectrometry after preconcentration with solvent extraction and back-extraction. Analytical Chemistry, 62: 2709–2714.

Shaw, T.J., Duncan, T., Schnetger, B., 2003. A Preconcentration/Matrix Reduction Method for the Analysis of Rare Earth Elements in Seawater and Groundwaters by Isotope Dilution ICPMS. Analytical Chemistry, 75: 3396–3403.

Sholkovitz, E.R., 1995. The aquatic chemistry of rare earth elements in rivers and estuaries. Aquatic Geochemistry, 1: 1–34.

Sholkovitz, E.R., Elderfield, H., Szymczak, R., Casey, K., 1999. Island weathering: river sources of rare earth elements to the Western Pacific Ocean. Marine Chemistry, 68: 39–57.

Sholkovitz, E.R., Landing, W.M., Lewis, B.L., 1994. Ocean particle chemistry: the fractionation of rare earth elements between suspended particles and seawater. Geochimica et Cosmochimica Acta, 58: 1567–1579.

Sholkovitz, E.R., Shaw, T.J., Schneider, D.L., 1992. The geochemistry of rare earth elements in the seasonally anoxic water column and porewaters of Chesapeake Bay. Geochimica et Cosmochimica Acta, 56: 3389–3402.

Siddall, M. et al., 2008. Towards explaining the Nd paradox using reversible scavenging in an ocean general circulation model. Earth and Planetary Science Letters, 274: 448–461.

Sigman, D.M., Boyle, E.A., 2000. Glacial/interglacial variations in atmospheric carbon dioxide. Nature, 407: 859–869.

Singh, S.P., Singh, S.K., Goswami, V., Bhushan, R., Rai, V.K., 2012. Spatial distribution of dissolved neodymium and εNd in the Bay of Bengal: Role of particulate matter and mixing of water masses. Geochimica et Cosmochimica Acta, 94: 38–56.

Sinninghe Damsté, J.S., van Bentum, E.C., Reichart, G.-J., Pross, J., Schouten, S., 2010. A CO_2 decrease-driven cooling and increased latitudinal temperature gradient during the mid-Cretaceous Oceanic Anoxic Event 2. Earth and Planetary Science Letters, 293: 97–103.

Snow, L.J., Duncan, R.A., Bralower, T.J., 2005. Trace element abundances in the Rock Canyon Anticline, Pueblo, Colorado, marine sedimentary section and their relationship to Caribbean plateau construction and oxygen anoxic event 2. Paleoceanography, 20: PA3005.

Soudry, D., Glenn, C.R., Nathan, Y., Segal, I., VonderHaar, D., 2006. Evolution of Tethyan phosphogenesis along the northern edges of the Arabian-African shield during the Cretaceous-Eocene as deduced from temporal variations of Ca and Nd isotopes and rates of P accumulation. Earth-Science Reviews, 78: 27–57.

Stichel, T., Frank, M., Rickli, J., Haley, B.A., 2012. The hafnium and neodymium isotope composition of seawater in the Atlantic sector of the Southern Ocean. Earth and Planetary Science Letters, 317–318: 282–294.

Stoll, H.M., Schrag, D.P., 2000. High-resolution stable isotope records from the Upper Cretaceous rocks of Italy and Spain: glacial episodes in a greenhouse planet? Geological Society of America Bulletin, 112: 308–319.

Stramma, L., England, M., 1999. On the water masses and mean circulation of the South Atlantic Ocean. J. Geophys. Res., 104: 20863–20883.

Stramma, L., Schott, F., 1999. The mean flow field of the tropical Atlantic Ocean. Deep Sea Research Part II: Topical Studies in Oceanography, 46: 279–303.

Tachikawa, K., Jeandel, C., Roy-Barman, M., 1999a. A new approach to the Nd residence time in the ocean: the role of atmospheric inputs. Earth and Planetary Science Letters, 170: 433–446.

Tachikawa, K., Jeandel, C., Vangriesheim, A., Dupr, B., 1999b. Distribution of rare earth elements and neodymium isotopes in suspended particles of the tropical Atlantic Ocean (EUMELI site). Deep Sea Research Part I: Oceanographic Research Papers, 46: 733–755.

Tachikawa, K., Toyofuku, T., Basile-Doelsch, I., Delhaye, T., 2013. Microscale neodymium distribution in sedimentary planktonic foraminiferal tests and associated mineral phases. Geochimica et Cosmochimica Acta, 100: 11–23.

Takeda, S., 1998. Influence of iron availability on nutrient consumption ratio of diatoms in oceanic waters. Nature, 393: 774–777.

Tarantola, A., 2005. Inverse problem theory and methods for model parameter estimation. siam.

Tebo, B.M. et al., 2004. Biogenic manganese oxides: Properties and Mechanisms of Formation. Annual Review of Earth and Planetary Sciences, 32: 287–328.

Tegner, C., Storey, M., Holm, P.M., Thorarinsson, S.B., Zhao, X., Lo, C.-H., Knudsen, M.F., 2011. Magmatism and Eurekan deformation in the High Arctic Large Igneous Province: ^{40}Ar-^{39}Ar age of Kap Washington Group volcanics, North Greenland. Earth and Planet. Sci. Lett. 303, 203–214.

Tomczak, M., Large, D.G.B., 1989. Optimum multiparameter analysis of mixing in the thermocline of the eastern Indian Ocean. Journal of Geophysical Research: Oceans, 94: 16141–16149.

Toner, B.M. et al., 2009. Preservation of iron(II) by carbon-rich matrices in a hydrothermal plume. Nature Geosci, 2: 197–201.

Topper, R.P.M., Trabucho Alexandre, J., Tuenter, E., Meijer, P.T., 2011. A regional ocean circulation model for the mid-Cretaceous North Atlantic Basin: implications for black shale formation. Clim. Past, 7: 277–297.

Trabucho Alexandre, J. et al., 2010. The mid-Cretaceous North Atlantic nutrient trap: Black shales and OAEs. Paleoceanography, 25: PA4201.

Turgeon, S.C., Creaser, R.A., 2008. Cretaceous oceanic anoxic event 2 triggered by a massive magmatic episode. Nature, 454: 323–326.

van Bennekom, A.J., Berger, G.W., 1984. Hydrography and silica budget of the Angola Basin. Netherlands Journal of Sea Research, 17: 149–200.

van Bentum, E.C. et al., 2009. Reconstruction of water column anoxia in the equatorial Atlantic during the Cenomanian-Turonian oceanic anoxic event using biomarker and trace metal proxies. Palaeogeography, Palaeoclimatology, Palaeoecology, 280: 489–498.

van de Flierdt, T. et al., 2012. GEOTRACES intercalibration of neodymium isotopes and rare earth element concentrations in seawater and suspended particles. Part 1: reproducibility of results for the international intercomparison. Limnology and Oceanography-Methods, 10: 234–251.

van de Flierdt, T., Robinson, L.F., Adkins, J.F., 2010. Deep-sea coral aragonite as a recorder for the neodymium isotopic composition of seawater. Geochimica et Cosmochimica Acta, 74: 6014–6032.

Vance, D., Burton, K., 1999. Neodymium isotopes in planktonic foraminifera: a record of the response of continental weathering and ocean circulation rates to climate change. Earth and Planetary Science Letters, 173: 365–379.

Vance, D. et al., 2004. The use of foraminifera as a record of the past neodymium isotope composition of seawater. Paleoceanography, 19.

Vanicek, M., Siedler, G., 2002. Zonal Fluxes in the Deep Water Layers of the Western South Atlantic Ocean. Journal of Physical Oceanography, 32: 2205–2235.

Voigt, S., Gale, A.S., Flögel, S., 2004. Midlatitude shelf seas in the Cenomanian-Turonian greenhouse world: temperature evolution and North Atlantic circulation. Paleoceanography, 19: PA4020.

Voigt, S. et al., 2013. Tectonically restricted deep-ocean circulation at the end of the Cretaceous greenhouse. Earth and Planetary Science Letters, 369–370: 169–177.

von Blanckenburg, F., 1999. Perspectives: Paleoceanography - Tracing past ocean circulation? Science, 286: 1862–1863.

Warren, B.A., Speer, K.G., 1991. Deep circulation in the eastern South Atlantic Ocean. Deep Sea Research Part A. Oceanographic Research Papers, 38, Supplement 1: S281–S322.

Wienders, N., Arhan, M., Mercier, H., 2000. Circulation at the western boundary of the South and Equatorial Atlantic: Exchanges with the ocean interior. Journal of Marine Research, 58: 1007–1039.

Willie, S.N., Sturgeon, R.E., 2001. Determination of transition and rare earth elements in seawater by flow injection inductively coupled plasma time-of-flight mass spectrometry. Spectrochimica Acta Part B: Atomic Spectroscopy, 56: 1707–1716.

Wilmsen, M., 2003. Sequence stratigraphy and palaeoceanography of the Cenomanian Stage in northern Germany. Cretaceous Research, 24: 525–568.

Wilmsen, M., 2007. Integrated stratigraphy of the upper Lower – lower Middle Cenomanian of northern Germany and southern England. *Acta Geologica Polonica*, 57: 263–279.

Wilson, D.J., Piotrowski, A.M., Galy, A., Clegg, J.A., 2013. Reactivity of neodymium carriers in deep sea sediments: Implications for boundary exchange and paleoceanography. Geochimica Et Cosmochimica Acta, 109: 197–221.

Wilson, P.A., Norris, R.D., Cooper, M.J., 2002. Testing the Cretaceous greenhouse hypothesis using glassy foraminiferal calcite from the core of the Turonian tropics on Demerara Rise. Geology, 30: 607.

Wood, S., 1990a. The aqueous geochemistry of the rare-earth elements and yttrium: 2. Theoretical predictions of speciation in hydrothermal solutions to 350° C at saturation water vapor pressure. Chemical Geology, 88: 99–125.

Wood, S.A., 1990b. The aqueous geochemistry of the rare-earth elements and yttrium: 1. Review of available low-temperature data for inorganic complexes and the inorganic REE speciation of natural waters. Chemical Geology, 82: 159–186.

Zhang, J., Nozaki, Y., 1996. Rare earth elements and yttrium in seawater: ICP-MS determinations in the East Caroline, Coral Sea, and South Fiji basins of the western South Pacific Ocean. Geochimica et Cosmochimica Acta, 60: 4631–4644.

Zhang, Y., Lacan, F., Jeandel, C., 2008. Dissolved rare earth elements tracing lithogenic inputs over the Kerguelen Plateau (Southern Ocean). Deep Sea Research Part II: Topical Studies in Oceanography, 55: 638–652.

Zheng, X.-Y., Jenkyns, H.C., Gale, A.S., Ward, D.J., Henderson, G.M., 2013. Changing ocean circulation and hydrothermal inputs during Ocean Anoxic Event 2 (Cenomanian–Turonian): Evidence from Nd-isotopes in the European shelf sea. Earth and Planetary Science Letters, 375: 338–348.

Zhu, Y., Itoh, A., Fujimori, E., Umemura, T., Haraguchi, H., 2006. Determination of rare earth elements in seawater by ICP-MS after preconcentration with a chelating resin-packed minicolumn. Journal of Alloys and Compounds, 408–412: 985–988.

Zhu, Y., Umemura, T., Haraguchi, H., Inagaki, K., Chiba, K., 2009. Determination of REEs in seawater by ICP-MS after on-line preconcentration using a syringe-driven chelating column. Talanta, 78: 891–895.